TECHNISCHE UNIVERSITÄT MÜNCHEN
Fachgebiet Computational Mechanics

Finite-Element Based Determination of Response Spectra of Viscoelastic Materials Subjected to Low-Velocity Impact Loading

Martin Johannes Herrenbrück

Vollständiger Abdruck der von der Ingenieurfakultät Bau Geo Umwelt der Technischen Universität München zur Erlangung des akademischen Grades eines

Doktor-Ingenieurs

genehmigten Dissertation.

Vorsitzender: Univ.-Prof. Dr.-Ing. Christoph Gehlen

Prüfer der Dissertation:

1. Univ.-Prof. Dr. techn. Roman Lackner, Leopold-Franzens-Universität Innsbruck, Österreich
2. Univ.-Prof. Dr.-Ing. habil. Fabian Duddeck

Die Dissertation wurde am 22.05.2013 bei der Technischen Universität München eingereicht und durch die Ingenieurfakultät Bau Geo Umwelt am 13.09.2013 angenommen.

Danksagung

Die vorliegende Arbeit entstand während meiner Zeit als wissenschaftlicher Assistent am Fachgebiet Computational Mechanics der Technischen Universität München (TUM). Viele Leute haben zu ihrem Gelingen beigetragen, sei es auf wissenschaftlicher oder persönlicher Ebene. Deshalb möchte ich mich bedanken bei

- Univ.-Prof. Dipl.-Ing. Dr. techn. Roman Lackner, Leiter des Arbeitsbereichs für Materialtechnologie (MTI) an der Universität Innsbruck, für die gute Betreuung aus der Ferne und während meiner Aufenthalte am MTI, aber auch für alles andere, was ich von ihm lernen konnte,
- Univ.-Prof. Dr.-Ing. habil. Fabian Duddeck, Inhaber des Fachgebiets Computational Mechanics an der TUM, für sein Interesse an meinem Forschungsgebiet und die Freiräume, die er mir dafür ließ,
- Univ.-Prof. Dr.-Ing. Christoph Gehlen, Inhaber des Lehrstuhls für Werkstoffe und Werkstoffprüfung im Bauwesen an der TUM, für den Vorsitz der Prüfungskommission,
- Univ.-Prof. Dr.-Ing. Kai-Uwe Bletzinger, Inhaber des Lehrstuhls für Statik an der TUM, für seine viele Jahre währende Begleitung,
- der International Graduate School of Science and Engineering (IGSSE) der TUM für die finanzielle und wissenschaftliche Unterstützung im Projekt 3.08 “Multiscale Optimization of Materials Subjected to Impact Loading”,
- meinem Projektpartner Casper Schousboe Andreasen (Danmarks Tekniske Universitet) für die angenehme Zusammenarbeit und das gute Verständnis während der jeweiligen Auslandsaufenthalte sowie bei seinen Betreuern Ole Sigmund und Martin Bendsøe,
- den Kollegen am Fachgebiet Computational Mechanics und am Lehrstuhl für Statik für die gute Atmosphäre und die fachlichen Diskussionen – insbesondere bei Önay Can, Gesche Diekmann, Ute Israel, Joseph Jordan, Johannes Linhard und Roland Wüchner,
- den Kollegen am MTI für die Hilfe bei der Durchführung von Experimenten, namentlich Peter Paulini, Sandro Weisheit, Andreas Saxer, Hans Lun und insbesondere Marcus Maier, sowie bei Christian Pichler für die fachliche Hilfe,
- den Mitarbeitern A.T. und T.M. des DampVisc-Schaumstoffherstellers sowie der Firma Getzner für die freundliche Überlassung der Probekörper,

- Helge Bergander, Emeritus der TU Dresden, für seine Hinweise bezüglich der Rücktransformation des Powerlaws,
- meinen Eltern Irmela und Fritz für ihre Liebe und Unterstützung und
- meiner Frau Susanne für ihr Dasein, ihr Verständnis und ihre Liebe.

Der Dank geht auch an diejenigen, die hier nicht namentlich genannt wurden. Es war eine schöne Zeit.

München, im Oktober 2013
Martin Zerrenbrück

Finite-Elemente-basierte Bestimmung der Antwortspektren viskoelastischer Materialien bei gemäßigter Stoßbelastung

Kurzfassung. In der vorliegenden Arbeit wird mit Hilfe der Finiten-Elemente-Methode das Verhalten von linear viskoelastischen Materialien untersucht, die einer Stoßbelastung durch eine nicht deformierbare Kugel ausgesetzt sind. Die Darstellung der Ergebnisse erfolgt in Form von dimensionslosen Parametern, wodurch die Komplexität des Problems deutlich reduziert wird. Damit ist es möglich, die Zusammenhänge als sogenannte Master Curves in übersichtlichen zwei-dimensionalen Diagrammen zu repräsentieren.

Zur Skalierung der dimensionsbehafteten Problemgrößen wird sowohl der Zeitverlauf der Eindringung des Impaktors verwendet als auch auf die analytische Lösung nach Heinrich Hertz für den Stoßvorgang im Falle eines rein elastischen Halbraums zurückgegriffen. Aus diesem Grund wird eine relativ geringe Anfangsgeschwindigkeit verwendet, welche eine entsprechend lange Kontaktzeit zur Folge hat. Somit ist es möglich, aufgrund von viskoelastischen Prozessen einen Teil der durch den Impaktor eingebrachten Energie zu dissipieren.

Dieser Vorgang wird bei Protektoren ausgenutzt, die im Fall einer ungewollten Stoßbelastung die auftretenden Kräfte minimieren sollen. Deshalb ist es notwendig, das viskoelastische Materialverhalten so auf die Belastung abzustimmen, dass eine minimale Belastung infolge der Abbremsung des Impaktors erreicht wird. Auf der anderen Seite darf die über die Kontaktzeit zunehmende Nachgiebigkeit des Materials nicht zu einer zu großen Penetration des Impaktors führen. Die Erfüllung dieser konträren Designkriterien wird in dieser Arbeit mit Hilfe einer Pareto-Optimierung gelöst.

Darüberhinaus können die Antwortspektren auch zur Bestimmung unbekannter Materialparameter einer viskoelastischen Materialprobe mit Hilfe von Stoßexperimenten verwendet werden. Diese Anwendung kommt zum Beispiel bei der Qualitätskontrolle von viskoelastischen Produkten zum Einsatz. Die in dieser Arbeit entwickelte Vorgehensweise wird mit Hilfe von Labor-Experimenten an Polyurethan-Schaumstoffen validiert.

Finite-Element Based Determination of Response Spectra of Viscoelastic Materials Subjected to Low-Velocity Impact Loading

Abstract. This work investigates by means of the finite element method the behaviour of viscoelastic materials subjected to an impact loading by a non-deformable sphere. The results are presented in form of dimensionless parameters; hence, the complexity of the problem is significantly reduced. Thus, it is possible to represent the governing relations through so-called master curves in accessible two-dimensional graphs.

For the scaling of the dimensional problem parameters the time history of the impactor's penetration is used together with the analytical solution for the impact event in case of a purely elastic half-space according to Heinrich Hertz. Thus, a comparatively small initial velocity is used which results in a rather long contact duration. Consequently, a part of the energy introduced by the impactor may be dissipated through viscoelastic processes.

This effect is utilised by protective equipment designed to minimise the forces occurring in unintentional impact situations. Thus, it is necessary to tune the viscoelastic material behaviour to the impact event such that a minimal loading due to the deceleration of the impactor is obtained. On the other hand, a too large penetration of the impactor owing to the increase in material compliance during contact must be prevented. The consideration of these two conflicting design criteria is realised in this work by a multi-objective optimisation.

Moreover, the response spectra can be used for the determination of unknown material parameters of a viscoelastic material sample by means of impact experiments. This application may be utilised e.g. in the quality control of viscoelastic products. The procedure developed in this work is validated by laboratory experiments using polyurethane foams.

Contents

List of Symbols

Indicating dimensions

In Newtonian mechanics, the three dimensions M (mass dimension), L (length dimension), and T (time dimension) are commonly used (please refer to Subsection C.1 for a deeper investigation of this topic). To save writing effort, the following notation will be sometimes applied, where "dim" should be read as "dimension of":

- "[kg]" for a mass-like quantity, say M, where $\dim\ M = \mathsf{M}^{+1}\,\mathsf{L}^{0}\,\mathsf{T}^{0}$.
- "[m]" for a length-like quantity, say u, where $\dim\ u = \mathsf{M}^{0}\,\mathsf{L}^{+1}\,\mathsf{T}^{0}$.
- "[m/s]" for a velocity-like quantity, say V, where $\dim\ V = \mathsf{M}^{0}\,\mathsf{L}^{+1}\,\mathsf{T}^{-1}$.
- "[m/s^2]" for an acceleration-like quantity, say a, where $\dim\ a = \mathsf{M}^{0}\,\mathsf{L}^{+1}\,\mathsf{T}^{-2}$.
- "[s]" for a time-like quantity, say t, where $\dim\ t = \mathsf{M}^{0}\,\mathsf{L}^{0}\,\mathsf{T}^{+1}$.
- "[1/s]" for a frequency-like quantity, say ω, where $\dim\ \omega = \mathsf{M}^{0}\,\mathsf{L}^{0}\,\mathsf{T}^{-1}$.
- "[N]" for a force-like quantity, say F, where $\dim\ F = \mathsf{M}^{+1}\,\mathsf{L}^{+1}\,\mathsf{T}^{-2}$.
- "[Pa]" for a pressure-like quantity, say σ, where $\dim\ \sigma = \mathsf{M}^{+1}\,\mathsf{L}^{-1}\,\mathsf{T}^{-2}$
- "[–]" for a non-dimensional quantity, say Π, where $\dim\ \Pi = \mathsf{M}^{0}\,\mathsf{L}^{0}\,\mathsf{T}^{0}$.

In the following, the most important symbols are listed. For brevity, not all symbols used in this work are included; also, a symbol listed below may occasionally be used with a different meaning than what is stated here.

Latin small letters

Symbol	M	L	T	Explanation
a	0	1	-2	acceleration/deceleration
d	-	-	-	normalised distance, see Eqn. (D.4)
e	-	-	-	deviatoric strain, see Section 2.4.1
e	-	-	-	Euler's number: e = exp(1) ≈ 2.71828
f	?	?	?	objective function, see Section D.1
$f(r)$	0	1	0	indenter shape function, see Section 2.5.1
i	-	-	-	imaginary unit, see Eqn. (A.1)
p	0	0	-1	coordinate in Laplace-Carson space
p	1	-1	-2	pressure distribution
r	0	1	0	radius direction in axisymmetric model, see Section 2.5.1
s	1	-1	-2	deviatoric stress, see Section 2.4.1
s	0	0	-1	coordinate in Laplace space
t	0	0	1	physical time
u	0	1	0	penetration depth, position of the impactor tip
v_{final}	0	1	-1	rebound velocity after contact

Latin capital letters

Symbol	M	L	T	Explanation
C_0, C_1	?	?	?	constants for $f(r)$, see Section 2.5.1
E	1	-1	-2	Young's modulus, or one-dimensional spring stiffness
F	?	?	?	multi-objective function, see Section D.1
F	1	1	-2	Force
G	1	-1	-2	shear modulus, see Eqn. (2.29)
$\mathsf{H}(t)$	-	-	-	Heaviside distribution (unit step function)
$J(t)$	-1	1	2	creep compliance, see Eqn. (2.3)
K	1	-1	-2	bulk modulus, see Eqn. (2.28)
M	1	0	0	mass of the impacting sphere
P	1	-1	-2	(max.) pressure
P_∂, Q_∂	-	-	-	differential operators, see Eqn. (2.12)
RHS	?	?	?	right hand side of an equation
R	0	1	0	radius of the impacting sphere

$R(t)$	1	-1	-2	relaxation modulus, see Eqn. (2.6)
$R^*(\omega)$	1	-1	-2	complex relaxation modulus, see Eqn. (2.9)
$R'(\omega)$	1	-1	-2	storage modulus, see Eqn. (2.10)
$R''(\omega)$	1	-1	-2	loss modulus, see Eqn. (2.10)
V	0	1	-1	initial velocity of the impacting sphere
V	0	3	0	volume of a body
Y	1	-1	-2	indentation modulus, see Eqn. (2.31)

Greek letters

Symbol	M	L	T	Explanation
α	-	-	-	stiffness ratio in the standard linear solid, see Section B.2
β	-	-	-	exponent for the power law model, see Section B.3
γ	-	-	-	factor for the square root Kelvin-Voigt model, see Section B.4
δ_{ij}	-	-	-	Kronecker delta
$\delta(t)$	-	-	-	Dirac distribution
$\delta(\omega)$	-	-	-	phase shift depending on harmonic excitation (loss angle)
$\tan\delta$	-	-	-	loss tangent, see Eqn. (2.11)
ε	-	-	-	strain
η	1	-1	-1	dynamic viscosity
θ	0	0	1	half the contact duration in elastic impact, see Eqn. (2.71)
ϑ	0	0	1	dummy variable for integration w.r.t. time
λ	-	-	-	factor for the logarithmic creep model, see Section B.5
ν	-	-	-	Poisson's ratio
Π	-	-	-	dimensionless parameter, see Eqn. (4.3)
ρ	1	-3	0	density
σ	1	-1	-2	stress, pressure
τ	0	0	1	characteristic time in the viscoelastic model
ω	0	0	-1	excitation frequency, see Eqn. (2.7)

Superscripts, subscripts and the like

Symbol	M	L	T	Explanation
$\widehat{(\bullet)}$	?	?	?	Laplace transform $\mathscr{L}$ of $(\bullet)$, see Section A.3
$(\bullet)^*$	?	?	?	Laplace-Carson transform $\mathscr{LC}$ of $(\bullet)$, see Section A.3

$(\bullet)^*$	?	?	?	the parameter $(\bullet)$ is at an optimum, see Appendix D
$(\bullet)^*$	?	?	?	$(\bullet)$ is a complex number, see Section A.1
$(\bullet)'$	?	?	?	real part of $(\bullet)$, see Section A.1
$(\bullet)''$	?	?	?	imaginary part of $(\bullet)$, see Section A.1
$(\dot{\bullet}), (\ddot{\bullet})$	?	?	?	(double) derivative w.r.t. time
c	-	-	-	contact
dev	-	-	-	deviatoric part
el	-	-	-	max. absolute value for the purely elastic case
h	-	-	-	Hertz solution (omitted in Subsection 2.5.5 and later)
$\kappa \in [1,2]$	-	-	-	numbering of the body in contact
m	-	-	-	mean
s, se, sp	-	-	-	Sneddon solution (for exact sphere and paraboloid)
ve	-	-	-	max. absolute value for the viscoelastic case
vol	-	-	-	volumetric part
0	-	-	-	instantaneous ($t = 0$)
∞	-	-	-	final ($t \to \infty$)

1. Introduction

When two bodies impinge on one another and rebound, the total momentum must be conserved, but some of the kinetic energy of the bodies will be changed to other forms of energy, and ultimately to heat, in two principal ways. First, elastic vibrations will generally be set up so that some energy goes into internal motion, and secondly, since the colliding bodies will not be perfectly elastic, energy will be lost in viscous and plastic effects in the region of contact.

TILLETT [1954], p. 677

The attempts at an analytical solution of the problem of impact of a rigid or elastic sphere on a linear viscoelastic half space are numerous and employ a variety of techniques. None are successful enough to predict the behaviour of a general linear viscoelastic solid.

CALVIT [1967A], p. 142

1.1. Motivation

Structural impact is an every-day phenomenon.

Impact processes take place frequently in daily life and in industrial applications, involving disciplines such as civil and mechanical engineering, physics, sports science, medicine and biology. To give some examples (see also Fig. 1.1), impact occurs

- in dynamic actions of machines (e.g. in industrial press operations),
- during sports and leisure activities (e.g. heel impact when walking),

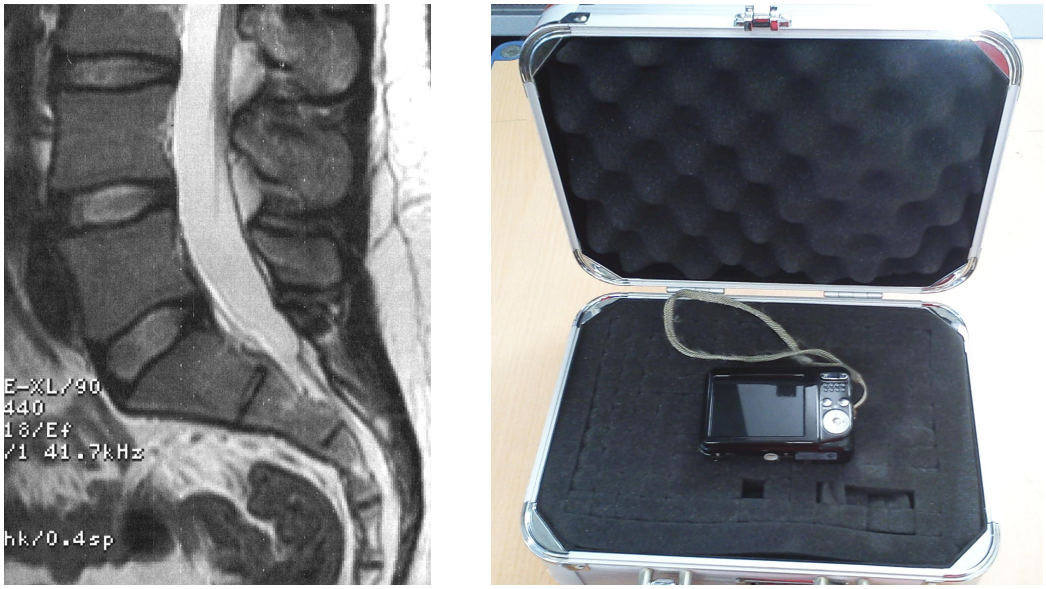

(a) Lower part of the author's spine (b) Transport case for technical equipment

Figure 1.1.: Examples for protection against impact damage. **(a)** In the human spine, the *nucleus pulposus* (inner part of a vertebral disc) serves as a shock-absorber due to its viscoelastic properties (magnetic resonance tomography). **(b)** Fragile merchandise embedded by a polymeric foam to prevent damage induced by repeated impact loading during shipment.

- in nature when objects are set in motion by gravitation (e.g. rock fall), or
- in accidents during transport of goods and human beings (e.g. traffic collisions).

Structural impact may be classified into intentional and accidental impact events. In the latter case, efficient precaution measures can reduce the severity of the impact, which is in general achieved by dissipating as much kinetic energy as possible. This design task is, however, not trivial to accomplish, since functional protection equipment has to be efficient for a variety of load cases, as the actual loading conditions may vary.

Structural mechanisms and types of material response during impact

It is thus instructive to analyse the general structural mechanisms and types of material response occurring during impact (see e.g. Section 1.3 in Lu and Yu [2003] for a similar portrayal).

1. Global buckling is observed on a structural level e.g. in slender beams loaded in longitudinal direction or shallow spheres. Local buckling occurs on a smaller scale, e.g. in the walls of cellular solids.
2. The body waves starting from the location of contact are strongly influenced by the initial impactor velocity and the material properties of the impacted material.
3. Elasto-plastic material behaviour dissipates energy due to internal friction processes on the atomistic scale.
4. In brittle materials suffering damage, fracture energy is required in order to initiate and propagate cracks.
5. In composite materials, friction and sliding processes at the component level also provide a mean of energy dissipation.
6. Viscous processes lead to dissipation of energy provided that their inherent time scale agrees to the duration of loading.

Obviously, not all phenomena mentioned occur simultaneously or have a considerable effect on the specific impact event. Thus, for the application-oriented development of impact absorbers, one specific mechanical concept has to be chosen initially.

Whereas loading by high-speed impact demands that energy dissipation is achieved through instantaneous inelastic material response (Points 3, 4, and 5 above), low-velocity impact events, to which attention is restricted here, can be restrained by non-destructive reactions, such as viscoelastic material behaviour, which is required in case of repetitive loads. Hereby, two design criteria may be applied: one is the minimisation of the maximum acceleration during the impact process to keep the impact forces low, which favours rather compliant (soft) materials. The other aim is to limit the maximum intrusion of the impactor, which is achieved by rather stiff materials.

1.2. Viscoelasticity and spherical impact problems

Viscoelasticity

The first observations of a time-delay between loading and structural response in certain materials appear to have been made long before the famous paper on the elastic “Nachwirkungen” (after-effects) by Boltzmann [1876], but it was him who laid the foundations of

what is known today as "theory of linear viscoelasticity"[1]. Based on torsion experiments on wires, he postulated that structural forces do not only depend on the current but also on previous strain conditions, where their influence on the current force state decreases with increasing time, which is nowadays often denoted by the term fading memory[2]. He claimed that the effects of the strain states are linearly additive, and in fact this superposition principle is the central idea in the theory of linear viscoelasticity.

To mention just a few other early works in this field, Leaderman [1941] gave a review of experiments published until that time and investigated creep and relaxation behaviour of polymers, while Zener [1948] discussed possible microstructural mechanisms in metals being the source for the observed time-delay in harmonic experiments. Alfrey [1948] presented phenomenological descriptions and molecular interpretations for various polymer types. In 1953, a thorough formal framework of the theoretical interrelations was given by Gross [1968], and some years later a comprehensive book on linear viscoelasticity was published by Bland [1960].

An important milestone in the field of viscoelastic stress analysis was the development of the correspondence principle (Read [1950], Lee [1955]). However, a proportional loading is required here, i.e. the same time dependence has to prevail in all prescribed quantities. This limitation does not apply to the so-called method of functional equations (Radok [1957]). Hence, it is possible to consider problems where one fixed point on the boundary is subjected to prescribed tractions *or* prescribed displacements in the course of time. On this basis, many theoretical papers on viscoelasticity were published in the following years, e.g. Lee and Radok [1960], Hunter [1960], or Ting [1966].

Contact and impact problems

Impact problems have attracted researchers for centuries; Szabó [1987] gave a worthwhile-to-read introduction to early experiments and theoretical considerations, the latter being sometimes based rather on philosophical than analytical reasoning. In these works, the colliding bodies were usually assumed to be rigid, and it is evident that refined impact theories

[1] See for instance Section 1.7 in Lakes [1998] for a short survey of historical works in this field, and Markovitz [1977] on how Boltzmann's work stands out as to previous publications.

[2] Boltzmann wrote "dass die Kräfte, die auf die Begränzungsflächen des Parallelepipedes zu einer bestimmten Zeit wirken, nicht blos abhängen von den Dehnungen des Parallelepipeds zu jener Zeit, sondern auch von den vorangegangenen Dehnungen desselben, wobei jedoch eine Dehnung einen um so geringeren Einfluss hat, vor je längerer Zeit sie stattfand" (*ibid.*, p. 629).

had to wait until first solutions to static contact problems of deformable bodies were developed.[3]

On this road, one important work was the potential theory by Boussinesq [1885] for stresses and displacements in an elastic isotropic homogeneous half-space loaded on its surface. Many contact problems may be solved on basis of this framework; noteworthy w.r.t. the present work was the development by Sneddon [1948] and, subsequently, his ready-to-use formulae for the contact between a rigid axisymmetric indenter and the elastic half-space (Sneddon [1965]). These relations – though further refined by follow-up developments, e.g. Bolshakov and Pharr [1996] – are of great use for today's solutions of contact problems.

A few years before, and thus independently of, Boussinesq's work Hertz [1881] formulated a theory for the contact of two elastic isotropic homogeneous bodies which are large in dimension in comparison to the area of contact, which he assumed to have the shape of an ellipse. The solution for the contact problem fulfilling all boundary conditions is then given by a specific distribution of the mutual contact pressure. Hertz presumed that the pressure is distributed according to the equation of an ellipsoid, where the maximum pressure occurs at the contact centre and the pressure magnitude diminishes the more one approaches the contact boundary, while it is zero outside the contact area. In case the two bodies are axisymmetric, the contact area becomes a circle and the pressure distribution within that circle has the equation of a sphere. This results in a rather simple relation between force F and penetration depth (mutual approach) u which is of the form $F = k\, u^{1.5}$, where k is some kind of stiffness[4].

Hertz also extended the contact problem to the quasi-static impact case. The neglect of wave propagation is justifiable for low-velocity impact where the smaller initial velocity of the impactor results in a longer (!) contact duration. Many corroborating investigations and extensions to the Hertzian contact relations have been proposed in the literature, like Deresiewicz [1968], Hunter [1957], Reed [1985], Tsai [1971], Graham [1973]), Willis [1966], Vlassak et al. [2003], Chen and Engel [1972], and Matthewson [1981]. For an overview, see also Kalker [1977].

However, when the indented material sample does not immediately recover its original shape

[3] Throughout the present work, attention is restrained to frictionless normal contact between smooth surfaces related to indentation-like contact and impact problems.

[4] Relations in the form of $F = k\, u^n$ are given by Sneddon [1965] for many different rigid indenters, e.g. $n = 1$ for a flat punch, $n = 1.5$ for a paraboloid of revolution, and $n = 2$ for a cone; the exponents are also valid in the viscoelastic case, see Sakai [2002].

upon removal of the load, the assumption of a purely elastic material behaviour is not justified. In the early 1900's, Brinell and Meyer suggested static hardness measures where a rigid sphere is pressed onto a metal sample and the hardness is computed from the applied force and the (curved or projected, respectively) area of the residual imprint[5]. Dynamic hardness measurements using a pendulum apparatus or free fall experiments were conducted by Martel, Herbert, Roudié, and Shore, where the latter used the rebound height of the spherical impactor for the hardness determination; the reader is referred to Tabor [1951]. Similarly, in the Leeb hardness test, the velocity of the spherical-tip impactor is measured and the hardness value is obtained from the coefficient of restitution, as is described e.g. in DIN 50156-1 [2007].

While these experiments were developed in order to characterise elasto-plastic materials, the behaviour of a viscoelastic medium subject to contact with a spherical indenter was intensely investigated much later, namely after the framework of functional equations had been established. Lee and Radok [1960] presented the solution for a rigid sphere on an incompressible viscoelastic half-space under the limitation of a non-decreasing contact area. This restriction was relieved by e.g. Hunter [1960], Graham [1965], Ting [1966], and others; however, many solutions presented apply only when the load history is prescribed, or when the behaviour is nearly elastic.

Whereas the determination of viscoelastic material parameters by a force- or displacement-controlled indentation program is based on a thorough theoretical foundation[6], the dynamic case of spherical impact has been investigated primarily by experiments, see e.g. Memmler [1930], Jenckel and Klein [1952], Tillett [1954], Flom [1960], Lifshitz and Kolsky [1964], Calvit [1967a], Pouyet and Lataillade [1975], Kren' and Rudnitskii [2000], Fujii and Yamaguchi [2005] and Constantinides et al. [2008].[7]

Some useful information on the indentation and impact testing of viscoelastic materials can also be found in national and international standards like DIN EN ISO 3385 [2010], DIN 53512 [2000], and DIN EN ISO 8307 [2008].

---

[5] i.e. after elastic recovery. Note that today the term hardness usually means either the ratio of the maximum load to the projected contact area under that load (see e.g. Oliver and Pharr [1992]) or the ratio of the current load to the current contact area (see for instance Borodich and Keer [2004]).

[6] See e.g. Larsson and Carlsson [1998], Sakai [2002], Cheng and Cheng [2005] or Cheng et al. [2005].

[7] In some of the mentioned publications, a comparison of the impact loading is made to a harmonic loading where half a sine is used to prescribe the penetration over time ("equivalent frequency concept"), see also Austrell and Olsson [2010]. However, even in the purely elastic case this simplification may have a doubtful influence on the results, compare Fig. 2.5.

Due to increasing computer power and the development of numerical methods over the last decades, the experimental investigations have been accompanied and replaced more and more by numerical simulations where the Finite Element Method (FEM, see e.g. Zienkiewicz et al. [2005]) is usually employed[8]. The virtual testing of materials paved the way for a different kind of analyses where answers to detailed questions concerning the design of a *specific* structure and/or the behaviour of a *specific* material are sought. Thus, recent publications concerning *general* solutions to impact on viscoelastic materials have become rare. These, however, could be attractive for two reasons: first, they allow for a quick assessment of the validity of refined analysis results; and second, they can be used as a design tool regarding the selection of suitable material properties.

Some publications on such design aspects are available in the literature. For example, Avalle et al. [2001] performed free fall impact experiments on polymeric foams measuring the force by a load cell, from which they obtained the relation between efficiency parameter and foam density. Thus, the optimal foam density for the maximal energy absorption can be determined. However, they allowed for a large straining of the foam samples (until densification) such that the so-obtained result can hardly be generalised.

Design aspects were also given by Chen and Lakes [1990]. For a standard linear solid, they obtained the optimal dissipation properties of a viscoelastic half-space such that the peak force under impact by a rigid sphere becomes minimum when there is a side constraint on the maximum penetration. On the other hand, for a given material with unknown properties the loss tangent can be determined from the ratio of the initial ball position to the rebound height. Furthermore, they examined the one-dimensional case of a viscoelastic buffer; a topic covered also by Larson et al. [1996] who compared the theoretical prediction from one-dimensional model equations for the force history with impact experiments on rubber samples.

1.3. Aims and objectives

The present work provides generally valid relationships for the impact of a rigid sphere on a viscoelastic medium. These can be applied as design charts when the optimal material behaviour under impact is sought. On the other hand, they may be used in order to reveal unknown material properties in an existing structure by means of an impact experiment.

[8] A review on indentation simulations using the FEM is given by Mackerle [2004].

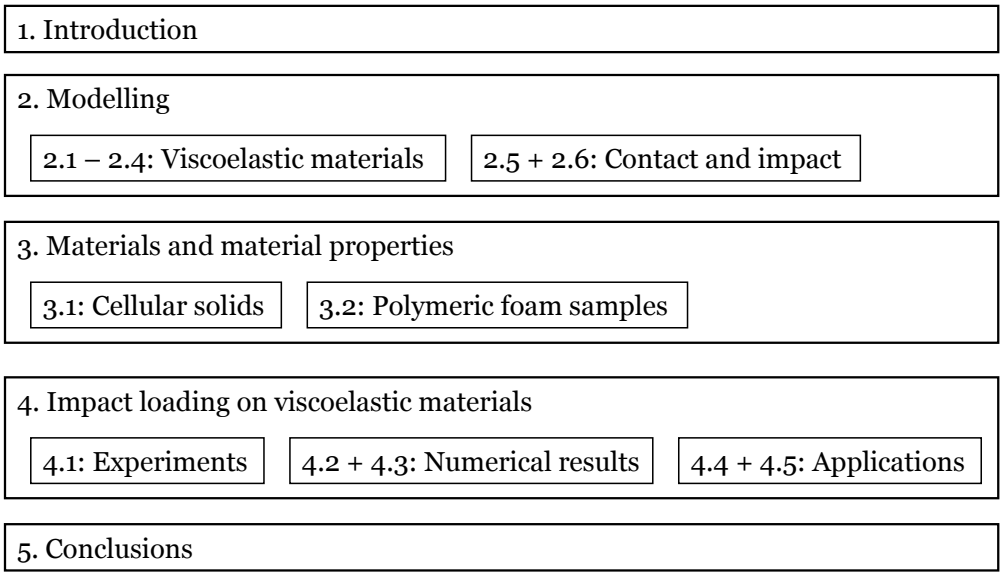

Figure 1.2.: Contents of this thesis

The relations between the governing parameters are presented in form of so-called master curves. These were obtained by means of numerical simulations using the Finite Element Method. It is noteworthy that it is not necessary here to model the viscoelastic material behaviour as "nearly elastic", as often had to be done in earlier research work on analytical solutions for viscoelastic impact. Rather, the time scale of the viscoelastic material is supposed to be of the same range as the impact duration, such that the obtained response strongly deviates from the elastic solution due to viscous effects. The general validity of the so-obtained results is assured by use of dimensionless parameters. The use of these master curves is shown by two applications: one is the optimisation of a viscoelastic protector subject to impact loading, e.g. for the objective of maximum energy dissipation. The other application is the identification of unknown material parameters by impact experiments, where impact experiments with viscoelastic foams conducted at Material Technology Innsbruck (MTI), Austria are employed.

The structure of this thesis is given in Fig. 1.2. For convenience, the most frequently used symbols are collected on pages IX to XII.

2. Modelling

Some people find spring-dashpot models to be useful in visualizing how viscoelastic behavior can arise, however they are not necessary in understanding or using viscoelasticity theory. Warning. *Spring-dashpot models have a pedagogic role, however real materials in general are not describable by models containing a small number of springs and dashpots.*

LAKES [2009], p. 22

Choc direct des corps élastiques. *[... On] distingue trois circonstances successives : la première est la compression ; la deuxième est un état* stationnaire *, qui ne dure qu'un tems très-court [...] ; enfin, le troisième est la restitution qui se fait avec un effort égal à la compression.*

PRONY [1802], p. 238–239

Wir denken uns zunächst die beiden Oberflächen in mathematische Berührung gebracht, und zwar so, dass die gemeinsame Normale parallel ist der Richtung des Druckes, welchen der eine Körper auf den anderen ausüben soll. In der gemeinsamen Tangentialebene richten wir das orthogonale geradlinige System der x, y ein, dessen Nullpunkt der Berührungspunkt sein soll, die dritte senkrechte Coordinate heisse z. [...] unmittelbar nach dem Stosse entfernen sich die Stosspunkte in Richtung der Normalen mit derselben relativen Geschwindigkeit, mit welcher sie sich vor dem Stosse einander näherten.

HERTZ [1881], p. 157

The first part of this chapter (Sections 2.1 to 2.4) concerns the modelling of linear viscoelastic materials[1]. It starts with the description of three types of experiments, by which the definitions of viscoelastic functions are motivated. Then, in Section 2.3, selected one-dimensional spring-dashpot models (Maxwell model, the standard linear solid, the power law creep model, the square root Kelvin-Voigt model, and the logarithmic creep model) are introduced, since these five models were employed in the numerical impact simulations. In Section 2.4, the deviatoric-volumetric split is presented for extending modelling of the viscoelastic behaviour to three dimensions.

The second part of this chapter deals with the modelling of contact and impact problems. In Section 2.5, an elastic half-space is considered. The Hertzian solution presented here is used later for the conversion of the numerical results into master curves. Section 2.6 gives a literature overview on contact and impact problems on viscoelastic media.

2.1. Modelling of linear viscoelastic material behaviour

In a **creep test** (DIN EN ISO 899-1 [2003]), the material sample is subject to constant stress[2]

$$\sigma(t) \;=\; \mathsf{H}(t)\,\sigma_0 \;, \tag{2.1}$$

where $\mathsf{H}(t)$ is the Heaviside distribution (sometimes also called unit step function, see e.g. Andrews and Shivamoggi [1988]). The sample will show increasing strain

$$\varepsilon(t) \;=\; J(t)\,\sigma_0 \;, \tag{2.2}$$

where the creep compliance $J(t)$ [1/Pa] is defined as the strain response divided by the applied stress level, i.e.

$$J(t) \;\stackrel{\text{def}}{=}\; \frac{\varepsilon(t)}{\sigma_0} \;. \tag{2.3}$$

[1] A viscoelastic material model is linear when the Boltzmann superposition principle holds: if the strain responses $\varepsilon_1(t)$ and $\varepsilon_2(t)$ are produced by the prescribed stresses $\sigma_1(t)$ and $\sigma_2(t)$, respectively, then $\sigma_1(t)+\sigma_2(t)$ result in $\varepsilon_1(t)+\varepsilon_2(t)$. For reference on the theory of viscoelasticity, see textbooks like Betten [2002], Brinson and Brinson [2008], Christensen [1982], Findley et al. [1976], Haddad [1995], Lakes [1998], Nowacki [1965], and Tschoegl [1989]. Also, general books on applied mechanics and material mechanics – e.g. Göldner and Pfefferkorn [1988], Gross et al. [1995], or Mang and Hofstetter [2004] – often contain some introductory sections on viscoelastic material behaviour, which give an easy access to the topic due to their brevity. Regarding polymers, their viscoelastic behaviour is treated e.g. in Aklonis and MacKnight [1983], Ferry [1970], Mills [2007], or Ward and Sweeney [2004].

[2] For later use, let's remark that $\sigma(t) = \mathsf{H}(t)\,\sigma_0$ in Eqn. (2.1) results in $\hat{\sigma}(s) = \sigma_0/s$ in the Laplace space. For selected pairs of the Laplace transform, refer to Table A.1.

When performing several creep tests at different stress levels, the assumption of linearity is confirmed when for an arbitrary but fixed time instant a straight curve in the stress-strain diagram is obtained from all experiments (i.e. straight isochronals).

In case of a **relaxation test** (DIN EN 10319-1 [2003]), a constant strain[3]

$$\varepsilon(t) \;=\; \mathsf{H}(t)\,\varepsilon_0 \tag{2.4}$$

is applied on the virgin sample at $t = 0$. It will show a decrease in stress

$$\sigma(t) \;=\; R(t)\,\varepsilon_0 \tag{2.5}$$

with the relaxation modulus $R(t)$ [Pa] defined as

$$R(t) \;\stackrel{\text{def}}{=}\; \frac{\sigma(t)}{\varepsilon_0}\;. \tag{2.6}$$

Short-time properties may only be revealed by **harmonic loading**[4] (see e.g. Lee [1956], DIN 53513 [1990])

$$\varepsilon(t) \;=\; \varepsilon_0\,\mathrm{e}^{i(\omega t - Fx)} \;=\; \varepsilon_0\,\mathrm{e}^{-iFx}\,\mathrm{e}^{i\omega t} \;=\; \varepsilon^*\,\mathrm{e}^{i\omega t}\;, \tag{2.7}$$

where ε_0 is the prescribed maximum strain, ε^* is the complex strain amplitude, ω is the angular frequency, and the term Fx results just in a shift on the time axis (Yilmaz [2011]). The harmonic excitation given in Eqn. (2.7) results in a harmonic stress answer[5]

$$\sigma(t) \;=\; \sigma_0\,\mathrm{e}^{i(\omega t - Fx + \delta)} \;=\; \sigma_0\,\mathrm{e}^{i(-Fx+\delta)}\,\mathrm{e}^{i\omega t} \;=\; \sigma^*\,\mathrm{e}^{i\omega t} \tag{2.8}$$

with σ_0 being the measured maximum stress and σ^* the complex stress amplitude. The phase shift δ, which itself is dependent on the excitation frequency ω, is also called loss angle, since $\delta = 0$ corresponds to a purely elastic and $\delta = \pi/2$ to a purely viscous material. Thus, the stress response shows the same angular frequency, but is ahead of the strain by the time difference δ/ω. It should be noted that the strain always lags the stress, regardless if the stress or the strain is controlled in the experiment.

The complex relaxation modulus [Pa]

$$R^* \;\stackrel{\text{def}}{=}\; \frac{\sigma(t)}{\varepsilon(t)} \;=\; \frac{\sigma^*}{\varepsilon^*} \;=\; \frac{\sigma_0}{\varepsilon_0}\,\mathrm{e}^{i\delta} \tag{2.9}$$

[3] Analogously to the previous footnote, $\varepsilon(t) = \mathsf{H}(t)\,\varepsilon_0$ in Eqn. (2.4) results in $\hat{\varepsilon}(s) = \varepsilon_0/s$.

[4] For later use, the Laplace transform of Eqn. (2.7) is $\hat{\varepsilon}(s) \;=\; \frac{\varepsilon_0}{s - i\omega}$. It should also be noted that in a strict notation this formula would read $\varepsilon(t) = \Re(\varepsilon^*\,\mathrm{e}^{i\omega t})$, where $\Re$ stands for the real part, but the $\Re$ is conventionally omitted, see p. 261 in Hunter [1967].

[5] Analogously to the previous footnote, the Laplace transform of Eqn. (2.8) is $\hat{\sigma}(s) \;=\; \frac{\sigma_0\,\mathrm{e}^{i\delta}}{s - i\omega}$

depends on the excitation frequency ω. Its length in the complex plane, the storage modulus, and the loss modulus are given as

$$|R^*| = \frac{\sigma_0}{\varepsilon_0} \ , \ R' = \frac{\sigma_0}{\varepsilon_0} \cos\delta \ , \text{ and } \ R'' = \frac{\sigma_0}{\varepsilon_0} \sin\delta \ , \tag{2.10}$$

respectively, where a prime refers to the real part and a double prime to the imaginary part of a complex quantity, see Eqn. (A.1)in the appendix. The tangent of the phase shift between stress and strain history is called loss tangent, given by

$$\tan\delta = \frac{R''}{R'} \ , \tag{2.11}$$

and is a measure for the damping by internal friction (see e.g. Lakes [2004]). The relation between loss and storage modulus for varying excitation frequency becomes apparent also from a Cole-Cole diagram (Cole and Cole [1941], see also e.g. Aklonis and MacKnight [1983]).

2.2. 1D stress-strain relations for linear viscoelastic materials

For linear viscoelastic material behaviour, the relationship between stress and strain can be put into the following general format (cf. Alfrey [1945], Radok [1957]):

$$P_\partial \, \sigma \ = \ Q_\partial \, \varepsilon \ , \ \text{ with the abbreviations } \ P_\partial \stackrel{\text{def}}{=} \sum_{h=0}^{p} p_h \frac{\partial^h}{\partial t^h} \ \text{ and } \ Q_\partial \stackrel{\text{def}}{=} \sum_{h=0}^{q} q_h \frac{\partial^h}{\partial t^h} \ . \tag{2.12}$$

P_∂ and Q_∂ are linear differential operators with p material constants p_h and q constant coefficients q_h related to the corresponding time derivatives of order h. The use of time derivatives is motivated by the spring-dashpot assemblies of simple rheological models.

However, the stress-strain relation can also be expressed in an integral format:[6]

$$\sigma(t) \ = \ \int_{\vartheta=0}^{t} R(t-\vartheta) \, \dot{\varepsilon}(\vartheta) \, \mathrm{d}\vartheta \ = \ R(t) * \dot{\varepsilon}(t) \ . \tag{2.13}$$

The picture behind this hereditary integral is that the current stress state depends on the strain states at the current and all earlier time instants, i.e. the entire strain history is "inherited" for the determination of the current stress state. The Boltzmann superposition integral expressed by Eqn. (2.13) can be thought of as the continuous limit[7] of $\sigma(t) = \sum R(t-\vartheta_i) \, \Delta\varepsilon_i$

[6] See also Markovitz [1977] for historical remarks on the two forms. For a more detailed treatment of the differential and the integral form, see for instance Findley et al. [1976] or Gross et al. [1995]. In general, the use of the hereditary integral form is preferred over the differential form (Lee and Rogers [1963]).

[7] Provided that $\mathrm{d}\varepsilon$ can be replaced by $\dot{\varepsilon}(\vartheta) \, \mathrm{d}\vartheta$. Also, it has to hold that $\varepsilon(0) = 0$.

due to infinitely many strain increments $\Delta\varepsilon_i$ at the respective time instant ϑ_i using Eqn. (2.5). In analogy to Eqn. (2.13), one can also express the stress-strain relation by the creep compliance as

$$\varepsilon(t) \;=\; \int_{\vartheta=0}^{t} J(t-\vartheta)\,\dot{\sigma}(\vartheta)\,\mathrm{d}\vartheta \;=\; J(t) * \dot{\sigma}(t)\;. \tag{2.14}$$

Alternatively, the constitutive relation can be expressed by the complex modulus R^* as

$$\sigma^* \;=\; R^*(\omega)\,\varepsilon^*\;. \tag{2.15}$$

It is sufficient to specify either of the three material properties $J(t)$, $R(t)$, and $R^*(\omega)$, as these are interconnected to each other as follows:

Relation between $R(t)$ and $J(t)$. Application of the Laplace transform to Eqns. (2.13) and (2.14) leads to

$$\hat{\sigma}(s) \;=\; s\,\hat{R}(s)\,\hat{\varepsilon}(s) \quad\text{and}\quad \hat{\varepsilon}(s) \;=\; s\,\hat{J}(s)\,\hat{\sigma}(s)\;, \tag{2.16}$$

from which

$$\hat{R}(s)\,\hat{J}(s) \;=\; \frac{1}{s^2} \tag{2.17}$$

is obtained. Thus, by help of the inverse Laplace transform, one receives

$$\int_{\vartheta=0}^{t} R(t)\,J(t-\vartheta)\,\mathrm{d}\vartheta \;=\; \int_{\vartheta=0}^{t} R(t-\vartheta)\,J(t)\,\mathrm{d}\vartheta \;=\; t\;. \tag{2.18}$$

Relation between $R(t)$, $\hat{R}(s)$, and $R^*(\omega)$. With $\varepsilon(\theta) = \varepsilon_0\,\mathrm{e}^{i\omega\theta}$ as strain input (i.e. Eqn. (2.7) with $Fx=0$), the unknown stress history[8] is

$$\sigma(t) \;=\; \int_{-\infty}^{t} R(t-\theta)\,\dot{\varepsilon}(\theta)\,\mathrm{d}\theta \;=\; \varepsilon_0\,i\omega \int_{-\infty}^{t} R(t-\theta)\,\mathrm{e}^{i\omega\theta}\mathrm{d}\theta \;=\; \varepsilon(t)\,i\omega \int_{0}^{\infty} R(\vartheta)\,\mathrm{e}^{-i\omega\vartheta}\mathrm{d}\vartheta\;, \tag{2.19}$$

where $\vartheta = t-\theta$ and, thus, $\mathrm{e}^{i\omega\theta} = \mathrm{e}^{i\omega t}\,\mathrm{e}^{-i\omega\vartheta}$ was introduced. From this, one gets

$$R^*(\omega) = \frac{\sigma(t)}{\varepsilon(t)} = i\omega \int_{0}^{\infty} R(\vartheta)\,\mathrm{e}^{-i\omega\vartheta}\mathrm{d}\vartheta\;. \tag{2.20}$$

Thus, the complex relaxation modulus $R^*(\omega)$ is just the Laplace-Carson transform (see p. 100) of the relaxation modulus $R(\vartheta)$, using $p = i\omega$ in Eqn. (A.31), and Eqn. (2.15) is nothing else than the Laplace-Carson transform of Eqn. (2.13). Also, the relation

$$R^*(\omega) = i\omega\,\hat{R}_{s=i\omega} \tag{2.21}$$

between the complex modulus $R^*(\omega)$ and the Laplace-transformed relaxation modulus $\hat{R}(s)$ becomes obvious (cf. the use of a half-sided Fourier transform, see e.g. Brinson and Brinson [2008]).

[8] Whereas throughout the present work a virgin state at time $t = 0$ is assumed, one allows here for non-zero loading also for $t < 0$.

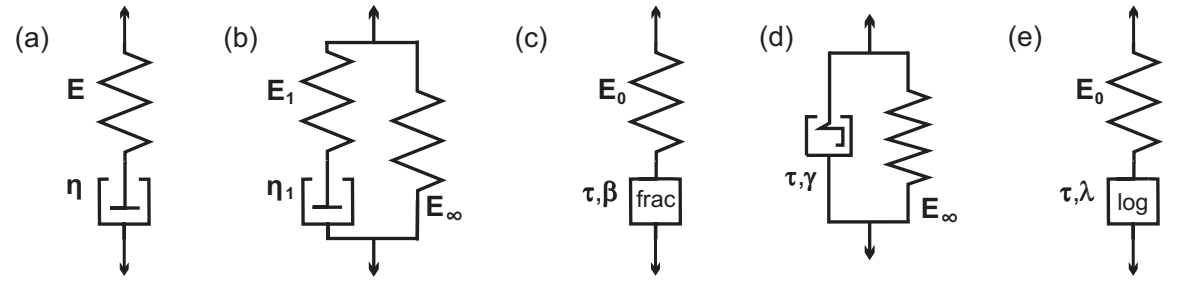

Figure 2.1.: Rheological models: **(a)** MX: the Maxwell element, **(b)** SLS: the standard linear solid, **(c)** PL: the 3-parameter power law creep model, a spring with the nonlinear $(t/\tau)^{\beta}$ dashpot in series, **(d)** SRKV: the 3-parameter square root Kelvin-Voigt model, where the spring is in parallel with the nonlinear $\sqrt{t/\tau}$ -dashpot, **(e)** LOG: the 3-parameter logarithmic model, consisting of a linear spring and a logarithmic dashpot.

2.3. Selected rheological models

In the numerical simulations presented in this work, the five models depicted in Fig. 2.1 have been used. While the respective creep compliance function given in this section is enough to describe the model behaviour, for convenience the derivation of the model equations and other viscoelastic functions as well as some illustrative diagrams can be found in Appendix B (pp. 103 to 121).

a) MX: The creep compliance of the Maxwell model is

$$J(t) = \frac{1}{E} + \frac{t}{\eta} = \frac{1}{E}\left(1 + \frac{t}{\tau}\right), \tag{2.22}$$

where $1/E$ is the instantaneous compliance and $\tau \stackrel{\text{def}}{=} \eta/E$ is termed characteristic time. The flow is unbounded, thus, this model is sometimes called Maxwell fluid.

b) SLS: When one Maxwell element (E_1, τ) is connected to an equilibrium spring E_∞ in parallel, the creep compliance

$$J(t) = \frac{1}{(1-\alpha)E_0}\left(1 - \alpha \exp\Big(-(1-\alpha)\,\frac{t}{\tau}\Big)\right) \tag{2.23}$$

is obtained, where $E_0 = E_\infty + E_1$ is the initial stiffness and $\alpha = \frac{E_1}{E_0}$ controls the influence of the MX element on the total assembly. The instantaneous compliance is $\frac{1}{E_\infty + E_1}$ and the flow is bounded due to the equilibrium spring.

c) PL: If the linear dashpot of the MX is replaced by a fractional dashpot, the creep compliance becomes

$$J(t) = \frac{1}{E_0}\left(1+\left(\frac{t}{\tau}\right)^{\beta}\right), \tag{2.24}$$

where β determines how much the fractional dashpot will behave like a linear dashpot ($\beta=1$) or, contrariwise, a linear spring ($\beta=0$). The instantaneous compliance is $1/E_0$ and the flow is unbounded (except for the two-spring limit case $\beta=0$).

d) SRKV: Here, the standard Kelvin-Voigt model is modified such that the ratio of the physical time to the dashpot time τ is taken to the power of 0.5. Also, the variable γ is introduced in order to steer the amount of stress flowing through the dashpot branch. The creep compliance reads

$$J(t) = \frac{1}{E_\infty}\left(1-\gamma\exp\left(-\sqrt{t/\tau}\right)\right). \tag{2.25}$$

The initial compliance is $(1-\gamma)/E_\infty$ and the flow is bounded since the compliance approaches $1/E_\infty$ for $t\to\infty$.

e) LOG: This model is similar to the MX, but the dashpot is non-linear due to the natural logarithm operating on the t/τ ratio:

$$J(t) = \frac{1}{E_0}\left(1+\lambda\ln\left(1+\frac{t}{\tau}\right)\right). \tag{2.26}$$

The scalar λ controls the amount of viscosity. The initial compliance is $1/E_0$ and the flow is unbounded.

It should be noted that the relaxation of the PL, SRKV and LOG model – in contrast to simple linear spring-dashpot models like MX and SLS showing a Debye peak (cf. Fig. B.2) – takes place over several decades of time; thus, they can well present a variety of real materials despite the small number of model parameters involved.

2.4. Modelling of three-dimensional material behaviour

2.4.1. Linear elastic isotropic homogeneous materials

Three-dimensional linear elastic material laws relate the second-order stress tensor $\boldsymbol{\sigma}$ with $3^2=9$ components to the strain tensor $\boldsymbol{\varepsilon}$ of the same appearance by a fourth-order constitu-

tive tensor with $3^4 = 81$ components, for which two independent engineering constants are sufficient when the material is isotropic.[9]

The components of the stress tensor can be split into a volumetric and a deviatoric portion by $\sigma_{ij} = \sigma_m \delta_{ij} + s_{ij}$ with the hydrostatic stress $\sigma_m = \frac{\sigma_{kk}}{3}$ and the deviator stresses s_{ij}. The components of the strain tensor $\varepsilon_{ij} = \varepsilon_m \delta_{ij} + e_{ij}$ are organised in an analogous way, where $\varepsilon_m = \frac{\varepsilon_{kk}}{3}$ is one third of the volumetric strain and e_{ij} are the components of the deviatoric strain. Then the bulk and the shear behaviour can be investigated separately by

$$\sigma_m \;=\; 3\,K\,\varepsilon_m \quad \text{and} \quad s_{ij} \;=\; 2\,G\,e_{ij}\;, \tag{2.27}$$

respectively, where

$$K \;=\; \frac{E}{3(1-2\nu)} \tag{2.28}$$

is the bulk modulus [Pa] and

$$G \;=\; \frac{E}{2(1+\nu)} \tag{2.29}$$

is the shear modulus [Pa]. In the above relations, Poisson's ratio ν [–] and Young's modulus E [Pa] have been introduced. Alternatively, one may use the generalised Hooke's law

$$\sigma_{ij} \;=\; 3\,\lambda\,\varepsilon_m\,\delta_{ij} \;+\; 2\,G\,\varepsilon_{ij}\;, \tag{2.30}$$

where $\lambda = \frac{\nu E}{(1+\nu)(1-2\nu)} = K - \frac{2}{3}G$ is the first Lamé constant [Pa].

From the above engineering constants, the indentation modulus [Pa]

$$Y \;\stackrel{\text{def}}{=}\; \frac{E}{1-\nu^2} \;=\; \frac{2G}{1-\nu} \;=\; 4G\,\frac{3K+G}{3K+4G} \tag{2.31}$$

can be constructed. A reduced modulus is given in Oliver and Pharr [1992] as

$$\frac{1}{Y_r} \;=\; \frac{1-{\nu_s}^2}{E_s} + \frac{1-{\nu_i}^2}{E_i} \tag{2.32}$$

for the indentation of a specimen "s" by an indenter "i".

2.4.2. Linear viscoelastic isotropic homogeneous materials

The viscoelastic analogue of Eqn. (2.30) reads

$$\sigma_{ij}(t) = 3\,\delta_{ij} \int_{\vartheta=0}^{t} \lambda(t-\vartheta)\,\dot{\varepsilon}_m(\vartheta)\,\mathrm{d}\vartheta \;+\; 2\int_{\vartheta=0}^{t} G(t-\vartheta)\,\dot{\varepsilon}_{ij}(\vartheta)\,\mathrm{d}\vartheta\;. \tag{2.33}$$

[9] For easier reading, the index notation is used in the following. See standard textbooks like Mang and Hofstetter [2004] for reference to this section.

In practice, however, one prefers to model the volumetric and the deviatoric behaviour separately (see e.g. Lee [1956]). This is motivated by the fact that more appropriate models can be established when the source for viscoelastic behaviour can be clearly identified and taken into consideration. For instance, polymers, where the molecular rearrangement is responsible for relaxation mechanisms, are often approximated to show time-dependent material behaviour only in the deviatoric part, while the volumetric part is assumed elastic – sometimes even incompressible – in order to ease the computational effort. On the other hand, when the causal mechanism is due to a fluid flowing through a porous network, a proper viscoelastic model for the dilatation must be used. (See for instance Chapter 8 in Lakes [2004] and references therein.)

Thus, analogously to Eqns. (2.27), the volumetric behaviour is modelled by

$$\sigma_m(t) = 3\int_{\vartheta=0}^{t} R_{\mathrm{vol}}(t-\vartheta)\,\dot{\varepsilon}_m(\vartheta)\,\mathrm{d}\vartheta \quad \text{or} \quad \varepsilon_m(t) = \frac{1}{3}\int_{\vartheta=0}^{t} J_{\mathrm{vol}}(t-\vartheta)\,\dot{\sigma}_m(\vartheta)\,\mathrm{d}\vartheta \tag{2.34}$$

and the deviatoric part by

$$s_{ij}(t) = 2\int_{\vartheta=0}^{t} R_{\mathrm{dev}}(t-\vartheta)\,\dot{e}_{ij}(\vartheta)\,\mathrm{d}\vartheta \quad \text{or} \quad e_{ij}(t) = \frac{1}{2}\int_{\vartheta=0}^{t} J_{\mathrm{dev}}(t-\vartheta)\,\dot{s}_{ij}(\vartheta)\,\mathrm{d}\vartheta\ , \tag{2.35}$$

where $R_{\mathrm{vol}}(t)$ and $R_{\mathrm{dev}}(t)$ are the relaxation moduli and $J_{\mathrm{vol}}(t)$ and $J_{\mathrm{dev}}(t)$ the creep compliances in bulk and shear, respectively. Throughout this work, a constant Poisson's ratio has been assumed[10]. In this case, similar viscoelastic response is assumed in bulk and shear behaviour, giving $\frac{R_{\mathrm{vol}}(t)}{R_{\mathrm{vol}}(0)} = \frac{R_{\mathrm{dev}}(t)}{R_{\mathrm{dev}}(0)}$ and $\frac{J_{\mathrm{vol}}(t)}{J_{\mathrm{vol}}(0)} = \frac{J_{\mathrm{dev}}(t)}{J_{\mathrm{dev}}(0)}$.

2.5. Impact of a rigid sphere on the elastic half-space

The second part of this chapter concerns the modelling of contact and impact problems[11]. First, static contact between a rigid sphere and a linear elastic isotropic half-space with the indentation modulus $Y = \frac{E}{1-\nu^2}$ is addressed, where the Sneddon solution and the classical Hertz relations are discussed. Then, the dynamic loading of the elastic half-space by a rigid

[10] This constraint has been chosen deliberately without any physical reasoning but with the purpose to keep the number of variables small, such that the results may be presented more efficiently. It is believed that a relaxation of this assumption would not change the principal procedure presented in the present work.

[11] Apart from the literature mentioned in the following, the reader is referred to general textbooks on this subject like Galin [2008], Gladwell [1980], Goldsmith [2001], Johnson [1985], Johnson [1972], Jones [1989] or Zukas [1982], where the book on contact mechanics by K. L. Johnson [1985] is quite extensive and may be nominated as standard reference in this field. Regarding the mentioned books on impact, the focus is mostly on plastic deformations, damage and fracture, and on wave propagation.

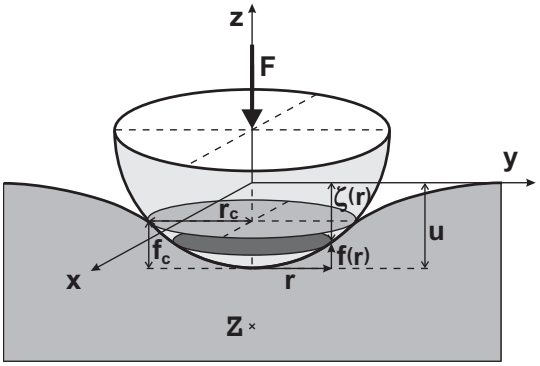

Figure 2.2.: Axisymmetric rigid indenter penetrating into an elastic half-space. The indenter shape is described by $f(r)$. The contact radius is r_c and the contact depth is f_c. The penetration depth u and the applied force F are related to the contact radius by the Sneddon or the Hertz solution. The auxiliary variable $\zeta(r) = u - f(r)$ is defined for $0 \le r \le r_c$ only. The point designated by "Z" marks the locus where the maximum shear stress will occur according to Hertz' theory. The distance between Z and the indenter tip depends on the Poisson ratio: for $\nu = 0.0$ it is $0.38 r_c$, for $\nu = 0.3$ it is $0.48 r_c$, and for $\nu = 0.5$ it is $0.55 r_c$, cf. Chapters 3.4 (here with a printing mistake) and 4.2 in Johnson [1985].

sphere (Hertzian impact) is treated. Section 2.6 covers contact and impact problems for viscoelastic media.

2.5.1. Preliminary remarks concerning the static contact problem

Geometrical description of the indenter tip. The contact problem of a rigid axisymmetric indenter and an infinite half-space is sketched in Fig. 2.2. The sufficiently smooth[12] indenter surface is described by the indenter shape function $f(r)$, which expresses the vertical distance $f \ge 0$ between the surface and the indenter apex as a function of the radial distance r where $f(0) = 0$. In literature (see for instance Jäger et al. [2007]), the ansatz

$$f(r) \;=\; \frac{1}{2\,C_0}\Big(\sqrt{(C_1)^2 + 4C_0\pi r^2} - C_1\Big) \tag{2.36}$$

is often used, from which the projected indenter area $A(r)$ follows as

$$A(r) \;=\; \pi\, r^2 \;=\; C_0 f^2(r) + C_1 f(r)\ . \tag{2.37}$$

[12] However, in order to not exclude conical indenters, one allows for C^0-continuity at the indenter tip, i.e. at $r = 0$.

	cone	exact sphere	classical sphere
C_0 [–]	$\pi \tan^2\gamma$	$-\pi$	n.a.
C_1 [m]	0	$2\pi R$	n.a.
$f(r)$ [m]	$\frac{r}{\tan\gamma}$	$R-\sqrt{R^2-r^2}$	$\frac{r^2}{4k}$ or $\frac{r^2}{2R}$
$f'(r) \stackrel{\text{def}}{=} \frac{\mathrm{d}f(r)}{\mathrm{d}r}$ [–]	$\frac{1}{\tan\gamma}$	$\frac{r}{\sqrt{R^2-r^2}}$	$\frac{r}{2k}$ or $\frac{r}{R}$
$A(r)$ [m^2]	πr^2	πr^2	πr^2
u [m]	$\frac{\pi r_c}{2\tan\gamma}$	Eqn. (2.42)	Eqns. (2.45) and (2.60)
F [kN]	$\frac{Y\pi {r_c}^2}{2\tan\gamma}$	Eqn. (2.43)	Eqns. (2.46) and (2.61)

Table 2.1.: Contact relations and Sneddon solution (see Subsection 2.5.2) for three different rigid indenters penetrating into an elastic isotropic half-space. **Left:** cone (given here just for comparison). Here, γ designates half of the opening angle, i.e. $\tan\gamma = \frac{r}{f(r)}$. **Middle:** exact sphere. **Right:** classical spherical indenter, i.e. a Hertzian sphere.

The constants C_0[–] and C_1[m] depend on the indenter shape. For the case of a perfect cone or a perfect sphere Table 2.1 lists these constants. When the radius of the contact circle r_c is inserted for r in Equations (2.36) and (2.37), the contact height f_c and the contact area A_c are obtained.

Analytical solutions for the elastic indentation problem. For the problem of a rigid spherical indenter penetrating into an elastic half-space two solutions relating the penetration depth u and the applied force F to a certain contact radius r_c are available (cf. Niederkofler et al. [2009]).

- Sneddon's [1965] solution is based on the potential theory of Boussinesq [1885]. As he uses an arbitrary function $f(r)$ for the geometrical description of the indenter tip in the derivations, his solution is not limited to spherical punches but can also be applied to indenters of other shapes. The Sneddon solution (which will be denoted by the index "s") is illustrated in more detail in the following subsection and specialised for the case of an exact sphere (index "se") and a paraboloid (index "sp").
- The solution by Hertz [1881], in the following denoted by the index "h", assumes that the geometry function of the spherical indenter can be described by a paraboloid, which is a valid approximation for small penetration depths. For this reason, Sned-

don's relations for the paraboloid are sometimes referred to as classical sphere (see e.g. Ting [1966]).

As shown in Subsection 2.5.4, for small penetrations Sneddon's sphere and the classical sphere practically coincide. This justifies the use of the Hertz solution, which is more convenient to the investigations performed in this work due to the power function format of the contact/impact equations, since large strains and non-linear material behaviour are excluded anyway.

Closed-form solutions for a prescribed pressure distribution over a circular region.

Johnson [1985] lists solutions in closed form for a normal pressure distribution

$$p_n(r) \;=\; P\left(1-\left(\frac{r}{r_c}\right)^2\right)^n \tag{2.38}$$

being applied to a circular region of radius r_c [m] on the surface of an elastic half-space, where P [Pa] is a constant. Depending on the value of the exponent n, the following values for the penetration depth u and the applied force F are obtained in terms of r_c:

- $n=-\frac{1}{2}$ (uniform normal displacement) $\Rightarrow\;\; u=\pi\frac{P}{Y}r_c$ and $F=2\pi P{r_c}^2$. Thus, $F(u)=\frac{2}{\pi}\frac{Y^2}{P}u^2$.
- $n=0$ (uniform pressure $p_0(r)=P$, i.e. frictionless flat-ended cylindrical punch) $\Rightarrow$ $u=2\frac{P}{Y}r_c$ and $F=\pi P{r_c}^2$. Thus, $F(u)=\frac{\pi}{4}\frac{Y^2}{P}u^2$.
- $n=\frac{1}{2}$ (Hertz pressure, i.e. frictionless paraboloid-shaped indenter). Then, Eqn. (2.38) becomes

$$p_{1/2}(r) \;=\; P\sqrt{1-\left(r/r_c\right)^2}\;. \tag{2.39}$$

$\Rightarrow\;\; u=\frac{\pi}{2}\frac{P}{Y}r_c$ and $F=\frac{2}{3}\pi P{r_c}^2$. Thus, $F(u)=\frac{8}{3\pi}\frac{Y^2}{P}u^2$.

Note that $F(u)$ depends on $\frac{Y^2}{P}u^2$ for all three cases, only a different scalar factor is obtained.

2.5.2. Sneddon solution for the contact problem of a rigid sphere on an elastic half-space

Sneddon [1965] solved the Boussinesq [1885] problem by application of Hankel transforms and dual integrations. For sufficiently smooth indenter profiles (such that the normal stress

remains finite around the circle of contact) he found the displacement field (in particular, the shape of the free surface), the pressure distribution under the indenter, the penetration

$$u_{\mathrm{s}}(r_c) \;=\; r_c \int_{r=0}^{r_c} \frac{f'(r)}{\sqrt{{r_c}^2 - r^2}}\,\mathrm{d}r \;, \tag{2.40}$$

and the total load

$$F_{\mathrm{s}}(r_c) \;=\; 2\,Y \int_{r=0}^{r_c} \frac{r^2\,f'(r)}{\sqrt{{r_c}^2 - r^2}}\,\mathrm{d}r \tag{2.41}$$

in terms of an arbitrary indenter shape function[13] $f(r)$ and its derivative $f'(r)$. Sneddon gave particular solutions for several indenter shapes, namely the flat-ended cylindrical punch (even though it is non-smooth), the spherical punch, the conical punch, and indenters in form of a paraboloid or ellipsoid of revolution. If the ansatz of Eqn. (2.36) is used, the penetration and the force depend on r_c and $f'(r, C_0, C_1)$. Jäger and Lackner [2009] expressed u_{s} and F_{s} by explicit functions of the contact radius r_c and the two constants C_0 and C_1.

Perfectly spherical indenter. Specialising Eqns. (2.40) and (2.41) for a perfect rigid spherical indenter where $f'(r)$ is given in Table 2.1, one obtains

$$u_{\mathrm{se}}(r_c) \;=\; r_c\,\ln\!\left(\frac{R + r_c}{\sqrt{R^2 - {r_c}^2}}\right) \;=\; \frac{r_c}{2}\,\ln\!\left(\frac{R + r_c}{R - r_c}\right) \tag{2.42}$$

and

$$\begin{aligned} F_{\mathrm{se}}(r_c) \;&=\; Y\left[\left(R^2 + {r_c}^2\right)\ln\!\left(\frac{R + r_c}{\sqrt{R^2 - {r_c}^2}}\right) \;-\; R\,r_c\right] \\ &=\; Y\left[\frac{R^2 + {r_c}^2}{2}\,\ln\!\left(\frac{R + r_c}{R - r_c}\right) \;-\; R\,r_c\right] \;, \end{aligned} \tag{2.43}$$

where in the original publication by Sneddon there is a printing mistake for the force, but the formula derived here is correct and conforms to e.g. Ting [1966] and Niederkofler et al. [2009].

Classical spherical indenter. For a paraboloid of revolution the indenter function is given by Sneddon as

$$f(r) \;=\; \frac{r^2}{4k} \;, \tag{2.44}$$

[13] The original formulae by Sneddon for the penetration and the force have $x \overset{\mathrm{def}}{=} \frac{r}{r_c}$ as independent variable (which appears advantageous to perform mathematical operations, but less intuitive to grasp the physical problem), so it seems that, compared to the original contribution, a change in the integration variable from x to r demands a multiplication by $\frac{1}{r_c}$ (since $\mathrm{d}x = \frac{1}{r_c}\mathrm{d}r$). However, the derivative in the integrand, $f'(x) = \frac{\mathrm{d}f(x)}{\mathrm{d}x}$, is not replaced by $f'(r) = r_c\frac{\mathrm{d}f(r)}{\mathrm{d}r}$ but rather by $f'(r) = \frac{\mathrm{d}f(r)}{\mathrm{d}r}$, and so $\frac{1}{r_c}$ from the integration cancels with r_c from the derivative.

where k is an arbitrary but fixed constant. Inserting $f'(r) = \frac{r}{2k}$ in Eqns. (2.40) and (2.41), respectively, one retrieves

$$u_{\mathrm{sp}}(r_c) = \frac{{r_c}^2}{2k} \tag{2.45}$$

and

$$F_{\mathrm{sp}}(r_c) = \frac{4}{3}\, Y\, \frac{{r_c}^3}{2k}\ . \tag{2.46}$$

From the last two equations, the relation

$$F_{\mathrm{sp}}(u_{\mathrm{sp}}) = \frac{4}{3}\, Y\, (2k)^{0.5}\, {u_{\mathrm{sp}}}^{1.5} \tag{2.47}$$

can be constructed. Also, Sneddon gives the distribution of stress under the paraboloidal indenter as

$$\sigma_{\mathrm{sp}}(r, z=0) = -\frac{2}{\pi} Y \sqrt{\left(\frac{r_c}{2k}\right)^2 - \left(\frac{r}{2k}\right)^2}\ . \tag{2.48}$$

When $2k = R$ is substituted, the formulae from Sneddon's paraboloid of revolution are identical to those for Hertz' rigid spherical indenter.

Note that for rigid indenters penetrating a viscoelastic half-space the same exponents (viz. 3/2 for a paraboloid of revolution) apply as for the elastic case, see e.g. Sakai [2002].

"Galin solution" or "Sneddon solution"? Borodich and Keer [2004] argue that the Galin solution from 1946 was established prior to Sneddon's solution (1965) and that Sneddon could have obtained his results from Galin, see also the appendix chapter by Borodich in Galin [2008] on Hertz type contact problems. It is also interesting to note that Ting [1966] found the Sneddon solution in a different approach, however, after Sneddon had published his findings.

2.5.3. Hertz solution for the contact problem of a rigid sphere on an elastic half-space

In [1881] Heinrich Hertz published his essay "Über die Berührung fester elastischer Körper" where he used an electrostatic analogy to consider the contact problem of two elastic bodies.[14] Neglecting frictional effects between the two smooth contact surfaces and assuming

[14] The following statements on Hertz' work go to some extent along the argument line of Chapter 4.3 in Johnson [1985]. The interested reader is also referred to e.g. Ziff. 79 in Geckeler [1928] or article 125 in Timoshenko and Goodier [1951].

that the semi-axes of the contact ellipse are much smaller than the main curvature radii and the overall dimensions of the two bodies, Hertz regarded each body as an infinite half-space loaded by a pressure small enough to provoke linear elastic material behaviour only. This type of problem is today commonly denoted by the term “Hertzian contact”.

Hertz’ formulae simplify for the case of axisymmetric bodies. Then, the contact ellipse becomes a circle with the radius r_c. Hertz approximated each body’s shape f_κ, where $\kappa \in \{1,2\}$ refers to the particular body, by a second-order expansion such that

$$f_\kappa(r) = \frac{r^2}{2\,R_\kappa} \tag{2.49}$$

describes a spherical body well in the vicinity of $r = 0$ and, thus, over the contact region provided that r_c is small enough, i.e. $r_c \ll R_\kappa$, where R_κ is the radius of the respective spherical body. He assumed a pressure distribution σ_h of the form

$$\sigma_\mathrm{h}(r) \;=\; P\,\sqrt{1-\left(\frac{r}{r_c}\right)^2} \tag{2.50}$$

over the contact area $0 \le r \le r_c$ (see Eqn. (2.39)), where P [Pa] is the maximum pressure at $r = 0$ depending on the overall applied force $F_\mathrm{h} = \int_0^{r_c}\int_0^{2\pi} \sigma_\mathrm{h}(r)\,\mathrm{d}\vartheta\,\mathrm{d}r$ by

$$P = \frac{3}{2\pi}\frac{F_\mathrm{h}}{{r_c}^2}\ . \tag{2.51}$$

This pressure distribution, which acts on each of the two bodies, results in the respective displacement[15]

$$\zeta_\kappa(r) \;=\; \frac{\pi}{4}\,\frac{P}{Y_\kappa}\,\frac{2{r_c}^2 - r^2}{r_c} \tag{2.52}$$

for $0 \le r \le r_c$. Since one body approaches the other by $u_\kappa = \zeta_\kappa(r) + f_\kappa(r)$, see Fig. 2.2, the overall approach u_h is

$$u_\mathrm{h} \;=\; u_1 + u_2 \;=\; \zeta_1(r) + f_1(r) + \zeta_2(r) + f_2(r)\ . \tag{2.53}$$

Inserting Eqns. (2.49) and (2.52) into (2.53) and simplifying, one gets

$$u_\mathrm{h} \;=\; \frac{\pi}{4}\,\frac{P}{Y_r}\,\frac{2{r_c}^2 - r^2}{r_c} + \frac{r^2}{2}\left(\frac{1}{R_1}+\frac{1}{R_2}\right), \tag{2.54}$$

where $1/Y_r = 1/Y_1 + 1/Y_2$ was used. Because u_h is the overall approach at the centre point ($r = 0$), all terms of Eqn. (2.54) which depend on r have to cancel each other. Hence, one finds the radius of the contact circle as

$$r_c \;=\; \frac{\pi}{2}\,\frac{P}{Y_r}\left(\frac{1}{R_1}+\frac{1}{R_2}\right)^{-1}, \tag{2.55}$$

[15] One may take without harm absolute values irrespective of any positive direction definitions in order to ease the writing effort.

and so one gets

$$u_\mathrm{h} = \frac{\pi}{2}\,\frac{P}{Y_r}\,r_c = \left(\frac{\pi}{2}\right)^2\left(\frac{P}{Y_r}\right)^2\left(\frac{1}{R_1}+\frac{1}{R_2}\right)^{-1} = \left(\frac{1}{R_1}+\frac{1}{R_2}\right){r_c}^2\ . \tag{2.56}$$

Considering Eqn. (2.51) in (2.55), taking the resulting expression for ${r_c}^3$ to the power of 2/3, and inserting into Eqn. (2.56), it is also possible to express the mutual approach in terms of the contact force by

$$u_\mathrm{h} = \left(\frac{9}{16}\right)^{1/3}\left(\frac{1}{R_1}+\frac{1}{R_2}\right)^{1/3}\left(\frac{1-\nu_1^2}{E_1}+\frac{1-\nu_2^2}{E_2}\right)^{2/3}{F_\mathrm{h}}^{2/3}\ . \tag{2.57}$$

Specialisation for a rigid sphere and an elastic half-space. Now, consider the case of a rigid sphere (radius $R \stackrel{\mathrm{def}}{=} R_1$, while $E_1 \to \infty$) being pressed onto an elastic half-space (Young's modulus $E \stackrel{\mathrm{def}}{=} E_2$ and Poisson's ratio $\nu \stackrel{\mathrm{def}}{=} \nu_2$, while $R_2 \to \infty$) by the force F. Noting that Y_r reduces to Y, the penetration depth depends on the force by

$$u_\mathrm{h} = \left(\frac{9}{16}\right)^{1/3}\frac{1}{R^{1/3}}\,\frac{(1-\nu^2)^{2/3}}{E^{2/3}}\,{F_\mathrm{h}}^{2/3} = \left(\frac{9}{16}\,R^{-1}\,Y^{-2}\,{F_\mathrm{h}}^2\right)^{1/3} \tag{2.58}$$

i.e. the force on the penetration by

$$F_\mathrm{h} = \left[\ \frac{4}{3}\,R^{1/2}\,Y\ \right]\,{u_\mathrm{h}}^{3/2}\ , \tag{2.59}$$

where the term in brackets can be regarded as some kind of stiffness [N·m$^{-1.5}$].

The penetration and the force according to Hertz are expressed as a function of the contact radius by

$$u_\mathrm{h}(r_c) = \frac{{r_c}^2}{R} \tag{2.60}$$

and

$$F_\mathrm{h}(r_c) = \frac{4}{3}\,Y\,\frac{{r_c}^3}{R}\ , \tag{2.61}$$

respectively, which is a suitable format for comparison with the Sneddon solution for an exact sphere (Eqns. (2.42) and (2.43)).

2.5.4. Comparison between the Hertz and the Sneddon solution for spherical contact

For the arbitrarily chosen case $R = 1$, Sneddon's exact sphere and Hertz' classical sphere are compared in Fig. 2.3, where the contact force and the contact radius are plotted as a function

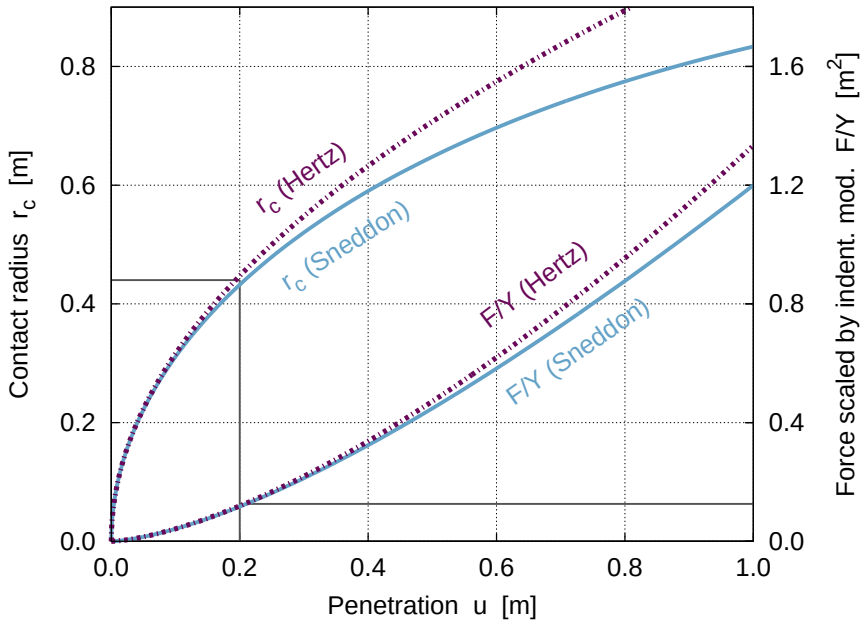

Figure 2.3.: Penetration of a rigid sphere with radius $R = 1$ [m] into a linear elastic half-space of arbitrary indentation modulus Y: dependence of contact radius r_c [m] and relative load F/Y [m^2] on the penetration u [m] for both the Sneddon and the Hertz solution. At the marked point ($u \approx 0.20$, $r_c \approx 0.44$ and $F/Y \approx 0.012$), the difference between the two solutions is approximately 6.8% for the penetration and 8.1% for the force.

of the penetration depth. For a relative penetration depth $\frac{u}{R} \approx 0.20$ the solutions deviate by 6.8% in the value for the penetration and by 8.1% for the force, i.e. for smaller penetrations the error should be small enough to be tolerated. Concerning the applicability of the derived formulae it should be noted that in most cases the assumption of linear elastic material behaviour will have to be questioned before the $\frac{r_c}{R}$-ratio becomes critical.

2.5.5. Hertzian impact of a rigid sphere on an elastic half-space

When a small body impacts the plane surface of a massive specimen, the portion of the initial kinetic energy which is transformed to wave energy is, according to Hunter [1957], negligible provided that the impact velocity is small[16]. Even though Reed [1985] determines a larger

[16] Compared to the wave propagation velocity in the elastic specimen. Hunter is quoting Love [1944], who states that "it is necessary that the duration of impact should be a large multiple of the gravest period of free vibration of either body" (*ibid.*, p. 198), but he comes to the conclusion that this criterion is too restrictive.

loss, this means for purely elastic material behaviour that after contact the impactor will be moving by the same magnitude of velocity, just the direction is opposite to the initial movement.

Hunter's analytical derivations and his comparison with experimental data are an *a posteriori* confirmation for just these assumptions in Hertzian impact[17], which is specialised here for the following case: a rigid sphere of radius R, mass M, and initial velocity V approaches a massless elastic half-space (Young's modulus E and Poisson's ratio ν, or indentation modulus Y), see Fig. 2.4a. The z-axis and the positive displacement u are defined upwards, but the initial movement of the sphere is positive downwards. Thus, during contact, $u(t) \leq 0$, so that $\dot{u}(t)$ is an increasing function (with $\dot{u}(0) = -V$) and $\ddot{u}(t) \geq 0$. From Newton's second law one finds the positive deceleration force acting on the half-space

$$F(t) \;=\; M\ddot{u}(t) \;. \tag{2.62}$$

During contact (see Fig. 2.4b), friction between the two bodies is neglected, and Eqn. (2.59) is valid at all times (Hertz [1881]). Thus, force equilibrium results in

$$M\ddot{u}(t) \;=\; \frac{4}{3}\, R^{1/2}\, Y\, u(t)^{3/2} \tag{2.63}$$

and, upon integration, in

$$M\frac{\dot{u}(t)^2 - V^2}{2} \;=\; \frac{8}{15}\, R^{1/2}\, Y\, u(t)^{5/2} \;. \tag{2.64}$$

The total contact duration is denoted by 2θ. Since the penetration history became an even function of time if it was shifted by θ (see e.g. Hertz [1881]), it is clear that the maximum absolute value of the penetration

$$u_{\mathrm{el}} \;\stackrel{\mathrm{def}}{=}\; \max_{0\leq t\leq 2\theta} |u(t)| \;=\; -\min_{0\leq t\leq 2\theta} u(t) \;=\; -u(t=\theta) \tag{2.65}$$

(see Fig. 2.4c) occurs at half the contact duration, i.e. at $t = \theta$. By putting $\dot{u}(t) = 0$ in Eqn. (2.64), the value of u_{el} is obtained as

$$u_{\mathrm{el}} \;=\; \left(\frac{15}{16}\right)^{0.4}\; R^{-0.2}\, M^{0.4}\, V^{0.8}\, Y^{-0.4} \;. \tag{2.66}$$

Hunter's analysis is applicable provided that "the thickness is sufficient to prevent the first reflected elastic wave returning to the contact area before the impact terminates" (p. 170 in Hunter [1957]).

[17] Hertz [1881]. Beside the references given in Section 1.2, see also Article 127 in Timoshenko and Goodier [1951], Article 140 in Love [1944], Chapter 1 in Johnson [1972], and Chapter 11 in Johnson [1985]. For brevity, the index "h" for the Hertz solution will be omitted in the remainder of this chapter.

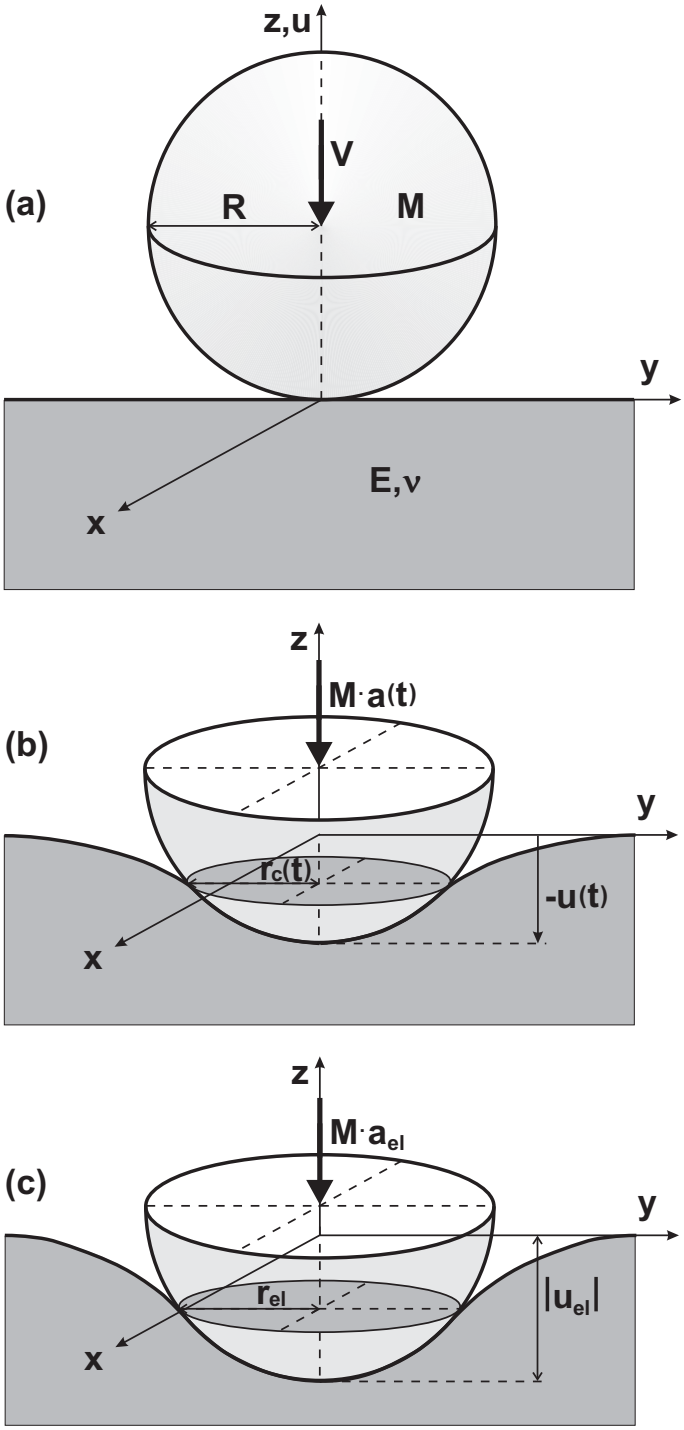

Figure 2.4.: Spherical impactor of radius R and mass M: **(a)** initiation of contact with an elastic half-space (Young's modulus E, Poisson's ratio ν) where the initial velocity V is prescribed, **(b)** contact relations during the loading or unloading phase, **(c)** relations at θ, i.e. half of the contact duration, where the velocity $\dot{u}(t) = 0$.

Inserting Eqn. (2.66) into (2.63) one obtains the maximum deceleration

$$a_{\mathrm{el}} \stackrel{\mathrm{def}}{=} \ddot{u}(t=\theta) \;=\; \frac{4}{3}\left(\frac{15}{16}\right)^{0.6} R^{0.2}\, M^{-0.4}\, V^{1.2}\, Y^{0.4}\;, \tag{2.67}$$

i.e. the maximum contact force is

$$F_{\mathrm{el}} \stackrel{\mathrm{def}}{=} F(t=\theta) \;=\; M\, a_{\mathrm{el}} \;=\; \frac{4}{3}\left(\frac{15}{16}\right)^{0.6} R^{0.2}\, M^{0.6}\, V^{1.2}\, Y^{0.4}\;. \tag{2.68}$$

Let's define the normalised penetration over time by $w\big(u(t)\big) \stackrel{\mathrm{def}}{=} \frac{-u(t)}{u_{\mathrm{el}}}$ such that $0 \le w\big(u(t)\big) \le 1$. The relation between a certain time instant $0 \le t \le \theta$ and the normalised penetration is given by Deresiewicz [1968] as

$$t \;=\; \frac{-1}{V}\int_0^{-u}\Big(1-\big(w(u)\big)^{2.5}\Big)^{-0.5}\,\mathrm{d}u\;. \tag{2.69}$$

Changing the integration variable, performing the integration and simplifying, one gets

$$\begin{aligned} t \;&=\; \frac{u_{\mathrm{el}}}{V}\int_0^{w}\left(1-w^{2.5}\right)^{-0.5}\mathrm{d}w \;=\; \frac{u_{\mathrm{el}}}{V}\Big[\, w\;{}_2\mathrm{F}_1(0.4;0.5;1.4;w^{2.5})\Big]_0^{w} \\ &=\; 0.4\, B(w^{2.5};0.4;0.5)\,\frac{u_{\mathrm{el}}}{V}\;. \end{aligned} \tag{2.70}$$

Thus, upon substitution of $w=1$ (meaning $u=-u_{\mathrm{el}}$), one obtains

$$\theta \;=\; 0.4\, B(0.4;0.5)\frac{u_{\mathrm{el}}}{V} \approx 1.472\,\frac{u_{\mathrm{el}}}{V} \;=\; 1.472\left(\frac{15}{16}\right)^{0.4} R^{-0.2}\, M^{0.4}\, V^{-0.2}\, Y^{-0.4}\;, \tag{2.71}$$

cf. Hertz [1881], Hunter [1957], Deresiewicz [1968], Johnson [1972]. In the above equations, ${}_2\mathrm{F}_1(a;b;c;z)$ denotes a hypergeometric function, $B(a;b)$ the beta function and $B(z;a;b)$ the incomplete beta function, see Section A.2 in the Appendix. It is perhaps of interest to mention that θ decreases when the initial velocity increases (to give an example in numbers, by 13% for double the velocity), which might not be expected by intuition.

From Eqn. (2.66) and (2.67) follows

$$u_{\mathrm{el}}\, a_{\mathrm{el}} \;=\; \frac{5}{4}V^2\;. \tag{2.72}$$

Use of this relationship in Eqn. (2.71) yields

$$\theta \approx 1.840\,\frac{V}{a_{\mathrm{el}}} \quad\text{and}\quad \frac{\frac{u_{\mathrm{el}}}{\theta}}{a_{\mathrm{el}}\,\theta} \;=\; 0.3692\;. \tag{2.73}$$

Combining Eqns. (2.70) and (2.71), for $0 \le t \le \theta$ one can plot the dimensionless penetration $w\big(u(t)\big)$ over the time scaled by θ using the relation

$$\frac{t}{\theta} \;=\; \frac{B(w^{2.5};0.4;0.5)}{B(0.4;0.5)} \;=\; I(w^{2.5};0.4;0.5)\;, \tag{2.74}$$

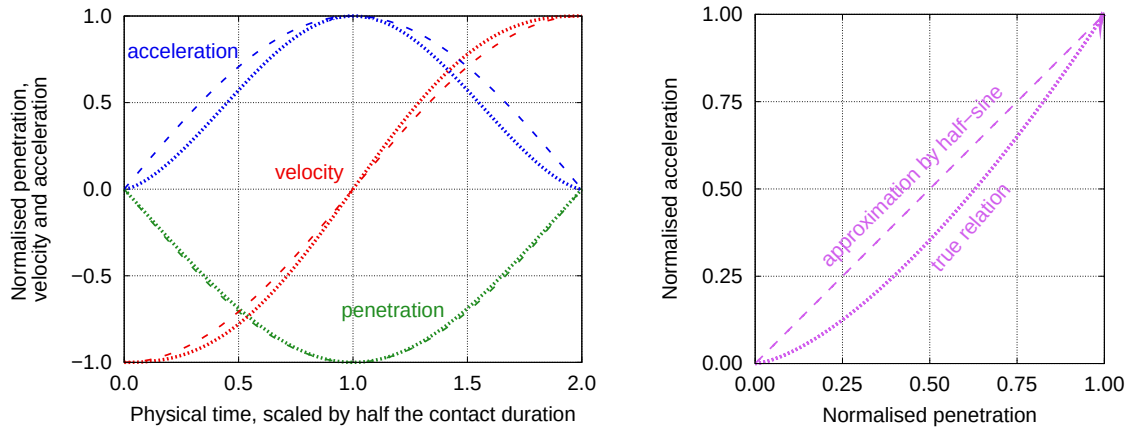

(a) Time history

(b) Acceleration over penetration

Figure 2.5.: Comparison of exact penetration (dotted lines, see e.g. Deresiewicz [1968]) and the half-sine approximation (dashed lines). **(a)** Time history (the physical time is scaled by half the contact duration, i.e. the abscissa is $\frac{t}{\theta}$) for penetration, velocity, and acceleration (normalised values on the ordinate, i.e. scaled such that they are within the unit range). **(b)** Acceleration as a function of penetration.

as has been done e.g. by Deresiewicz [1968]. In the above formula, the regularised beta function $I(z;a;b)$ was used, see Eqn. (A.21). The plot, enhanced by the time derivatives for the velocity and the acceleration, is given in Fig. 2.5a where the normalised penetration was multiplied by -1 in order to plot the penetration downwards. The approximation by half a sine, which has been intensely used in literature for simplification of the impact problem (see e.g. Hunter [1957]), is also shown. Whereas this simplification seems to be acceptable for the penetration, there are remarkable deviations for the acceleration, see also Fig. 2.5b.

2.6. Contact and impact of a rigid sphere on a viscoelastic half-space

The correspondence principle (Lee [1955]) is based on the application of the Laplace transform to the underlying basic equations as well as to the boundary conditions in order to eliminate the time-dependence of the viscoelastic problem in favour of the transform variable. In this way, the viscoelastic problem is turned into an associated elastic problem, for which solutions regarding the quantity of interest (usually stresses or displacements) exist in the literature, and the desired solution of the viscoelastic problem is just obtained by ap-

plication of the inverse transform to the associated solution. In the theoretical deduction of this method it is, however, required that the same time dependence prevails in all prescribed quantities[18], such that their transformation leaves their spatial distribution unaltered and, thus, equal to the associated elastic problem.

Hence, the correspondence principle may be applied to the indentation or impact of a flat circular punch on a viscoelastic half-space[19], but it fails for the case of curved indenters, since the interface between stress and displacement boundary conditions moves with the passage of time. The handling of such problems had to wait until Radok [1957] presented the method of functional equations where he showed that one can just replace the elastic constants in the elastic solution by the differential time operators describing the viscoelastic stress-strain relations. The so-obtained "functional equations" are then to be solved by operational methods[20] giving the solution to the viscoelastic problem. On this basis, Lee and Radok [1960] were able to solve the contact problem for a rigid spherical indenter and a viscoelastic half-space – starting from the Hertzian contact relations – in terms of the penetration depth or the applied force. The solution is limited by the restriction that the area of contact must not decrease, because otherwise a tensile stress would be present on those points of the boundary which earlier had been in contact with the sphere but are not at a later time instant. For simplicity they assumed for the derivation that the material is incompressible, thus, only the shear modulus has to be taken into account as material operator. The authors give examples for a Maxwell material and also discuss more general problem types, e.g. non-spherical indenters, inclusion of dilatational effects, sudden unloading and the like.

The restriction to a non-decreasing contact area is a severe limitation regarding the possibility of an extension towards the dynamic impact case. In an earlier publication, Pao [1955] tried to apply the correspondence principle to solve, based on the Hertzian contact relations, the problem of a moving viscoelastic body impacting a rigid stationary surface. To this end, he regarded the dilatational behaviour as purely elastic and assumed that viscoelastic effects in the deviatoric part change neither the contact area nor the stress distribution compared to the elastic case. However, he failed to see that tensile stresses were occurring after the maximum compression has been reached, which leads to erroneous results for the rebound.

[18] viz. "proportional loading". Lee also shows how to deal with moving loads, but the procedure seems of minor practical use due to the complexity of the resulting equations.

[19] See e.g. Hunter [1967]

[20] And a very convenient mathematical tool to do so is, in fact, just the application of the inverse Laplace transform, in which case the method of functional equations is equivalent to the correspondence principle.

Realising that a proper stress boundary condition for points on the surface outside the contact area should not be expressed by $\sigma = 0$ but rather by

$$\int_{\xi=0}^{t} G(t-\xi)\frac{\partial \sigma}{\partial \xi}\ \mathrm{d}\xi\ =\ 0\ , \tag{2.75}$$

where $G(t)$ is a proper stress relaxation function, Hunter [1960] generalised the solution of Lee and Radok [1960] using a somewhat different method[21] to the case where the contact area is allowed to decrease after having reached a single maximum at the time instant t_{turn}. For simplicity, he assumed an "unequivocal" (i.e. constant over time) Poisson's ratio. The relation between the indentation force $F(t)$ and the contact radius r_c is then found to be

$$F(t)\ =\ \frac{8}{3R(1-\nu)}\int_{\xi=0}^{t} G(t-\xi)\frac{\mathrm{d}\left({r_c}^3(\xi)\right)}{\mathrm{d}\xi}\ \mathrm{d}\xi \tag{2.76}$$

for increasing contact area ($0 \le t \le t_{\mathrm{turn}}$) and

$$F(t)\ =\ \frac{8}{3R(1-\nu)}\int_{\xi=0}^{t_{\mathrm{incr}}(t)} G(t-\xi)\frac{\mathrm{d}\left({r_c}^3(\xi)\right)}{\mathrm{d}\xi}\ \mathrm{d}\xi \tag{2.77}$$

for decreasing contact area ($t_{\mathrm{turn}} \le t \le t_{\mathrm{tot}}$), where t_{tot} is the total contact duration and t_{incr} is that time instant during an increasing contact area at which the same contact radius occurred as at the present time t during the unloading part with decreasing contact area, i.e. it is defined by $r_c\left(t_{\mathrm{incr}} \le t_{\mathrm{turn}}\right) = r_c\left(t \ge t_{\mathrm{turn}}\right)$. Now, Hunter is able to tackle even the dynamic impact problem since the relation between the penetration $u(t)$, the contact radius, and the sphere's radius is known at least for the first phase (see Eqn. (2.60)), thus, the equation of motion (cf. Eqn. (2.62)) can be set up and solved by numerical methods. An (approximate) analytical solution is, however, possible for the case of a Maxwell material with a characteristic time τ being much larger than the total impact duration. Thus, for the first phase ($0 \le t \le t_{\mathrm{turn}}$) the differential equation

$$\ddot{u}(t) + \frac{\dot{u} - V}{\tau}\ =\ \frac{8}{3}R^{0.5}M^{-1}\frac{G_0}{1-\nu}u^{1.5} \tag{2.78}$$

is obtained, where G_0 is the initial shear modulus. For the second phase ($t_{\mathrm{turn}} \le t \le t_{\mathrm{tot}}$), insertion of the relaxation function of the Maxwell model (replace parameter E in Eqn. (B.8) by G_0) and simplification yields the relation between sphere's radius, penetration rate, and contact radius for the second phase as

$$R\dot{u}\ =\ \exp\left(-\frac{t - t_{\mathrm{incr}}}{\tau}\right)\frac{\mathrm{d}{r_c}^2(t)}{\mathrm{d}t} \tag{2.79}$$

in analogy to Eqn. (2.60) which was valid only for increasing contact area. Hence it also follows that maximum contact radius and maximum penetration depth occur at the same

[21] Based on the Boussinesq solution he obtained a pair of dual integral equations.

time t_{turn}. Since a Maxwell material shows purely elastic behaviour for $\tau \to \infty$ (and $\tau \gg t_{\text{tot}}$ had to be claimed earlier anyway) Hunter showed that he may use the relationship $t_{\text{incr}} = 2t_{\text{turn}} - t$, which is actually correct for the purely elastic case. Now, the equation of motion can be solved, leading to formulae for the coefficient of restitution

$$\Pi_{\text{rest}}^{\text{MX}} = 1 - \frac{8\theta}{9\tau} , \tag{2.80}$$

by which the value for the characteristic time can be determined from experiments, and for the contact duration

$$t_{\text{tot}} = 2\,\theta \left(1 - 0.074\frac{\theta}{\tau}\right) , \tag{2.81}$$

giving access to the initial shear modulus from experimental measurements. In these formulae, θ is half the elastic impact duration as earlier introduced in Eqn. (2.71).

Hunter's publication has gained much interest from other researchers. For instance, Chen and Lakes [1990] use Eqns. (2.76) and (2.77) as the starting point for the determination of optimal material parameters for a viscoelastic half-space under spherical impact.

Starting with Boussinesq's formula for the displacement of an elastic half-space due to a normal force, Graham [1965] expressed the spatial and temporal stress and displacement distribution for a viscoelastic half-space under a distributed normal load satisfying the generalised Papkovich-Neuber solution (Gurtin and Sternberg [1962]). He then obtained the contact pressure distribution under a rigid punch acting on a viscoelastic half-space expressed in terms of the contact pressure of the purely elastic problem, where the contact area is allowed to increase to a single maximum at t_{turn} and to decrease thereafter. Specialising the indenter geometry to be of spherical shape, he constructed integral expressions for the force and the penetration in terms of the contact radius, which, for the special case of an unequivocal Poisson's ratio, agree with Hunter's [1960] solution. On the other hand, in the incompressible case the solution of Lee and Radok [1960] is retrieved.

Graham also gave the governing equation for the impact of a rigid sphere on a viscoelastic half-space (cf. Eqns. (2.31), (2.60) and (2.63) for the purely elastic case) as

$$M\ddot{u} = \frac{4}{3\pi} R^{-1} \int_{-\infty}^{\zeta(t)} E_{\text{aux}}(t-\xi)\ \mathrm{d}{r_c}^3(\xi) , \tag{2.82}$$

where $\zeta = t$ for $t \le t_{\text{turn}}$ and $\zeta = t_{\text{incr}}(t)$ for $t > t_{\text{turn}}$, but does not carry out any evaluation of this equation. In the above formula, $E_{\text{aux}}(t)$ is a rather involved kind of viscoelastic material stiffness, which in the purely elastic case reduces to $\frac{4\pi G\,(3K+G)}{3K+4G}$. Later, the same author relieved the restriction to a single maximum of the contact radius by setting up proper recurrence relations for an arbitrary loading (Graham [1967]).

Yang [1966] derived the pressure distribution and surface displacements for viscoelastic bodies characterised by the same second-order surface description as in Hertz' [1881] paper. The solution is restricted to an increasing contact area, or to the case where the penetration depth is applied suddenly, held constant, and removed suddenly (disregarding dynamic effects). Yang also gave an example for the indentation of an incompressible three-parameter standard linear solid half-space (where $E_0 = 2E_\infty$ was used for simplicity) by a rigid sphere, showing elastic-like contact stresses both for $t = 0$ (with respect to E_0) and for $t \to \infty$ (w.r.t. E_∞) as could be expected.

Ting [1966] considered the contact problem of a rigid indenter and the viscoelastic half-space for an arbitrary time history of the contact radius. In analogy to Boussinesq's elastic problem – one may note that Ting was also successful here in deriving solutions concerning the force and penetration depth of some typical indenter shapes for the elastic case – he affirmed the more confined solutions by Lee and Radok [1960] and Hunter [1960]. Ting also showed that the maximum force and the maximum contact radius not necessarily occur at the same time instant; as an example he prescribed a sinusoidal force history to a paraboloid indenter (i.e. classical sphere) acting on an incompressible Maxwell half-space where one observes an increase in contact area also for decreasing force. His follow-up paper (Ting [1968]) brought the earlier presented solutions for a viscoelastic contact problem with an arbitrary contact radius history in a more amenable form.

A general solution of the static indentation problem of a rigid sphere and an anisotropic viscoelastic material was presented in Dahan and Predeleanu [1983].

It was noted by Aksel and Buggisch [1982] that the quasi-static contact between a viscoelastic half-space and a moving rigid sphere could also be solved by adding a disturbance solution to the Hertzian purely elastic case, which is justifiable when the material is either nearly elastic or has a very short or very long time scale compared to the impact duration. The quasi-static impact case is presented in Aksel [1986], where the contact radius (instead of the time) is taken as independent variable in order to easily distinguish between the approach and the restitution period. As opposed to most of the other literature on viscoelastic impact, Aksel was thus able to find, for either a very fast or a very slow half-space material, an analytical expression for the coefficient of restitution without the need to specialise a certain viscoelastic material model.

Assuming an unequivocal Poisson's ratio, closed-form analytical expressions for the rebound of a rigid sphere were derived by Argatov [2012]; however, not for a true impact problem but the scenario where the indenter is driven in at constant velocity until a prescribed indenta-

tion depth (i.e. the displacements are known during the first phase) from which it is allowed to rebound (meaning no force was prescribed during the second phase).

Among the analytical methods addressed above, the two important contributions regarding spherical impact on a viscoelastic half-space are by Hunter [1960] and Graham [1965][22]. However, in practice their formulae appeared too involved for an analytical treatment except for simple nearly-elastic models for which some additional assumptions could be included. For this reason, and facilitated by increasing computer power, numerical evaluations became the method of choice.

Calvit [1967b] used Hunter's [1960] dual integral equations as the starting point for a numerical integration using finite time increments. Regarding the single integro-differential equation for the first phase (monotonically increasing contact radius) he obtained an explicit system of equations by using forward differences. As concerns the second phase of decreasing contact radius, the pair of coupled integro-differential equations has to be solved iteratively. The material data used in the numerical calculations was obtained from free torsional experiments conducted on PMMA (polymethylmethacrylate) rods for different temperature levels. Comparison between the computed and experimentally measured results for the contact duration and rebound height showed good agreement for low temperatures. Calvit also demonstrated the amount of error introduced if one assumed that Eqn. (2.60) also holds for the withdrawal.

The dynamic problem of a rigid sphere impacting a viscoelastic half-space was treated in Aboudi [1979] by an iterative numerical integration scheme where increments both in time and in space had to be used. The procedure was set up by inserting the viscoelastic material behaviour, expressed in form of a generalised Maxwell model, in the dynamic equations of motion and by fulfilling the boundary conditions iteratively, as the proper contact radius is not known *a priori*. For several examples – viz. the indentation to a prescribed penetration depth, the indentation at uniform speed, and a loading-unloading indentation where the contact radius was prescribed to vary sinusoidally over time – he discussed the difference between his numerical results including wave propagation and quasi-static solutions from literature. Finally, Aboudi considered the dynamic impact problem using a standard linear solid for the deviatoric part but purely elastic material for the hydrostatic behaviour, where also the influence of friction was investigated.

A numerical integration scheme is also employed in Sabin [1987] who found, assuming an

[22] An illustration of their methods and results is also given e.g. in the conference paper by Hunter [1967], Section 2.12 in Christensen [1982], or Section 9.7 in Haddad [1995].

unequivocal Poisson's ratio, a solution to the equations of motion subject to the proper boundary and initial conditions for the rigid impactor and the viscoelastic half-space (notably that the displacements within the contact area have to conform to the indenter geometry). This solution, as he claimed, reduces to Graham's [1967] relations when the dynamic terms are neglected and to Sneddon's [1965] elastic indentation formulae when the relaxation function is taken as constant. Specialising the impactor to be a rigid sphere and the half-space as Maxwell material, Sabin solved the resulting iterative equation numerically. However, it seems that due to the very involved mathematical operations employed, his publication has not gained much interest from other researchers. This may be owing to a more intuitive and, already at that time, quite powerful tackling of impact problems by the Finite Element Method.

2.7. Concluding remarks

In this chapter, the creep compliance, the relaxation modulus and the complex relaxation modulus were introduced to describe the behaviour of linear isotropic viscoelastic materials. The viscoelastic functions were specialised for five different rheological models employed in the numerical simulation of spherical impact. In the general case of three-dimensional problems, the volumetric part is modelled separately from the deviatoric behaviour.

The second part of this chapter started with spherical contact and impact for a purely elastic half-space. The difference between the Sneddon solution and the Hertzian relations is negligible for small penetrations, which are necessary anyway when the material is supposed to show linear behaviour. For viscoelastic media, there are no analytical solutions available for spherical impact on a realistic material with pronounced viscoelastic behaviour.

3. Materials and material properties

Experimenting in science is an exploration, a search into the unknown: this is what makes it so enjoyable.

GIBBINGS [1986], p. vii

Es unterliegt keinem Zweifel, daß eine eingehende experimentelle Prüfung der elastischen Nachwirkung einen Aufwand von freier Zeit erfordern würde, welcher mir jetzt keineswegs zur Verfügung steht.

BOLTZMANN [1876], p. 649-650

In order to validate the method for the material parameter identification described in Section 4.5 two different kinds of polyurethane foams were used in the experiments. For this reason, this chapter starts (Section 3.1) with a rather short introduction to solid foams and polymeric materials in general. The interested reader is referred to, for example, Ashby [2005], Gibson and Ashby [1997], Knippers et al. [2010], Mills [2007], Oertel [1993], and Reinhardt [1997] for a deeper investigation of this topic.

Section 3.2 reports on specific properties of the material samples used in the study at hand, such as density, absorbance spectrum, and microscopical structure. Finally, the response for static loading scenarios is illustrated.

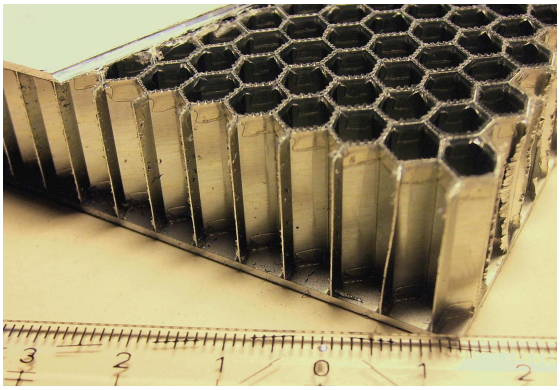

(a) Metal honeycomb

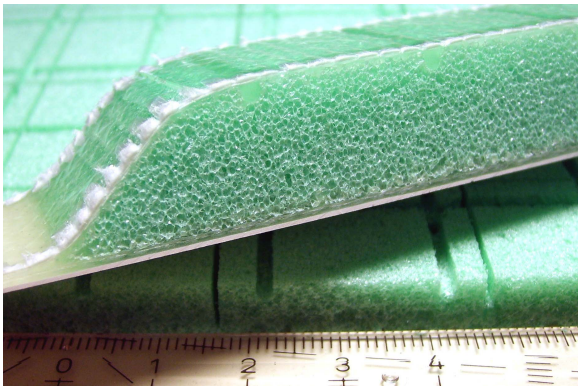

(b) Polymeric foam

Figure 3.1.: Two examples for cellular solids: **(a)** metal honeycomb and **(b)** polymeric foam. In these pictures, the cellular solid is used in a sandwich structure, where it serves as a light but relatively stiff layer between the outer plates of the composite structure.

3.1. Cellular solids

3.1.1. Types of cellular materials

In a cellular solid, the material is arranged such that the cell walls build a regular or an unordered network, while the free volume is occupied by a fluid, often air. Cellular structures with a regular pattern usually consist of hexagonal cells, in which case they are called honeycombs, see Fig. 3.1a. More often, however, the individual cells differ from each other in size and/or shape and show an unordered connectivity; in this case, one uses the term foam (where in the present work we will disregard liquid foams). An example is depicted in Fig. 3.1b. In solid foams, the bulk material may be, to mention just a few examples, a metal (e.g. for barriers for energy absorption in an automobile crash test), a biomaterial (e.g. in a human bone), or a polymer (e.g. in case of an extruded polystyrene foam).

It is important to distinguish between foams with open and those with closed cells, as this geometric detail has a great impact on the mechanical behaviour: in closed cells, the fluid is trapped, which results in a mechanical stiffening effect when the pore volume is changing, whereas open cells allow for an intercellular fluid transport which in general results in a time-dependent response due to viscous flow effects.

3.1.2. Characteristics of polymeric foams

Under compression, cellular foams typically show a three-staged behaviour: the linear elastic/viscoelastic region is followed by a plateau in the stress-strain diagram owing to buckling, plastic yielding and/or brittle failure of the cell walls; for larger deformations, the cell walls come into self-contact (densification), leading to a large increase in structural stiffness. Different kinds of modelling are discussed e.g. in Avalle et al. [2007]. However, the described large strain phenomena need here not be elaborated further, as the limitation to small strains is necessary for the present work in view of both the underlying linear viscoelastic material behaviour and the use of the Hertzian contact relations.

Concerning the mechanical properties, all polymer materials show a high dependency on the temperature, which may in the easiest cases be accounted for by a shift in the time scale, see e.g. Williams et al. [1955]. However, throughout this work the effect of temperature is not considered.

Polymeric foams possess many advantageous features such as low density, good acoustic absorptivity, low thermal conductivity, high air permeability, easy manufacturing and rather low production costs (see e.g. Ashby [2005]). Since they show good damping properties, they are well suited for protection against impact loads. Also, because these materials usually recover their original shape upon removal of the loads, they can be used even in case of repetitive loading such as e.g. structural vibrations.

Thus, polymeric foams are employed in various applications requiring impact protection or improving comfort, e.g. for seats and mattresses, sport shoes and sport mats, body protection (helmets, knee pads, shin guards), packaging of fragile goods, or vibration damping (see Mills [2007]).

3.2. Characteristics of the investigated foam specimens

The specimens investigated in this thesis are flexible polyurethane (PUR-F) foams. This material was chosen because it shows pronounced viscoelastic effects which can be observed typically over some milliseconds to some hundred seconds; thus, access to a characterisation of mechanical properties may be given by conventional creep and relaxation tests (see Subsections 3.2.3 to 3.2.6) but also by the impact experiments detailed in Chapter 4. Also, the occurrence of damage or plastic flow can be excluded in the small strain regime.

It should be kept in mind that in this work the purpose of the experimental investigations is not to establish a new procedure for the identification of material parameters but to validate the impact testing method described in Section 4.5 which is based on numerical results; thus, it is sufficient to consider just a few exemplary sample specimens. These were obtained from materials provided by two different manufacturers in order to guarantee a certain generality of the results.

- One type of specimens is produced by Getzner Werkstoffe GmbH in Bürs, Austria, and is available under the name Sylomer® SR-110D.
- The other type of specimens tested stems from a mattress manufacturer. Due to confidentiality reasons the name is not given here and the material is called "DampVisc" in the frame of this thesis.

The process of polymerisation and industrial production is illustrated in Winterstein [2012]. Regarding the sample properties and the experimental investigations described in the following subsections, the reader is referred to the book by Oertel [1993] for a detailed treatment.

3.2.1. General sample properties

The Sylomer samples have a size of approximately 0.3 m by 0.3 m with 0.1 m thickness, while the dimensions of the DampVisc samples are 0.4 m by 0.4 m by 0.05 m, see Fig. 3.2. Since a loading by negative air pressure in a vacuum desiccator (see Fig. 3.3a) did not lead to a significant volume change both specimen types can be regarded as open cells.[1]

Apparent density. The bulk density is the ratio of the total mass to the total volume. The volume can be obtained by measuring the length, width and thickness of a sample when its shape is a rectangular parallelepiped. However, when too large inaccuracies are to be expected, or in case of other geometries, a reliable alternative is to submerge the sealed sample in water and to measure the volume of the displaced fluid (provided that the volume change of the sample due to the water pressure is negligible). For the DampVisc sample, the bulk density is approximately 71 $\frac{\mathrm{kg}}{\mathrm{m}^3}$, while it is 195 $\frac{\mathrm{kg}}{\mathrm{m}^3}$ for the Sylomer.

[1] In case of closed-cell foams, the pressure difference between the entrapped air and the ambient conditions would result in an increase of the specimen's volume. Since this was not observed, at least the larger pores have to be open. However, it cannot be strictly excluded that the sample contains some closed cells which are too small in volume to have a measurable effect on this kind of inspection. See also the micrographs in Subsection 3.2.2.

(a) Sylomer sample (b) DampVisc sample

Figure 3.2.: Polyurethane foam samples used for the experimental investigations: **(a)** Sylomer, **(b)** DampVisc.

True density. For the solid density (nominal density) the pore volume must not be taken into account, thus, the sample is not sealed when immersed into water. A vacuum desiccator, see Fig. 3.3a, can be used to completely fill the pore space by water. One can directly measure the displaced water volume (which equals the volume of the the solid material) and calculate

$$\rho_{\text{solid}} = \frac{M_{\text{dry}}}{V_{\text{solid}}} \; ; \tag{3.1}$$

however, there is a potential source of inaccuracy in the determination of the displaced volume. This disadvantage is avoided by hydrostatic weighing (see Fig. 3.3b), where just the weight of the dry sample and the one of the fully immersed sample M_{imm} have to be measured when the fluid density[2] is known.

The idea of this method is based on the fact that a body which is completely immersed in water (no air bubbles shall be trapped) is subjected to an upwards force corresponding to the weight of the displaced water

$$M_{\text{disp}} = \rho_{\text{water}} \, V_{\text{solid}} \; . \tag{3.2}$$

Thus, a balance on which the submerged body is placed would show the net weight

$$M_{\text{imm}} = M_{\text{dry}} - M_{\text{disp}} \; . \tag{3.3}$$

[2] Even though water was used here, it may be of advantage to use other fluids to avoid the problem of similar densities between the fluid and the sample material.

(a) Desiccator (b) Hydrostatic weighing of a DampVisc sample

Figure 3.3.: **(a)** Vacuum desiccator for evacuation of air, **(b)** hydrostatic weighing to determine the solid (true) density.

Since the DampVisc samples have a solid density smaller than the water density (as becomes apparent from the floating sample in Fig. 3.3b), M_{imm} was measured negative. Combining Eqns. (3.1), (3.2) and (3.3), one can construct the relation for the true density as

$$\rho_{\text{solid}} = \rho_{\text{water}} \frac{M_{\text{dry}}}{M_{\text{disp}}} = \rho_{\text{water}} \frac{M_{\text{dry}}}{M_{\text{dry}} - M_{\text{imm}}} \,. \tag{3.4}$$

It is important to realise that for this method measuring inaccuracies have a large impact when M_{imm} is small, i.e. when the solid density is of similar magnitude to the water density or when the pore space is close to the total volume. As this was, unfortunately, the case for the DampVisc samples, the solid density determined as 860 $\frac{\text{kg}}{\text{m}^3}$ can not be seen as a reliable reference. For polyurethane, the solid density can be assumed as approx. 1200 $\frac{\text{kg}}{\text{m}^3}$. Thus, it seems that not the whole pore space of the DampVisc sample could be filled by water due to very small pores or closed cells.

3.2.2. Microscale investigations

Infrared spectroscopy. A Fourier transform infrared (FT-IR) spectroscopy, where a Bruker Alpha FT-IR spectrometer with ATR module was used, gave the absorption spectra of the two samples shown in Fig. 3.4. The FT-IR method and the results related to the DampVisc sample are discussed in Winterstein [2012].

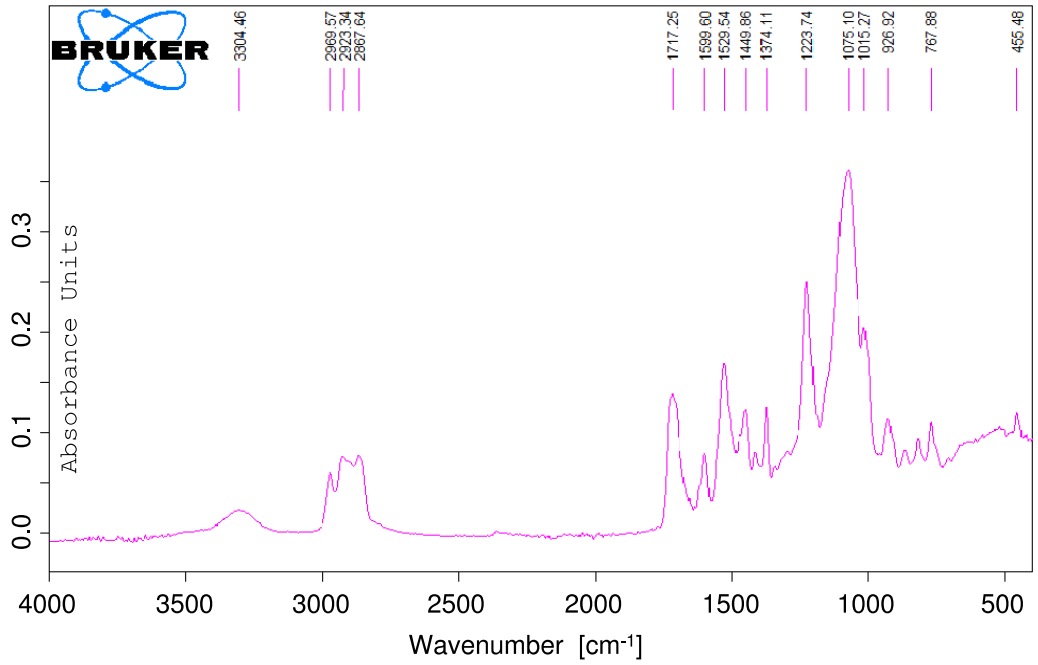

(a) Absorbance spectrum of the DampVisc sample

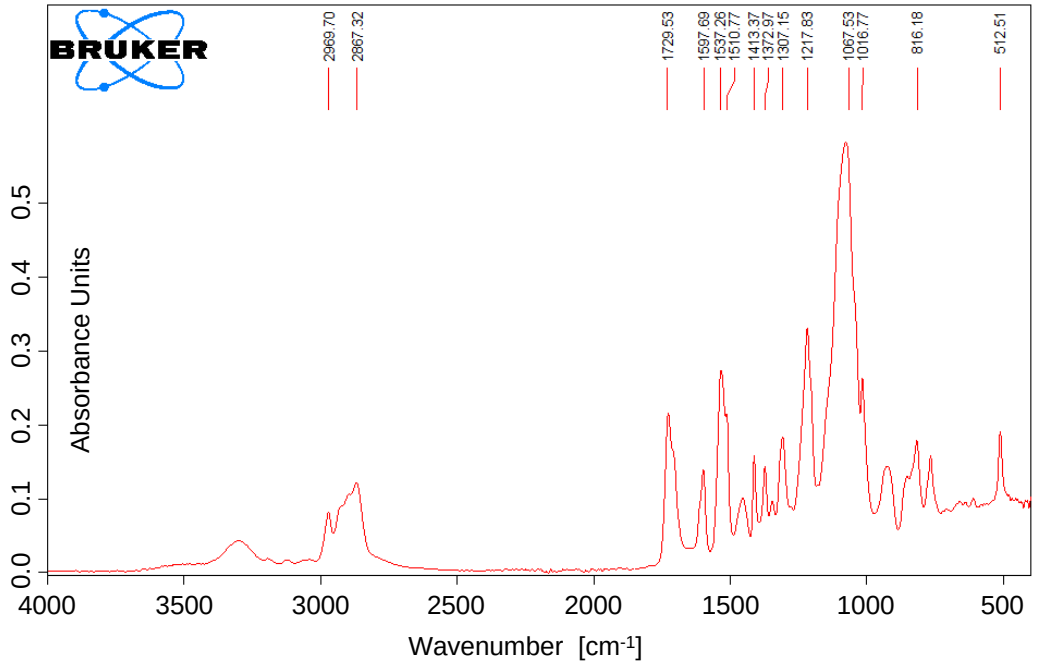

(b) Absorbance spectrum of the Sylomer sample

Figure 3.4.: Fourier transform infrared spectroscopy. On the abscissa, the wave number $\tilde{\nu}$ is plotted in a range from 4000/cm (corresponding to a wave length of 2.5 μm) to 400/cm (wave length 25 μm). On the ordinate the measured absorbance is shown; a low value means a high transmittance, see Bruker Optics Inc [2011]. **(a)** DampVisc, **(b)** Sylomer sample.

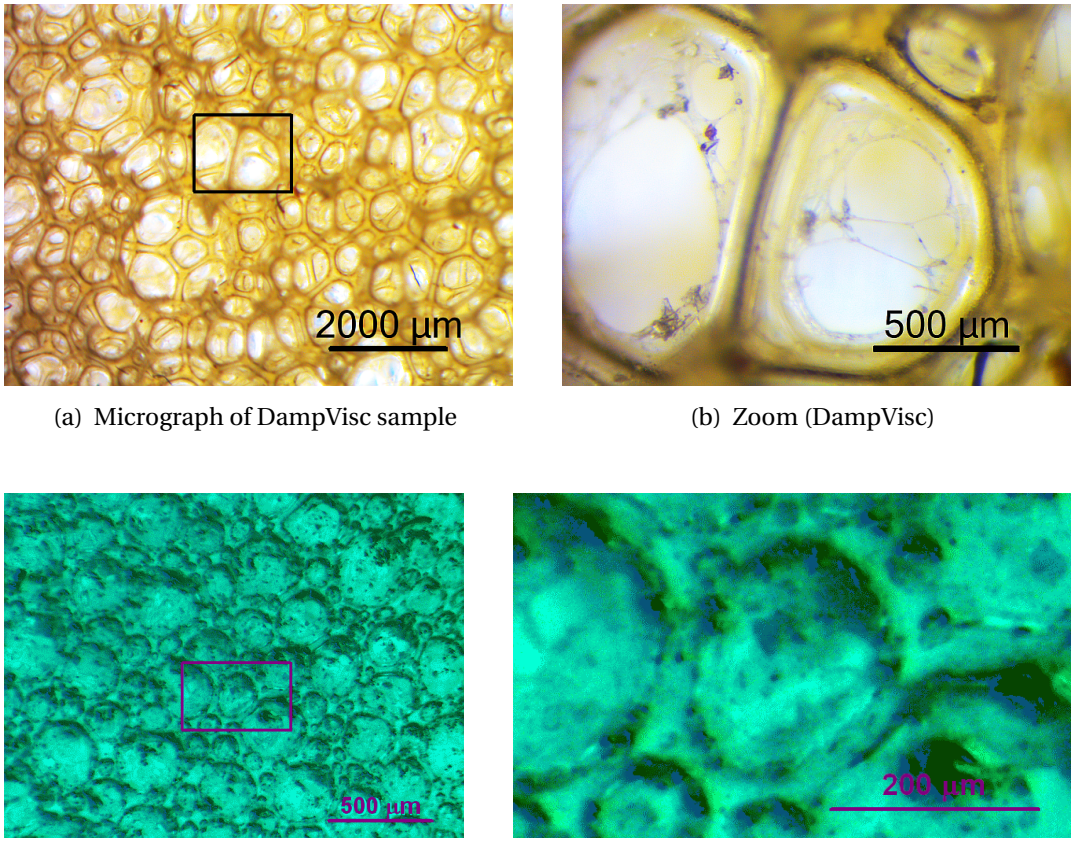

(a) Micrograph of DampVisc sample

(b) Zoom (DampVisc)

(c) Micrograph of Sylomer sample

(d) Zoom (Sylomer)

Figure 3.5.: Micrographs of the DampVisc and the Sylomer sample. **(a)** DampVisc, dimensions approx. 8600 μm by 6500 μm. **(b)** Zoom into the box (approx. 1750 μm by 1300 μm). **(c)** Sylomer, dimensions approx. 2200 μm by 1700 μm. **(d)** Zoom into the box (approx. 550 μm by 300 μm).

Microscopy. The morphology became visible from the inspection of the sample by an optical microscope, see Fig. 3.5. The micrographs of the DampVisc sample were taken using a thin slice allowing for good transparency of light, which is why a clear picture of the individual cells is obtained. Note the great variety of cell sizes in Fig. 3.5a (even though some of the cells might require a different cutting plane in order to appear in full size). For the Sylomer sample, the average pore size is much smaller than for the DampVisc (approximately by a factor of 4). Here, the micrographs were taken from the sample surface, such that the cells' back faces are seen. Even though both sample types show a mixture of closed and open cells, it seems that the relative amount of openings is much higher for the DampVisc sample compared to the Sylomer. Reliable quantification of openings would, however, have to be determined from a permeability experiment.

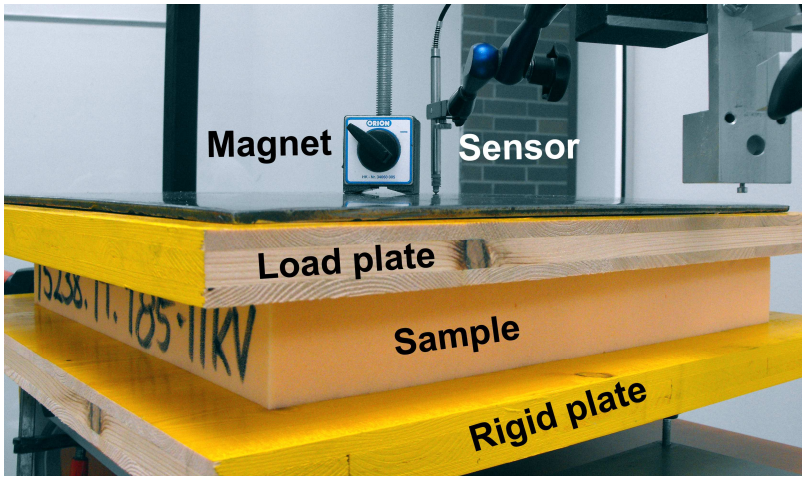

(a) Load plate set-up for very compliant samples

(b) Set-up for Shimadzu

Figure 3.6.: One-dimensional creep experiments (the photographs show samples similar to the ones considered here). **(a)** DampVisc: due to the large compliance, suitable deformations were obtained by the small load from a 12.769 kg load plate. Once the magnet releases the load plate, the sensor measures the plate displacement over time. **(b)** Sylomer: using a testing machine, the load was ramped until a deformation of 3 mm or 6 mm, respectively, was obtained, and then held constant. The creep displacement was measured by two sensors.

3.2.3. One-dimensional creep experiment (compression)

The DampVisc sample was subject to a creep experiment as shown in Fig. 3.6a. The loading can be considered as one-dimensional because the length and width dimension are much larger than the thickness. The sample was loaded by a 12.769 kg wood/steel plate, and the displacement was tracked over time by a displacement sensor or a laser device (see also Herrenbrück [2011]).

The recorded displacement history is given in Fig. 3.7a. Since the displacement rate over time makes a straight line in a log-log diagram, it seems on the first glance that the material sample can be modelled with the power law, cf. Eqn. (B.31). However, from the procedure described in Section B.3, a negative value of β would be obtained, which has to be excluded for physical reasons. With hindsight, this makes sense since a polymeric foam at room temperature should not show unbounded creep behaviour, and thus should not be of power law type.

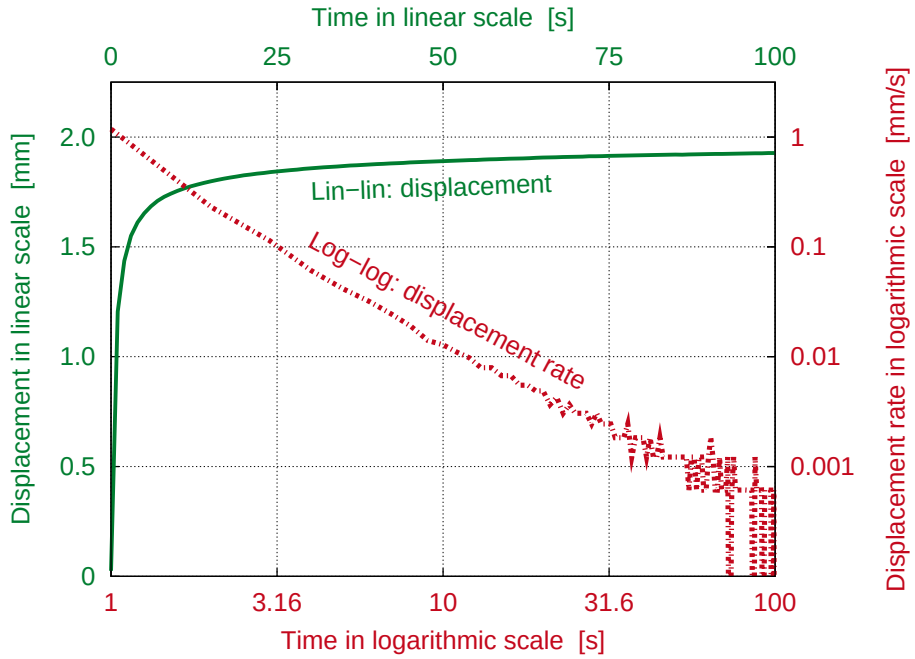

(a) DampVisc: the slope of the displacement rate is too steep here for the power law creep or the logarithmic creep model (compare to Figs. B.3 and B.8).

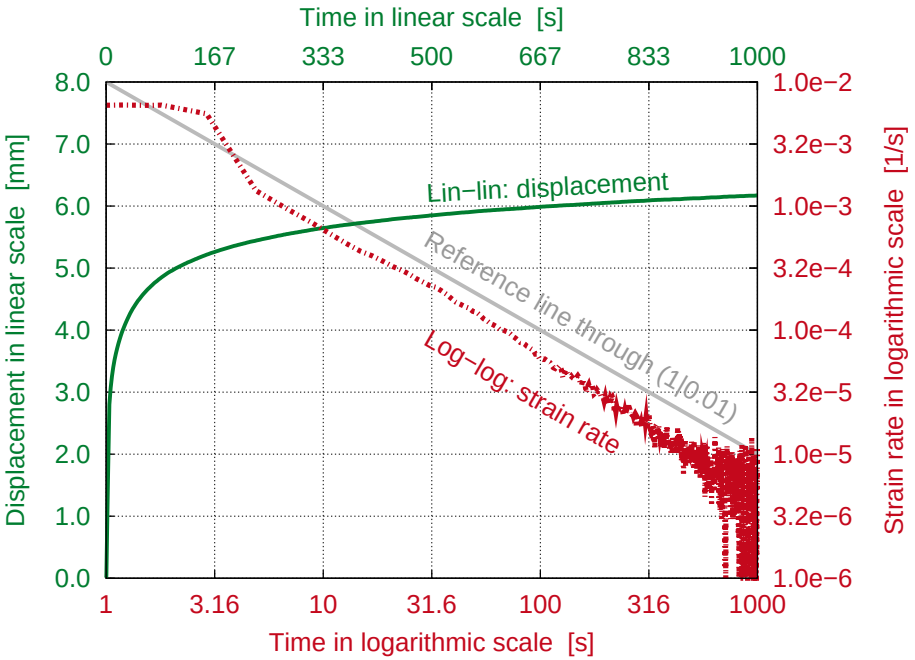

(b) Sylomer: the strain rate slope of −1 agrees well with the logarithmic creep model, see Fig. B.8.

Figure 3.7.: Experimental results from a one-dimensional creep experiment. **(a)** DampVisc, **(b)** Sylomer. Absolute values of measured displacement are plotted against time (lin-lin plot) and computed displacement rate or strain rate, respectively, over time (log-log plot). The oscillations in the rate are due to measurement inaccuracies of the displacement transducer for small displacement differences.

A different one-dimensional creep test[3] was conducted for the Sylomer sample, see Fig. 3.6b. Since this type of material is much stiffer, the compression load was applied by a machine (Shimadzu Autograph AG-X plus). To this end, a sample with the dimensions 0.1 m by 0.1 m by 0.1 m was used. Admittedly, the boundaries have a rather large influence on the stress state in the sample, but it is believed that the salient characteristics as regards the time-dependence of this material can be still obtained sufficiently well, see Fig. 3.7b. Due to the slope of -1 in the log-log plot of strain rate over time, the logarithmic creep model can be used to describe the one-dimensional behaviour of the Sylomer sample.

For this specific material model – see Eqn. (2.26) – one can determine the time-dependent portion of the compliance $\frac{\lambda}{E_0}$ directly from the log-log plot of strain rate over time, as described in Section B.5. This value is necessary later for the parameter identification for the logarithmic creep model (see Subsection 4.5.2). From Fig. 3.7b one obtains $\log\left(\sigma_0\right) + \log\left(\lambda/E_0\right) \approx -2.21$ (note that here the reference line goes through (1|0.01); thus, one has to add two decades in the vertical direction). Inserting the stress level of 11,300 Pa, one obtains

$$\frac{\lambda}{E_0} \approx \frac{10^{-2.21}}{11{,}300} \approx 0.55 \cdot 10^{-6} \, \frac{1}{\mathrm{Pa}} \, . \tag{3.5}$$

Because the load was ramped within the first six seconds, one should not use the data at the beginning of the creep experiment; thus, the determination of the characteristic time from the strain rate (as described in Section B.5) is not possible from this experiment.

3.2.4. Shear test: experimental investigations and numerical re-analysis

The shear behaviour of the DampVisc sample was investigated by a creep experiment accompanied by numerical simulations (see Fig. 3.8). A detailed report can be found in Winterstein [2012], from which the most important results are reviewed in the following.

In elasticity theory, for an infinitesimally small element subject to a constant shear straining in the x–y plane, the relation

$$\tau_{xy} = G\,\gamma_{xy} \quad \text{with } \tau_{xy} = \frac{F_y}{\ell_y\,\ell_z} \quad \text{and } \gamma_{xy} = \frac{u_y}{\ell_x} \tag{3.6}$$

holds as long as linearity[4] can be assumed, where τ_{xy} and γ_{xy} are the shear stress and strain,

[3] The experiment was carried out by Verginer [2013], who compares this specific material sample to other Sylomer types.

[4] i.e. small strains. For the experimental data, the assumption of linearity was confirmed in Winterstein [2012] by comparing to non-linear solutions from continuum mechanics for “pure shear” and “simple shear”.

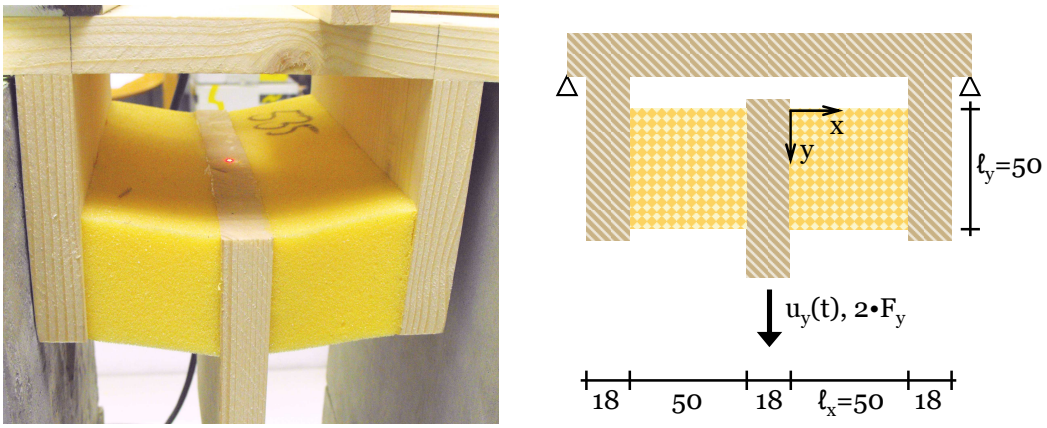

(a) DampVisc sample in shear experiment (b) Geometrical dimensions (2D) in mm

Figure 3.8.: DampVisc: **(a)** Experimental set-up of shear creep experiment, **(b)** geometry details, where for the numerical model (plane strain conditions) the wood's compliance was disregarded. Due to the use of symmetry, half of the total force was considered (i.e. F_y at $x = 0$), while all displacements were constrained at $x = \ell_x$.

respectively, F_y and u_y are the force and displacement in y-direction, respectively, ℓ_x, ℓ_y and ℓ_z are the width, height and depth of the sample, respectively, and G is the shear modulus. Based on this relation, the latter could be retrieved directly from measured force and displacement data by

$$G = \frac{F_y\,\ell_x}{u_y\,\ell_y\,\ell_z}\,. \tag{3.7}$$

However, the assumption of a constant shear straining can not be justified in the real experiment[5], since boundary and size effects influence the shear stress distribution, as becomes obvious from Fig. 3.9a. Due to the fact that the numerical/experimental shear stresses are smaller than in the idealised linear case, the shear modulus would be underestimated when the recorded F_y and u_y were directly inserted into Eqn. (3.7). Rather, the force has to be increased (or, equivalently, the displacement to be decreased) by a factor $f_{\text{corr}} \geq 1$ such that the real shear modulus is obtained as

$$G_{\text{corr}} = f_{\text{corr}}\,\frac{F_y\,\ell_x}{u_y\,\ell_y\,\ell_z}\,. \tag{3.8}$$

The dependence of the correction factor f_{corr} on the sample dimensions was determined numerically in Winterstein [2012] for different values of Poisson's ratio (see Fig. 3.9b for the

[5] This problem has been addressed also in literature, see e.g. Wada et al. [2003] who devised an experimental layout consisting of four foam blocks, which served as starting point for the arrangement used here; however, in Wada's experiment the outer planes are allowed to move horizontally.

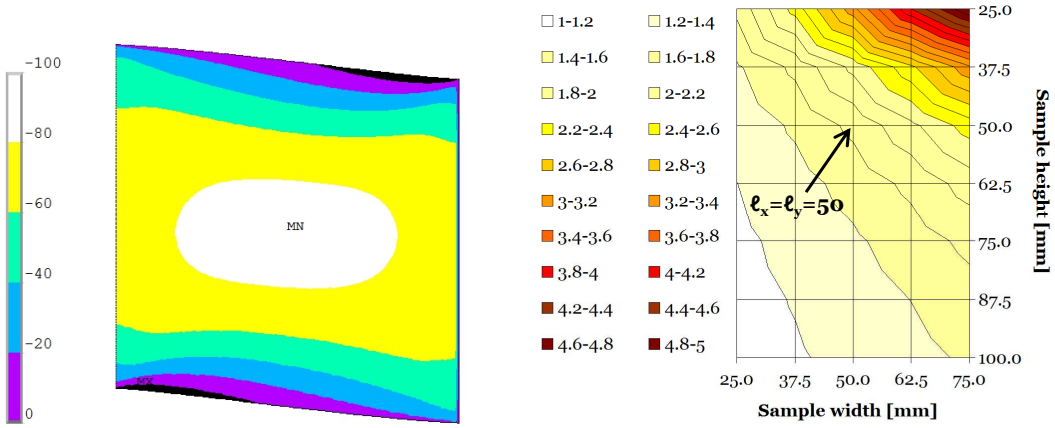

(a) Shear stress distribution (in N/m^2) (b) Correction factor f_{corr} for varying sample sizes

Figure 3.9.: Non-homogeneous shear straining ($\nu = 0$): **(a)** Numerical results (ANSYS) for the shear stress distribution for $\ell_x = \ell_y = 50$ mm and $u_y = 5$ mm for linear elastic material behaviour for which $\tau_{xy} = \pm 100$ N/m^2 would be expected from Eqn. (3.6). **(b)** Dependence of correction factor f_{corr} on ℓ_x and ℓ_y for a fixed value $u_y = 5$ mm and $\nu = 0.0$ [−]. *Fig. 3.9b created by E. Winterstein.*

case $\nu = 0.0$). It approaches unity when thin samples with a very large height are used ($\ell_y \gg \ell_x$). On the other hand, the more slender the sample is, the more pronounced is the effect from the boundary conditions as well as from beam-like bending. However, it appears that for a fixed width-to-height ratio size effects play a minor role, even though the sample should evidently not be too small in order to avoid influences from the foam's micro-structure.

Upon consideration of the correction factor, the experimental creep data was used to ascertain the relaxation modulus in shear for the DampVisc sample. Assuming no Poisson effects (this was motivated by the open-cell structure of the DampVisc sample), Winterstein determined the relaxation modulus[6] using a generalised Maxwell model with three characteristic times as

$$G_{\text{corr}}(t) \;=\; 10{,}583 + 20{,}115\,\exp\!\left(\frac{-t}{0.56}\right) + 17{,}595\,\exp\!\left(\frac{-t}{1.00}\right) + 3{,}090\,\exp\!\left(\frac{-t}{10.00}\right) . \qquad (3.9)$$

Using this relaxation function for the shear part, the numerical results from ANSYS show satisfactory agreement with the experimental data, see Fig. 3.10. As can be seen from the rate data included in Fig. 3.10a, it is rather challenging to apply the "step" load in the experiment, which leads to problems for a proper identification of material parameters related to the instantaneous and short-time behaviour. A three-dimensional numerical analysis, where

[6] By Eqn. (3.9) the relaxation modulus is obtained in Pascal when the time is inserted in seconds.

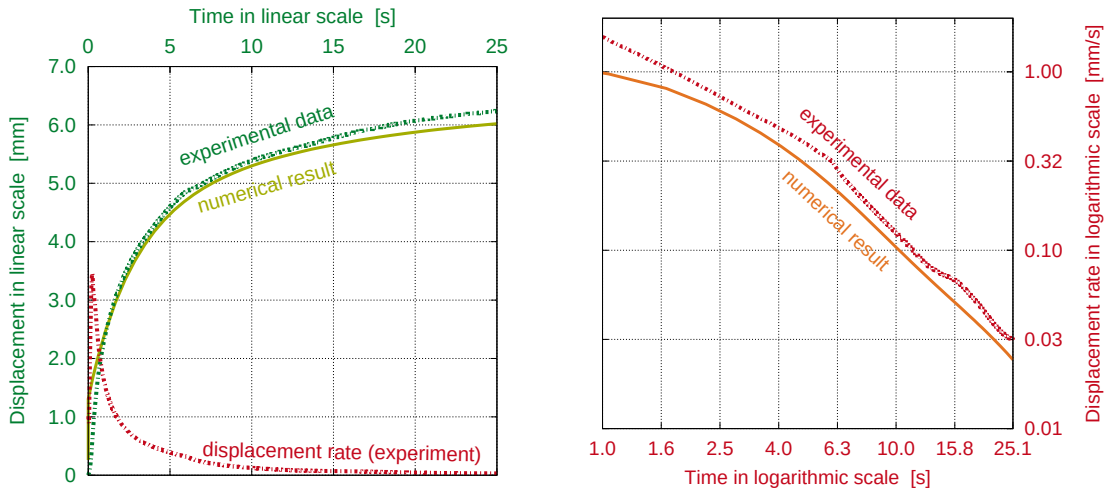

(a) Displacement and rate over time (lin-lin plot) (b) Displacement rate over time (log-log plot)

Figure 3.10.: History for the DampVisc creep shear experiment (see Fig. 3.8): **(a)** Creep displacements over time for experiment and numerical simulation (green curves), where the displacement rate shows the problem of applying a step load. **(b)** Displacement rates from experiment and numerical simulation. Compare also with Fig. 3.7a for the 1D creep experiment.

the compliance of the wood frame was also included, led to the same results (Winterstein [2012]). It should be kept in mind that the quality and the repeatability of the experimental results presented her is influenced by many factors – such as the effect of the glue layer on the overall compliance, the representativeness of the sample for the specimen material, measurement inaccuracies, etc. – but the mechanical properties revealed here are sufficient to give insight to the relevant viscoelastic characteristics.

3.2.5. Spherical indentation

Using a displacement-controlled loading by the Shimadzu Autograph AG-X plus, the relaxation of force in a spherical indentation experiment (see Fig. 3.11a) was measured for the Sylomer sample. The indenter tip had a radius of 25 mm and was identical to the one used in the impact experiments. After 500 s, the measured force reached a more or less constant level $F \approx 12.3$ N for a prescribed penetration depth of 5 mm, see Fig. 3.12.

(a) Spherical indentation (b) Triaxial compression

Figure 3.11.: Three-dimensional identification experiments: **(a)** spherical indentation, **(b)** triaxial compression comparable to an oedometer test

3.2.6. Triaxial compression

Verginer [2013] performed compression experiments on the Sylomer sample where a lateral straining was disabled just like in an oedometer test, see Fig. 3.11b. Thus, a three-dimensional stress state is provoked. Together with one-dimensional tension/compression experiments, this allows for a more accurate modelling of the volumetric and deviatoric material behaviour. From his results, it seems reasonable to assume a constant Poisson's ratio, which is done within the present work.

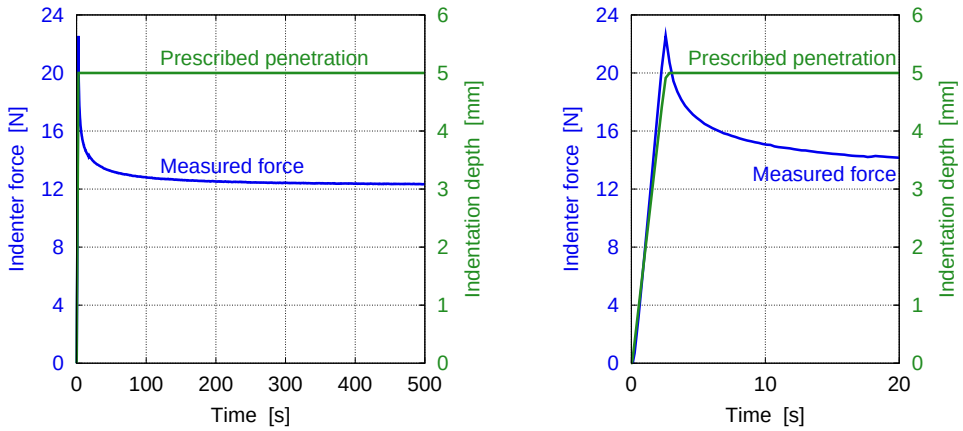

(a) Full range (b) Zoom

Figure 3.12.: Spherical indentation on Sylomer (see Fig. 3.11a): **(a)** Relaxation of force over time when the indentation depth is held constant. **(b)** Zoom: load application and relaxation during the first seconds.

3.3. Concluding remarks

This chapter revealed the most salient features of the polymeric foam samples employed in the impact experiment. In comparison to the DampVisc sample, the Sylomer showed a larger bulk density, a smaller average pore size, and a smaller compliance. The absorbance spectra were quite similar. Both samples showed a distinct viscoelastic behaviour which can be observed by conventional creep and relaxation tests; however, these experiments can not give access to the instantaneous and short-time mechanical properties. Thus, the impact investigations detailed in Section 4.1 are important for a complete description of the mechanical behaviour.

4. Impact loading on viscoelastic materials

For very short times the approach in terms of the relaxation modulus or creep compliance does present difficulties [...] because of the difficulty of measuring these quantities immediately following the suddenly applied strain or stress, respectively. The sudden loading causes oscillations due to the inertia of the testing machine and specimen, so that the conditions cannot be considered to represent the ideal discontinuity of the relaxation or creep test until these have died down, quite irrespective of the speed of response and recording of the measurement devices.

LEE AND ROGERS [1963], p. 132

This chapter starts with a description of the test rig for the impact experiments on the DampVisc and the Sylomer material described in the previous chapter. Then, the numerical modelling and results are discussed, leading to a general representation in form of master curves for the five viscoelastic models introduced in Section 2.3. The chapter finishes with the use of these master curves for two applications: (i) the determination of optimal material parameters of a viscoelastic half-space subjected to impact loading, and (ii) the identification of material parameters by means of an impact experiment.

For the description of the viscoelastic impact problem, the same notation as in Subsection 2.5.5 is used. Some additional parameters are defined as follows: From the time history of the impactor tip displacement $u(t)$, the maximum penetration (in terms of absolute values) is obtained as

$$u_{\mathrm{ve}} \stackrel{\mathrm{def}}{=} \max_t |u(t)| \tag{4.1}$$

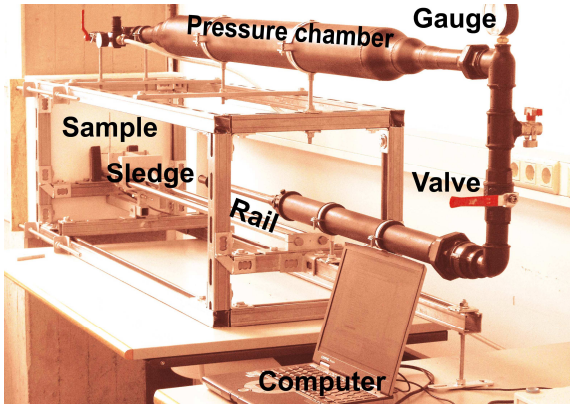

(a) Apparatus for dynamic impact experiments

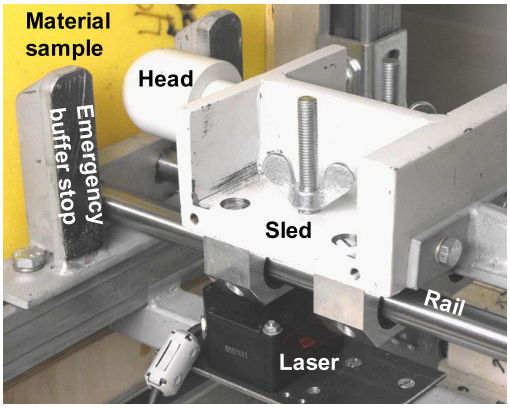

(b) impactor penetrating into sample

Figure 4.1.: Experimental set-up for spherical impact testing: **(a)** view of the complete test rig, **(b)** detail. See also Maier [2011]

occurring at the time instant t_u, while the maximum acceleration

$$a_{\text{ve}} \overset{\text{def}}{=} \max_t \ddot{u}(t) \tag{4.2}$$

occurs at $t = t_a \leq t_u$. The velocity after contact is denoted by v_{final}.

4.1. Impact experiments

4.1.1. Description of test apparatus

The impact test rig was devised in a diploma thesis by Marcus Maier [2011]. The hemispherical impactor is mounted on a sledge (total mass $M = 6.28$ kg) which moves horizontally towards the material sample (see Fig. 4.1). The motion of the sledge is initiated by opening the valve of the pressure chamber. A laser device tracks the penetration depth over time, where sampling rates of approximately 1000..1200 per second turned out to be an ideal compromise between accuracy, smoothness and memory efficiency.

4.1.2. Curve fitting for the determination of time derivatives

Due to the limited accuracy of the measured penetration values at discrete time instances, a direct determination of the corresponding velocity and acceleration history by finite differences would result in highly oscillating data, rendering useless any subsequent mathemat-

ical operations. Thus, the discrete time-penetration data was fitted locally: for each time instant the corresponding penetration value is taken into account plus the data pairs for the n previous and n subsequent time instants. Here, n is an integer number which should be large enough such that the second time derivative appears sufficiently smooth, but small enough in order to capture local peaks in the displacement history. The procedure of the local polynomial approximation is described in Section A.4, where $k = 2n+1$ is the total number of data pairs considered.

4.1.3. Experimental results

The initial velocity V has to be chosen such that the penetrations are small enough to preserve the conditions of small strains necessary for the linear modelling of the foam samples. However, when the sled moves very slowly, the influence of friction between sled and rails becomes important. It is not possible to give a general statement on the required minimum velocity because this value depends on many different factors, especially the surface slip of the rails and the fine-tuning of the bearing. Rather, one should analyse the decrease of velocity due to friction (free movement without impact) in order to relate the friction force[1] to the reaction forces occurring during impact. For very compliant materials such as the DampVisc samples, it may help to decrease the impacting mass and increase the sphere's radius in order to raise the initial velocity, cf. Eqn. (2.66) for the theoretical relationship between the input parameters and the max. penetration in the purely elastic case; otherwise, it is recommended to use a pendulum device instead (see e.g. Memmler [1930]).

An example result for three different levels of smoothing is given in Fig. 4.2 where $V = 0.285\ \frac{\mathrm{m}}{\mathrm{s}}$ was prescribed. The influence of friction effects is negligible because at the end (free movement) the velocity and, thus, the kinetic energy is constant. Note that the value of the maximum penetration u_{ve} and the final velocity v_{final} are quite unaffected by the smoothing, which is not true for the value of the maximum acceleration a_{ve}. Some difficulties would also be encountered if the time instant of the maximum acceleration or the overall contact duration had to be determined. For the latter, more reliable methods (e.g. measurement of electrical conductance where the sample surface is covered by a conducting layer) are re-

[1] From impact experiments on an elastic membrane and simple numerical investigations using an explicit time integration scheme according to Belytschko et al. [2000] it was concluded that the influence of friction can be modelled by a constant force which acts against the direction of movement. In these experiments, the friction force had a magnitude $6.28\ \mathrm{kg} \cdot 0.067\ \mathrm{m/s^2}$, but this value will not hold in general because the friction conditions may change.

ported in the literature (see for instance Flom [1960], Lifshitz and Kolsky [1964], or Pouyet and Lataillade [1975]).

4.2. Numerical simulations: modelling and example results

4.2.1. Numerical modelling of impact problem

Regarding the impact problem described in Section 4.1, numerical parameter studies were conducted using the Finite Element Method (FEM, see e.g. Zienkiewicz et al. [2005]). Unless otherwise stated, by "numerical simulations" reference is made to these FEM computations which were performed using the commercial software ANSYS MECHANICAL® (see Ansys 12.1. [2009]) and an in-house research code. Both programs make use of an implicit time stepping scheme (Newmark method); thus, the primary unknowns are the nodal displacements at each discrete time step, where the impactor tip displacement $u(t)$ is the degree of freedom of central interest. Similarly to the experimental data treatment, the velocity and acceleration history were retrieved from $u(t)$ by finite differences for the numerical results; however, a smoothing of the penetration history was not necessary (note that the accuracy of the so-obtained acceleration data can be checked by help of the current force equilibrium in the Newmark scheme). Due to the fact that the impact angle is 90 degrees, an axisymmetric model was used. All analyses were performed using four-noded structural solids except for some comparison studies with eight-noded quadrilaterals. The influence of wave propagation was considered in Yilmaz [2011] but the results presented here do not take into account a distributed mass in the viscoelastic body due to the findings detailed in Subsection 2.5.5. A typical FEM model is depicted in Fig. 4.3.

Even though one objective of the numerical simulations is the identification of material parameters through an impact experiment, care was taken to vary all input parameters for the numerical simulations over a large range whenever possible (i.e. several decades). Thus, it can be guaranteed that the so-obtained master curves represent valid relations between the problem parameters for the general case of spherical impact on viscoelastic material.

As opposed to free fall tests often used in the literature, the horizontal set-up of the experimental test rig allows for the elimination of gravity effects in the numerical simulations. The impactor is modelled as rigid body. In order that the elastic solutions from Section 2.5 may be used both for validation and for scaling of the numerical results, the input parameters are tuned such that the maximum penetration is about 10% (sometimes up to 20%) of the im-

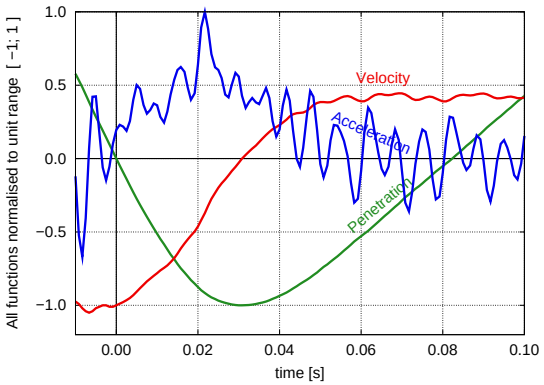

(a) $k = 2{\cdot}3{+}1$ data points

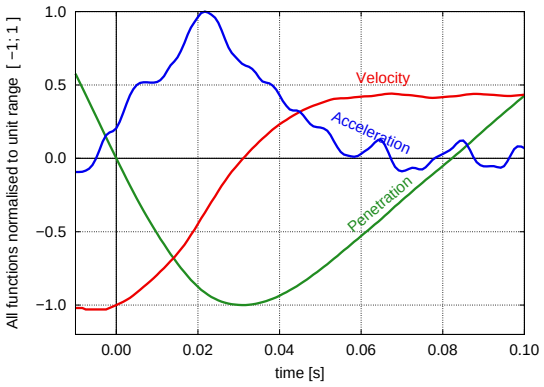

(b) $k = 2{\cdot}8{+}1$ data points

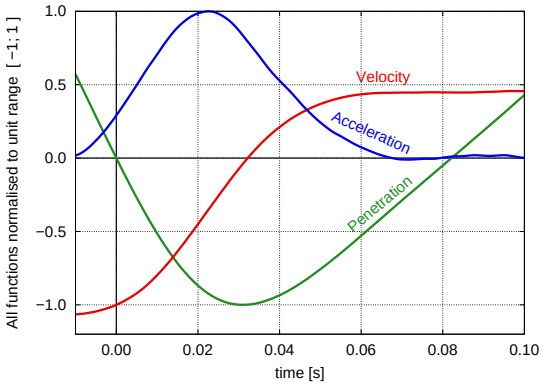

(c) $k = 2{\cdot}20{+}1$ data points

Figure 4.2.: Results from an impact experiment (Sylomer) where the recorded penetration (sampling rate $1200\frac{1}{\mathrm{s}}$) is smoothed before retrieving the velocity and acceleration history. All functions are normalised. **(a)** Coarse smoothing (where the $k = 7$ data points make up an interval of 0.0058 s), giving $u_{\mathrm{ve}} = 5.03$ mm, $v_{\mathrm{final}} \approx 0.13$ m/s^2, and $a_{\mathrm{ve}} = 19.4$ m/s^2. **(b)** Medium level of smoothing (interval 0.0142 s), giving $u_{\mathrm{ve}} = 5.03$ mm, $v_{\mathrm{final}} \approx 0.13$ m/s^2, and $a_{\mathrm{ve}} = 13.4$ m/s^2. **(c)** Strong smoothing (interval 0.0342 s), giving $u_{\mathrm{ve}} = 5.03$ mm, $v_{\mathrm{final}} \approx 0.13$ m/s^2, and $a_{\mathrm{ve}} = 10.9$ m/s^2.

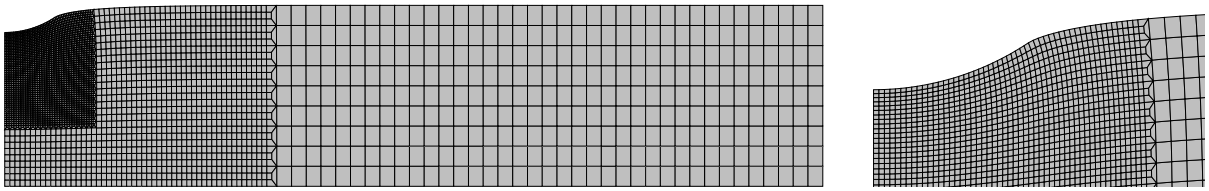

(a) (b)

Figure 4.3.: Axisymmetric model for a 0.05 m thick sample impacted by a sphere of 0.025 m radius: **(a)** full view, **(b)** zoom. At this time instant, the penetration depth is 0.0075 m, i.e. $u/R = 0.30$. Usually, however, the boundary conditions were chosen such that the maximum value for u/R is around 0.10 in order to stay in the valid range of the Hertz solution and to keep the strains small.

pactor's radius. Thus, the initial velocity of the impactor is so small that wave propagation in the sample material can be excluded[2]. However, while in the Hertzian solution a half-space is considered, in the experiments the thickness of the material sample is finite. Whereas the influence of the sample thickness on the final velocity v_{final} is not quite pronounced, the values for the maximum penetration/acceleration decrease/increase for a small thickness, as is shown later for the case where the thickness is only twice the impactor's radius (see Fig. 4.5 on p. 61).

Nonetheless, besides the computations with a finite thickness suitable for comparison with the experiments, also the numerical results for the case of an "infinite" thickness are presented in the following. These solutions may be useful for indentation problems where the indenter tip is much smaller than the probed material sample.

4.2.2. Example results

Obviously, viscous effects can be observed only when the time scale of loading (the typical contact time is in the order of some ten milliseconds) has the same magnitude as the characteristic time of the material. This is demonstrated in the following for two of the viscoelastic models introduced in Section 2.3.

In the first example, the standard linear solid (SLS) is considered where the spectrum is just a Dirac at the characteristic time τ (see Figure B.2). The SLS shows a practically elastic be-

[2] This was confirmed by numerical simulations as reported in Sevim [2008].

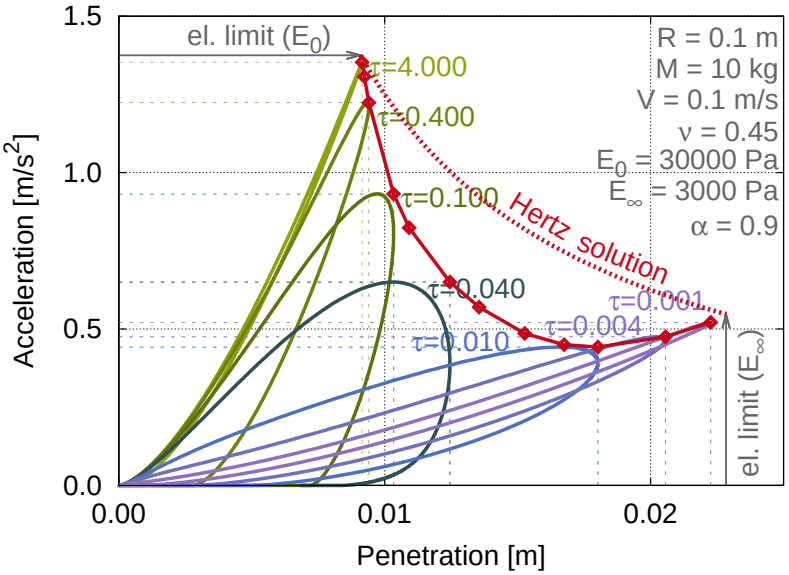

Figure 4.4.: Standard linear solid: Numerical parameter study for varying characteristic time τ in the range from 0.001 to 4.0 s. For each of the seven simulations, the acceleration is plotted vs. the absolute value of the penetration, where the physical time is a curve parameter. From this, the maximum values for acceleration and penetration are marked by diamonds. For comparison, the dotted line shows the relationship between u_{el} and a_{el} according to the Hertz solution.

haviour both for a very large and a very small characteristic time[3]. To illustrate this, a simulation series was conducted where all parameters (loading and material) are constant except for the characteristic time τ. In Fig. 4.4, for each time instant the acceleration is plotted over the penetration. For suitable values of the characteristic time quite pronounced hysteresis curves are obtained, where the area of the hysteresis corresponds to the total amount of energy dissipated. For each simulation, the maximum penetration and maximum acceleration $(u_{\mathrm{ve}}|a_{\mathrm{ve}})$ are marked by a diamond; the solid curve connecting these discrete points is displayed just for a clearer representation. On the other hand, the dotted line represents the elastic solution according to the Hertzian relations if one was just varying the Young's modulus within the limit values. By comparison of these two curves, it becomes evident that the maximum acceleration and/or penetration can be significantly diminished by energy dissipation through viscous processes in the material.

[3] Compared to the load time scale. In the limit, for the first case the dashpot blocks, thus the modulus of the SLS equals to the initial stiffness, but for the latter case, the dashpot shows no resistance, thus only the equilibrium spring with the final stiffness is of relevance.

As an other example, consider the logarithmic model, which is a viscoelastic fluid. Fig. 4.5a shows the penetration and acceleration over time for a varying characteristic time while all other parameters remain unchanged. Again, the hysteresis plot in Fig. 4.5b shows that τ has to be tuned to the impact duration such that viscous damping becomes visible. This effect is shown in Figs. 4.5c,d,e as regards the maximum penetration, final velocity, and maximum acceleration, respectively, where five different values for the model parameter λ were used. The deviation from the elastic half-space solution for a large characteristic time is due to the fact that a finite thickness was used in the numerical simulations.

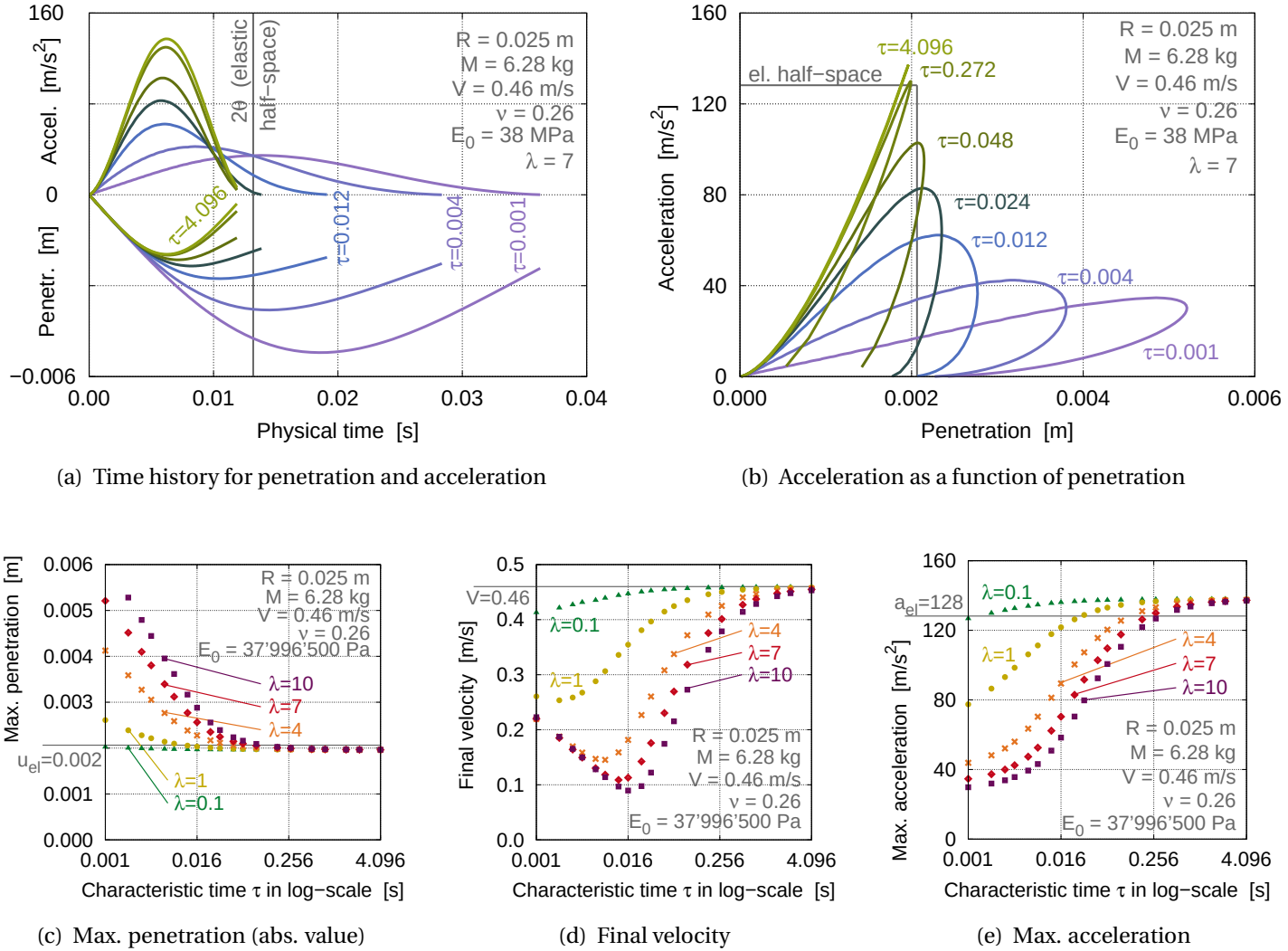

(a) Time history for penetration and acceleration

(b) Acceleration as a function of penetration

(c) Max. penetration (abs. value)

(d) Final velocity

(e) Max. acceleration

Figure 4.5.: Numerical results for the LOG model where a finite thickness of 0.05 m was used. **(a)**, **(b)**: Influence of τ on $u(t)$, $a(t)$, and $a(u)$ for $\lambda = 7$. **(c)**, **(d)**, **(e)**: Dependence of u_{ve}, v_{final}, and a_{ve} on the characteristic time τ for various values of λ.

4.3. Representation of the numerical results by master curves

4.3.1. Generation of master curves using dimensionless parameters

In this section generally valid results for the spherical impact on a viscoelastic half-space (or a viscoelastic sample with a finite thickness) are given in form of two-dimensional diagrams. This is insofar noteworthy as at least six parameters (three loading: R, M, V; two material: Y, τ; and one output quantity of interest, e.g. u_{ve}) describe the viscoelastic impact problem. Thus, a mere projection from the six-dimensional to a two-dimensional space would lead to unreadable diagrams.

However, by use of dimensional reasoning (see Chapter C in the appendix), it is possible to construct dimensionless parameters which can be used for the abscissa and the ordinate of the x-y diagram. Thus, based on appropriate dimensionless quantities, the results may lead to simple curves for different parameter variations, for which reason they are called master curves.

In the following, for each of the viscoelastic models presented in Section 2.3, these master curves are constructed. This is achieved by scaling the parameters of interest w.r.t.

- quantities which can be measured during the experiment or obtained from numerical simulations, e.g. the value of the max. penetration u_{ve} or the related time instant t_u or the final velocity v_{final}, and/or
- the Hertz solution for a purely elastic half-space, notably θ, u_{el} and a_{el} (see Subsection 2.5.5).

Thus, with the latter point in mind, it is obvious that the method presented here works the better the larger the deviations are from the elastic solution. This feature is beneficial because, to the author's knowledge, to date all solutions published for the viscoelastic impact problem rely on the assumption that the viscoelastic material behaves "nearly elastic" (e.g. concerning the duration of contact).

For future reference, the dimensionless parameters used in the following are defined here as

$$\Pi_u = \frac{u_{\mathrm{ve}}}{u_{\mathrm{el}}} \quad , \quad \Pi_{\mathrm{rest}} = \frac{v_{\mathrm{final}}}{V} \quad , \quad \Pi_a = \frac{a_{\mathrm{ve}}}{a_{\mathrm{el}}} \quad ,$$
$$\Pi_{\tau tu} = \frac{\tau}{t_u} \quad , \quad \Pi_{\tau\theta} = \frac{\tau}{\theta} \quad , \qquad \Pi_{\tau ta} = \frac{\tau}{t_a} \quad . \tag{4.3}$$

The dimensionless maximum penetration Π_u, the coefficient of restitution Π_{rest}, and the dimensionless maximum acceleration Π_a are unity for elastic material behaviour. Moreover,

for later use, the dimensionless parameter

$$\Pi_{\theta tu} = \frac{\theta}{t_u} = \frac{\Pi_{\tau tu}}{\Pi_{\tau\theta}} \tag{4.4}$$

is defined additionally; however, it depends on the set of dimensionless parameters given in Eqn. (4.3).

4.3.2. Master curves for the MX model

Fig. 4.6a,c,e (see page 65) shows the dimensional results for the maximum penetration, the final velocity, and the maximum acceleration depending on the characteristic time. In Fig. 4.6b,d,f the dimensionless parameters Π_u, Π_{rest}, and Π_a are used on the ordinate and $\Pi_{\tau tu}$, $\Pi_{\tau\theta}$, and $\Pi_{\tau ta}$ on the abscissa, respectively, by which all results are mapped onto the respective master curves. When the characteristic time τ is large (i.e. for large values on the abscissa), the dashpot is too slow to influence the spring stiffness; thus, the behaviour is similar to the purely elastic case. On the contrary, for too small τ, the Maxwell material shows a rapid decrease in stiffness leading to large penetrations, where in extreme cases[4] the impacting sphere is not ejected but continues to penetrate into the half-space.

4.3.3. Master curves for the SLS model

The standard linear solid has the peculiarity that it shows elastic behaviour not only for the limit $\tau \to \infty$ but also for the limit $\tau \to 0$. For a scaling with the Hertz solution (see Fig. 4.7 on page 66), the initial stiffness E_0 corresponding to $\tau \to \infty$ was used. Thus, when the characteristic time decreases, the dimensionless max. penetration and acceleration approach the values $(1-\alpha)^{-0.4}$ and $(1-\alpha)^{+0.4}$, respectively, as $E_\infty = (1-\alpha)E_0$ and the indentation modulus shows the power $\stackrel{+}{-}0.4$ in Eqns. (2.66) and (2.67).

4.3.4. Master curves for the PL model

As for the MX and the SLS, the results for the power law model given here apply to an infinite half-space. In Fig. 4.8 (page 67), all six diagrams possess dimensionless axes. However, use of $\frac{\Pi_{\tau ta}}{\Pi_{\tau tu}}$ on the abscissa in Fig. 4.8c does not result in distinct curves for the coefficient of restitution for different values of β. For the dimensionless plots of the max. penetration and

[4] These, however, were excluded here.

max. acceleration in Fig. 4.8a,e, the same parameters span the diagrams as in Figs. 4.6b,f and 4.7b,f. However, whereas for the MX and the SLS useful curves were obtained, the use of $\Pi_{\tau tu}$ and $\Pi_{\tau ta}$, respectively, on the abscissa leads to data clouds for the PL.

In order to obtain a meaningful family of curves, the time axis should rather be spanned by $\Pi_{\tau\theta}$, see Fig. 4.8b,d,f. Here, the curves for different β intersect each other, but this must not be interpreted as a flaw; rather, it seems logical when one considers that intersections also occur for the storage and loss modulus over frequency for different β (see Fig. B.5).

4.3.5. Master curves for the SRKV model

Unlike all other viscoelastic models of Section 2.3, the elastic constant E_∞ in the square root Kelvin-Voigt model refers to the final stiffness $R(t\to\infty)$. Thus, the scaled max. penetration is below and the scaled max. acceleration above unity. The results shown here apply to a finite thickness of 0.05 m, where the impactor's radius was variable (in the order of half the thickness). While the diagrams in Fig. 4.9a,c,e (page 68) are not too helpful due to the use of an unsuitable dimensionless time axis, the results plotted in Fig. 4.9b,d,e show meaningful curves for different values of γ.

4.3.6. Master curves for the LOG model

A finite thickness of 0.05 m was also used in the numerical simulations for the logarithmic creep model. The impactor's radius was varied between 0.008 m and 0.032 m. The dimensionless representations are shown in Fig. 4.10 on page 69. The master curves in Fig. 4.10a,b,e,f show some scattering, because both Π_u and Π_a relate the results for a sample with a finite thickness to equations valid for an infinite half-space. For the coefficient of restitution, however, this effect does not become apparent, see Fig. 4.10c,d. Thus, the final velocity of the impactor is not so sensitive to the thickness of the viscoelastic body.

From Fig. 4.10d, it was found that for an arbitrary but fixed λ the coefficient of restitution becomes a minimum when the empirical relation $\Pi_{\tau\theta}\approx 0.316\,\lambda^{0.92}$ holds.

4.3.7. Concluding remarks

Apart from cases where an analytical formula is available it is necessary to construct dimensionless parameters in order to obtain generally valid solutions suitable for a representa-

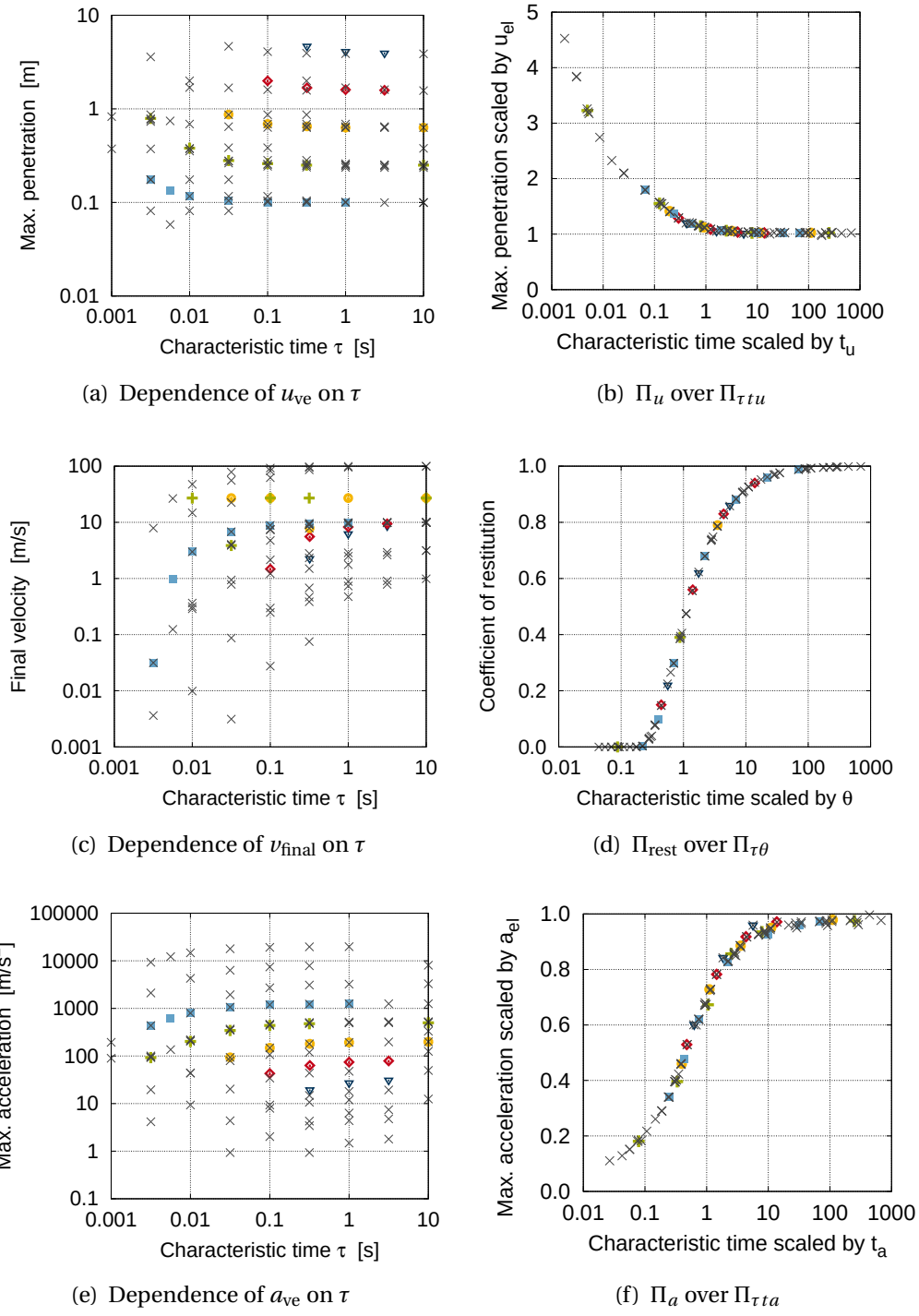

(a) Dependence of u_{ve} on τ

(b) Π_u over $\Pi_{\tau tu}$

(c) Dependence of v_{final} on τ

(d) Π_{rest} over $\Pi_{\tau\theta}$

(e) Dependence of a_{ve} on τ

(f) Π_a over $\Pi_{\tau ta}$

Figure 4.6.: Maxwell model (half-space): each symbol represents the result from one numerical simulation. While the crosses stand for arbitrary combinations of input parameters, the other symbols differ by one decade in Young's modulus. **(a)**, **(c)**, **(e)**: dimensional results, where the vertical distance between the non-crosses is 0.4 decades; cf. the exponent for E in the Hertzian solution. **(b)**, **(d)**, **(f)**: master curves obtained by the use of dimensionless abscissa and ordinate.

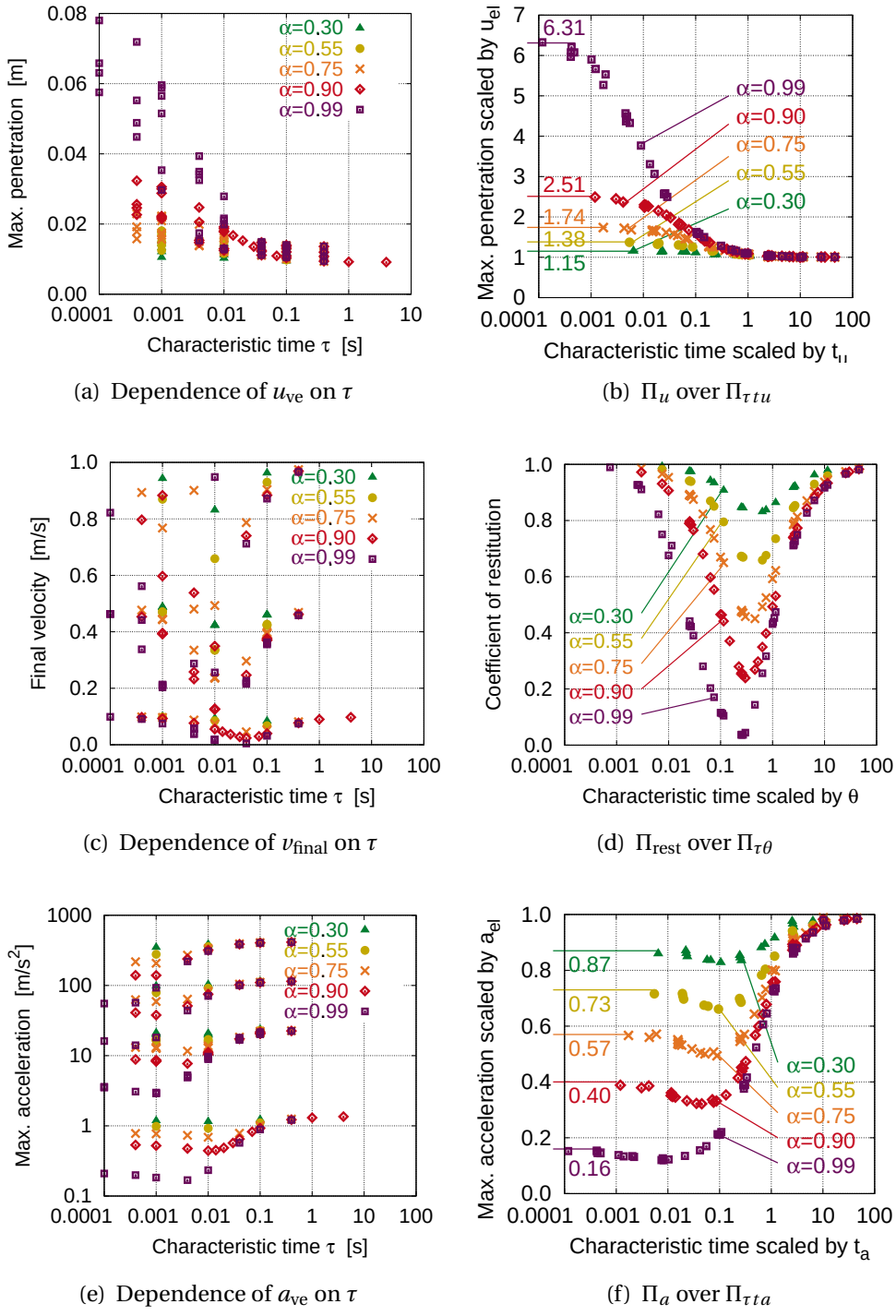

(a) Dependence of u_{ve} on τ

(b) Π_u over $\Pi_{\tau tu}$

(c) Dependence of v_{final} on τ

(d) Π_{rest} over $\Pi_{\tau\theta}$

(e) Dependence of a_{ve} on τ

(f) Π_a over $\Pi_{\tau ta}$

Figure 4.7.: Standard linear solid, where five different values for α were used. **(a)**, **(c)**, **(e)**: dimensional results. **(b)**, **(d)**, **(f)**: master curves obtained by the same scaling as in Fig. 4.6. The Hertzian solution refers to the initial stiffness E_0. The horizontal lines given in (b) and (f) for small τ indicate the limit values $(1-\alpha)^{-0.4}$ and $(1-\alpha)^{+0.4}$, respectively.

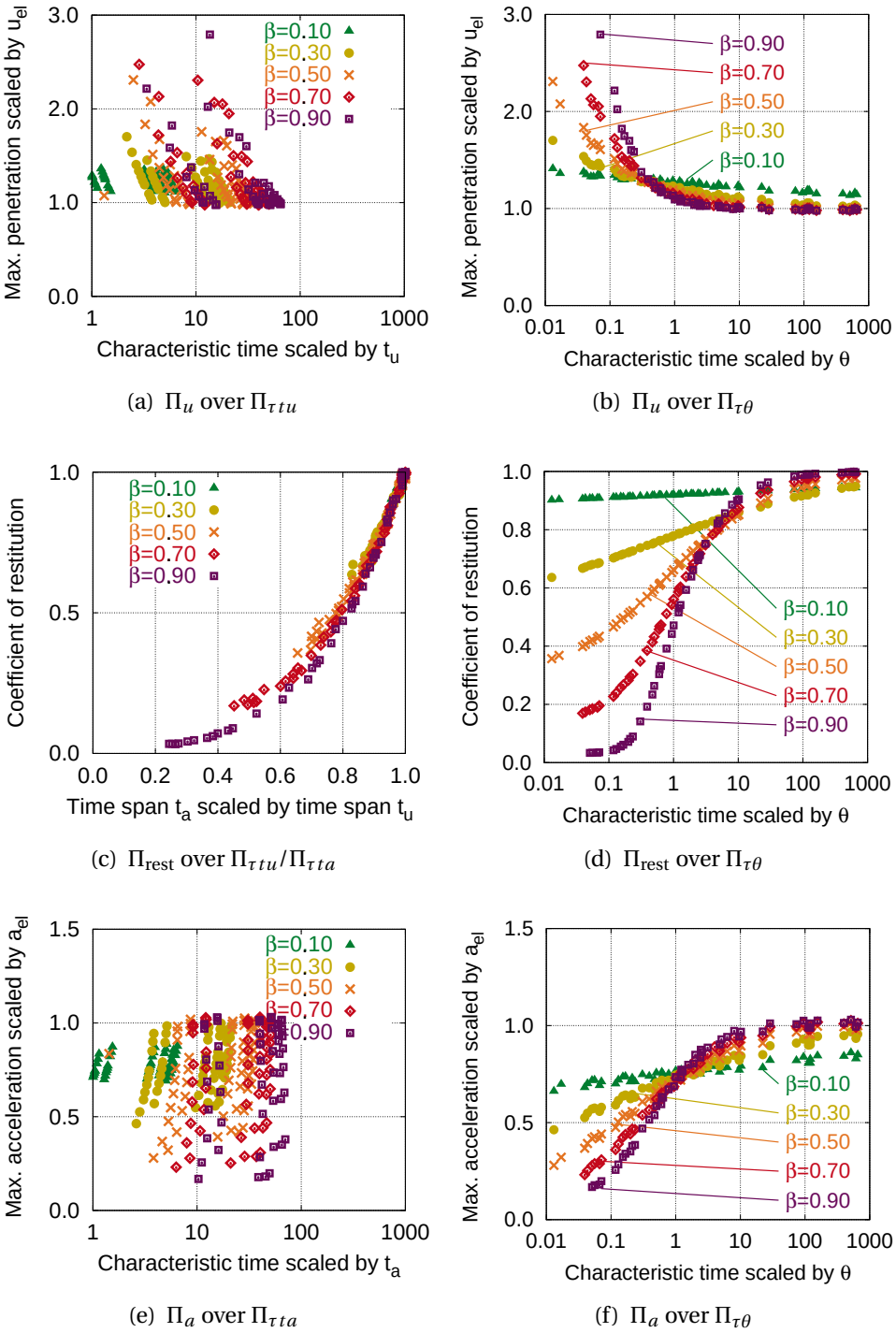

(a) Π_u over $\Pi_{\tau tu}$ (b) Π_u over $\Pi_{\tau\theta}$

(c) Π_{rest} over $\Pi_{\tau tu}/\Pi_{\tau ta}$ (d) Π_{rest} over $\Pi_{\tau\theta}$

(e) Π_a over $\Pi_{\tau ta}$ (f) Π_a over $\Pi_{\tau\theta}$

Figure 4.8.: Power law results, where five different values for β were used. **(a)**, **(c)**, **(e)**: even though dimensionless parameters are used both for the abscissa and the ordinate, the resulting diagrams are not very helpful. **(b)**, **(d)**, **(f)**: master curves obtained by the same scaling for the ordinate as in (a),(c),(e), but for the abscissa the characteristic time τ is scaled by half the elastic impact duration θ, resulting in valuable diagrams.

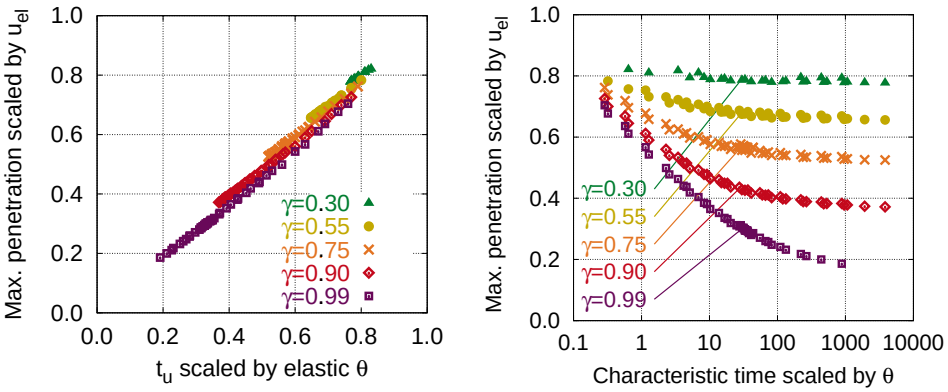

(a) Π_u over $\Pi_{\tau\theta}/\Pi_{\tau tu}$ (b) Π_u over $\Pi_{\tau\theta}$

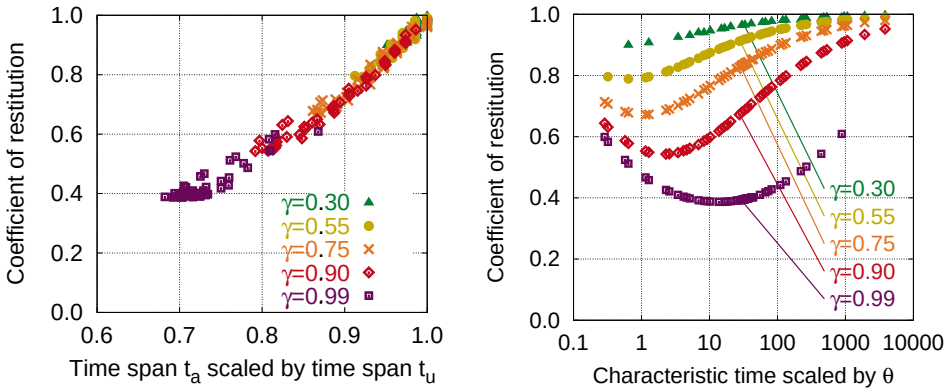

(c) Π_{rest} over $\Pi_{\tau tu}/\Pi_{\tau ta}$ (d) Π_{rest} over $\Pi_{\tau\theta}$

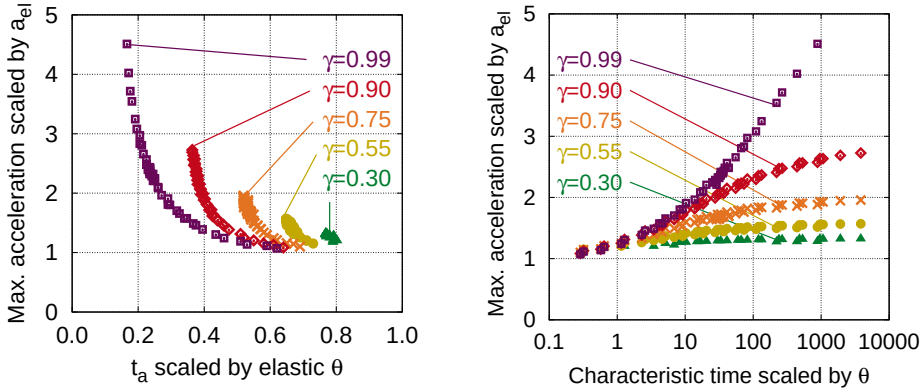

(e) Π_a over $\Pi_{\tau\theta}/\Pi_{\tau ta}$ (f) Π_a over $\Pi_{\tau\theta}$

Figure 4.9.: Square root Kelvin-Voigt, where five different values for γ were used. **(a)**, **(c)**, **(e)**: using the same scaling as in Fig. 4.8a,c,e, the resulting curves look different but are not too meaningful, either. **(b)**, **(d)**, **(f)**: master curves obtained by the same scaling for the ordinate as in (a),(c),(e), but for the abscissa the characteristic time τ is scaled by half the elastic impact duration θ, resulting in useful diagrams.

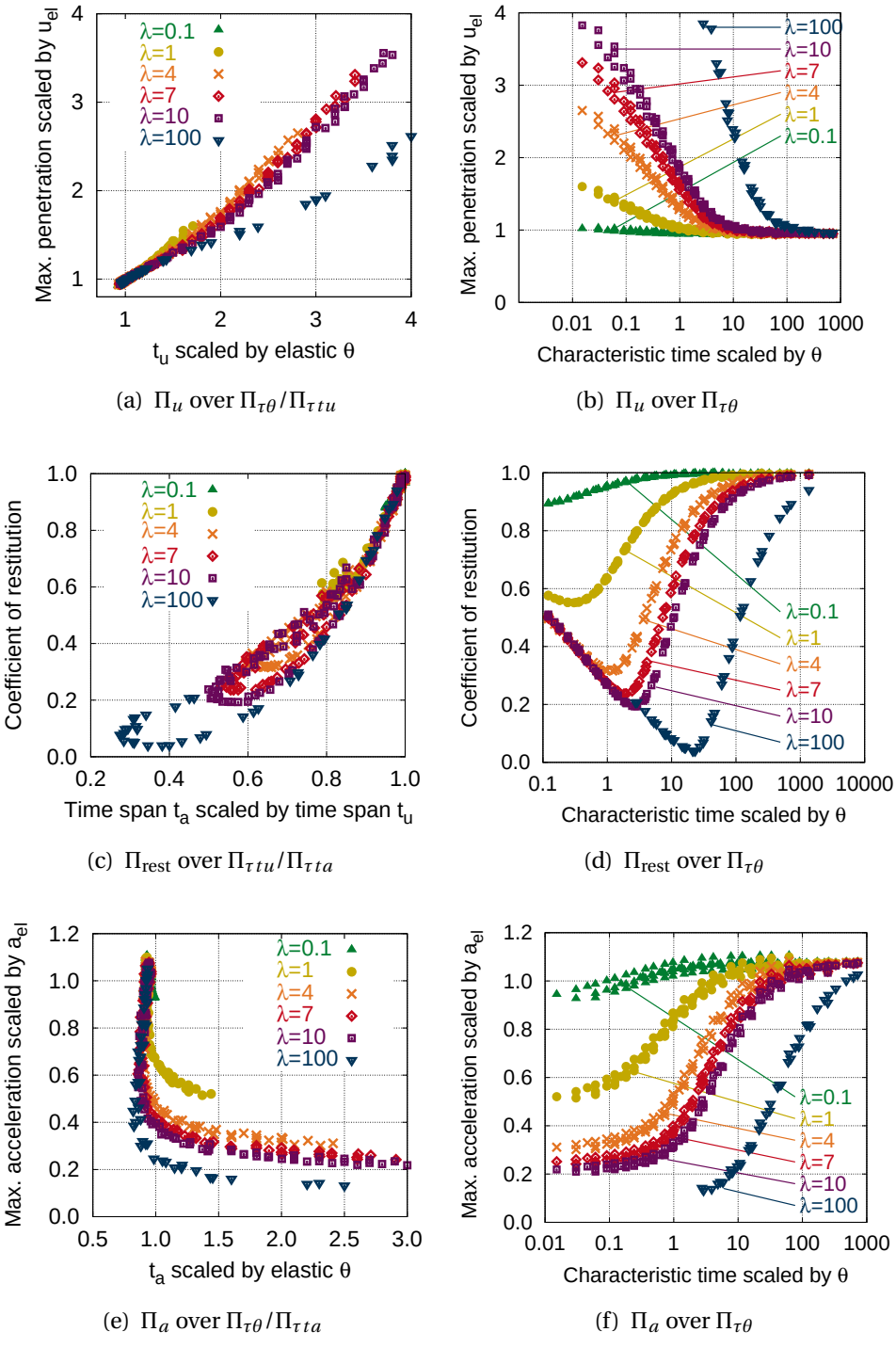

(a) Π_u over $\Pi_{\tau\theta}/\Pi_{\tau tu}$ (b) Π_u over $\Pi_{\tau\theta}$

(c) Π_{rest} over $\Pi_{\tau tu}/\Pi_{\tau ta}$ (d) Π_{rest} over $\Pi_{\tau\theta}$

(e) Π_a over $\Pi_{\tau\theta}/\Pi_{\tau ta}$ (f) Π_a over $\Pi_{\tau\theta}$

Figure 4.10.: Logarithmic creep model, where six different values for λ were used. **(a)**, **(c)**, **(e)**: application of the same scaling as in Figs. 4.8a,c,e and 4.9a,c,e results in diagrams of limited benefit. **(b)**, **(d)**, **(f)**: however, when the characteristic time is expressed by the dimensionless quantity $\Pi_{\tau\theta}$, one obtains useful curves.

tion by simple means such as easy-to-read diagrams. Otherwise (as shown in Fig. 4.6a,c,e), the mapping from the n-dimensional space (where n indicates the number of parameters involved) onto a two-dimensional plane will be completely useless. However, the sole fact that dimensionless parameters were used does not guarantee that one will obtain useful diagrams (i.e. distinct lines instead of data clouds); thus, it needs some serendipity, mechanical understanding, and perseverance for a successful solution.

The dimensionless parameters given in Eqn. (4.3) can also be used to re-consider the reverse relationship between the max. penetration and the max. acceleration already discovered in Subsection 4.2.2, where some example results had been given in terms of dimensional quantities. For the SLS, the dimensionless analogue to Fig. 4.4 (page 59) is given in Fig. 4.11a, for which numerical results related to arbitrary input data were used. For the LOG, where the dimensional acceleration was plotted over the dimensional penetration in Fig. 4.5b (page 61), the dimensionless relationship can be seen in Fig. 4.11b.

Figs. 4.11a and 4.11b look very similar to each other. Therefore, in Fig. 4.11c this relation is investigated for all rheological models introduced in Section 2.3 (where the MX is just a special case of the SLS or PL). Here, it should be kept in mind that for the SRKV the elastic solution was calculated using E_∞, whereas E_0 was employed for the PL, the SLS, and the LOG, leading to a separation of data into two blocks. The solid line representing the elastic case is motivated by the fact that $u_{\mathrm{el}} \cdot a_{\mathrm{el}} =$ constant in Eqn. (2.72) when the initial velocity V remains unchanged.

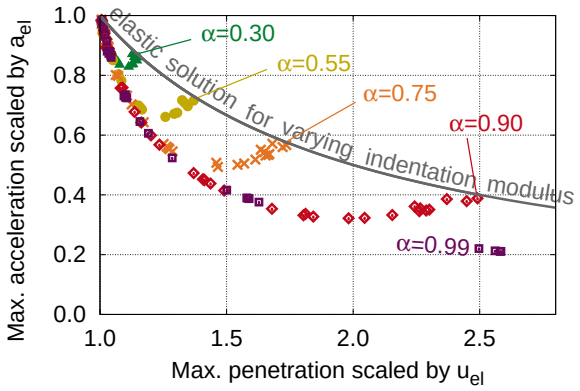

(a) Π_a over Π_u for the standard linear solid

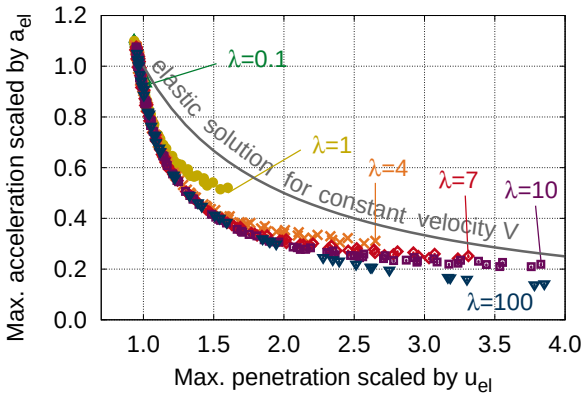

(b) Π_a over Π_u for the logarithmic creep model

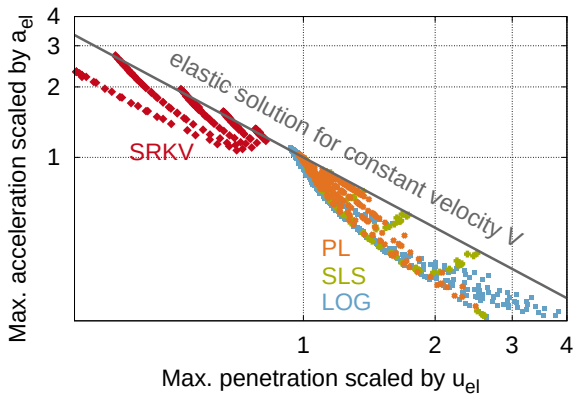

(c) Π_a over Π_u for all models from Section 2.3

Figure 4.11.: Plots of Π_a over Π_u for different rheological models. **(a)** Standard linear solid. This diagram is a generalisation of the dimensional plot in Fig. 4.4. The solid line indicates the Hertzian solution using $E = (1-\alpha)E_0$ for a varying parameter α. **(b)** Logarithmic creep model: This diagram is a generalisation of the max. acceleration and max. penetration retrieved from the dimensional plot in Fig. 4.5b. The solid line, constructed by $u_{\mathrm{el}} \cdot a_{\mathrm{el}} = 1$, indicates the elastic solution. **(c)** Results for different rheological models (log-log plot), where some computations were made for an infinite half-space, some for a medium with finite (but not too small) thickness.

4.4. Optimal material properties for structures under impact

4.4.1. Optimisation objectives

In this section it is shown how to use the master curves introduced in Section 4.3 in order to determine optimal parameters of a viscoelastic material subjected to spherical impact. Several objectives are possible:

- maximise the dissipation of energy through inelastic effects, or
- minimise the maximum penetration over time, or
- minimise the maximum acceleration over time.

Regarding the first of these objectives, the task is equal to tuning the characteristic time to the time scale of loading such that the final velocity becomes minimal. Thus, the optimal dimensionless characteristic time can be identified directly from the master curves showing the coefficient of restitution[5].

Thus, in this section attention is restricted to the latter two objectives, which are obviously contradictory to each other: regarding the penetration, a rather stiff material is favourable, while a soft material leads to small accelerations. This reverse effect can be seen, for instance, in Fig. 4.5a for the logarithmic creep model.

Therefore, a multi-objective optimisation approach (see Appendix D) is employed here for the Maxwell model, the standard linear solid, and the power law model. For each of these three models, a half-space was considered in the numerical simulations; thus, the obtained results can also be used for other applications whenever the dimensions of the sample are large with respect to the impactor size.

The two contrary objectives are plotted in Figs. 4.6b,f for the MX, Figs. 4.7b,f for the SLS, and Figs. 4.8b,f for the PL. However, in case of the former two models, it should be noted that the dimensionless max. penetration is plotted over $\Pi_{\tau tu}$, but for the dimensionless max. acceleration $\Pi_{\tau ta}$ was used on the abscissa; thus, one is not allowed to just add these two graphs. Instead, for both objectives, the characteristic time will be expressed by $\Pi_{\tau\theta}$. This modification of the abscissa results only in minor changes regarding the general shape of the curves. For the power law model, the master curves in Figs. 4.8b,f were already given in terms of $\Pi_{\tau\theta}$.

[5] i.e. Fig. 4.6d for the MX (page 65), Fig. 4.7d for the SLS (page 66), Fig. 4.8d for the PL (page 67), Fig. 4.9d for the SRKV (page 68), and Fig. 4.10d for the LOG (page 69).

Regarding the ordinate, a comparable range for the numerical values of each of the objectives should be used. Thus, for the dimensionless max. penetration, the inverse of the original objective is taken. However, the so-modified function has to be multiplied by -1 in order to deal with a *minimisation* task. Moreover, it is useful for visual clarity to move both of the objectives such that they approach zero for the E_0-solution (i.e. for large $\frac{\tau}{\theta}$), representing the elastic solution which is used for the scaling of u_{ve} and a_{ve}.

From these considerations, the two objectives become

$$\min_{\tau/\theta} \left\{ f_u\left(\tau/\theta\right) \right\} = \min_{\tau/\theta} \left\{ 1 - \frac{u_{\mathrm{el}}}{u_{\mathrm{ve}}\left(\tau/\theta\right)} \right\} \tag{4.5}$$

and

$$\min_{\tau/\theta} \left\{ f_a\left(\tau/\theta\right) \right\} = \min_{\tau/\theta} \left\{ \frac{a_{\mathrm{ve}}\left(\tau/\theta\right)}{a_{\mathrm{el}}} - 1 \right\} . \tag{4.6}$$

The multi-objective function – cf. Eqn. (D.1) – reads

$$F(\tau/\theta) = w_u\, f_u(\tau/\theta) + w_a\, f_a(\tau/\theta) , \tag{4.7}$$

where the weights w_u and w_a have to fulfil the conditions $0 \le w_u, w_a \le 1$ and $w_u + w_a = 1$.

4.4.2. Optimal characteristic time for the MX model

In order to follow the procedure described in Appendix D it is necessary to obtain an analytical equation for f_u and f_a from the discrete simulation results for the Maxwell model. Thus, the function

$$f_u\left(\tau/\theta\right) = u_1 \exp\!\left(-\left(\frac{\tau/\theta}{u_2}\right)^{u_3}\right) + u_4 \exp\!\left(-\left(\frac{\tau/\theta}{u_5}\right)^{u_6}\right) + (1-u_1-u_4) \exp\!\left(-\left(\frac{\tau/\theta}{u_7}\right)^{u_8}\right) \tag{4.8}$$

was fitted to the discrete values of $\left(1 - \frac{u_{\mathrm{el}}}{u_{\mathrm{ve}}}\right)$, where the free parameters $u_1 \ldots u_8$ are given in Table 4.1. The function was constructed such that it approaches unity for $\tau/\theta \to 0$ since u_{ve} becomes very large compared to u_{el} for a fast Maxwell material and it approaches zero for $\tau/\theta \to \infty$ since the viscoelastic results would not be different from the purely elastic case if the characteristic time is large, see Fig. 4.6b.

Regarding the acceleration, the function

$$f_a\left(\tau/\theta\right) = -a_1 \exp\!\left(-\left(\frac{\tau/\theta}{a_2}\right)^{a_3}\right) - a_4 \exp\!\left(-\left(\frac{\tau/\theta}{a_5}\right)^{a_6}\right) + (a_1+a_4-1) \exp\!\left(-\left(\frac{\tau/\theta}{a_7}\right)^{a_8}\right) \tag{4.9}$$

was used, where the free parameters $a_1 \ldots a_8$ are listed in Table 4.1 as well.

index	1	2	3	4	5	6	(p)	7	8
u	0.680	0.210	1.095	0.230	0.878	0.741	0.090	1.648	0.090
a	0.081	53.33	0.298	0.434	1.385	0.722	−0.485	0.354	0.947

Table 4.1.: Numerical values for the free parameters in Eqns. (4.8) and (4.9) from curve fitting. The column marked by "(p)" gives the pre-factor of the last term, i.e. $(1-u_1-u_4)$ and (a_1+a_4-1), respectively.

These functions are shown in Fig. 4.12 (page 76) together with their weighted sum for selected weights. The optimal value F^* of the multi-objective problem varies between $f_u^*=0$ at $\tau/\theta\to\infty$ for $w_a=0$ and $f_a^*=-1$ at $\tau/\theta\to 0$ for $w_a=1$. The optimal dimensionless time τ^*/θ can be easily computed from the derivative of the multi-objective function in terms of an arbitrary weighting analogously to Eqn. (D.3). For equal weighting ($w_a=w_u=0.5$), τ^*/θ is 0.399. In general, except for the limit cases where one objective dominates the other, the optimal value of τ/θ is found within 0.1 and unity.

Consider now suitable normalised distances representing the two single objective functions. Since the function values of both f_u and f_a are within unit range, it is not necessary to consider the denominator in Eqn. (D.4). Thus, the normalised distances are

$$d_u(\tau/\theta) \;=\; f_u(\tau/\theta)-f_u^* \;=\; f_u(\tau/\theta)-0 \;=\; 1-\frac{u_{\mathrm{el}}}{u_{\mathrm{ve}}\,(\tau/\theta)} \quad \text{and} \tag{4.10}$$

$$d_a(\tau/\theta) \;=\; f_a(\tau/\theta)-f_a^* \;=\; f_a(\tau/\theta)+1 \;=\; \frac{a_{\mathrm{ve}}\,(\tau/\theta)}{a_{\mathrm{el}}}\;, \tag{4.11}$$

respectively. From minimisation of the function $\sqrt{(d_u)^2+(d_a)^2}$, the L_2-optimum is found at $\left(\tau/\theta\right)^*=0.301$, see Fig. 4.13a. Here, ${w_u}^*=0.448$ and ${w_a}^*=0.552$ and the slope of the dashed tangent in Fig. 4.13b is $\frac{-0.448}{0.552}=\frac{-1}{1.23}=-0.812$. The normalised distances are ${d_u}^*=0.339$ and ${d_a}^*=0.417$. Thus, the distance between the origin in the space of normalised distances and the L_2-optimum is 0.538, and a circle around the origin with this radius would just touch the Pareto front.

On the other hand, when the min-max criterion is applied, ${d_u}^*={d_a}^*=0.383$ for $\left(\tau/\theta\right)^*=0.261$. Thus, ${w_u}^*=0.429$ and ${w_a}^*=0.571$. Graphically, the L_∞-optimum is obtained by the intersection of the dotted line with slope 1 and the Pareto front in Fig. 4.13b.

4.4.3. Optimal characteristic time for the SLS model

Analogously to the Maxwell model, it is possible for the SLS to fit the single objectives for each discrete value α by analytical expressions and derive the optimal characteristic time according to the L_2 norm or the L_∞ norm of the normalised distances. However, for brevity, for the SLS and the PL just the graphical results for the multi-objective function will be given for arbitrarily selected weights.

For different α-parameters of the SLS, the single objectives regarding the max. penetration (Eqn. (4.5)) are shown in Fig. 4.14a, while the objectives concerning the max. acceleration (Eqn. (4.6)) are given in Fig. 4.14f (see page 78). The multi-objective functions (Eqn. (4.7)) are shown in Figs. 4.14b,c,d,e for different weights. When an equal weighting is used, the optimal ratio $\frac{\tau}{\theta}$ is approximately 0.3 for all example values of α, except maybe for $\alpha = 0.99$ (see Fig. 4.14c). Moreover, it is interesting to note that the multi-objective function for $w_u = w_a = 0.5$ becomes zero also for the E_∞-solution (i.e. for small $\frac{\tau}{\theta}$), which is due to $E^{-0.4}$ and $E^{0.4}$ appearing in the Hertzian equations (2.66) and (2.67) for u_{el} and a_{el}.

4.4.4. Optimal characteristic time for the PL model

For the power law model, the single objective functions are given in Fig. 4.15a regarding the penetration and in Fig. 4.15f regarding the acceleration for various values of β (page 79). The multi-objective functions according to Eqn. (4.7) are given in Fig. 4.15b,c,d,e, where different weights were used.

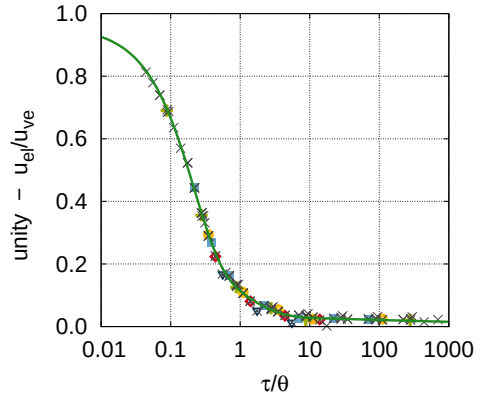

(a) Single objective: minimise u_{ve}

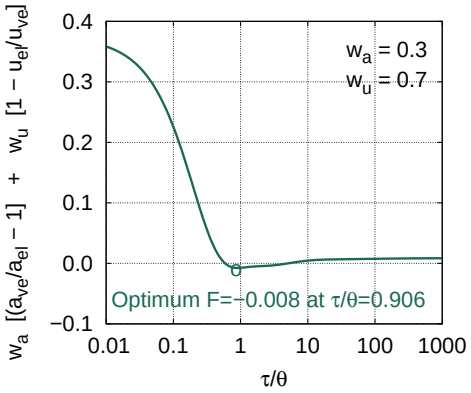

(b) $w_a / w_u = 43\%$

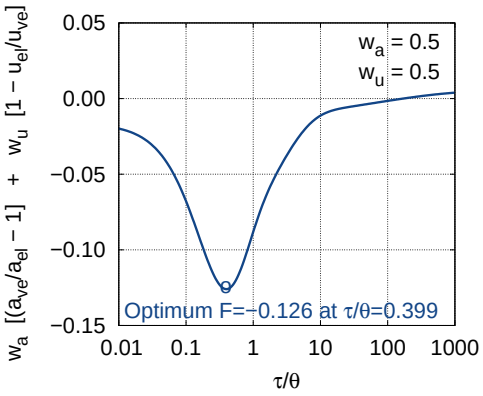

(c) $w_a / w_u = 100\%$

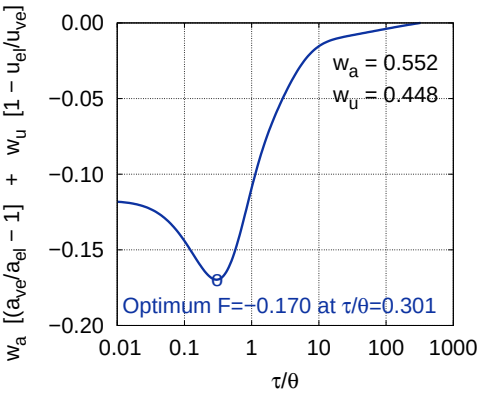

(d) L_2-optimum: $w_a / w_u = 123\%$

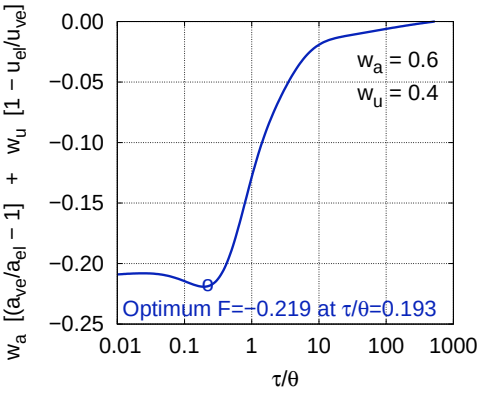

(e) $w_a / w_u = 150\%$

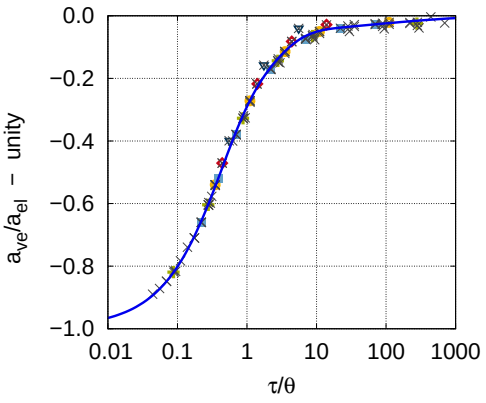

(f) Single objective: minimise a_{ve}

Figure 4.12.: Maxwell model: Optimisation for the two objectives of minimising the max. penetration and minimising the max. acceleration. **(a)**: Only u_{ve} is of interest. This plot is a modification of Fig. 4.6b. **(b)**, **(c)**, **(d)**, **(e)**: using different weights for the two objectives. **(f)**: Only a_{ve} is of interest. This plot is a modification of Fig. 4.6f.

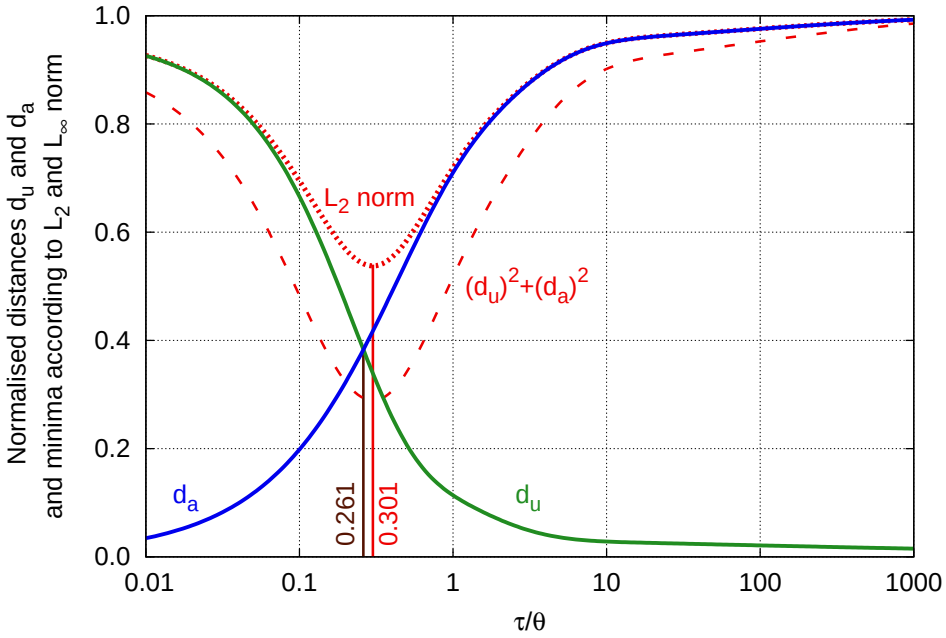

(a) Design space

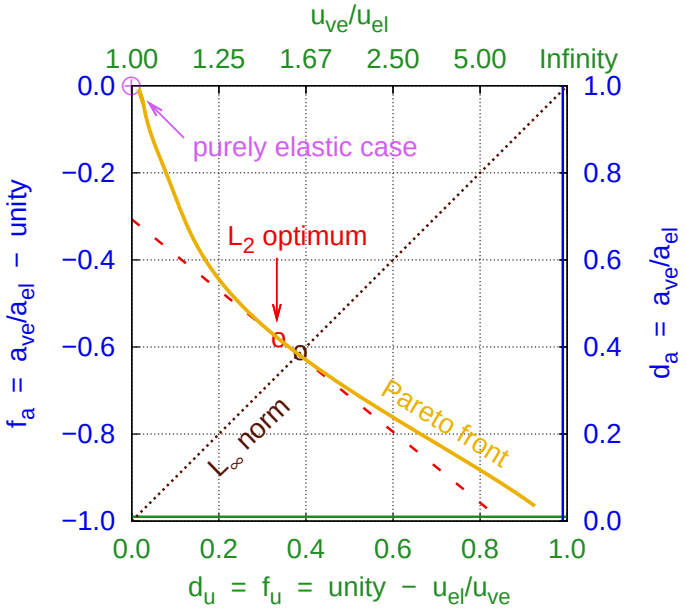

(b) Objective function space / space of normalised distances

Figure 4.13.: Optima according to the L_2 and the L_∞ norm: **(a)** Plot of the normalised distances d_u and d_a over the design variable τ/θ. The sum of the squared distances and its square root (L_2 norm) are minimum at $(\tau/\theta)^* = 0.301$. The intersection of d_1 and d_2 is located at $(\tau/\theta)^* = 0.261$. Compare with Fig. D.1. **(b)** L_2 and L_∞ optimum in the objective function space. All designs are Pareto optimal. Compare with Fig. D.2.

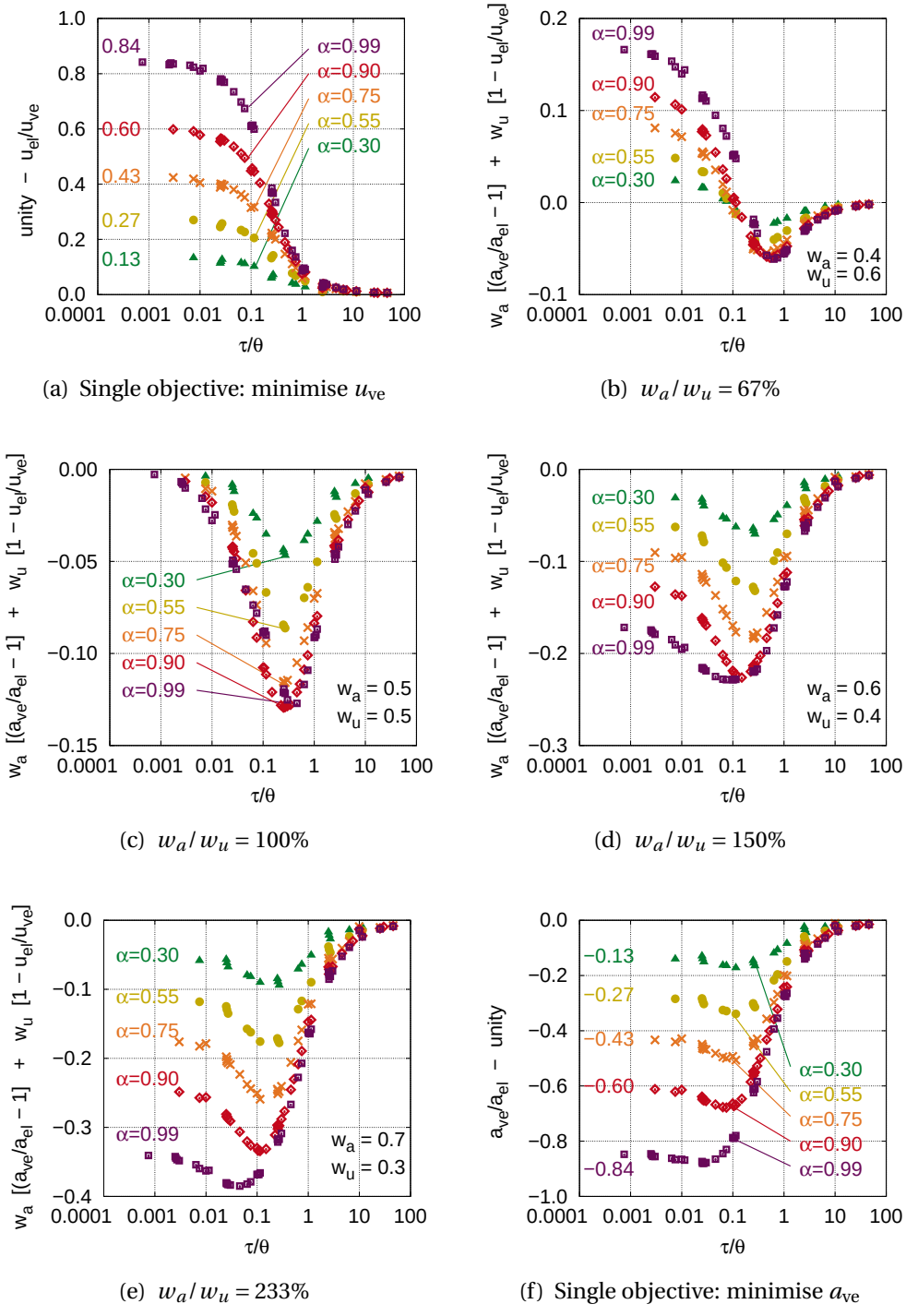

(a) Single objective: minimise u_{ve}

(b) $w_a / w_u = 67\%$

(c) $w_a / w_u = 100\%$

(d) $w_a / w_u = 150\%$

(e) $w_a / w_u = 233\%$

(f) Single objective: minimise a_{ve}

Figure 4.14.: Standard Linear Solid: Optimisation for the two objectives of minimising the max. penetration and minimising the max. acceleration. **(a)**: Only u_{ve} is of interest. This plot is a modification of Fig. 4.7b. **(b)**, **(c)**, **(d)**, **(e)**: using different weights for the two objectives. **(f)**: Only a_{ve} is of interest. This plot is a modification of Fig. 4.7f.

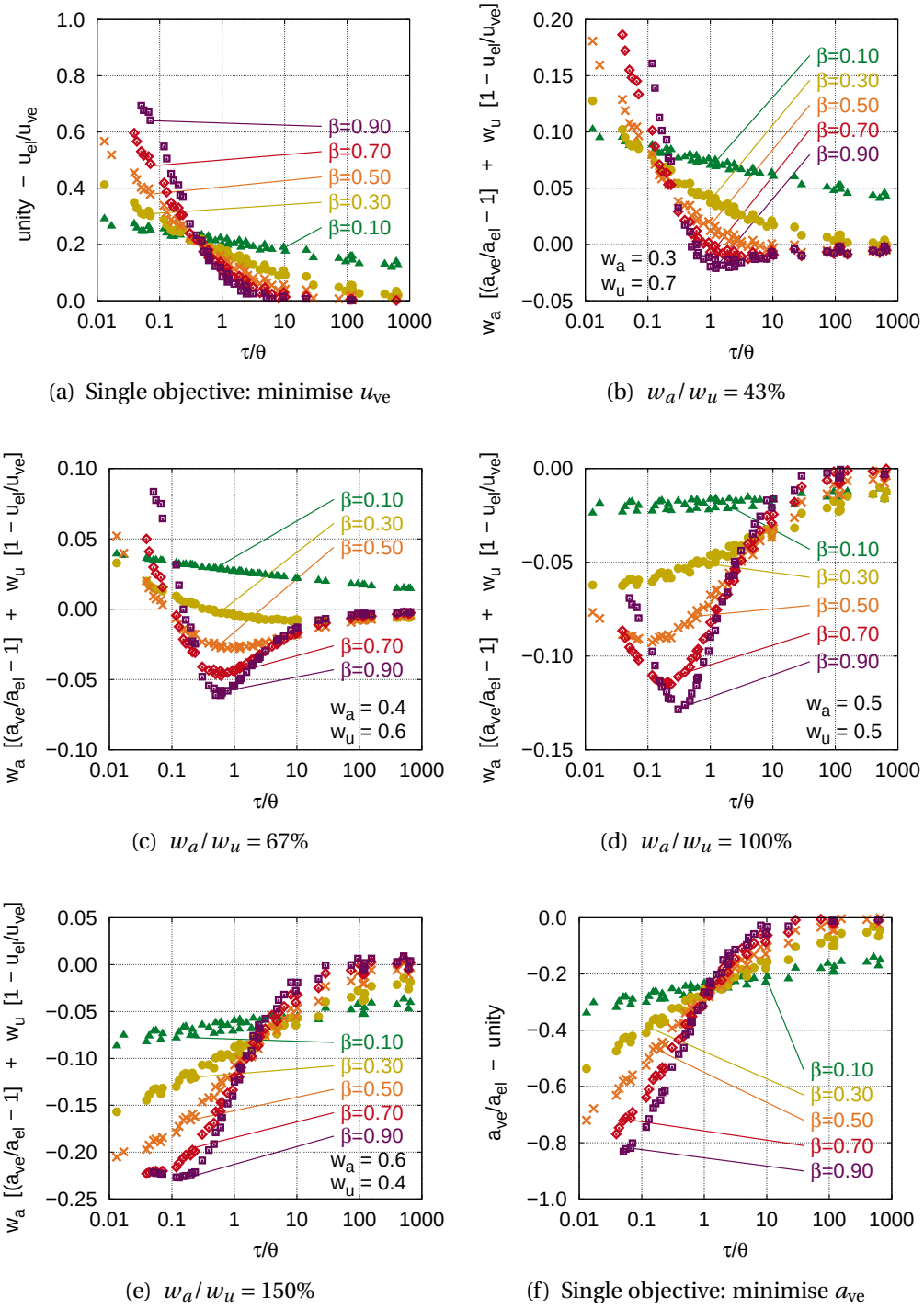

(a) Single objective: minimise u_{ve}

(b) $w_a / w_u = 43\%$

(c) $w_a / w_u = 67\%$

(d) $w_a / w_u = 100\%$

(e) $w_a / w_u = 150\%$

(f) Single objective: minimise a_{ve}

Figure 4.15.: Power law: Optimisation for the two objectives of minimising the max. penetration and minimising the max. acceleration. **(a)**: Only u_{ve} is of interest. This plot is a modification of Fig. 4.8b. **(b)**, **(c)**, **(d)**, **(e)**: using different weights for the two objectives. **(f)**: Only a_{ve} is of interest. This plot is a modification of Fig. 4.8f.

4.5. Material characterisation / re-analysis by impact tests

In the previous section, the optimal material behaviour was sought for a given type of loading; thus, the material parameters were free variables. In the following, a second mode of application of the presented methodology will be shown: now, the task is to determine the characteristic properties of a viscoelastic material sample, i.e. the model parameters for a specific material model have to be identified. For this purpose, the use of impact experiments is proposed in this thesis. Since the viscoelastic behaviour becomes only visible when the material time scale is close to the time scale of loading, impact experiments give access to model parameters describing the instantaneous (elastic) behaviour and the fast (short-term) viscoelastic behaviour.

4.5.1. Parameter identification for the SRKV model

The three unknown model parameters of the square root Kelvin-Voigt model are the indentation modulus Y, the dimensionless parameter γ and the characteristic time τ, see Eqn. (2.25) for the one-dimensional case. Since Y refers here to the case of an infinitely long loading $\left(Y=\frac{E_\infty}{1-\nu^2}\right)$, this parameter can be easily determined by a creep or relaxation test. Using the stress relaxation experiment for the Sylomer sample described in Subsection 3.2.5, the indentation modulus can be computed by Eqn. (2.59) as

$$Y \;=\; \frac{3}{4}\,F\,R^{-0.5}\,u^{-1.5} \;=\; 165\cdot 10^6\ \text{Pa}\ . \tag{4.12}$$

The remaining two parameters are identified from an impact experiment where the loading parameters were prescribed as $R=0.025$ m, $M=6.28$ kg, and $V=0.285\ \frac{\text{m}}{\text{s}}$. The time history for the penetration, velocity, and acceleration is given in Fig. 4.2, indicating that results related to the impactor acceleration are subject to large uncertainties. Thus, in the procedure described here, only the value of the maximum penetration $u_{\text{ve}}=0.00503$ m, the corresponding time instant $t_u=0.031$ s, and the final velocity $v_{\text{final}}=0.128\ \frac{\text{m}}{\text{s}}$ are required:[6]

1. From v_{final} and V, compute the coefficient of restitution: $\Pi_{\text{rest}}=0.45$.
2. From the loading parameters and the elastic material constant Y, compute $u_{\text{el}}=0.0129$ m according to Eqn. (2.66). Thus, $\Pi_u=\frac{0.00503}{0.0129}=0.39$.
3. Use Fig. 4.16a to determine γ from the intersection of Π_u and Π_{rest}: $\gamma\approx 0.97$.

[6] The acceleration plot in Fig. 4.17 is just included for comparison with the numerical results. Here, a medium level of smoothing (the same as in Fig. 4.2b) was used.

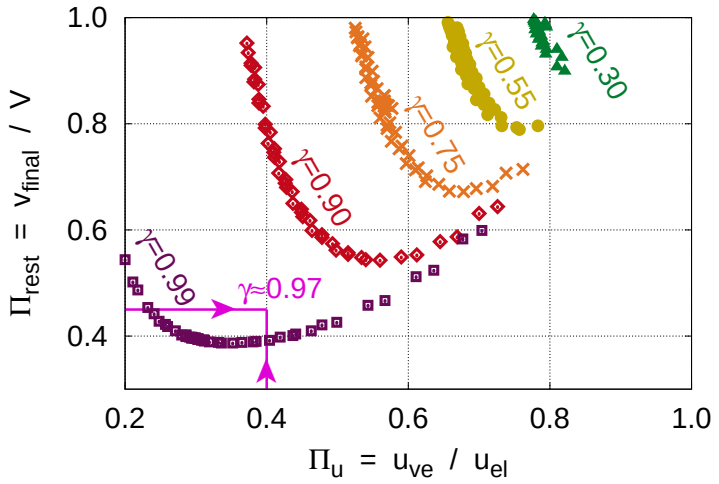

(a) Identification of γ

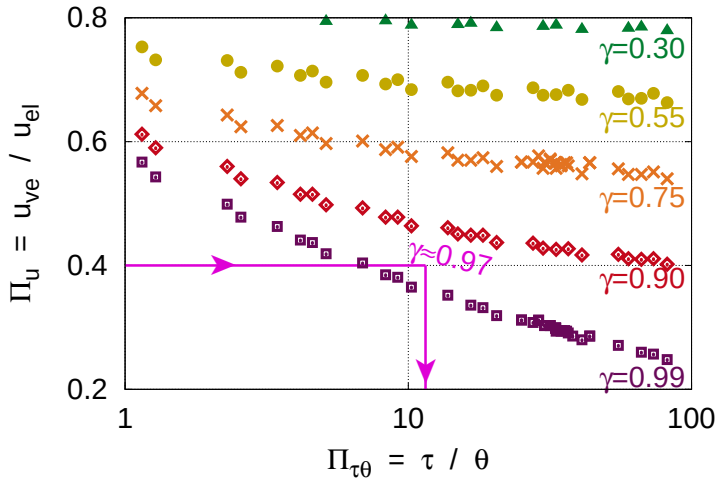

(b) Identification of $\Pi_{\tau\theta}$

Figure 4.16.: Parameter identification for the square root Kelvin-Voigt model. **(a)** Π_{rest} as a function of Π_u for different values of γ. **(b)** Π_u as a function of $\Pi_{\tau\theta}$ for different values of γ. This plot was already given in Fig. 4.9b.

4. In Fig. 4.16b, walk along the line $\Pi_u = 0.39$ until $\gamma = 0.97$; thus $\Pi_{\tau\theta} = \frac{\tau}{\theta}$ is approximately 11.5.

5. Compute $\theta = 0.066$ s by Eqn. (2.71); hence, the characteristic time is retrieved as $\tau \approx 0.76$ s.

Thus, all material parameters are known. For comparison, a numerical simulation with these parameters and the same loading as in the impact experiment was conducted. The results given in Fig. 4.17 show a good agreement with the experimental data. It shall be remarked that the evaluation of further physical impact experiments – preferably at different levels of initial velocity in order to vary the contact time – could have a beneficial effect towards a reliable determination of the model parameters, since small errors in the measurement data could possibly lead to noticeable deviations in the results from the procedure described above. However, the initial velocity must neither be too small (because of friction effects in the test rig) nor too large (application of the Hertzian contact conditions, linearity of results, wave propagation).

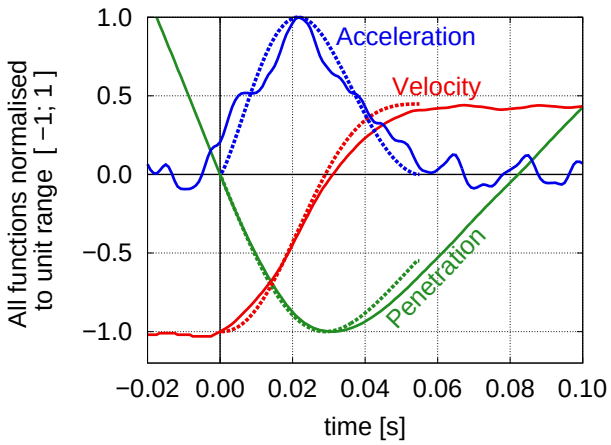

(a) Data in a normalised range

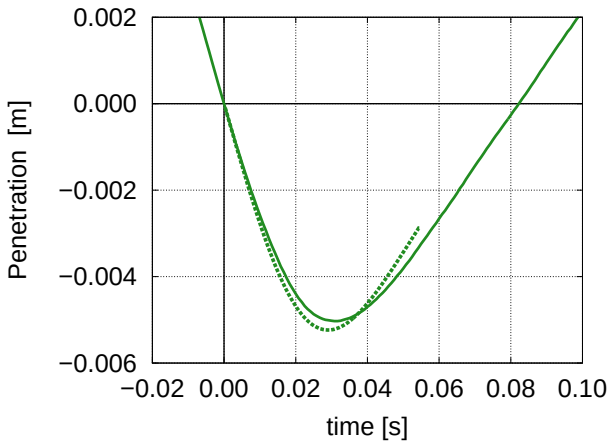

(b) Penetration (dimensional values)

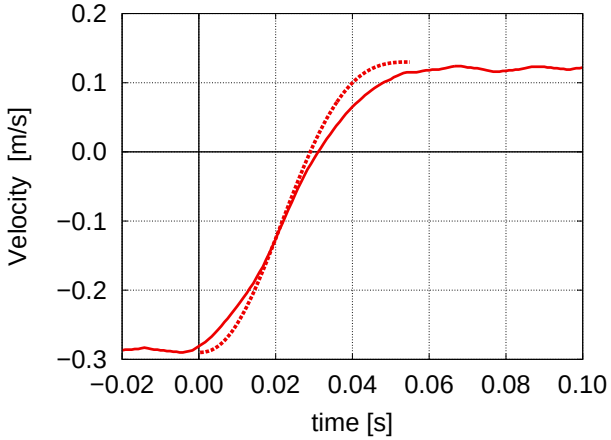

(c) Velocity (dimensional values)

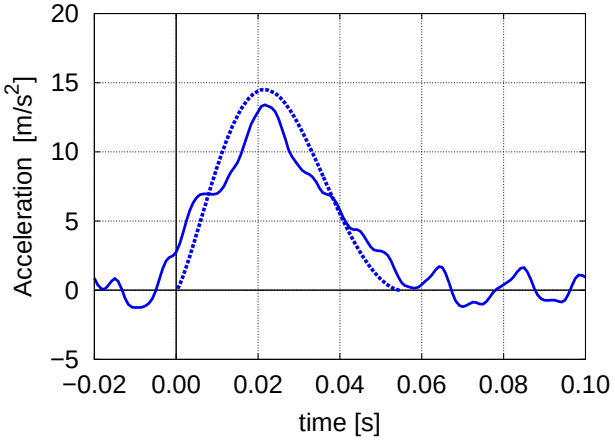

(d) Acceleration (dimensional values)

Figure 4.17.: Comparison between experimental (Sylomer: full line) and numerical (square root Kelvin-Voigt model: dotted line) results. **(a)** Normalised data over time. **(b)** Penetration over time. **(c)** Velocity over time. **(d)** Acceleration over time.

4.5.2. Parameter identification for the LOG model

The one-dimensional creep experiment described in Subsection 3.2.3 leads to the conclusion that the Sylomer is well-described by the logarithmic creep model. Here, the unknown material parameters are the indentation modulus Y (related to the instantaneous Young's modulus[7]), the dimensionless parameter λ, and the characteristic time τ, see. Eqn. (2.26). These three parameters can be determined by the following procedure:

1. Perform an impact experiment with known radius R, mass M, and initial velocity V. Measure the max. penetration u_{ve} at time t_u and the final velocity v_{final}. Again, no information regarding the max. acceleration or the overall contact duration is needed.

2. Perform a static creep test and determine the offset of the strain rate w.r.t. the reference line, from which one gets the ratio λ/E_0.

3. Express $\Pi_{\theta tu} = \frac{\theta}{t_u}$ in terms of λ as follows: since θ depends on the indentation modulus Y by Eqn. (2.71), one may write

$$\Pi_{\theta tu} = \frac{1}{t_u}\, 1.472 \left(\frac{15}{16}\right)^{0.4} R^{-0.2}\ M^{0.4}\ V^{-0.2}\ Y^{-0.4} \quad , \text{ thus,}$$

$$\Pi_{\theta tu}(\lambda) = 1.434\ R^{-0.2}\ M^{0.4}\ V^{-0.2}\ \left(\lambda/E_0\right)^{0.4}\ {t_u}^{-1}\ \lambda^{-0.4} \,. \tag{4.13}$$

4. Use Fig. 4.18a to determine λ: guess a certain value for λ and compute $\Pi_{\theta tu}$ from Eqn. (4.13). The intersection of this value for the abscissa and the measured coefficient of restitution on the ordinate has to match the corresponding curve of the numerical results in order to support a correct assumption for λ. Otherwise, estimate a new value for λ and repeat this step.

5. With the value of λ at hand, use Fig. 4.18b to determine $\Pi_{\tau\theta}$ from Π_{rest}. In general, one will obtain two solutions.

6. Since λ and λ/E_0 are known, one is able to compute Y and, thus, all solutions referring to the purely elastic case, notably u_{el} and θ. Thus, using Π_u in Fig. 4.18d, one can identify the correct value for $\Pi_{\tau\theta}$ and, hence, calculate τ.

---

[7] Throughout this work an unequivocal (constant) Poisson's ratio is assumed. Setting $\nu \stackrel{!}{=} 0$, which is of common practice for many open-cell foams, $Y = E_0$ by Eqn. (2.31). On the other hand, for a non-vanishing Poisson's ratio (see for instance Friis et al. [1988]), a minor modification of Eqn. (4.13) is necessary, but the procedure sketched below is still applicable.

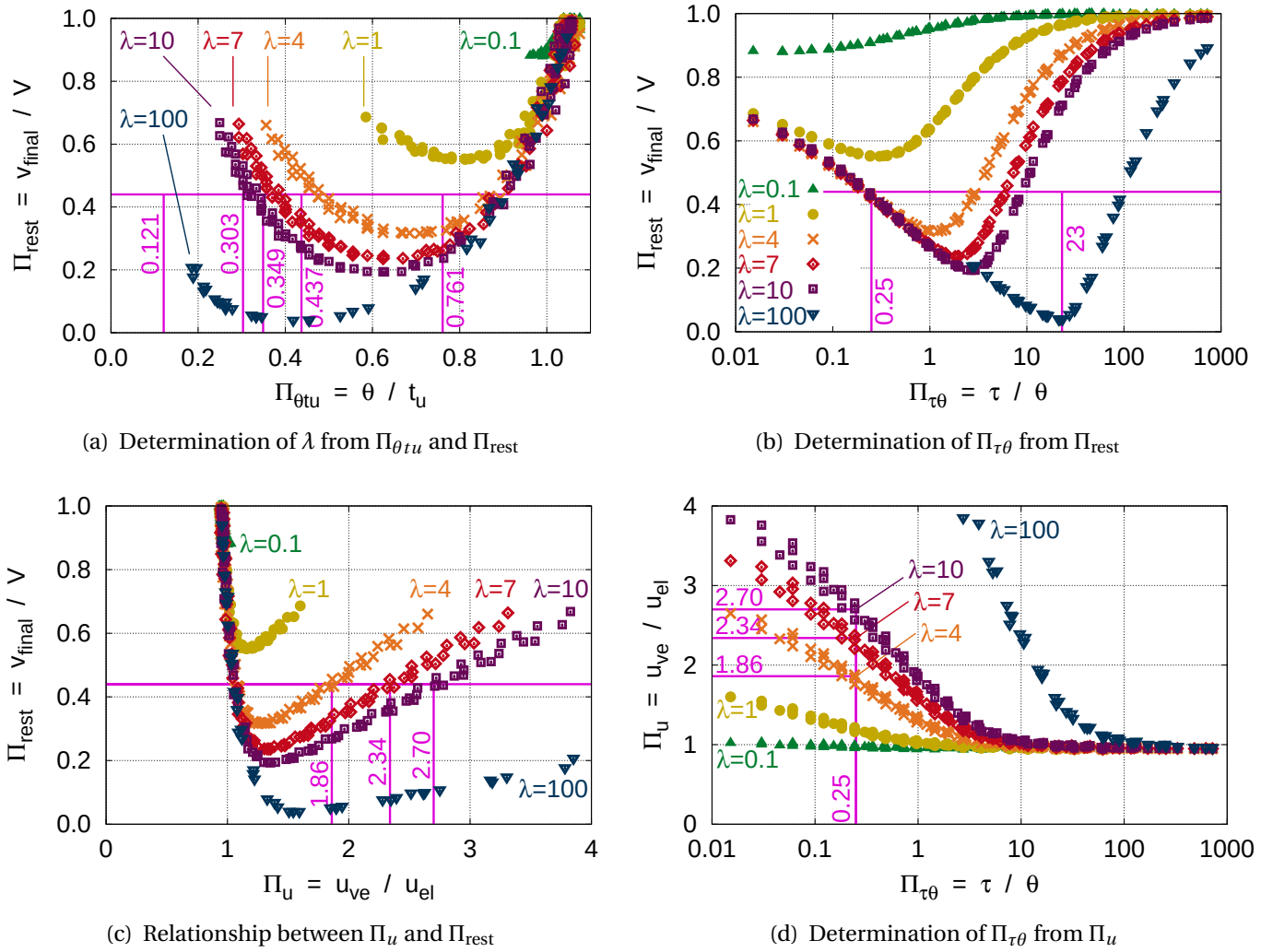

(a) Determination of λ from $\Pi_{\theta tu}$ and Π_{rest}

(b) Determination of $\Pi_{\tau\theta}$ from Π_{rest}

(c) Relationship between Π_u and Π_{rest}

(d) Determination of $\Pi_{\tau\theta}$ from Π_u

Figure 4.18.: Parameter identification for the LOG model: **(a)** Determination of λ. **(b)** For a known λ, two candidates for $\Pi_{\tau\theta}$ can be identified from Π_{rest}, see also Fig. 4.10d. **(c)** This diagram is not necessary for the parameter identification procedure but it is included here since it combines (b) and (d). **(d)** Out of the two solutions from (b), the correct one can be identified using Π_u.

λ	1	4	7	10	20	25	50	100
$\Pi_{\theta tu}$	0.761	0.437	0.349	0.303	0.230	0.210	0.159	0.121

Table 4.2.: Evaluation of Eqn. (4.13) for the impact experiment on the Sylomer sample in order to determine λ by Fig. 4.18a.

These steps will now be applied to the Sylomer sample.

1. In the impact experiment, $u_{\text{ve}} = 0.00775$ m at $t_u = 0.030$ s and $\Pi_{\text{rest}} = 0.44$ were obtained for a loading[8] of $R = 0.025$ m, $M = 6.28$ kg, and $V = 0.465\ \frac{\text{m}}{\text{s}}$.
2. In Subsection 3.2.3 the ratio λ / E_0 was obtained as $0.55\ \frac{1}{10^6\ \text{Pa}}$.
3. Inserting values into Eqn. (4.13), one obtains $\Pi_{\theta tu} = 0.761\ \lambda^{-0.4}$. This expression is evaluated in Table 4.2 for some values of λ.
4. From Fig. 4.18a, $\lambda \approx 25$ is obtained.
5. Using Fig. 4.18b, the two possible solutions for $\Pi_{\tau\theta}$ are 0.25 and 23, respectively.
6. Compute $E_0 = \frac{25}{5.5 \cdot 10^{-7}} = 45 \cdot 10^6$ Pa; thus, $\theta = 0.0063$ s and $u_{\text{el}} = 0.0020$ m, giving $\Pi_u = 3.9$. From Fig. 4.18d, it becomes obvious that $\Pi_{\tau\theta} = 0.25$ is correct. Thus, τ is determined as 0.0016 s.

Using these values, a numerical simulation was conducted with the same loading as in the impact experiment. As shown in Fig. 4.19, the numerical and experimental results agree very well. This is especially true as concerns the acceleration, even though here the experimental data often is problematic due to the double differentiation of the physical measurements.

[8] The experimental results given here and in Fig. 4.19, where a very mild smoothing with $k = 2{\cdot}3{+}1$ data points was applied, refer to the arithmetic mean of three experiments with an identical loading.

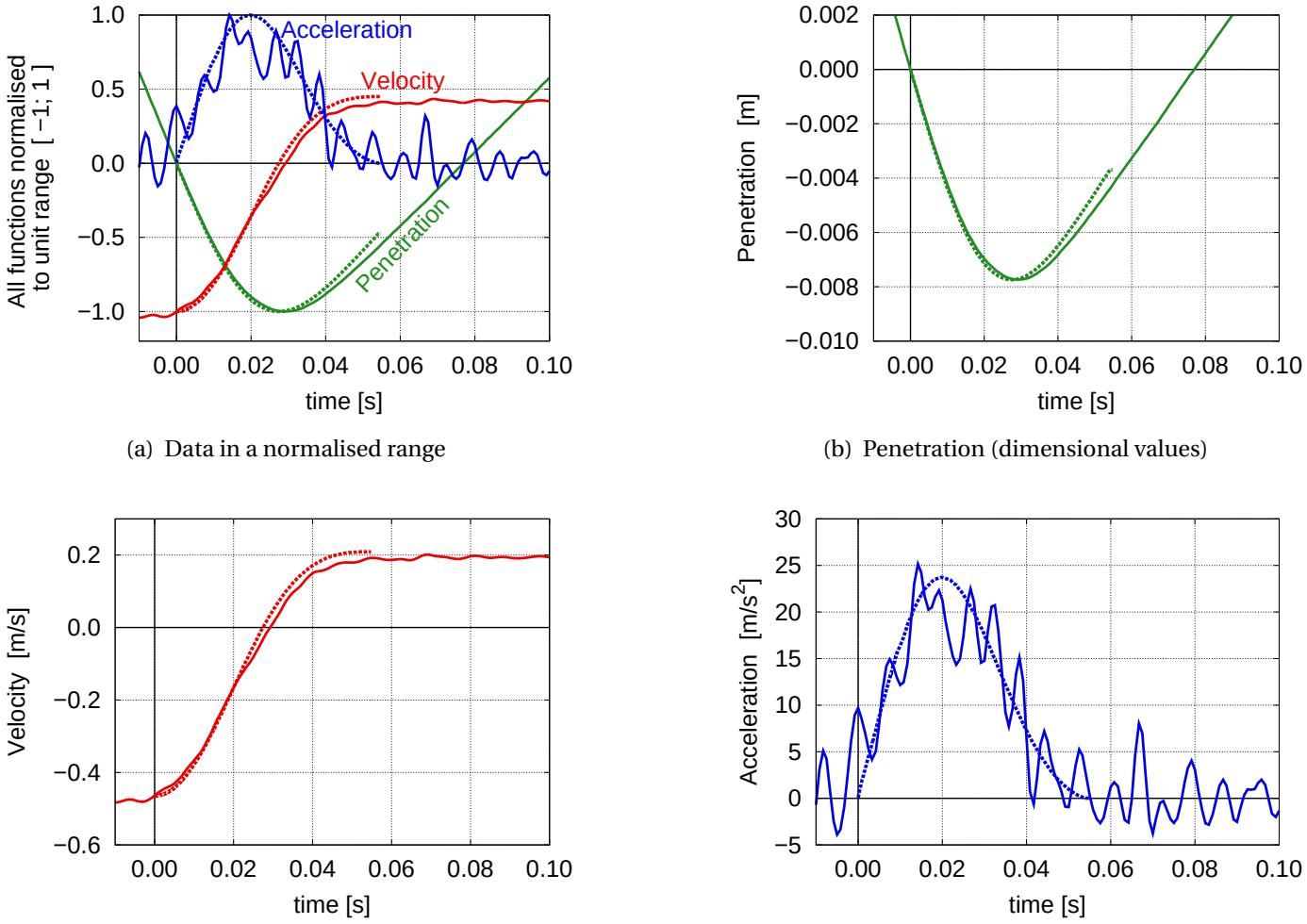

(a) Data in a normalised range

(b) Penetration (dimensional values)

(c) Velocity (dimensional values)

(d) Acceleration (dimensional values)

Figure 4.19.: Numerical results for an impact simulation using the logarithmic creep model (dotted line) and the arithmetic mean of three physical experiments using the Sylomer sample (full line). **(a)** Normalised data over time. **(b)** Penetration over time. **(c)** Velocity over time. **(d)** Acceleration over time.

4.6. Concluding remarks

This chapter started with the description of the impact test rig. Since the equipment was originally designed for a rather high velocity level for the testing of stiffer materials, too soft material samples may cause problems because friction between the impactor and the rails may become too dominant in case of small impact velocities. In this case, a pendulum device is recommended.

The measured impactor position history has to be differentiated in order to obtain velocity and acceleration data; thus, a mild smoothing has to be applied to the penetration data in order to avoid too large oscillations of the derived quantities.

The numerical results were obtained by Finite Element analyses using ANSYS MECHANICAL® and RLEAP. By means of dimensional analysis and the use of the Hertzian solution for the purely elastic case, the numerical data was brought into a generally valid format. The so-obtained master curves have the advantage that the dimensionality of the problem is reduced. Thus, they can be drawn in form of readable two-dimensional diagrams. These plots were constructed for the final velocity as well as for the maximum penetration and acceleration during impact for the five rheological models introduced in Section 2.3.

For three of these, a half-space was modelled, which is why the so-obtained results are comparable to the Hertzian relations. In practice, the modelling of a half-space is appropriate in case of sufficient material thickness. As an application, it was shown how to determine optimal material parameters for structures under impact using either a single or two conflicting objectives.

For the other two rheological models, a finite thickness was used, which led to some scattering when the numerical results were scaled by the analytical elastic relationship. However, when the sample thickness is not too small (w.r.t. the impactor radius and the penetration depth), the obtained curves are still usable. The applicability of the results was demonstrated for the identification of unknown model parameters. These were validated by physical impact experiments, where a good agreement between numerical and experimental results was obtained.

5. Conclusions

Tho' much is taken, much abides; and tho'
We are not now that strength which in old days
Moved earth and heaven, that which we are, we are,–
One equal temper of heroic hearts,
Made weak by time and fate, but strong in will
To strive, to seek, to find, and not to yield.

TENNYSON [1938] (written in 1833), p.168

5.1. Summary

Viscoelastic materials provide proper protection against repeated impact loading. When a body hits an inelastic material, a portion of its kinetic energy is converted into other energy forms. Instantaneously responding inelastic material mechanisms like plastic yielding and accumulation of damage are crucial for proper energy dissipation under high-velocity loading; however, in these cases the structural degradation due to irreversible deformations requires a repair or an exchange of the protective system after each impact event. On the other hand, in case of a small initial impactor velocity and a rather soft material sample, the smaller momentum induces a correspondingly long contact duration, such that energy dissipation by viscous processes can be achieved provided that the viscoelastic material characteristics conform to the loading time scale.

Standard parameter identification methods. Creep and relaxation experiments may reveal only those model parameters related to the long-term behaviour of a viscoelastic material. In contrast, a harmonic straining allows for loading with a high frequency, thus giving

access to the short-term properties of the material sample under inspection even though the physical set-up of the experiment may be difficult and time-consuming. In general, it is sufficient to use either the creep compliance or the relaxation modulus or the complex relaxation modulus, because all these viscoelastic functions are interrelated to each other.

Solutions for spherical contact and impact. For the case of purely elastic materials, several solutions for the contact relations between a rigid sphere and a deformable half-space exist; here, the solutions according to Sneddon and Hertz were discussed. Whereas for large penetrations the former is more exact, in case of small penetrations the latter may be preferred due to its simpler mathematical form which allows for an analytical solution even for the more involved case of dynamic impact (it was shown in the literature that for small initial velocities the propagation of waves through the elastic half-space is negligible).

In general, the solution to a certain elastic problem may be taken as the starting point for the solution of the related viscoelastic problem by the correspondence principle or the method of functional equations; however, for the spherical impact problem these approaches fail, such that up to date no general solution for the impact of a rigid sphere on a viscoelastic half-space exists. In the literature, some approximate solutions are reported for the special case of very simple viscoelastic material models and near-elastic behaviour. As opposed to those findings, the approach of the current work is applicable for highly non-elastic material response.

Characterisation of foam samples used for impact validation experiment. The validity of the presented approach was confirmed by impact experiments in which two different kinds of polyurethane samples were used. In order to get a clearer picture of the most salient features of these specimens, conventional mechanical tests were performed as well as other inspection methods, such as micrography or infrared spectroscopy.

Impact experiments and simulations. The impact experiments were conducted in the laboratory of Material Technology Innsbruck where the test rig was constructed for just this kind of experiment. Here, it is necessary to ensure a certain level of impactor velocity before contact in order to allow for the neglect of friction effects. On the other hand, at the same time the restriction to small penetration depths had to be imposed in the experimental planning. This was necessary because the experiments with the viscoelastic foams had to be scaled by the Hertzian case of purely elastic material behaviour which only holds when the sphere can be approximated as paraboloid of revolution, see the discussion on Sneddon's and Hertz's static contact solution. The velocity history and acceleration history over time were obtained by taking the time derivatives of the tracked penetration data; however, this

required some smoothing of the measurements in order to get meaningful quantities. Thus, if one intents to consider quantities related to acceleration data these should be used cautiously because of some arbitrariness in the smoothing method. It should be kept in mind that the specimen thickness is finite and, thus, may only be regarded as a half-space when the thickness is large enough compared to the impactor's length dimension.

In the numerical simulations, axisymmetric models were used in order to save computational effort, which was necessary due to the large amount of parameter studies conducted. By dimensional reasoning, it was possible to reduce the dimensionality of the problem which led to a format suitable for simple two-dimensional diagrams. These so-called master curves express a generally valid solution for the spherical impact on a viscoelastic half-space describable by the respective rheological model.

Optimal viscoelastic material parameters for impact protection. The task of material design for impact protecting structures is to answer the question "What are, for a certain material and thus material behaviour, the optimal model parameters leading to a desirable structural response to a given impact loading?", where typical design objectives are the maximum dissipation of energy, or the minimisation of the maximum penetration/acceleration. Whereas – in absence of any wave propagation effects – the former objective corresponds to a minimisation of the final impactor velocity, the simultaneous fulfilment of a small penetration depth and small deceleration forces were handled by a Pareto optimisation where the weight factor controls the influence of the one or the other objective.

Identification of viscoelastic material parameters. The second application presented in this work is the task of material parameter identification, where the question "What parameters of a chosen material model describe best the observed material behaviour?" arises. For two selected material models the approach to this question was shown, using the master curve diagrams and the respective experimental data.

5.2. Novelty of the work and limitations

Novel findings developed in this thesis and practical applications. In this work, a general solution for the structural behaviour of viscoelastic materials subject to low-velocity impact loading by a rigid sphere was developed. To the author's knowledge, no general solution to this problem exists up to date. The advantage of such a solution is evident:

- Analytical solutions, intensely studied in the 1960s, take into account only simple rheological models; also, they assume nearly-elastic behaviour, such that they can not be applied to highly dissipative materials.
- Problem-specific analyses by Finite Element simulations are time-consuming to set up and to evaluate since the obtained results are intrinsically depending on the input quantities; thus, the influence of the individual parameters remains obscure.
- On the other hand, a general solution shows the interrelation between input parameters and results. Thus, it can be employed both for the identification of unknown parameters from the observed structural response and for the determination of optimal parameters for a desirable structural behaviour.
- Also, a general solution allows for a quick and reliable validation of more detailed investigations, which is an important aspect in the evaluation of numerical analyses.

Unlike in the simpler case of spherical impact on a purely elastic half-space (Hertzian impact), the solution to the viscoelastic problem can not be formulated by an analytical equation. Thus, this work developed non-dimensional quantities in order to reduce the complexity of the given problem. By this means it became possible to represent the structural response of (even highly dissipative) viscoelastic materials, considering five different rheological models, when subjected to spherical impact in form of easy-to-read response curves. In order to give examples for possible applications of the so-obtained generally valid solution, it was shown how to determine optimal model parameters for three different objectives. On the other hand, the numerically obtained solution can also be employed for the determination of unknown material model parameters. This application was validated by laboratory experiments using polyurethane foams.

Discussion on requirements, limitations, and applicability. Since the results presented here were related to the purely elastic solution, it is obvious that the same limitations apply as in the Hertzian case. These are, especially,

- the justification to neglect wave propagation effects, which is usually not problematic as long as the initial impactor velocity is small enough, as has been intensely discussed in the literature on Hertzian impact;
- the restriction to small penetration depths (compared to the impactor's radius), since the static contact relations according to Hertz actually apply to paraboloids of revolution, as was shown earlier in comparison with Sneddon's solution;

- and the demand for a large enough material sample such that the specimen's boundaries do not perturb the structural response compared to a true half-space. It was shown by examples that it is sufficient to use "rather thick" material samples (i.e. showing a thickness of twice the sphere's radius), leading to a difference between penetration depth and specimen thickness by at least one order of magnitude.

Another important limitation is the neglect of material deterioration due to plastic flow and damage. However, when the viscoelastic material is well adapted to the applied loading, these effects will not largely influence the specimen's response, if they appear at all.

5.3. Future work

The following research tasks are given as suggestions for further investigations based on the results presented in this work.

Refined laboratory experiments. Since Young's modulus plays an important role for the determination of parameters related to the purely elastic solution and thus for the application of the dimensionless master curves, it is of great interest to obtain information on the elastic parameter of the viscoelastic model (denoted by E_0 and E_∞, respectively, in the models discussed) directly through the impact experiment. Thus, it could be advantageous to measure the speed of wave propagation in order to deduce Young's modulus when the material density is known.

Refined phenomenological material laws. The loading of a material specimen by spherical impact results in a combination of volumetric (dilatational) and deviatoric response. In this work, an unequivocal Poisson's ratio was used; this assumption was chosen deliberately, since much of the literature regarding an analytical approach of the viscoelastic impact problem is based on this principle, resulting in some simplifications due to the same time dependence of all moduli. It should also be noted that a considerable number of material examples are given in the literature where, in fact, this assumption is justified (especially for short loading times), see e.g. Larsson and Carlsson [1998] or Ramesh Kumar and Narasimhan [2004]. However, depending on the specific material sample under inspection, it might be advantageous to examine the physical origin of the time-dependent effects in the observed behaviour more closely and to use different material models to describe the deviatoric and the volumetric response. For instance, many solids show significant time-dependent effects under deviatoric loading while the volumetric response exhibits less pro-

nounced time-dependent behaviour, which may – in some cases – considered to be elastic, or even incompressible. On the other hand, the time-dependent behaviour originating from fluid flow is induced through volumetric deformations. In this case, a viscoelastic model should be used to describe the volumetric behaviour, while for deviatoric loading – not inducing any fluid flow – a purely elastic model might be sufficient.

Optimisation on two scales. The final goal could be to build a general design toolbox which may have the following set-up:

- On the macroscale, loading conditions for the impact problem are specified and the material model for the volumetric and the deviatoric behaviour is chosen.
- Based on the respective master curves, optimal values for the material parameters involved are found.
- These values are handed over to the inverse homogenisation process (topology optimisation). Here, the task is to distribute two or more material phases in the unit cell (a periodic structure on the microscale) such that the desired effective (macroscopic) properties are obtained.

Thus, this toolbox could combine the present work with the investigations in the partner project (see Section D.2) where the time-dependent response due to fluid motion through a porous elastic network was optimised through upscaling methods.

5.4. Real-life applications

The findings presented in this thesis are the result of a research work on the fundamental relationships for a viscoelastic body under spherical impact. It is the author's hope that the results are useful as a starting point for applications such as e.g.

- a professional automatic design tool for early construction phases of equipment for shock absorption or vibration damping,
- quality control instruments in the production of goods (mechanical engineering, food industry, leisure articles, etc.), or
- diagnosis tools in medical science which determine the patient's state parameters through an automatic evaluation of the obtained response to percussion testing.

A. Mathematical foundations

A.1. Basic relations

Complex numbers. The complex number z^* consists of a real part $\Re(z^*) = z'$ and an imaginary part $\Im(z^*) = z''$:

$$z^* = z' + i\, z'' \ , \tag{A.1}$$

where $i \stackrel{\text{def}}{=} \sqrt{-1}$ is the imaginary unit. From the geometrical relations in the complex plane one easily deduces the polar form

$$z^* = |z^*| \cos\phi + i\ |z^*| \sin\phi \ , \tag{A.2}$$

where $\phi = \arctan\frac{z''}{z'}$ for $z' > 0$ is the angle with respect to the real axis (called argument of z^*). Comparison with Eqn. (A.1) yields immediately

$$z' = |z^*| \cos\phi \quad \text{and} \quad z'' = |z^*| \sin\phi \ . \tag{A.3}$$

The length of z^* in the complex plane is

$$|z^*| = \sqrt{(z')^2 + (z'')^2} \ . \tag{A.4}$$

Comparing the series expansion for the sine function

$$\sin\phi = \phi - \frac{\phi^3}{3!} + \frac{\phi^5}{5!} - \frac{\phi^7}{7!} \pm \dots \tag{A.5}$$

and for its derivative, the cosine function

$$\cos\phi = 1 - \frac{\phi^2}{2!} + \frac{\phi^4}{4!} - \frac{\phi^6}{6!} \pm \dots \ , \tag{A.6}$$

with the Taylor series for the exponential function

$$\mathrm{e}^x = \exp(x) = 1 + \frac{x^1}{1!} + \frac{x^2}{2!} + \frac{x^3}{3!} + \frac{x^4}{4!} + \dots \ , \tag{A.7}$$

one retrieves, by substituting $x = i\phi$, Euler's formula

$$\exp(i\phi) \;=\; \cos\phi + i\,\sin\phi \;. \tag{A.8}$$

This is a special case of the identity

$$\exp(z^*) \;=\; \exp(z')\cdot\left(\cos z'' \;+\; i\,\sin z''\right) \;. \tag{A.9}$$

Using Eqns. (A.2) and (A.8), the complex number z^* can also be expressed as

$$z^* \;=\; |z^*|\,\exp(i\phi) \;. \tag{A.10}$$

These results can be extended by de Moivre's formula (e.g. Rießinger [2004])

$$\left(z^*\right)^n \;=\; \left(|z^*|\,(\cos\phi + i\,\sin\phi)\right)^n \;=\; |z^*|^n\left(\cos n\phi + i\,\sin n\phi\right) \;=\; |z^*|^n\exp(in\phi) \tag{A.11}$$

for n being an integer number.

As examples to the above relations, the following identities can be constructed:

$$i \;=\; \exp\!\left(i\frac{\pi}{2}\right) \;\text{ and }\; i^n \;=\; \exp\!\left(i\frac{n\pi}{2}\right) \;=\; \cos\frac{n\pi}{2} + i\,\sin\frac{n\pi}{2} \;. \tag{A.12}$$

Convolution. The convolution of the functions $f(t)$ and $g(t)$ is defined as

$$f(t) * g(t) \;\stackrel{\text{def}}{=}\; \int_{\vartheta=0}^{t} f(t-\vartheta)\;g(\vartheta)\;\mathrm{d}\vartheta \;. \tag{A.13}$$

A.2. Special functions

Remark: The definitions and identities given in this section are taken from Abramowitz and Stegun [1972] and Andrews and Shivamoggi [1988]. For convenience, numbers in ⟨angle brackets⟩ refer to the equation numbers in the former book. For brevity, not all mathematical peculiarities and restrictions are given here in detail; the reader is referred to standard mathematical literature. In the following, x is a real variable, z^* a complex number, ζ is a dummy variable for integration, and $n = 0, 1, 2, \ldots$, unless stated otherwise.

The gamma function. The gamma function is defined as

$$\Gamma(z^*) \;=\; \int_0^\infty \zeta^{z^*-1}\,\exp(-\zeta)\,\mathrm{d}\zeta \;,\;\; \Re(z^*) > 0 \quad \langle 6.1.1\rangle \;. \tag{A.14}$$

Two properties are of special importance: the recurrence formula

$$\Gamma(z^*+1) \;=\; z^*\,\Gamma(z^*) \quad \langle 6.1.15\rangle \tag{A.15}$$

and thus, for integers, the relation to the factorial function:

$$\Gamma(n+1) \;=\; (n)! \;=\; n\,(n-1)! \quad \langle 6.1.15 \rangle \;. \tag{A.16}$$

The beta function. The beta function is defined as

$$B(a;b) \;=\; \int_0^1 \zeta^{a-1}\,(1-\zeta)^{b-1}\,\mathrm{d}\zeta \;,\; \Re(a)>0 \;,\; \Re(b)>0 \quad \langle 6.2.1 \rangle \;. \tag{A.17}$$

The value of the beta function can also be computed from the gamma function by

$$B(a;b) \;=\; \frac{\Gamma(a)\,\Gamma(b)}{\Gamma(a+b)} \quad \langle 6.2.2 \rangle \;. \tag{A.18}$$

The incomplete beta function is defined as

$$B(x;a;b) \;=\; \int_0^x \zeta^{a-1}\,(1-\zeta)^{b-1}\,\mathrm{d}\zeta \quad \langle 6.6.1 \rangle \;, \tag{A.19}$$

thus, for $x=1$, the incomplete beta function $B(1;a;b)$ is equivalent to the beta function $B(a;b)$. The relation between the incomplete beta function and the hypergeometric function (see below) is given as

$$B(x;a;b) \;=\; \frac{x^a}{a}\;{}_2\mathrm{F}_1(a;1-b;a+1;x) \quad \langle 6.6.8 \rangle \;. \tag{A.20}$$

The regularised beta function is defined as

$$I(x;a;b) \;=\; \frac{B(x;a;b)}{B(a;b)} \quad \langle 6.6.2 \rangle \;. \tag{A.21}$$

Note: Different definitions may be used in practice. For example, in MATLAB® (see Matlab [2012]) the `betainc` command corresponds not to the incomplete (Eqn. (A.20)) but the regularised beta function (Eqn. (A.21)).

The hypergeometric function. The Gauss hypergeometric series ${}_2\mathrm{F}_1$ appearing in Eqn. (2.70) is defined as

$${}_2\mathrm{F}_1(a;b;c;x) \;=\; \frac{\Gamma(c)}{\Gamma(a)\,\Gamma(b)} \sum_{n=0}^{\infty} \left(\frac{\Gamma(a+n)\,\Gamma(b+n)}{\Gamma(c+n)} \frac{x^n}{n!} \right) \quad \langle 15.1.1 \rangle \;, \tag{A.22}$$

whence it is evident that the values of a and b may be interchanged. Many simplifications are available depending on the properties of the input arguments.

The exponential integral. The exponential integral used in Eqn. (B.44) is defined as the Cauchy principal value integral

$$\mathrm{Ei}(x) \;=\; -\int_{-x}^{\infty} \frac{\exp(-\zeta)}{\zeta}\,\mathrm{d}\zeta \;=\; \int_{-\infty}^{x} \frac{\exp(\zeta)}{\zeta}\,\mathrm{d}\zeta \;,\; x>0 \quad \langle 5.1.2 \rangle \;. \tag{A.23}$$

From the definition of the E_n-function

$$\mathrm{E}_n(z^*) \;=\; \int_1^\infty \frac{\exp(-z^*\,\zeta)}{\zeta^n}\,\mathrm{d}\zeta \;,\; \Re(z^*)>0 \quad \langle 5.1.4\rangle \;, \tag{A.24}$$

the special case $n=1$ yields

$$\mathrm{E}_1(z^*) \;=\; \int_1^\infty \frac{\exp(-z^*\,\zeta)}{\zeta}\,\mathrm{d}\zeta \;=\; \int_{z^*}^\infty \frac{\exp(-\xi)}{\xi}\,\mathrm{d}\xi \;,\; |\arg z^*|<\pi \quad \langle 5.1.1\rangle \;, \tag{A.25}$$

where the substitution $\xi = z^*\,\zeta$ was used for the latter identity. Note that in MAPLE® (see Maple [2012]) the function $\mathrm{Ei}(x)$ refers to Eqn. (A.23) and $\mathrm{Ei}(a,z)$ to Eqn. (A.24), while in MATLAB® the `expint` command refers to Eqn. (A.25). For interrelations between $\mathrm{Ei}(x)$ and $\mathrm{E}_n(z^*)$ see mathematical literature.

The error function. The error function is defined as

$$\mathrm{erf}(z^*) \;=\; \frac{2}{\sqrt{\pi}}\int_0^{z^*} \mathrm{e}^{-t^2}\,\mathrm{d}t \quad \langle 7.1.1\rangle \;. \tag{A.26}$$

For real z, it is an odd function being 0 at $z=0$ and approaching 1 for $z\to\infty$. It is sometimes helpful to use the series expansion

$$\mathrm{erf}(z^*) \;=\; \frac{2}{\sqrt{\pi}}\sum_{n=0}^{\infty}\frac{(-1)^n\,(z^*)^{2n+1}}{n!\,(2n+1)} \quad \langle 7.1.5\rangle \;. \tag{A.27}$$

The complementary error function is defined as

$$\mathrm{erfc}(z^*) \;=\; \frac{2}{\sqrt{\pi}}\int_{z^*}^{\infty} \mathrm{e}^{-t^2}\,\mathrm{d}t \;=\; 1-\mathrm{erf}(z^*) \quad \langle 7.1.2\rangle \;. \tag{A.28}$$

A.3. Laplace transform

The Laplace transform maps a function $f:[0;\infty[\,\to\,\mathbb{R}$ onto the function $\hat{f}(s)$ by the rule

$$\mathscr{L}\{f(t)\} \;\equiv\; \hat{f}(s) \;\stackrel{\mathrm{def}}{=}\; \int_0^\infty \mathrm{e}^{-st}\,f(t)\,\mathrm{d}t \;, \tag{A.29}$$

where the term e^{-st} is called the kernel of the integral transform. To ensure convergence of the integral, some demands have to be made on the properties of the original function $f(t)$ which are not critical for the use in the present work. The interested reader is referred to mathematics books like Abramowitz and Stegun [1972], Andrews and Shivamoggi [1988], Ditkin [1965], Rießinger [2004] or Sneddon [1972]. Many viscoelastic problems can easily be solved by application of the Laplace transform, thus, most textbooks on theory of viscoelasticity also include some introductory theory notes and basic transformation pairs (see page 10 for a list of references).

The following properties hold:

$f(t)$ for $t>0$		$\hat{f}(s) \stackrel{\text{def}}{=} \mathscr{L}\{f(t)\}$
t	$\circ\!\!-\!\!\bullet$	$\frac{1}{s^2}$
a	$\circ\!\!-\!\!\bullet$	$\frac{a}{s}$
$\mathsf{H}(t)$	$\circ\!\!-\!\!\bullet$	$\frac{1}{s}$
$\delta(t)$	$\circ\!\!-\!\!\bullet$	1
$\delta(t-a)$	$\circ\!\!-\!\!\bullet$	e^{-as}
e^{-at}	$\circ\!\!-\!\!\bullet$	$\frac{1}{s+a}$
$1-\mathrm{e}^{-at}$	$\circ\!\!-\!\!\bullet$	$\frac{a}{s(s+a)}$
$\exp\bigl(-\sqrt{t/a}\bigr)$	$\circ\!\!-\!\!\bullet$	$\frac{1}{s} - \frac{\sqrt{\pi}}{s}\sqrt{\frac{1}{4as}}\,\exp\Bigl(\frac{1}{4as}\Bigr)\,\operatorname{erfc}\Bigl(\sqrt{\frac{1}{4as}}\Bigr)$
$\ln\bigl(1+\frac{t}{a}\bigr)$	$\circ\!\!-\!\!\bullet$	$-\frac{\exp(as)\,\operatorname{Ei}(-as)}{s}$
$\dot{g}(t)=\frac{\mathrm{d}g(t)}{\mathrm{d}t}$	$\circ\!\!-\!\!\bullet$	$s\,\hat{g}(s) - g(0)$
t^k (for $k>-1$)	$\circ\!\!-\!\!\bullet$	$\frac{\Gamma(k+1)}{s^{k+1}}$

Table A.1.: Selected transformation pairs for the Laplace transform.

- Property of linearity: $\mathscr{L}\{\alpha_1 f_1(t) + \alpha_2 f_2(t) + \ldots\} = \alpha_1 \hat{f}(s) + \alpha_2 \hat{f}(s) + \ldots$ for α_1, α_2, ... independent of t
- Property of similitude: $\mathscr{L}\{f(\alpha t)\} = \frac{1}{\alpha}\,\hat{f}\bigl(\frac{s}{\alpha}\bigr)$ for any constant α.
- Transformation of derivatives: $\mathscr{L}\bigl\{\frac{\mathrm{d}}{\mathrm{d}t} f(t)\bigr\} = s\,\hat{f}(s) - f(0)$
- Transformation of integrals: $\mathscr{L}\Bigl\{\int_{\vartheta=0}^{t} f(\vartheta)\,\mathrm{d}\vartheta\Bigr\} = \frac{1}{s}\,\hat{f}(s)$
- Transformation of the convolution $f(t) * g(t)$ yields $\mathscr{L}\bigl\{f(t) * g(t)\bigr\} = \hat{f}(s)\,\hat{g}(s)$.

Table A.1 lists some useful transformation pairs.

Inverse Laplace transform. The inverse Laplace transform $\mathscr{L}^{-1}$, defined by

$$\mathscr{L}^{-1}\bigl\{\hat{f}(s)\bigr\} \stackrel{\text{def}}{=} f(t)\ , \tag{A.30}$$

maps functions from the Laplace domain back to the time domain.

Laplace-Carson transform. The Laplace-Carson transform (cf. Carson [1953], even though this transformation calculus seems to have been used earlier) is defined as

$$\mathscr{LC}\{f(t)\} \equiv f^*(p) \stackrel{\text{def}}{=} p\,\hat{f}(p) = p\int_0^\infty \mathrm{e}^{-pt}\,f(t)\,\mathrm{d}t\ . \tag{A.31}$$

Application of the Laplace-Carson transform to the viscoelastic relaxation modulus yields the complex modulus when the transform variable p is replaced by $i\omega$ (see e.g. page 262 in Hunter [1967]). An example is given for the complex relaxation modulus of the MX model (see page 104). As another example, this relationship is used in Eqn. (2.20).

Transformation of a convolution including a time derivative. Since

$$\mathscr{L}\left\{f(t) = g(t) * \frac{\partial}{\partial t}h(t)\right\} \text{ yields } \hat{f}(s) = \hat{g}(s)\,s\hat{h}(s)\ , \tag{A.32}$$

it is easily shown (substitute $p = s$, multiply both sides by p and use the definition in Eqn. (A.31)) that

$$\mathscr{LC}\left\{f(t) = g(t) * \frac{\partial}{\partial t}h(t)\right\} \text{ yields } f^*(p) = g^*(p)\,h^*(p)\ , \tag{A.33}$$

see for instance Eqn. (2.15).

A.4. Curve-fitting by polynomial approximations

This section sketches the use of polynomial approximations for curve fitting purposes[1] in the simple case of one independent variable x and the related discrete output y. It is assumed that the deviations between measurement and approximating curve are due to normally distributed inaccuracies, thus the least squares method can be used as quality criterion.

Now, the task is to find m scalar coefficients for a polynomial approximation of order $m-1$ which fit best (in a least-squares sense) some discrete values obtained from an experiment. Let y denote the measured response at a certain sampling point x. Then, the error

$$e \stackrel{\text{def}}{=} y - \mathbf{x}^{\mathrm{T}}\mathbf{c} \tag{A.34}$$

can be calculated, where the polynomial approximation is written as dot product of the m-dimensional vector $\mathbf{x}^{\mathrm{T}} = [1, x, x^2, \ldots\ x^{m-1}]$ and the vector $\mathbf{c}$ containing the m yet unknown

[1] Since this problem plays also an important role when generating response surface models with polynomial surrogate functions, the interested reader is referred to the literature on regression analysis and metamodelling techniques, such as Myers and Montgomery [2002], Montgomery and Peck [1992], and Jurecka [2007], where the latter served as basis for the following lines.

scalar coefficients. Doing so for all relevant[2] data points, the approximation errors can be collected in the k-dimensional vector

$$\mathbf{e} \stackrel{\text{def}}{=} \mathbf{y} - \mathbf{X}\,\mathbf{c}\ . \tag{A.35}$$

In the j^{th} column and the i^{th} row of the matrix $\mathbf{X}$ ($i = 1..k,\ j = 1..m$), the value of the $(j-1)^{\text{th}}$ power is computed for the sampling point x_i:

$$\mathbf{X} = \begin{bmatrix} 1 & x_1 & x_1^2 & \dots & x_1^{m-1} \\ 1 & x_2 & x_2^2 & \dots & x_2^{m-1} \\ \vdots & \vdots & \vdots & \ddots & \vdots \\ 1 & x_k & x_k^2 & \dots & x_k^{m-1} \end{bmatrix} \tag{A.36}$$

Minimising the square of the error defined by Eqn. (A.35) with respect to the m free variables (these are the scalar coefficients gathered in $\mathbf{c}$), i.e.

$$\min_{\mathbf{c}} \mathbf{e}^{\mathrm{T}}\mathbf{e} \;=\; \min_{\mathbf{c}} \left(\mathbf{y}^{\mathrm{T}}\mathbf{y} - 2\cdot\mathbf{c}^{\mathrm{T}}\mathbf{X}^{\mathrm{T}}\mathbf{y} + \mathbf{c}^{\mathrm{T}}\mathbf{X}^{\mathrm{T}}\mathbf{X}\,\mathbf{c}\right)\ , \tag{A.37}$$

the analytical relation

$$\frac{\partial}{\partial \mathbf{c}}\left(\mathbf{e}^{\mathrm{T}}\mathbf{e}\right) \;=\; 0 - 2\cdot\mathbf{X}^{\mathrm{T}}\mathbf{y} + 2\cdot\mathbf{X}^{\mathrm{T}}\mathbf{X}\,\mathbf{c} \stackrel{!}{=} 0 \tag{A.38}$$

is obtained. Thus, the coefficients of

$$\mathbf{c} \;=\; \left(\mathbf{X}^{\mathrm{T}}\mathbf{X}\right)^{-1}\mathbf{X}^{\mathrm{T}}\,\mathbf{y} \tag{A.39}$$

can be determined provided that $\mathbf{X}^{\mathrm{T}}\mathbf{X}$ can be inverted, i.e. at least m sampling points with their response values are included.

Remark: The format of the involved operations in Eqns. (A.36) and (A.39) is suitable for a ready computation in spreadsheets such as EXCEL® (see Microsoft Excel 2010 [2010]) using the commands `mmult()`, `minv()`, `mtrans()` and `indirect()`.

[2] The number of data points taken into account for the local smoothing shall by denoted by k. When k equals to the total number of data points, a global fit is obtained. However, it is also possible to fit the response locally by considering only the current point and just $(k-1)/2$ neighbours to the left and the right. This can be regarded as a moving least squares procedure where only the neighbouring points are weighted by 1, all others by 0.

B. Mathematical derivations concerning the used rheological models

In the following, for the five models depicted in Fig. 2.1 the viscoelastic functions are derived, which were given in Section 2.3 without further reasoning.

B.1. Maxwell element (MX)

The Maxwell element consists of one spring (with stiffness E [Pa], thus $\varepsilon^E = \frac{\sigma}{E}$ and so $\dot{\varepsilon}^E = \frac{\dot{\sigma}}{E}$) and one dashpot (with dynamic viscosity η [Pa·s], thus $\dot{\varepsilon}^\eta = \frac{\sigma}{\eta}$) in series, see Fig. 2.1a. Inserting these relations in $\dot{\varepsilon} = \dot{\varepsilon}^E + \dot{\varepsilon}^\eta$, one obtains

$$\frac{1}{E}\,\dot{\sigma}(t) \;+\; \frac{1}{\eta}\,\sigma(t) \;=\; \dot{\varepsilon}(t) \tag{B.1}$$

giving $p_1 = 1/E$, $p_0 = 1/\eta$, $q_1 = 1$, and $q_0 = 0$ in Eqn. (2.12).

For determination of the creep compliance, Eqn. (2.1) is inserted into Eqn. (B.1), yielding

$$\frac{1}{E}\sigma_0\,\delta(t) \;+\; \frac{1}{\eta}\sigma_0\,\mathsf{H}(t) \;=\; \dot{\varepsilon}(t)\;, \tag{B.2}$$

where $\delta(t)$ is the Dirac distribution. Performing the Laplace transform and solving for $\hat{\varepsilon}$ results in

$$\hat{\varepsilon}(s) \;=\; \sigma_0\left(\frac{1}{sE} + \frac{1}{s^2\eta}\right)\;, \tag{B.3}$$

which, upon back-transformation and application of Eqn. (2.3), yields

$$J(t) \;=\; \frac{1}{E} + \frac{t}{\eta}\;. \tag{B.4}$$

The relaxation modulus is obtained by inserting Eqn. (2.4) into Eqn. (B.1):

$$\frac{1}{E}\dot{\sigma}(t) \;+\; \frac{1}{\eta}\sigma(t) \;=\; \varepsilon_0\,\delta(t)\;. \tag{B.5}$$

Applying the Laplace transform, this becomes

$$\frac{1}{E}\, s\, \hat{\sigma}(s) \;+\; \frac{1}{\eta}\, \hat{\sigma}(s) \;=\; \varepsilon_0 \;. \tag{B.6}$$

Solving for $\hat{\sigma}(s)$, one gets

$$\hat{\sigma}(s) \;=\; E\, \varepsilon_0\, \frac{1}{s + 1/\tau} \;, \tag{B.7}$$

where the ratio $\tau \stackrel{\text{def}}{=} \eta/E$ is called "characteristic time". If it is small (compared to the physical time scale of the load), a rapid stiffness loss is observed. On the other hand, a large characteristic time results in a very slow dashpot and, thus, nearly elastic behaviour.

By application of the inverse Laplace transform to Eqn. (B.7), the relaxation modulus for the MX is obtained, using Eqn. (2.6):

$$R(t) \;=\; E\, \mathrm{e}^{-t/\tau} \;. \tag{B.8}$$

Inserting Eqns. (2.7) and (2.8) into Eqn. (B.1) leads to

$$\frac{i\omega}{E}\, \sigma^*\, \mathrm{e}^{i\omega t} + \frac{1}{\eta}\, \sigma^*\, \mathrm{e}^{i\omega t} \;=\; i\omega\, \varepsilon^*\, \mathrm{e}^{i\omega t} \;. \tag{B.9}$$

Solving for σ^* and using Eqn. (2.9), the complex relaxation modulus

$$R^* \;=\; \frac{\sigma^*}{\varepsilon^*} \;=\; E \frac{(\tau\omega)^2 \;+\; i\,(\tau\omega)}{(\tau\omega)^2 + 1} \tag{B.10}$$

is obtained. From this,

$$R' \;=\; \frac{(\tau\omega)^2 E}{1 + (\tau\omega)^2} \;,\; R'' \;=\; \frac{(\tau\omega) E}{1 + (\tau\omega)^2} \;, \text{ and } \quad \tan\delta = \frac{1}{\tau\omega} \;. \tag{B.11}$$

Remark: Alternatively, one could use the Laplace-Carson transform to obtain $R^*(\omega)$ from $R(t)$. To this end, transform Eqn. (B.8) into the Laplace space and multiply both sides by s to obtain $s\hat{R}(s) = \frac{\tau s\, E}{\tau s + 1}$. Now, replace s by $i\omega$, giving $R^* = \frac{i\tau\omega\, E}{i\tau\omega + 1}$. Simplification of the last term leads to Eqn. (B.10).

B.2. Standard linear solid (SLS)

The standard linear solid[1] consists of one spring (with stiffness E_∞) in parallel with a Maxwell arm (with spring stiffness E_1 and dashpot viscosity η_1), see Fig. 2.1b. The characteristic time

[1] In literature, an alternative form of arranging one linear dashpot with two linear springs exists; however, the resulting functionality is the same since the parameter values from one model can easily be transferred to the other model, see e.g. Gross et al. [1995]. Here, we will always refer to the generalised Maxwell form of the SLS as sketched in Fig. 2.1.

of the Maxwell element is $\tau = \eta_1/E_1$. The initial stiffness of the whole assembly is $E_0 = E_\infty + E_1$. Then the spring stiffness of the MX branch can be expressed by $E_1 = \alpha E_0$, where $\alpha \in]0;1[$ is a dimensionless factor[2]. Analogously, the stiffness of the isolated spring is $E_\infty = \alpha_\infty E_0$ where $\alpha_\infty = 1-\alpha$ holds.

For the SLS, the strains in both branches are equal: $\varepsilon(t) = \varepsilon_\infty(t) = \varepsilon_1(t)$. The stress is $\sigma(t) = \sigma_\infty(t) + \sigma_1(t)$, and the Laplace transform of this expression yields

$$\hat{\sigma}(s) = \hat{\sigma}_\infty(s) + \hat{\sigma}_1(s) \ , \tag{B.12}$$

where the first term is simply $\hat{\sigma}_\infty(s) = E_\infty\, \hat{\varepsilon}(s)$. Regarding the second term, apply the Laplace transform to Eqn. (B.1) giving $\frac{s}{E}\, \hat{\sigma}_1(s) + \frac{1}{\tau E}\, \hat{\sigma}_1(s) = s\, \hat{\varepsilon}(s)$. Thus, the sum yields

$$\hat{\sigma}(s) = \left(E_\infty + \frac{sE_1}{s + 1/\tau}\right) \hat{\varepsilon}(s) \ . \tag{B.13}$$

Re-ordering, performing the inverse Laplace transform, and simplifying, one gets the stress-strain relation for the SLS:

$$\tau\, \dot{\sigma}(t) \ + \ \sigma(t) \ = \ \tau\, E_0\, \dot{\varepsilon}(t) \ + \ E_\infty\, \varepsilon(t) \ . \tag{B.14}$$

This corresponds to $p_1 = \tau$, $p_0 = 1$, $q_1 = \tau\, E_0$, and $q_0 = E_\infty$ in Eqn. (2.12).

The creep compliance is obtained by inserting the prescribed strain of Eqn. (2.1) into Eqn. (B.14), resulting in

$$\tau\sigma_0\, \delta(t) \ + \ \sigma_0\, \mathsf{H}(t) \ = \ \tau E_0\, \dot{\varepsilon}(t) + E_\infty\, \varepsilon(t) \ . \tag{B.15}$$

Upon transformation in the Laplace space one can solve for $\hat{\varepsilon}$:

$$\hat{\varepsilon}(s) \ = \ \frac{\sigma_0}{E_0} \frac{1}{s + (E_\infty/\tau E_0)} \ + \ \frac{\sigma_0}{E_\infty} \frac{E_\infty/\tau E_0}{s\big(s + (E_\infty/\tau E_0)\big)} \ . \tag{B.16}$$

The inverse Laplace transformation yields

$$\varepsilon(t) \ = \ \frac{\sigma_0}{E_0} \exp\!\Big(-(1-\alpha)\frac{t}{\tau}\Big) \ + \ \frac{\sigma_0}{E_\infty} \left(1 \ - \ \exp\!\Big(-\big(1-\alpha\big)\frac{t}{\tau}\Big)\right) , \tag{B.17}$$

where the relation $\frac{E_\infty}{E_0} = 1-\alpha$ was used. From this and Eqn. (2.3), the creep compliance is obtained as

$$J(t) \ = \ \frac{1}{E_\infty}\left(1 - \alpha\, \exp\!\Big(-\big(1-\alpha\big)\frac{t}{\tau}\Big)\right) . \tag{B.18}$$

[2] For $\alpha = 1$, the MX would be obtained, whereas for $\alpha = 0$ a single elastic spring was left over.

The negative inverse of the pre-factor for the time in the exponent, $\frac{\tau}{1-\alpha}$, is commonly referred to as retardation time. The creep compliance is plotted in Fig. B.1a for various values of the parameter α.

In order to determine the relaxation modulus, start by inserting $\hat{\varepsilon}(s) = \varepsilon_0/s$ (cf. Eqn. (2.4) and the related footnote on page 11) into Eqn. (B.13) to obtain

$$\hat{\sigma}(s) = \Big(\frac{E_\infty}{s} + \frac{E_1}{s+1/\tau}\Big)\varepsilon_0 \ . \tag{B.19}$$

Application of the inverse Laplace transform and use of Eqn. (2.6) lead to

$$R(t) = E_\infty + E_1\, \mathrm{e}^{-t/\tau} = E_0\left(\alpha_\infty + \alpha\, \mathrm{e}^{-t/\tau}\right) . \tag{B.20}$$

This function is shown in Fig. B.1b.

For the complex modulus, the harmonic stress and strain from Eqns. (2.7) and (2.8) are incorporated into Eqn. (B.14):

$$\left(1 + i\,\tau\omega\right)\sigma^* = \left(E_\infty + i\,E_0\,\tau\omega\right)\varepsilon^* \ . \tag{B.21}$$

Thus, by definition in Eqn. (2.9), one obtains

$$R^* = E_\infty + \frac{E_1\,(\tau\omega)^2 \,+\, i\,E_1\,\tau\omega}{1+(\tau\omega)^2} \ , \tag{B.22}$$

and hence

$$R' = E_0\,\frac{\alpha_\infty + (\tau\omega)^2}{1+(\tau\omega)^2} \ , \ R'' = E_0\,\frac{\alpha\,\tau\omega}{1+(\tau\omega)^2} \ , \text{ and } \ \tan\delta = \frac{\alpha\,\tau\omega}{\alpha_\infty + \,(\tau\omega)^2} \ . \tag{B.23}$$

The maximum value of the loss modulus $(R'')_{\max} = \frac{\alpha}{2}E_0$ is received for the angular frequency $\omega = \frac{1}{\tau}$. The loss tangent reaches its maximum value $(\tan\delta)_{\max} = \frac{\alpha\sqrt{\alpha_\infty}}{2\,\alpha_\infty}$ when $\tau\omega = \sqrt{\alpha_\infty}$. As an example, the absolute value of the complex modulus, the storage modulus, the loss modulus, and the loss tangent are shown for varying angular frequency in Fig. B.2 for $\alpha = 0.90$.

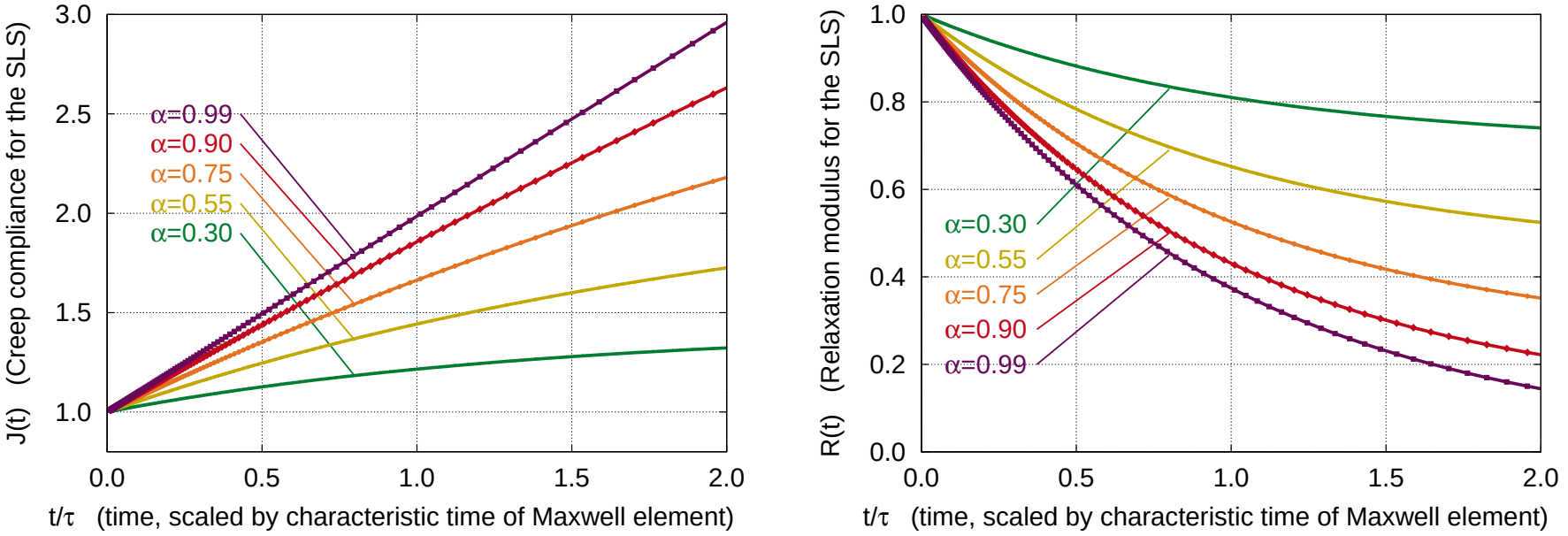

(a) Creep compliance: Eqn. (B.18)

(b) Relaxation modulus: Eqn. (B.20)

Figure B.1.: Standard Linear Solid where $E_0 = 1$ was used: **(a)** creep compliance and **(b)** relaxation modulus over time (scaled by the characteristic time τ of the Maxwell element).

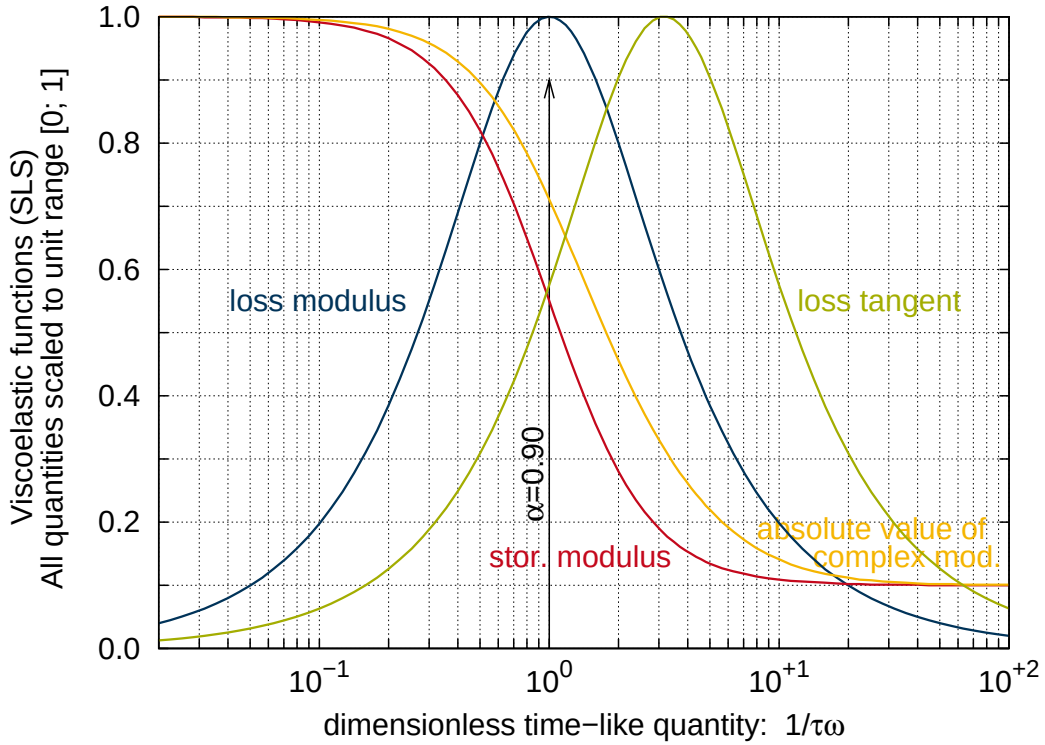

Figure B.2.: Viscoelastic functions for SLS (all function values scaled to unit range for better readability). On the abscissa a time-like quantity is plotted: the inverse of the excitation frequency ($1/\omega$), which is made dimensionless by the characteristic time of the Maxwell arm (τ). The stiffness ratio α is 0.90 as can be seen from the stiffness drop of the dynamic modulus or the storage modulus. The effect of the dashpot (seen from loss modulus and loss tangent) is limited to a certain excitation range (the shape of these curves is called Debye peak). For faster excitations, the dashpot blocks (left end of this plot) and for slower excitations, the dashpot is sliding without much resistance, thus rendering an unloaded spring of its MX element (right end).

B.3. Three-parameter power law creep model (PL)

The three-parameter power law model[3] is composed of a spring and a non-linear dashpot in series, see Fig. 2.1c. Using fractional derivatives, the stress-strain relationship for the non-linear dashpot alone is

$$\frac{\mathrm{d}^\beta \varepsilon(t)}{\mathrm{d}t^\beta} = \frac{\Gamma(\beta+1)}{E_0\,\tau^\beta}\,\sigma(t)\ , \tag{B.24}$$

where $\Gamma(x)$ is the Gamma function and β is a dimensionless parameter with $\beta \in]0;1]$. For $\beta = 1$ this becomes a linear dashpot.

Combining this dashpot with the spring (with stiffness E_0) in series, the stress-strain relation of the PL is, since the stress in the spring and in the non-linear dashpot is equal but the total strain is the sum of the two, given by

$$\frac{\mathrm{d}^\beta \varepsilon(t)}{\mathrm{d}t^\beta} = \frac{\mathrm{d}^\beta}{\mathrm{d}t^\beta}\left(\frac{\sigma(t)}{E_0}\right) + \frac{\Gamma(\beta+1)}{E_0\,\tau^\beta}\,\sigma(t)\ . \tag{B.25}$$

For deduction of the creep compliance, transform Eqn. (B.25) in the Laplace space, giving

$$s^\beta\,\hat{\varepsilon}(s) = \frac{1}{E_0}s^\beta\,\hat{\sigma}(s) + \frac{\Gamma(\beta+1)}{E_0\,\tau^\beta}\,\hat{\sigma}(s)\ . \tag{B.26}$$

In this equation, the Laplace-transformed prescribed stress history $\hat{\sigma}(s)$ (cf. Eqn. (2.1) and the corresponding footnote) is inserted. Solving for $\hat{\varepsilon}(s)$ results in

$$\hat{\varepsilon}(s) = \frac{\sigma_0}{E_0}\frac{1}{s} + \frac{\sigma_0}{E_0\,\tau^\beta}\,\frac{\Gamma(\beta+1)}{s^{\beta+1}}\ . \tag{B.27}$$

Back-transformation and use of Eqn. (2.3) yields the creep compliance for the PL:

$$J(t) = \frac{1}{E_0}\left(1+\left(\frac{t}{\tau}\right)^\beta\right)\ . \tag{B.28}$$

Thus, the characteristic time τ denotes the time span needed for a doubling of the creep strain with respect to the instantaneous answer. For $\beta = 1$ and $\tau = \frac{\eta}{E_0}$, the creep compliance of the Maxwell model is obtained: $J(t) = \frac{1}{E_0} + \frac{t}{\eta}$. For the inadmissible case $\beta = 0$, the creep compliance is constant: $J = \frac{2}{E_0}$. Thus, a purely elastic material is obtained, however, blurred

[3] In literature, different viscoelastic material models are given the name "power law". The model introduced here is also called power law creep and is alternatively described by the creep compliance function $J(t) = \frac{1}{E_0} + J_1\ t^\beta$, where comparison with Eqn. (B.28) gives that $J_1 = \frac{1}{E_0 \cdot \tau^\beta}$. It should not be confused with other power law models, e.g. power law relaxation defined by $R(t) = E_0\,\exp\left(\left(\frac{-t}{\tau}\right)^\beta\right)$, which yields an identical behaviour for $\beta = 1$ (the Maxwell case) only, but e.g. for $\beta \to 0$ the two models differ by a factor of 2.

by a factor of 2 (since, effectively, two springs are in series, each with the constant E_0). Fig. B.4a shows the creep compliance for various values of β.

In case of creep loading, one obtains from Eqns. (2.3) and (B.28) the creep strain

$$\varepsilon(t) \;=\; \frac{\sigma_0}{E_0}\left(1+\frac{t^\beta}{\tau^\beta}\right) \tag{B.29}$$

and upon differentiation with respect to time

$$\dot{\varepsilon}(t) \;=\; \frac{\sigma_0}{E_0}\,\frac{\beta}{\tau^\beta}\,t^{\beta-1}\;. \tag{B.30}$$

This is equivalent to

$$\log\bigl(\dot{\varepsilon}(t)\bigr) \;=\; (\beta-1)\,\log(t) \;+\; \log\Bigl(\frac{\sigma_0\,\beta}{E_0\,\tau^\beta}\Bigr)\;, \tag{B.31}$$

thus, one obtains a straight line with slope $(\beta-1)$ when the strain rate is plotted in a double-logarithmic diagram over time, see Fig. B.3. This fact is helpful for the direct determination of the material parameter β from experimental data.[4]

The relaxation modulus can be determined from the relationship $\hat{R}(s)\;\hat{J}(s) = \frac{1}{s^2}$, see Eqn. (2.17). Application of the Laplace transform to Eqn. (B.28) yields

$$\hat{J}(s) = \frac{1}{E_0}\Bigl(\frac{1}{s}+\frac{\Gamma(\beta+1)}{\tau^\beta s^{\beta+1}}\Bigr)\;, \tag{B.32}$$

and thus, the Laplace-transformed relaxation modulus is

$$\hat{R}(s) \;=\; E_0\Bigl(s+\Gamma(\beta+1)\;\tau^{-\beta}\;s^{1-\beta}\Bigr)^{-1}\;. \tag{B.33}$$

By back-transformation from the Laplace space to the original space the relaxation modulus is obtained as (see p. 316 in Bergander [1992])

$$R(t) \;=\; E_0\sum_{n=0}^{\infty}(-1)^n\frac{\Bigl(\Gamma(\beta+1)\Bigr)^n}{\Gamma(n\beta+1)}\Bigl(\frac{t}{\tau}\Bigr)^{n\beta}\;. \tag{B.34}$$

Wang [2012] points out that implementation of this equation in a computer program could cause numerical problems. By numerical examples, she confirmed that for $\beta < 0.5$ the difference between Eqn. (B.34) and the approximate form

$$R_{\text{approx}}(t) \;=\; E_0\frac{1\;+\;\Gamma(\beta+1)\,\bigl(\frac{t}{\tau}\bigr)^\beta}{1\;+\;2\,\Gamma(\beta+1)\,\bigl(\frac{t}{\tau}\bigr)^\beta\;+\;\frac{\beta\pi}{\sin(\beta\pi)}\,\Gamma(\beta+1)\,\bigl(\frac{t}{\tau}\bigr)^{2\beta}}\;, \tag{B.35}$$

[4] As becomes apparent from comparison with Eqn. (B.30), one should not confuse the PL model used here with the quite popular thermal power-law creep of the form $\dot{\varepsilon} = B\;\sigma^n\exp\bigl(-\frac{Q}{RT}\bigr)$, also known as Norton creep, where B, n, Q, and R are constants and T is the temperature, see for instance Rösler et al. [2012].

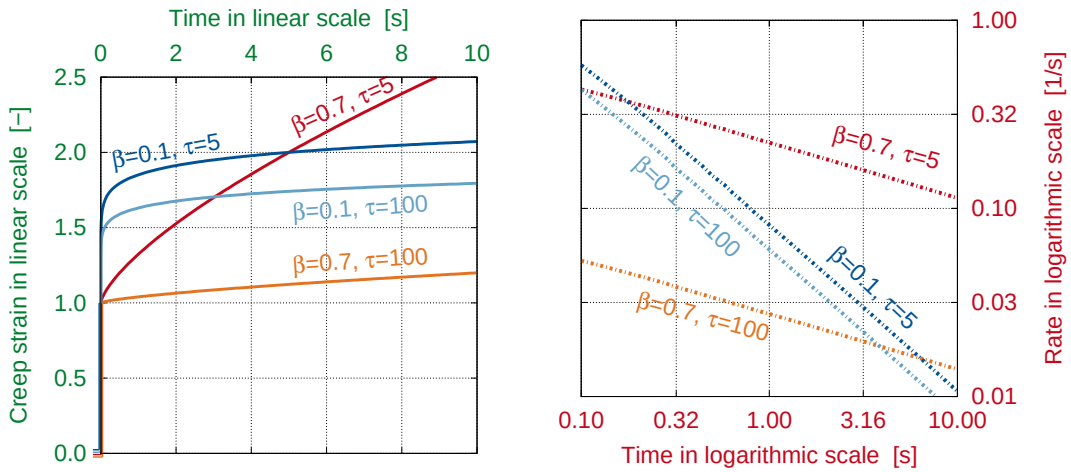

(a) Creep strain (lin-lin) (b) Strain rate (log-log)

Figure B.3.: Creep behaviour of power law model: **(a)** creep strain over time (lin-lin plot), **(b)** strain rate over time (log-log plot). For the sake of illustration $\beta = 0.1,\ 0.7$ [–] and $\tau = 5,\ 100$ [s], respectively, were chosen. Data for the creep strain created by use of the formula $\varepsilon(t) = \frac{\sigma_0}{E_0}\left(1 + \left(\frac{t}{\tau}\right)^{\beta}\right)$, where $\frac{\sigma_0}{E_0} = 1.0$ was chosen arbitrarily, and for the strain rate by finite differences.

which was presented e.g. in Nielsen [2006], is negligible.

The complex modulus is easily obtained by multiplying Eqn. (B.33) by s and substituting $s = i\omega$ as

$$R^* = E_0 \frac{i^\beta (\tau\omega)^\beta}{\Gamma(\beta+1) + i^\beta (\tau\omega)^\beta} = \frac{E_0}{1 + \Gamma(\beta+1)\,(i\tau\omega)^{-\beta}} \,. \tag{B.36}$$

The real and the imaginary parts (see Jäger and Lackner [2008]) and, from this, the loss tangent are[5]

$$\begin{aligned} R' &= E_0 \frac{(\tau\omega)^{2\beta} + (\tau\omega)^\beta\,\Gamma(\beta+1)\,\cos(\beta\frac{\pi}{2})}{(\tau\omega)^{2\beta} + 2\,(\tau\omega)^\beta\,\Gamma(\beta+1)\,\cos(\beta\frac{\pi}{2}) + \left(\Gamma(\beta+1)\right)^2} \,, \\ R'' &= E_0 \frac{(\tau\omega)^\beta\,\Gamma(\beta+1)\,\sin(\beta\frac{\pi}{2})}{(\tau\omega)^{2\beta} + 2\,(\tau\omega)^\beta\,\Gamma(\beta+1)\,\cos(\beta\frac{\pi}{2}) + \left(\Gamma(\beta+1)\right)^2} \,, \text{ and} \\ \tan\delta &= \frac{\Gamma(\beta+1)\,\sin(\beta\frac{\pi}{2})}{(\tau\omega)^\beta + \Gamma(\beta+1)\,\cos(\beta\frac{\pi}{2})} \,. \end{aligned} \tag{B.37}$$

The Cole-Cole representation of R^* is given in Fig. B.4b. The dependence of the storage modulus R' and the loss modulus R'' on the excitation frequency is shown in Fig. B.5.

[5] Alternative formulae were given by Aigner et al. [2009].

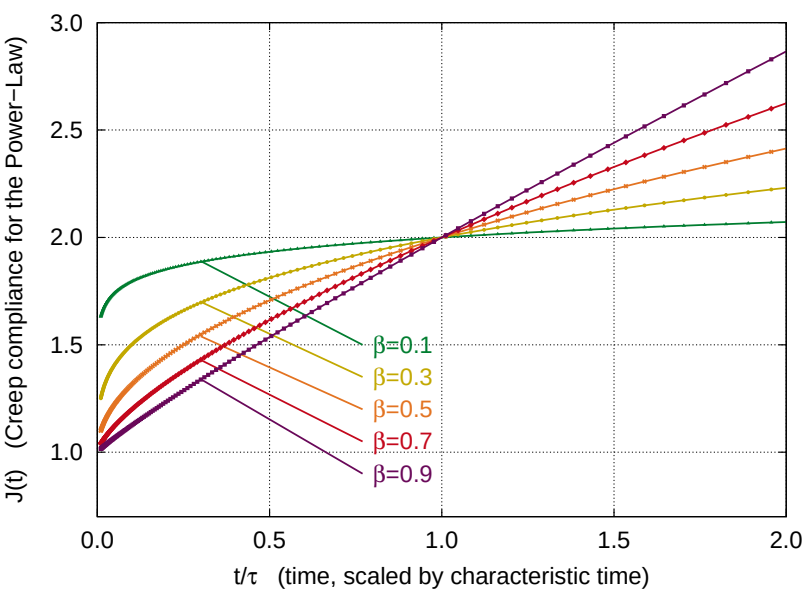

(a) Creep compliance, see Eqn. (B.28)

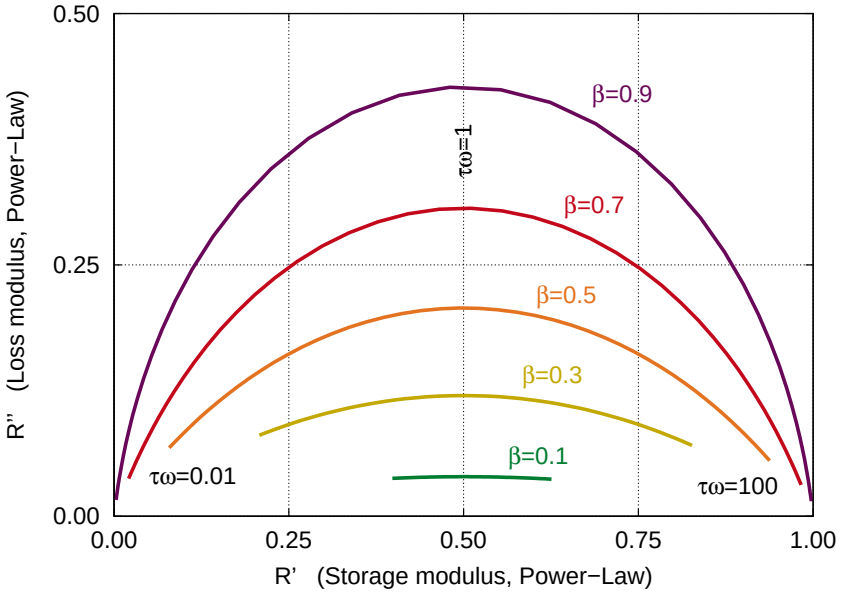

(b) Cole-Cole plot, where $\tau\omega$ is the curve parameter

Figure B.4.: Power law where $E_0 = 1$ was chosen arbitrarily: **(a)** Creep compliance over time (scaled by the characteristic time τ). **(b)** Loss modulus vs. storage modulus ("Cole-Cole diagram"). For a fast material and a slow loading (indicated by $\tau\omega = 0.01$), the storage modulus is low. In the limit $\tau\omega \to 0$, the slope is $\tan(\beta\frac{\pi}{2})$, as can be computed from the loss tangent. On the other hand, for a slow material and a rapid loading (indicated by $\tau\omega = 100$), the storage modulus approaches E_0 . In the limit $\tau\omega \to \infty$, the slope is just $\tan(2\pi - \beta\pi/2)$ due to symmetry considerations. If the loading time scale and the material time scale are close to each other, the largest losses are obtained (around $\tau\omega = 1$).

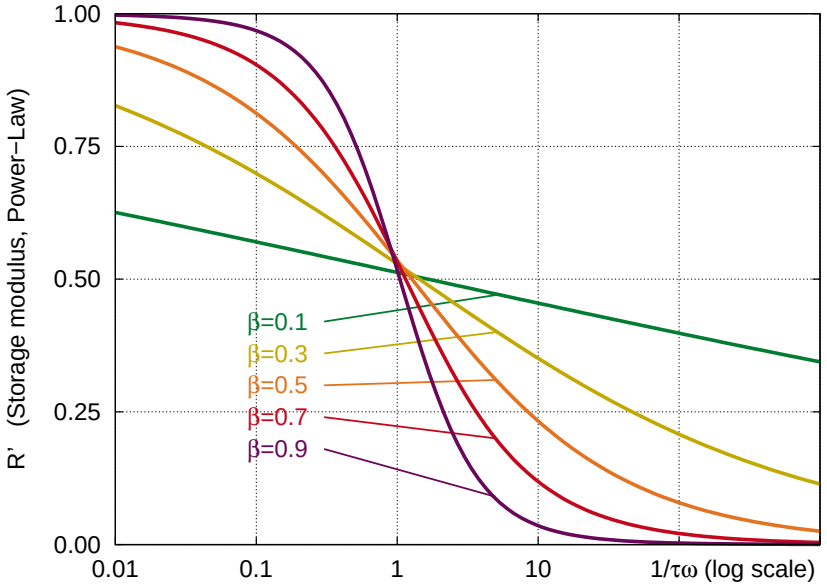

(a) Storage modulus for various values of β

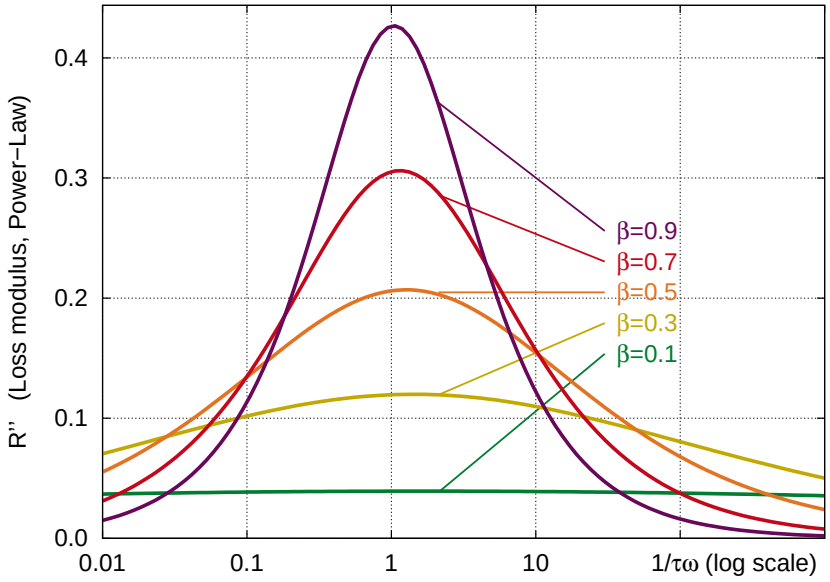

(b) Loss modulus for various values of β

Figure B.5.: Real and imaginary part of the complex modulus over dimensionless time (that is, inverse of excitation frequency scaled by the characteristic time τ) for the power law model. **(a)** Storage modulus: since the functions approach zero for a slow enough excitation frequency it is clear that this model is a fluid, just as the Maxwell model is. **(b)** Loss modulus: the larger β, the larger losses become possible.

B.4. Three-parameter square root Kelvin-Voigt model (SRKV)

The three-parameter square root Kelvin-Voigt model consists of a non-linear dashpot parallel to a linear spring, see Fig. 2.1d. While a linear dashpot shows a stress linearly related to the time derivative of the strain, in this model the square root of the physical time is used. As usual, τ is a parameter to scale the physical time, i.e. τ is large in a slowly reacting material. The non-dimensional factor $\gamma \in]0;1]$ is used to control the amount of stress flowing through the nonlinear dashpot. Thus, for $\gamma \to 0$, the behaviour becomes more and more elastic, while for $\gamma \to 1$ the instantaneous stiffness gets smaller.

The stress-strain relation in Laplace space[6] reads

$$\hat{\varepsilon}(s) \;=\; \frac{\hat{\sigma}(s)}{E_\infty}\left(1-\gamma+\gamma\,\sqrt{\pi}\;W_s\;\exp\!\left({W_s}^2\right)\;\operatorname{erfc}\!\left(W_s\right)\right)\,, \tag{B.38}$$

where $\operatorname{erfc}(z)$ is the complementary error function, see Eqn. (A.28), and for convenience the abbreviation

$$W_s \;=\; (4\,\tau\,s)^{-0.5} \tag{B.39}$$

was used.

The most convenient form to define the behaviour of the SRKV is actually the creep compliance (see Fig. B.6a for various values of γ):

$$J(t) \;=\; \frac{1}{E_\infty}\left(1-\;\gamma\,\exp\!\left(-\sqrt{t/\tau}\,\right)\right)\,. \tag{B.40}$$

For $\gamma = 1$, this definition would be identical to the well-known standard Kelvin-Voigt model if one was disregarding the use of the square root. While due to its singlet spectrum the standard Kelvin-Voigt model shows a small bandwidth of time or frequency for viscous processes, the square root form covers several decades[7], see Fig. B.7. For the SRKV, the slope of the creep compliance is infinite for $t = 0$, which is not the case in the linear Kelvin-Voigt model. However, the two models have in common that the creep is bounded with $J(t) \to 1/E_\infty$ for $t \to \infty$, thus, they describe viscoelastic solids.

[6] An analytical back-transformation of this formula seems not possible.

[7] Because the term (t/τ) is taken to the power of 0.5, whereas in the linear Kelvin-Voigt model the power is unity. The square root form is suggested in Betten [2002], who relates it to the so-called $\sqrt{t}$-law in diffusion processes (*ibid.*, pp. 207–217). On the other hand, a more flexible model may be obtained by introducing the exponent of (t/τ) as a fourth parameter $\in]0;1]$. The so-enhanced creep function would then resemble the so-called stretched exponential model $R(t) = \exp\!\left(-(t/\tau)^\beta\right)$, which is often used to describe relaxation processes, see for instance Palmer et al. [1984] or – regarding a more advanced formulation – Baeurle et al. [2005] .

By Eqn. (2.17), the Laplace-transformed relaxation modulus is obtained from the Laplace transform of Eqn. (B.40) as[8]

$$\hat{R}(s) \;=\; \frac{E_\infty}{s}\left(1-\gamma+\gamma\,\sqrt{\pi}\;\; W_s\;\; \exp\!\left(W_s{}^2\right)\;\; \mathrm{erfc}\!\left(W_s\right)\right)^{-1}\;. \tag{B.41}$$

The complex modulus is obtained from Eqns. (2.21) and (B.41) as

$$R^*(\omega) \;=\; E_\infty\left(1-\gamma+\gamma\,\sqrt{\pi}\;\; W_\omega\;\; \exp\!\left(W_\omega{}^2\right)\;\; \mathrm{erfc}\!\left(W_\omega\right)\right)^{-1}\;, \tag{B.42}$$

where $W_\omega \;=\; (i\;4\tau\omega)^{-0.5}$ is defined analogously to Eqn. (B.39). The complex modulus can be separated into the real and the imaginary part by numerical programs (MATLAB), see Figs. B.6b and B.7.

[8] An analytical back-transformation to retrieve the relaxation modulus in the time domain seems not possible. Thus, numerical schemes have to be used, as has been done in Wang [2012] for this particular model.

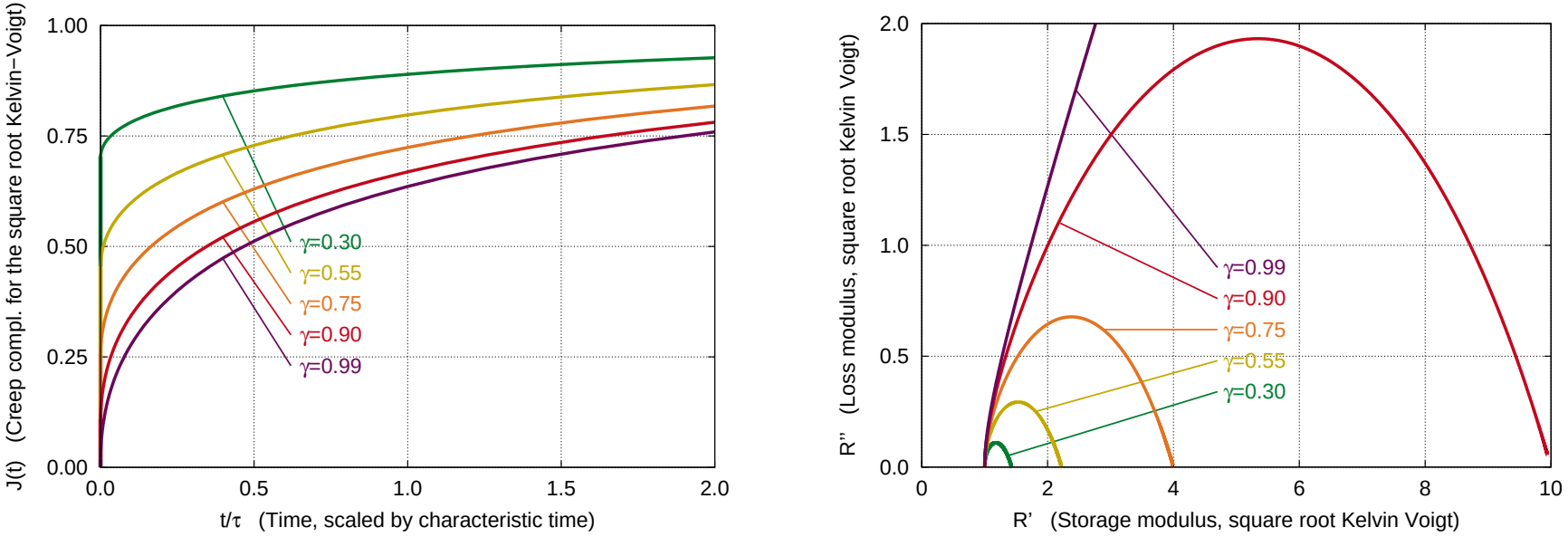

(a) Creep compliance, see Eqn. (B.40)

(b) Cole-Cole plot (numerically obtained from Eqn. (B.42))

Figure B.6.: Square root Kelvin-Voigt where $E_\infty = 1$ was chosen arbitrarily: **(a)** Creep compliance over time (scaled by the characteristic time τ). At $t = 0$, the creep compliance jumps from 0 to $(1-\gamma)/E_\infty$, thus, there exists some instantaneous stiffness. Furthermore, $J = (1-0.5\gamma)/E_\infty$ at $t/\tau \approx 0.48$, $J \approx (1-0.368\gamma)/E_\infty$ at $t/\tau = 1$, and $J = 1/E_\infty$ for $t/\tau \to \infty$. **(b)** Cole-Cole plot. For a very slow loading (where $1/\tau\omega \to \infty$), the curves coincide ($R' \to E_\infty$ and $R'' \to 0$), while $R' \to E_\infty/(1-\gamma)$ for $\tau\omega \to \infty$. For comparison, the complex modulus of the linear Kelvin-Voigt model is $R^*(\omega) = E_\infty + i\eta\omega$, such that the Cole-Cole plot would be just a vertical line since here the storage modulus will not depend on the frequency.

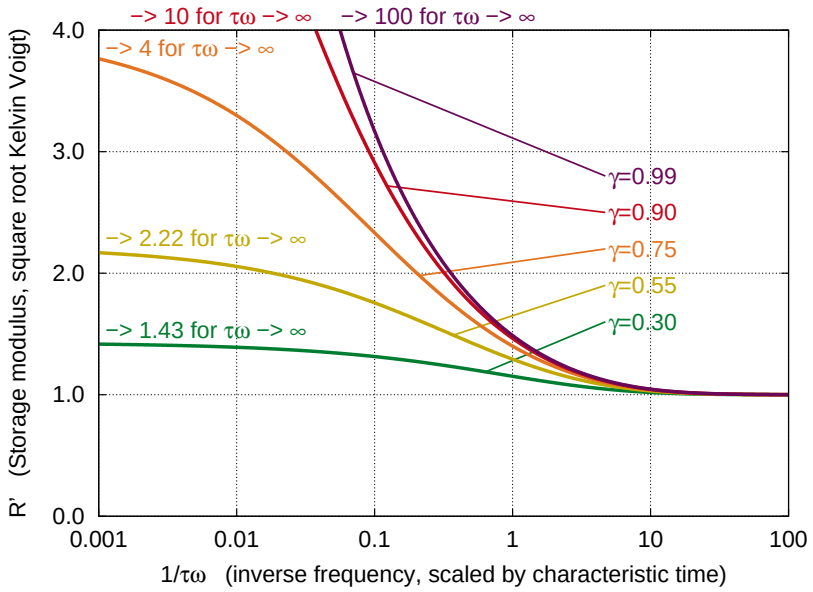

(a) Storage modulus for various values of γ

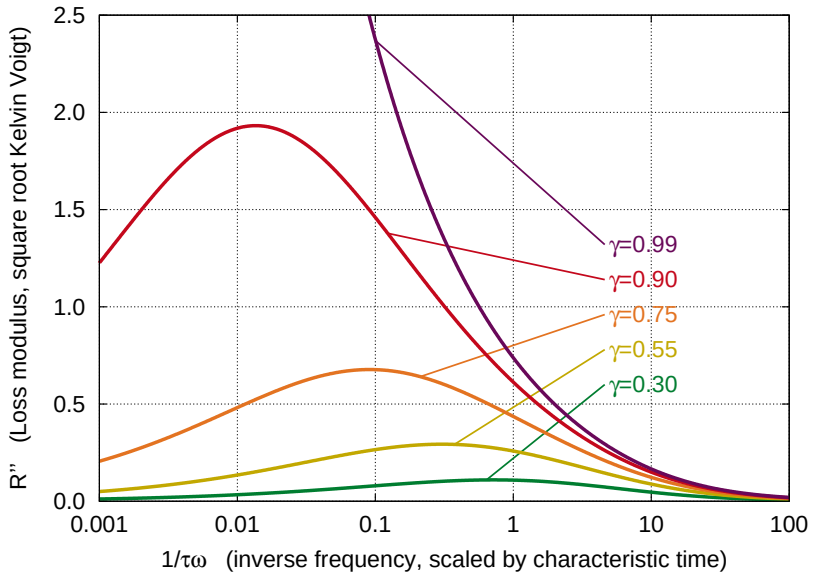

(b) Loss modulus for various values of γ

Figure B.7.: Square root Kelvin-Voigt model: Real and imaginary part of the complex modulus over inverse of excitation frequency (scaled by the characteristic time τ). **(a)** Storage modulus: the slower the excitation frequency is, the more approaches the stiffness the value E_∞. It is obvious that this model represents a solid. **(b)** Loss modulus: the larger γ is, the larger losses are possible.

B.5. Logarithmic creep (LOG)

The logarithmic creep[9] model, see Fig. 2.1e, is a modification of the MX model where the linear dashpot is replaced by a logarithmic dashpot. Moreover, a scalar factor λ between 0 and ∞ is introduced, relating the time-dependent answer to the instantaneous stiffness.

The creep compliance is defined as

$$J(t) \;=\; \frac{1}{E_0}\left(1+\;\lambda\,\ln\!\left(1+\frac{t}{\tau}\,\right)\right)\,, \tag{B.43}$$

see Fig. B.9a for an illustration.

The Laplace-transformed creep compliance reads

$$\hat{J}(s) \;=\; \frac{1-\;\lambda\,\exp(\tau s)\,\mathrm{Ei}(-\tau s)}{s\,E_0}\quad, \tag{B.44}$$

where $\mathrm{Ei}(x)$ is the exponential integral (see Eqn. (A.23)).

When considering creep, the combination of Eqns. (2.3) and (B.43) yields

$$\varepsilon(t) \;=\; \frac{\sigma_0}{E_0}\left(1+\;\lambda\,\ln\!\left(1+\frac{t}{\tau}\,\right)\right)\,, \tag{B.45}$$

which gives, performing differentiation w.r.t. time, just

$$\dot{\varepsilon}(t) \;=\; \frac{\sigma_0}{E_0}\,\frac{\lambda}{\tau+t}\;. \tag{B.46}$$

This is equivalent to

$$\log\!\left(\dot{\varepsilon}(t)\right) \;=\; \log\!\left(\sigma_0\right)+\log\!\left(\frac{\lambda}{E_0}\right)-\log\!\left(\tau+t\right)\,, \tag{B.47}$$

where the first term of the RHS is known in a laboratory experiment and the last term can be simplified as $\log\left(t\right)$ for $t \gg \tau$. Thus, when a log-log plot (see Fig. B.8) is used to draw the displacement rate over physical time, one will obtain a straight line with a slope of -1 for large values of time. If a reference line passing through $(1|1)$ with the same slope is included in the diagram, the vertical distance between the straight part of the displacement rate and the reference line is just $\log\left(\sigma_0\right)+\log\left(\lambda/E_0\right)$, from which the ratio λ/E_0 can be obtained.[10]

[9] The observation of logarithmic creep in a variety of different solids can be explained by the so-called exhaustion theory which is based on the assumption that different elements of the specimen start to flow at different activation energies, but after they have contributed to the overall creep deformation they are used up, which is why with the passage of time there are fewer and fewer elements flowing (see for instance Cottrell [1997] and Cottrell [1952]).

[10] Of course, the same units have to be used for σ_0 and E_0. Also, note that a *negative* number has to be used for the distance if the strain rate data lies *below* the reference line.

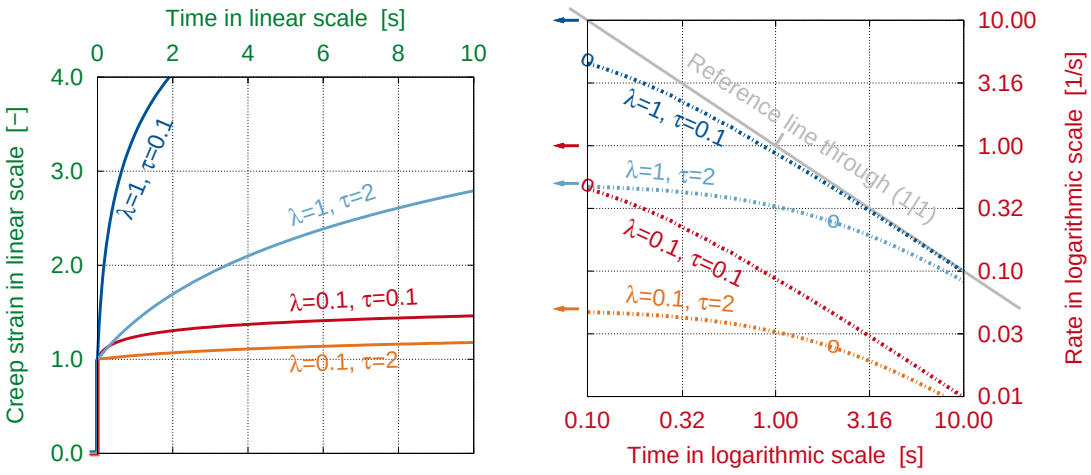

(a) Strain (lin-lin) (b) Strain rate (log-log)

Figure B.8.: LOG model under creep. **(a)** Creep strain over time (lin-lin plot), **(b)** strain rate over time (log-log plot), where the rate at $t=\tau$ is indicated by circles and for the limit $\tau \to 0$ by arrows. For the sake of illustration $\lambda = 0.1,\ 1$ [–] and $\tau = 0.1,\ 2$ [s], respectively, were chosen. Data for the creep strain created by use of the formula $\varepsilon(t) = \frac{\sigma_0}{E_0}\left(1 + \lambda \ln\left(1 + \frac{t}{\tau}\right)\right)$, where $\frac{\sigma_0}{E_0} = 1.0$ was set arbitrarily, and for the strain rate by finite differences.

Also, from Eqn. (B.46) one readily notices that at $t=\tau$ the rate will have exactly half the value of the rate for $t \to 0$ (as indicated in Fig. B.8), which may be helpful in order to determine the characteristic time. However, in practice, this task may become difficult since τ usually is quite small and the reliability of data for $t \leq \tau$ is affected by the mode of application of the creep load. Thus, τ should be determined from an impact experiment.

Using Eqns. (2.17) and (2.21), the complex modulus is obtained from Eqn (B.44) as

$$R^*(\omega) \;=\; E_0 \left(1 - \lambda \exp(i\omega\tau)\, \mathrm{Ei}(-i\omega\tau)\right)^{-1} \quad . \tag{B.48}$$

The corresponding Cole-Cole diagram is given in Fig. B.9b, while Fig. B.10 shows the dependence of the storage and loss modulus, respectively, on the excitation frequency.

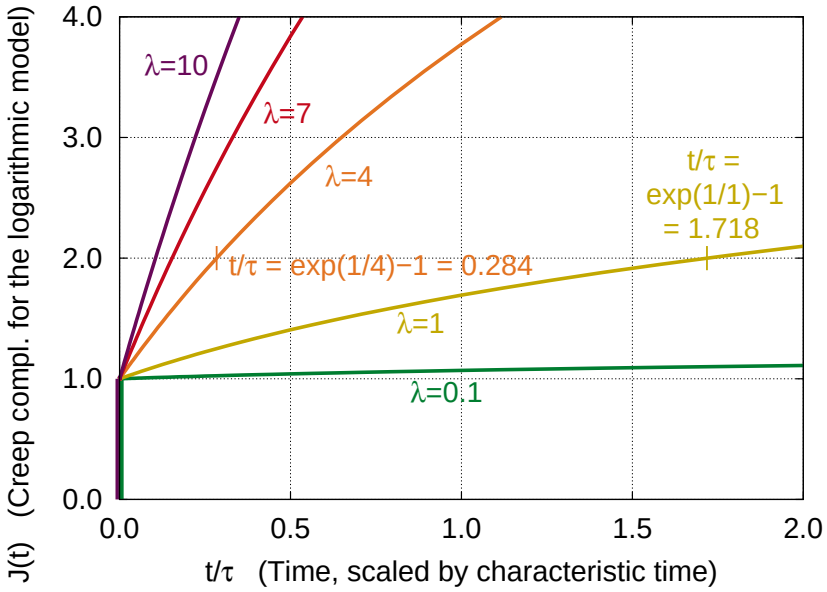

(a) Creep compliance, see Eqn. (B.43)

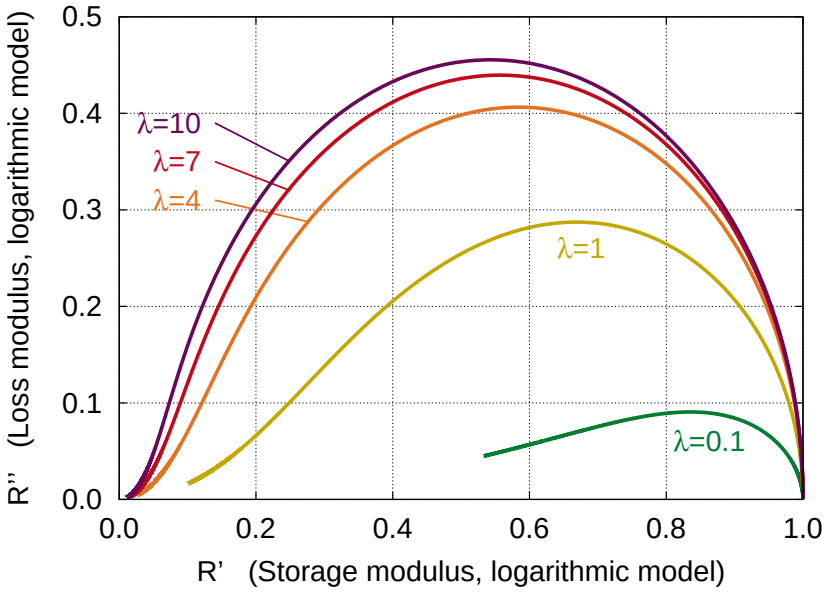

(b) Cole-Cole plot (numerically obtained from Eqn. (B.48))

Figure B.9.: Logarithmic creep for arbitrarily chosen $E_0 = 1$: **(a)** Creep compliance over time (scaled by the characteristic time τ). $J(t)$ becomes twice the initial value at the time instant $t/\tau = \exp(1/\lambda) - 1$. **(b)** Cole-Cole plot for the excitation frequency range from $\tau\omega = 10^{-4}$ (left end of the curves) to 10^4 (right end, $R' = E_0$).

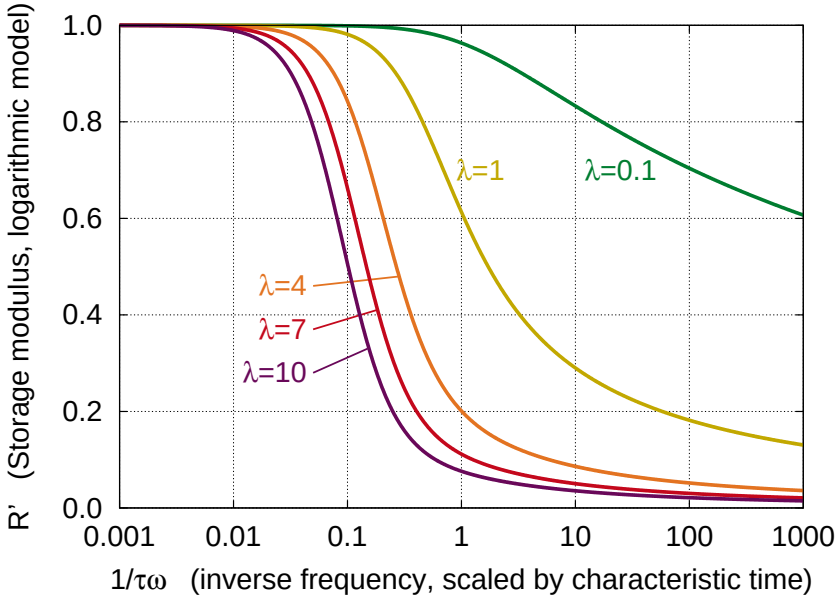

(a) Storage modulus for various values of λ

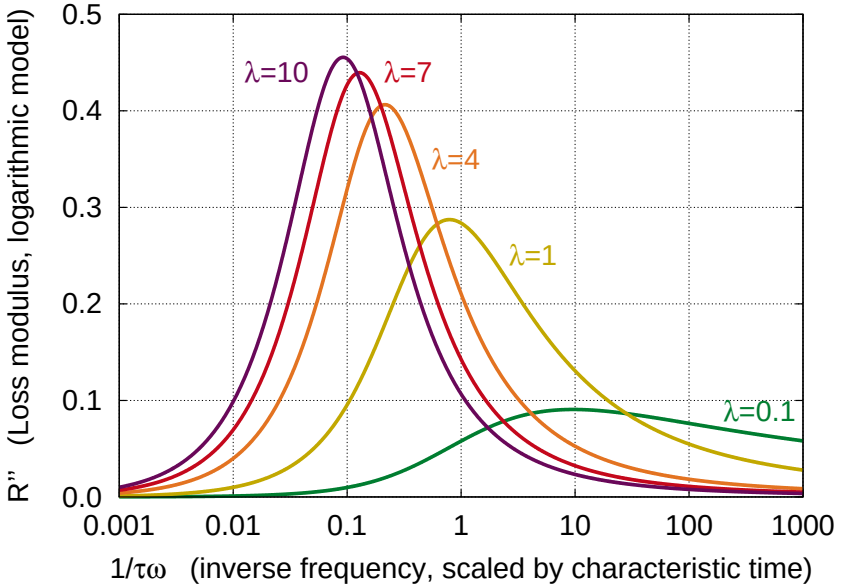

(b) Loss modulus for various values of λ

Figure B.10.: Real and imaginary part of the complex modulus over dimensionless time (that is, inverse of excitation frequency scaled by the characteristic time τ) for the logarithmic creep. **(a)** Storage modulus: It is obvious that this model represents a fluid. **(b)** Loss modulus: the larger λ is, the larger losses are possible.

C. Dimensional analysis

Wer also bei einem Riesen die gewöhnlichen Verhältnisse beibehalten wollte, müsste entweder festere Materie finden, oder er müsste verzichten auf die Festigkeit, und den Riesen schwächer als Menschen von gewöhnlicher Statur werden lassen; bei übermässiger Grösse müsste er durch das Eigengewicht zerdrückt werden und fallen [...] Daher glaube ich, würde ein kleiner Hund zwei oder drei andere von gleicher Grösse tragen können, während ein Pferd wohl kaum im Stande wäre, auch nur ein einziges Pferd auf seinem Rücken zu tragen.

GALILEI [1995], p. 109

The basic idea of dimensional analysis is that the physical laws do not depend on the arbitrariness in the choice of units of physical quantities. This concept often allows the number of arguments in functions describing physical phenomena to be reduced, thus making them simpler to obtain either from calculations or experiments.

CHENG AND CHENG [2004]

For the description of a certain mechanical problem, the governing parameters have to be identified and their interrelation has to be modelled by mathematical equations of the format

$$x_0 = f(x_1, x_2, \ldots, x_n) \ , \tag{C.1}$$

where x_0 is the dependent quantity of interest (output variable) and x_i ($i = 1..n$) make up a complete set of physically independent input variables[1]. To this end, the application of

[1] The term "complete" requires that x_0 does not depend on any other quantities than x_1 to x_n, and "physically independent" means that one input quantity does not affect the value of an other one.

dimensional analysis may help in two ways: first, *a priori* knowledge on the interrelation between the input parameters helps to reduce the number of laboratory experiments or numerical simulations necessary to establish a relationship in the form of Eqn. (C.1); second, dimensional results can be transformed into generally valid relationships between dimensionless input and output quantities. In the present work, the latter point was intensively used in order to generate master curves for the impact of a sphere on a viscoelastic medium.

Thus, in this chapter the principal procedure of dimensional analysis[2] is sketched. Then, an example is given where the equation for the Hertzian penetration depth is developed; finally, it is shown how a master curve is constructed graphically by the use of dimensionless parameters on the diagram's axes.

C.1. Principal idea and procedure

The physical character of a quantity x is revealed by its dimension (denoted by $\dim x$). It is independent of the chosen system of units for measurement and computation. For instance, the dimension of the impactor radius is the length L, the dimension of the impactor's mass is the mass M, and the dimension of the contact duration is the time T. In Newtonian mechanics, to which attention is restricted, these three dimensions make up an independent set on which all other dimensions depend; e.g. the dimension of a force F is expressed by

$$\dim F = \mathsf{M}^{+1}\,\mathsf{L}^{+1}\,\mathsf{T}^{-2} \,. \tag{C.2}$$

The key idea of dimensional analysis is that the yet unknown functional relationship of Eqn. (C.1) can be expressed in a dimensionless format

$$\Pi_0 = f_{\mathrm{dl}}\left(\Pi_1, \Pi_2, \cdots, \Pi_{n-r}\right) \,, \tag{C.3}$$

where Π denotes a dimensionless product of the governing parameters, i.e.

$$\dim \Pi = 1 \,. \tag{C.4}$$

By going from Eqn. (C.1) to Eqn. (C.3), the number of arguments of the function on the RHS was reduced by r, which is the number of dimensionally independent variables in the original equation. Thus, in Newtonian mechanics, $r \leq 3$.

[2] For literature, see e.g. Buckingham [1914], Cheng and Cheng [2004], Gibbings [1986], Goodier [1950], Jones [1989], Lu and Yu [2003], Misic et al. [2010], Montgomery [2005], Palacios [1964], Rayleigh [1915], or Young [1971].

	Quantity	M	L	T
x_1	Sphere's radius R	0	1	0
x_2	Young's modulus E	1	-1	-2
x_3	Poisson's ratio ν	0	0	0
x_4	Contact force F_h	1	1	-2

Table C.1.: Complete set X_n of four independent quantities related to x_0 (penetration depth u_h in the Hertz problem of a rigid sphere pressed on an elastic half-space).

Procedure. A dimensional analysis consists of the following steps:

1. Identify X_n, by which the complete set of the n physically independent (but, possibly, dimensionally dependent) input variables x_i is denoted on which the quantity of interest x_0 depends. For each x_i note down its dimension.
2. From this set, choose a subset $X_r \subseteq X_n$ of $r \leq n$ dimensionally independent quantities. The remaining $p = n - r$ quantities belong to the subset $X_p \stackrel{\text{def}}{=} X_n \setminus X_r$.
3. For each $x_i \in X_p$ as well as for x_0, find a combination with all parameters $x_j \in X_r$ (or rather powers of x_j) such that their product Π_i is dimensionless.
4. These $p+1$ dimensionless quantities Π_i make up Eqn. (C.3). Obviously, this is not a unique result, as a new dimensionless quantity can be built from two or more dimensionless quantities defined earlier; however, one of them has then to be discarded such that the number of variables in Eqn. (C.3) stays constant.

C.2. Example: Hertz contact problem

As an example, consider the Hertzian contact of a rigid sphere and an elastic half-space (see Subsection 2.5.3) where the penetration depth shall be related to the applied force, the sphere's radius and material properties of the half-space.

1. The penetration depth x_0 depends on the $n = 4$ parameters listed in Table C.1.
2. Choose $\dim x_1$ ("length") and $\dim x_4$ ("force") as independent dimensions, i.e. $r = 2$. Thus, X_p consists of $p = 4 - 2 = 2$ quantities, viz. x_2 and x_3.

3. Construction of $p+1=3$ dimensionless quantities:

$$\Pi_0 = x_0 \cdot (x_1)^{-1} \cdot (x_4)^0 = \frac{u_\mathrm{h}}{R} \tag{C.5}$$

$$\Pi_1 = x_2 \cdot (x_1)^2 \cdot (x_4)^{-1} = \frac{E\,R^2}{F_\mathrm{h}} \tag{C.6}$$

$$\Pi_2 = x_3 \cdot (x_1)^0 \cdot (x_4)^0 = \nu \tag{C.7}$$

4. The physical relation is thus expressed by these 3 dimensionless products as

$$\Pi_0 = f_\mathrm{dl}\left(\Pi_1, \Pi_2\right) \text{ , i.e. } \quad \frac{u_\mathrm{h}}{R} = f_\mathrm{dl}\left(\frac{E\,R^2}{F_\mathrm{h}}, \nu\right) . \tag{C.8}$$

   To show that the obtained relation is not unique, a modified dimensionless parameter $\Pi_{1\mathrm{mod}} = (\Pi_1)^{-1} \cdot (\Pi_0)^{-2}$ is constructed; now,

$$\Pi_0 = f_\mathrm{dlmod}\left(\Pi_{1\mathrm{mod}}, \Pi_2\right) \text{ yields } \quad \frac{u_\mathrm{h}}{R} = f_\mathrm{dlmod}\left(\frac{F_\mathrm{h}}{E\,{u_\mathrm{h}}^2}, \nu\right) , \tag{C.9}$$

   where the function f_dlmod is different from the previously used function f_dl.

The true relation for the penetration (cf. Eqn. (2.58)) reads

$$\Pi_0 = C_0 \left(\Pi_1\right)^{-2/3} \left(1 - \left(\Pi_2\right)^2\right)^{+2/3} \tag{C.10}$$

or, when $\Pi_{1\mathrm{mod}}$ is used instead of Π_1,

$$\Pi_0 = C_{0\mathrm{mod}} \left(\Pi_{1\mathrm{mod}}\right)^{-2} \left(1 - \left(\Pi_2\right)^2\right)^{-2} , \tag{C.11}$$

where the constant $C_0 = 0.825$ (or $C_{0\mathrm{mod}} = 1.778$, respectively) and the exponents of the dimensionless parameters have to be found by physical experiments and/or numerical simulations. This might seem tedious, as Π_2 is involved in a somewhat complex manner; however, the effort is still substantially reduced compared to the dimensional point of view, where five quantities have to be related to each other.

C.3. Master Curves

A master curve can be used for the compact graphical representation of a physical relationship, because this curve is usually obtained by mapping several response curves through

suitable scaling relations[3]. Hence, the application of dimensional analysis is helpful in order to construct master curves, as it reduces the number of parameters, thus leading to the compact format.

To show this, consider the example of 1-D tension bars with linear behaviour, where the problem parameters are the applied force F, Young's modulus E, the cross section area A, the initial length L, and the current length l. Fig. C.1 shows how the measured data (e.g. from a physical experiment or a numerical simulation) can be transformed into dimensionless quantities leading to a simple graph. In this example, due to the low complexity of the dimensionless master curve, even the mathematical formulation of a general law is easily established from the two observations that:

- the dimensionless stress $\Pi_\sigma = \frac{\sigma}{E}$ (where $\sigma = \frac{F}{A}$) is proportional to the strain $\Pi_\varepsilon = \varepsilon = \frac{\Delta l}{L}$ (where $\Delta l = l - L$), and
- the factor of proportionality is one.

From this, Hooke's law $\Pi_\sigma\left(\frac{F}{EA}\right) = \Pi_\varepsilon\left(\frac{l-L}{L}\right)$, or $\sigma = E\varepsilon$, and thus

$$F = \frac{EA}{l}\,\Delta l \tag{C.12}$$

is constructed, which is valid for the linear range of 1-D tension/compression problems.

[3] As an example, in material mechanics the term master curve is often associated with the time-temperature equivalence of thermorheologically simple materials (see, for instance, Williams et al. [1955] or any textbook on viscoelastic materials), whence e.g. short-time relaxation experiments conducted at elevated temperature can be treated as if the experiment had been performed at reference temperature but with a longer duration (or smaller relaxation time).

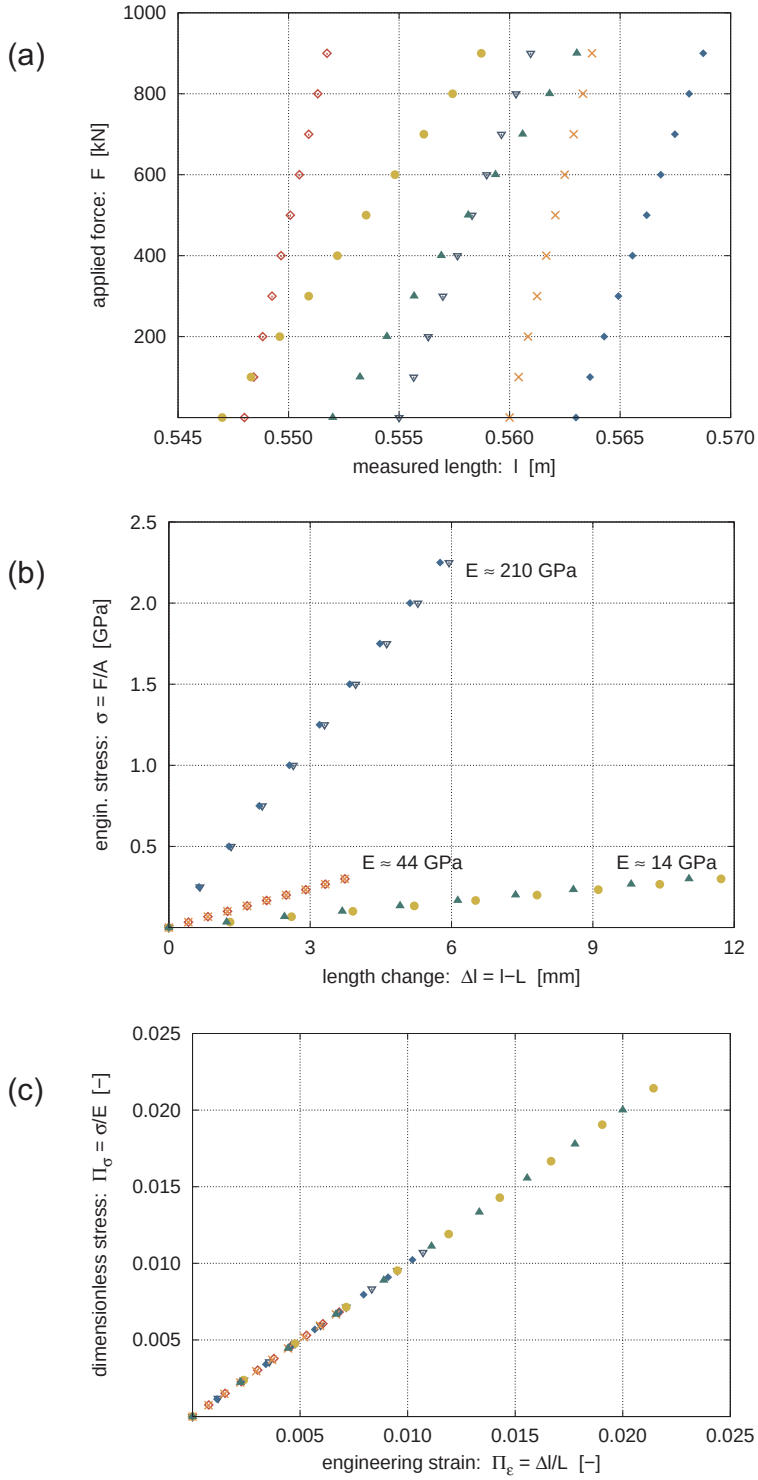

Figure C.1.: **(a)** Applied force F and measured length l for six rods of different Young's modulus E, initial cross section area A and initial length L under 1-D tension loading. **(b)** Computed engineering stress $\sigma = \frac{F}{A}$ versus computed length change (displacement) $\Delta l = l - L$. **(c)** Dimensionless stress $\Pi_\sigma = \frac{\sigma}{E}$ versus engineering strain $\Pi_\varepsilon = \frac{\Delta l}{L}$, where data points fall onto a single master curve.

D. Structural optimisation

Es gibt nix Bessers wie was Guats.

SPRICHWORT

Structural optimisation[1] is the discipline where one seeks to methodically improve the parametric response of a structure subjected to static or transient loads by changing the structural design. The criterion to be optimised is called objective function. In the following, this function is assumed to be *minimised*. This can always be accomplished by multiplying maximum objectives by -1.

In structural optimisation, an iterative scheme is usually employed, where, based on current information, the design space is explored in order to find a better solution. This is necessary because the relation between design variables and objective function is in general unknown. However, the master curves derived in the present work for the spherical impact on a viscoelastic half-space give an exact relationship between loading and material parameters on one hand and the maximum penetration, final velocity, and maximum acceleration on the other hand, such that optimal design parameters can be determined graphically depending on the objective function. However, when two or more conflicting objectives are to be minimised, a compromise has to be found. This subject is illustrated in the next section.

Moreover, in Section D.2 the multiscale topology optimisation of a poroelastic structure is briefly addressed since this subject can be combined with the macroscopic impact investigations presented here, resulting in a two-stage optimisation framework for spherical impact on poroelastic materials.

[1] A comprehensive list of references is out of scope of this work. The literature used here comprises Collette and Siarry [2003], Eschenauer et al. [1990], Eschenauer et al. [1997], Haftka and Gürdal [1992], Jurecka [2007], Kirsch [1993], and Vanderplaats [1984].

D.1. Multi-objective optimisation

If there are several objective functions $f_1, f_2, \ldots, f_n$ which are to be minimised, a trade-off between the individual criteria has to be sought, since the objective functions usually conflict with each other. This dilemma can be solved by identifying one of the objectives as the most important one and re-modelling the other ones as inequality constraints. Alternatively, one may assign a positive weight w_i to each objective. Then, a single objective

$$F(\mathbf{x}) \stackrel{\text{def}}{=} \sum_{i=1}^{n} w_i f_i(\mathbf{x}) \text{ , where } 0 \le w_i \le 1 \text{ and } \sum_{i=1}^{n} w_i = 1 \text{ ,} \tag{D.1}$$

can be constructed with the optimal solution $\mathbf{x}^*$ depending on the chosen weights.

As an example, consider the two objective functions

$$f_1(x) = 0.5x^2 + 0.8 \text{ and } f_2(x) = 0.3(x-2)^2 + 2.2 \tag{D.2}$$

depending on one design variable x. The respective optima are $f_1^* \stackrel{\text{def}}{=} f_1(x_1^*) = 0.8$ at $x_1^* = 0$ and $f_2^* \stackrel{\text{def}}{=} f_2(x_2^*) = 2.2$ at $x_2^* = 2$. The weighted objective $F(x)$ is shown in Fig. D.1a for different weighting factors, where $w \stackrel{\text{def}}{=} w_1 = 1 - w_2$ was used. The optimal value for the design variable can be computed in terms of w:

$$\left.\frac{\partial F(x,w)}{\partial x}\right|_{x^*} \stackrel{!}{=} 0 \;\Rightarrow\; x^*(w) = \frac{6-6w}{3+2w} \text{ , e.g. } x^*(0) = 2 \text{ and } x^*(1) = 0 \text{ .} \tag{D.3}$$

Table D.1 gives an overview on the interrelations between the optimal design variable x^*, the weight w, the individual objectives f_1 and f_2, the minimum of the weighted objective F^*, and the individual distances d_1, d_2. Here, the normalised distance is defined as

$$d_i(x) = \frac{f_i(x) - f_i^*}{f_i^*} \text{ ,} \tag{D.4}$$

where care should be taken to not divide by zero.

As is evident, the choice for the best w is not unique. Usually, w is a minimiser of either the L_2 norm[2] of the normalised distances:

$$\min \left[\sum_{i=1}^{n} \big(d_i(x)\big)^2 \right]^{0.5} \text{ ,} \tag{D.5}$$

or of the L_∞ norm (Tchebychev distance)[3], i.e. the optimisation problem

$$\min \max_i \big(d_i(x)\big) \tag{D.6}$$

is solved.

[2] See the dotted line in Fig. D.1b: the analytical solution is $w^* = 0.623$, $x^* = 0.532$, and $F^* = 1.659$

[3] See the intersection of d_1 and d_2 at $x^* = 0.637$ in Fig. D.1b whence $w^* = 0.526$, and $F^* = 1.771$ are obtained.

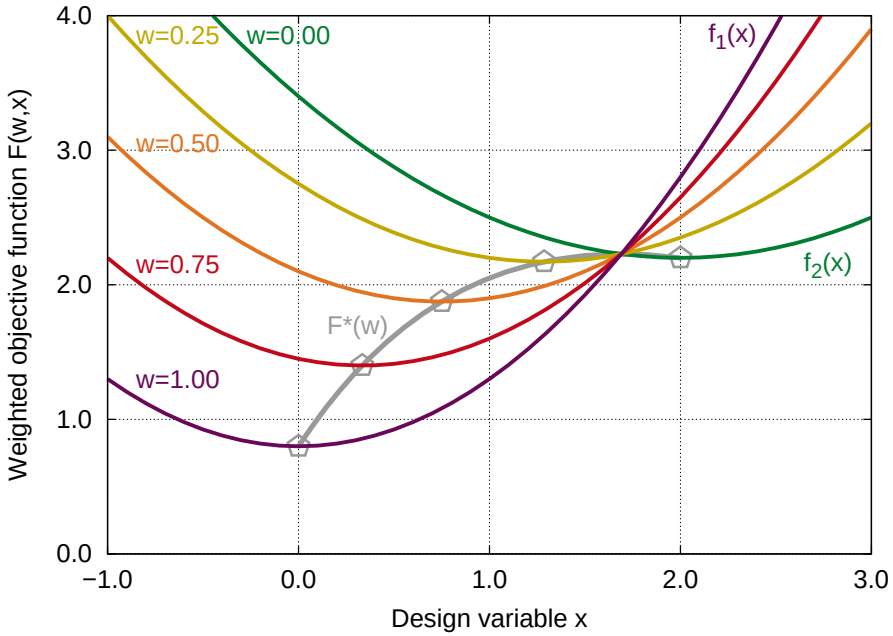

(a) Effect of different weights

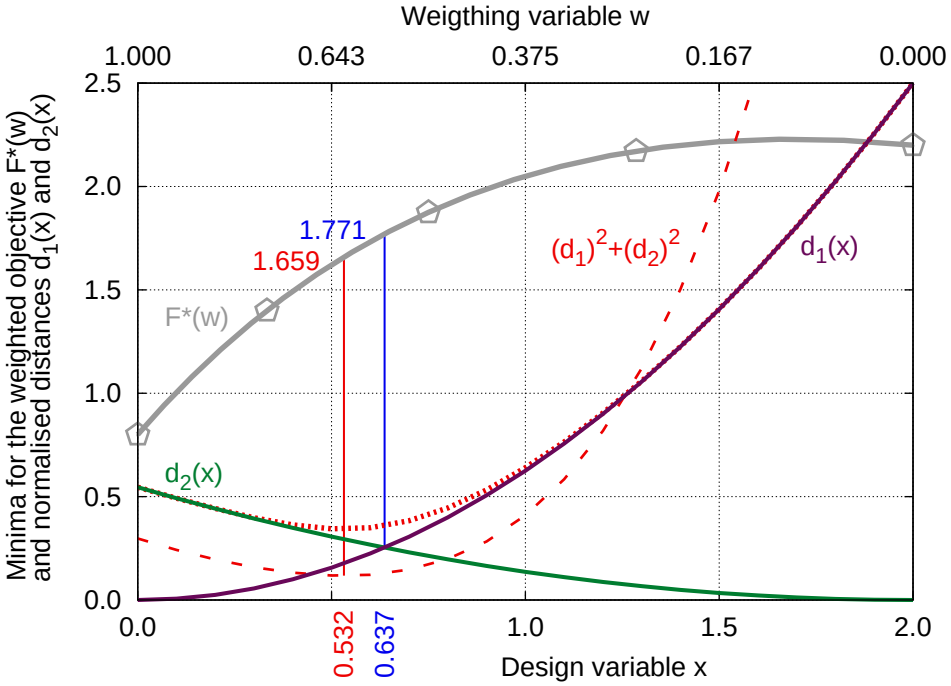

(b) Weighted objective $F^*(w)$ and normalised distances $d_1(x)$ and $d_2(x)$.

Figure D.1.: Effect of weighting using the two objective functions from Eqn. (D.2): **(a)** Influence of weighting factor w on F, where the respective minima are indicated by the line $F^*(w)$. **(b)** Normalised distances d_1 and d_2, the sum of the squared distances (dashed line) and the square root of the sum (dotted line, L_2 norm), from both of which $x^* = 0.532$ is obtained as optimal location. On the other hand, when the min-max criterion is used, x^* is located at the intersection of d_1 and d_2 at 0.637.

w	**0.000**	0.125	0.250	0.375	0.500	0.625	0.750	0.875	**1.000**
$x^*(w)$	2.000	1.615	1.286	1.000	0.750	0.529	0.333	0.158	0.000
$f_1(x^*)$	2.800	2.105	1.627	1.300	1.081	0.940	0.856	0.812	**0.800**
$d_1(x^*)$	2.500	1.631	1.033	0.625	0.351	0.175	0.069	0.016	**0.000**
$f_2(x^*)$	**2.200**	2.244	2.353	2.500	2.669	2.849	3.033	3.218	3.400
$d_2(x^*)$	**0.000**	0.020	0.070	0.136	0.213	0.295	0.379	0.463	0.545
$F^*(w)$	2.200	2.227	2.171	2.050	1.875	1.656	1.400	1.113	0.800

Table D.1.: Influence of the weighting factor w on the optimal value for design variable x^* and the minimum of the weighted function F^*. Also, for each $x^*(w)$, the two objectives f_1, f_2 and their normalised distances d_1, d_2 are evaluated. It is evident that always at least one w can be found for which the corresponding F^* is larger than for the "no compromise" decisions $w=0$ and $w=1$.

Plotting f_2 in terms of f_1, a smooth line in the space of objective functions is obtained. In Fig. D.2, the thick line between the single-objective optima marks the so-called Pareto front or functional efficient edge. Outside the Pareto front, i.e. for $w \ni [0;1]$, one can always improve the value of one objective function without deteriorating the other objective. For more than two objectives, this statement holds analogously.

Fig. D.2 shows the optima according to the L_2 and the L_∞ norm, respectively, in the objective function space. Alternatively, one could use the space of normalised distances (i.e. d_2 vs. d_1). Then, the L_2 optimum is graphically detected by the smallest circle around the origin[4] touching the graph, and the slope to locate the L_∞ optimum is equal to unity.

[4] It is assumed that the demand levels are the respective minima, thus, $d_i = 0$.

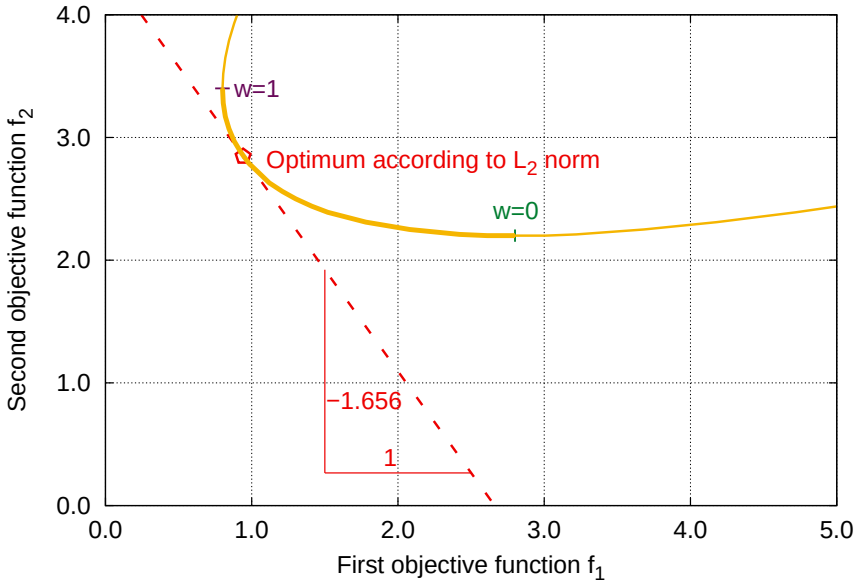

(a) Detection of optimum from the L_2 norm

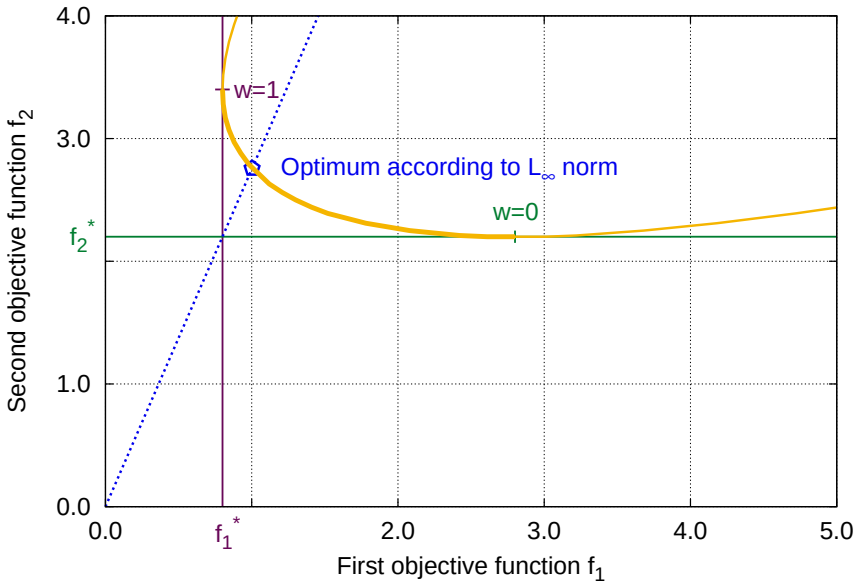

(b) Detection of optimum from the L_∞ norm

Figure D.2.: The objective function space: the Pareto front is marked by the thick line between $w=0$ and $w=1$. Since w is a curve parameter, the choice for w defines uniquely the values for f_1 and f_2. Graphically, the point $(f_1|f_2)$ can be determined by the tangent to the Pareto front with the slope $\frac{-w^*}{1-w^*}$, as is demonstrated by the dashed line in the upper plot. **(a)** Optimum according to Eqn. (D.5): $f_1^* = 0.941$, $f_2^* = 2.846$. Also, $w^* = 0.623$, thus the tangent has a slope of -1.656. **(b)** Optimum using Eqn. (D.6): $f_1 = 1.003$, $f_2 = 2.758$. The dotted line has a slope of $f_2^*/f_1^* = {}^{2.2}/_{0.8} = 2.75$. Also, the vertical tangent (infinite slope, since $w = 1$) to the Pareto front indicates the f_1^* optimum, while the horizontal tangent (zero slope from $w = 0$) marks the f_2^* optimum.

D.2. Multiscale topology optimisation of a saturated poroelastic structure

In this research project, a collaboration with the Department of Mechanical Engineering, section of Solid Mechanics[5] at the Technical University of Denmark was established within the framework of IGSSE[6] and DCAMM[7]. One of the applications investigated by the former Ph.D. student Casper Schousboe Andreasen is the topology optimisation of a poroelastic impact absorber, as reported in Andreasen [2011] and Andreasen and Sigmund [2013]. This subject shall be shortly sketched in the following.

In this problem, the topological design of a cuboid-shaped impact absorber (plane strain conditions) shall be optimised. Five faces of the cuboid have sealed boundary conditions and fixed displacements, while the surface consists of two permeable parts and a sealed load part (uniform pressure applied). The aim is to approximate a desired time-dependent function for the displacement under the load in the best possible manner by a proper material distribution in the design space. The impact absorber consists of a fluid-saturated pore structure which is divided into periodic unit cells. The incompressible Navier-Stokes equations apply to the Newtonian fluid part, while the solid skeleton is subject to elastostatic equilibrium (Navier-Cauchy equations). The unit cell has a density[8] ρ ranging from 0 (no solid material, only fluid) to 1 (all space is occupied by solid material).

As multiscale approach, a two-scale asymptotic expansion (cf. Bensoussan et al. [1978] and Sanchez-Palencia [1980]) is chosen. The idea is that any relevant function is slowly varying on the macroscale x (length scale L) but rapidly on the microscale $y = \epsilon^{-1}x$ (length scale l), where $\epsilon \stackrel{\text{def}}{=} l/L \ll 1$ has to be small enough such that the scales are separable. The problem variables (viz. the solid displacement, the fluid velocity and the fluid pressure) are expanded and inserted in the governing equations. Then, the orders are separated, i.e. terms with equal powers of ϵ are collected.

Under certain assumptions not further specified here, a set of equations for the macroscopic description is obtained as well as one for the microstructure behaviour, where the latter is

[5] Directed by Ole Sigmund, www.topopt.dtu.dk

[6] International Graduate School of Science and Engineering, www.igsse.tum.de

[7] Danish Center for Applied Mathematics and Mechanics, www.dcamm.dk

[8] ρ should be considered as relative amount of solid material, not as mass density, as inertia effects are neglected in this problem.

used to generate design interpolation functions: by a series of Finite Element simulations with periodic boundary conditions applied, homogenised values (for the macroscopic stiffness tensor, the pressure coupling coefficient, the microstructure compressibility, and the permeability) are computed for the unit cell for discrete values of the solid density[9]. They are interpolated by a curve fitting[10], i.e. a smooth non-linear relation between the design variable ρ and the effective properties is obtained.

The received macroscopic model is equivalent to Biot's phenomenologically motivated consolidation theory (Biot [1941]). The unknown state variables are the solid displacement and the pressure. Now, the macroscopic topology optimisation problem, having the density distribution as design variable and the squared difference between real and desired deflection over time as objective, can be solved by the usual numerical methods[11] – however, with the challenge that the objective function is transient, as opposed to e.g. the well-known static "min compliance" designs from the dawn of topology optimisation. On the other hand, intermediate densities need not be punished in order to end up in a black-and-white design, but can be well interpreted physically.

Already after a few iterations the obtained displacement history approaches the desired one in a satisfactory manner. However, for the subsequent iterations, the results do not improve too much, even though the density distribution is still changing significantly. This is a hint that – as the prescribed displacement history has been chosen quite arbitrarily – there may be no physical solution at all satisfying the imposed demands. In any case, it has been possible to derive sensitivities for a general objective being a function of the density distribution, displacements, velocity, and time, and to find optimal topologies for the case that the prescribed load is defined as constant over time[12]. Clearly, for the impact case the boundary conditions are more involved, but one can certainly conclude that an extension of this approach to true impact problems including inertia effects is possible.

It should be remarked that the viscous processes in this consolidation problem only take

[9] Here, the microstructure morphology was not allowed to change. Rather, a fixed topology was used for the unit cell such that the scalar ρ alone controls the macroscopic behaviour.

[10] To be precise, for the stiffness tensor on the basis of the SIMP (Solid Isotropic Material with Penalisation) and the RAMP (Rational Approximation of Material Properties) scheme, see e.g. Bendsøe and Sigmund [2003]. Since the microscopic base material is isotropic, the pressure coupling and the compressibility can be computed directly from the stiffness properties. For the permeability, an own interpolation function was used.

[11] Here, COMSOL MULTIPHYSICS for the Finite Element Analysis and MATLAB for the optimisation control

[12] Apart from the ramping for time instants below a certain small threshold value

place under bulk loading, not under shear loading where the fluid is not pushed into or out of the unit cell. This is quite different from the behaviour of polymeric materials, where the bulk part may often be modelled as constant, sometimes even incompressible, but the shear modulus is time-dependent.

Bibliography

For convenience, all entries are enhanced by personal comments, marked by ♢ , referring sometimes to the contents of the reference in general, sometimes only to those parts which were important for the present work. Numbers in [square brackets] refer to the page of this thesis where the item was cited. All figures are own work (except for Fig. 3.9b) and are, thus, not furnished with reference annotations.

J. Aboudi. The dynamic indentation and impact of a viscoelastic half-space by an axisymmetric rigid body. *Computer Methods in Applied Mechanics and Engineering*, 20(2):135–150, 1979. ♢ *Journal paper presenting a numerical procedure to solve the dynamic impact of a sphere on the viscoelastic half-space.* [34]

M. Abramowitz and I. Stegun. *Handbook of Mathematical Functions. With Formulas, Graphs, and Mathematical Tables.* Dover Publications, 1972. ♢ *Extensive reference, e.g. on the Exponential Integral (Chapter 5), the Gamma and the Beta function (Chapter 6), the Error function (Chapter 7), hypergeometric functions (Chapter 15), and Laplace Transforms (Chapter 29).* [96, 98]

E. Aigner, R. Lackner, and C. Pichler. Multiscale prediction of viscoelastic properties of asphalt concrete. *Journal of Materials in Civil Engineering*, 21:771, 2009. ♢ *On the upscaling of viscoelastic properties from the bitumen to the asphalt scale using the power-law creep model.* [111]

J. J. Aklonis and W. J. MacKnight. *Introduction to polymer viscoelasticity.* Wiley, 1983. ♢ *Textbook which provides a good access to fundamental concepts of viscoelasticity and polymer mechanics. A nice bonus are the Chapters on dielectric relaxation and chemical stress relaxation.* [10, 12]

N. Aksel. On the impact of a rigid sphere on a viscoelastic half-space. *Archive of Applied Mechanics (Ingenieur Archiv)*, 56:38–54, 1986. ♢ *Abbreviated version of a doctoral thesis using a perturbation ansatz for the quasi-static spherical impact, where the half-space is assumed to react very slowly or very fast w.r.t. the loading time scale.* [33]

N. Aksel and H. Buggisch. Über das Problem des Kontakts zwischen einer starren Kugel und einem viskoelastischen Halbraum. *ZAMM - Zeitschrift für Angewandte Mathematik und Mechanik*, 62: T101–T102, 1982. ♢ *Journal paper on the contact of a rigid sphere and a viscoelastic half-space*

solved by adding a disturbance parameter to the Hertz solution, which seems justifiable for nearly elastic materials or a very short/long contact duration. [33]

T. Alfrey. Methods of representing the properties of viscoelastic materials. *Quarterly of Applied Mathematics*, 3:143–150, 1945. ♢ *Publication relating the differential form of the viscoelastic relations to the parameters of the Generalised Kelvin-Voigt and the Generalised Maxwell element.* [12]

T. Alfrey. *Mechanical behavior of high polymers.* New York, Interscience Publ., 1948. ♢ *Good review of other early works on polymer mechanics and viscoelasticity due to the many quotations incorporated in the book.* [4]

C. S. Andreasen. Multiscale topology optimization of solid and fluid structures. Technical report, DCAMM Special Report No. S131, 2011. ♢ *Ph.D. thesis on the optimal material design of porous materials with fluid-structure interaction, where some of the applications presented are the design of a microfluidic mixer, of an impact-absorbing structure, and of a poroelastic actuator.* [134]

C. S. Andreasen and O. Sigmund. Topology optimization of fluid-structure-interaction problems in poroelasticity. *Computer Methods in Applied Mechanics and Engineering*, 258:55–62, 2013. ♢ *Paper on the optimal design of a saturated poroelastic medium, where one application is to find the optimal compliance of a pressurised lid, and a second application is the material design of an energy absorber in order to achieve a prescribed deflection over time. The investigation of this topic has emerged from a collaboration between DCAMM and IGSSE as is described in Subsection D.2.* [134]

L. C. Andrews and B. K. Shivamoggi. *Integral transforms for engineers and applied mathematicians.* Macmillan Publishing Company, 1988. ♢ *Very helpful textbook, where Chapters 1, 4, 5, C were especially useful for the present work.* [10, 96, 98]

Ansys 12.1. *Theory reference for the Mechanical APDL and Mechanical Applications.* ANSYS, Inc., Canonsberg, 2009. ♢ *Section 4.10 on viscoelasticity, section 14.182 on the four-noded structural solid used here, section 17.2. on transient analysis.* [56]

I. Argatov. An analytical solution of the rebound indentation problem for an isotropic linear viscoelastic layer loaded with a spherical punch. *Acta Mechanica*, 223:1441–1453, 2012. ♢ *Rebound of a spherical indenter from a specified indentation depth reached by constant speed indentation. For the special case of a viscoelastic half-space the solution can be validated by the results of Lee and Radok [1960]. The author also presents dimensionless charts for the rebound displacement of an SLS.* [33]

M. F. Ashby. *Materials Selection in Mechanical Design.* Butterworth-Heinemann, 2005. ♢ *Esp. chapter 4 on "material property charts" and section 13.6 on "Lattices", i.e. foams and other cellular structures.* [37, 39]

P.-E. Austrell and A. K. Olsson. *Constitutive Models for Rubber VI*, chapter Dynamic characterization of elastomers using impact testing, pages 160–166. CRC Press, 2010. ♢ *Theoretical investigation on the question whether one-dimensional impact could be used to determine frequency-dependent parameters of a viscoelastic-plastic material model.* [6]

M. Avalle, G. Belingardi, and R. Montanini. Characterization of polymeric structural foams under compressive impact loading by means of energy-absorption diagram. *International Journal of Impact Engineering*, 25:455–472, 2001. ♢ *Journal paper on experimental results for optimal energy absorption under impact, where three different foams (PPE, PUR, NORYL GTX) have been used.* [7]

M. Avalle, G. Belingardi, and A. Ibba. Mechanical models of cellular solids: Parameters identification from experimental tests. *International Journal of Impact Engineering*, 34:3–27, 2007. ♢ *Comparison between micro-mechanical and phenomenological models for polymeric foams. Contains also a discussion on impact absorbers, where their quality is defined to be the ratio of the specific absorbed energy to the maximum stress value.* [39]

S. Baeurle, A. Hotta, and A. Gusev. A new semi-phenomenological approach to predict the stress relaxation behavior of thermoplastic elastomers. *Polymer*, 46(12):4344–4354, 2005. ♢ *Journal paper on an advanced formulation of exponential stress relaxation, which in its basic form may be seen as the counterpart of the creep function of the square-root Kelvin-Voigt model in the present work.* [114]

T. Belytschko, W. Liu, and B. Moran. *Nonlinear finite elements for continua and structures.* John Wiley & Sons, 2000. ♢ *Well-written standard reference for FEM from which the explicit time integration scheme (Box 6.1) was used here in a modified version regarding the influence of friction during impact on an elastic membrane.* [55]

M. P. Bendsøe and O. Sigmund. *Topology optimization – theory, methods, and applications.* Springer, 2003. ♢ *Textbook and standard reference for topology optimisation, including an extensive literature survey.* [135]

A. Bensoussan, J. Lions, and G. Papanicolaou. *Asymptotic analysis for periodic structures*, volume 5. North Holland, 1978. ♢ *Useful reference w.r.t. the multi-scale poroelastic problem as investigated by the project partner C. S. Andreasen, see Subsection D.2.* [134]

H. Bergander. Einführung in die Viskoelastizitätstheorie. In H. Göldner, editor, *Lehrbuch Höhere Festigkeitslehre, Band 2*, pages 315–348. Fachbuchverlag Leipzig-Köln, 1992. ♢ *A book chapter on the theory of viscoelasticity, which has been quite helpful as it also includes the Power Law model used in the present work.* [110]

J. Betten. *Creep mechanics.* Springer Verlag, 2002. ♢ *Textbook with a chapter on viscoelastic materials. Here, the author introduces the square root Kelvin-Voigt model (called $\sqrt{t}$ law) and relates the creep strain to diffusion processes.* [10, 114]

M. Biot. General theory of three-dimensional consolidation. *Journal of Applied Physics*, 12(2):155–164, 1941. ♢ *Journal paper introducing the general relations between load, stress distribution, water content, and settlement by physical equations as functions of time.* [135]

D. R. Bland. *The theory of linear viscoelasticity*. Pergamon, 1960. ♢ *One of the early textbooks on viscoelasticity, where the first part focuses on the foundations of the theory, while in the second part some harmonic, quasistatic, and dynamic example problems are solved using the correspondence principle.* [4]

A. Bolshakov and G. Pharr. Inaccuracies in Sneddon's solution for elastic indentation by a rigid cone and their implications for nanoindentation data analysis. Technical report, Rice Univ., Houston, TX (United States), 1996. ♢ *Journal paper on corrections to Sneddon's cone indentation solution necessary for large deformations.* [5]

L. Boltzmann. Zur Theorie der elastischen Nachwirkung. *Annalen der Physik und Chemie*, Ergänzungsband 7:624–654, 1876. ♢ *Journal paper introducing the superposition principle devised from the observed fading memory in creep ("Verschiebungsnachwirkung") and relaxation ("Kraftnachwirkung") experiments. See also the publication by Markovitz [1977].* [3, 37]

F. Borodich and L. Keer. Contact problems and depth-sensing nanoindentation for frictionless and frictional boundary conditions. *International Journal of Solids and Structures*, 41(9-10):2479–2499, 2004. ♢ *Well-written review paper on hardness and depth-sensing techniques, where Hertzian type of contact is considered in Section 2 on frictionless indentation. Discusses also the relations between Galin, Sneddon and BASh solution.* [6, 22]

J. Boussinesq. *Application des potentiels à l'étude de l'équilibre et du mouvement des solides élastiques [...]*. Gauthier-Villars, 1885. ♢ *Treatise giving the theoretical solution for the displacements and stresses at a point within an elastic isotropic homogeneous half-space loaded by a force on the surface (see especially §III.22 on p. 92).* [5, 19, 20]

H. F. Brinson and L. C. Brinson. *Polymer engineering science and viscoelasticity: an introduction*. Springer New York, 2008. ♢ *Easy textbook suitable for a start into the two subjects.* [10, 13]

Bruker Optics Inc. Guide for Infrared Spectroscopy. Available at www.bruker.com, 2011. ♢ *Gives tables on the wavenumber range for the absorption of common chemical groups. Also, some tables on the conversion of units are included.* [43]

E. Buckingham. On physically similar systems; illustrations of the use of dimensional equations. *Physical Review*, 4:345–376, 1914. ♢ *Detailed illustration of the use of dimensional analysis, including a variety of examples, where the symbol* Π *is introduced to denote a dimensionless product of the problem parameters.* [124]

H. H. Calvit. Experiments on rebound of steel balls from blocks of polymer. *Journal of the Mechanics and Physics of Solids*, 15:141–150, 1967a. ♢ *On the dynamic testing of polyethylene and polymethylmethacrylate samples subjected to temperatures between 25°C and 290°C in order to obtain the loss tangent assuming a half-sine for the penetration and the validity of the Hertzian contact duration.* [1, 6]

H. H. Calvit. Numerical solution of the problem of impact of a rigid sphere onto a linear viscoelastic half-space and comparison with experiment. *International Journal of Solids and Structures*, 3:951–960, 1967b. ♢ *On the numerical treatment of Hunter's [1960] pair of dual integral equations for spherical impact on a viscoelastic half-space (with an unequivocal Poisson's ratio). The analytical results for contact duration and rebound height were compared with experiments on PMMA.* [34]

J. R. Carson. *Electric circuit theory and the operational calculus.* Chelsea Publishing Company, 1953. ♢ *Book on solving electric circuit problems ("Laplace-Carson transform"), see esp. Chapter IV.* [100]

C. P. Chen and R. S. Lakes. Design of viscoelastic impact absorbers: Optimal material properties. *International Journal of Solids and Structures*, 26:1313–1328, 1990. ♢ *Relations between deflection, impact force and loss tangent for a one-dimensional viscoelastic buffer (approximating the impact process as half a cycle of free decay vibration) and for ball impact on a viscoelastic half-space (using a numerical integration scheme for Hunter's [1960] equations).* [7, 32]

W. T. Chen and P. A. Engel. Impact and contact stress analysis in multilayer media. *International Journal of Solids and Structures*, 8:1257–1281, 1972. ♢ *An approximate method for the indentation of one or two layers bonded to an elastic half-space, including an extension for quasi-static ball impact.* [5]

L. Cheng, X. Xia, L. E. Scriven, and W. W. Gerberich. Spherical-tip indentation of viscoelastic material. *Mechanics of Materials*, 37:213–226, 2005. ♢ *Journal paper presenting the solution for spherical indentation of a viscoelastic half-space modelled by the Standard Linear Solid (for the deviatoric behaviour, while the volumetric part is considered elastic), where Radok's method of functional equations has been applied on the Hertzian contact relations.* [6]

Y.-T. Cheng and C.-M. Cheng. Scaling, dimensional analysis, and indentation measurements. *Materials Science and Engineering: R: Reports*, 44:91–149, 2004. ♢ *Very well-prepared review paper on instrumented indentation measurements for isotropic linear elastic, linear visco-elastic, visco-plastic ("power-law creep") and elasto-plastic ("power-law work-hardening") material behaviour with a helpful introduction on similarity, scaling, size effects, and dimensional analysis.* [123, 124]

Y.-T. Cheng and C.-M. Cheng. Relationships between initial unloading slope, contact depth, and mechanical properties for spherical indentation in linear viscoelastic solids. *Materials Science and Engineering: A*, 409:93–99, 2005. ♢ *FEM simulations for a discussion on the determination of viscoelastic material parameters from load- or displacement-driven indentation experiments using the*

initial unloading slope (a method being originally developed for elasto-plastic material behaviour). [6]

R. Christensen. *Theory of viscoelasticity: an introduction.* Academic Press New York, 1982. ♢ *Helpful textbook covering the fundamentals of viscoelasticity, where Chapters 1 and 2 have been useful, especially the paragraph on spherical indentation of a viscoelastic half-space (pp. 67-72).* [10, 34]

K. S. Cole and R. H. Cole. Dispersion and absorption in dielectrics: I. Alternating current characteristics. *The Journal of Chemical Physics*, 9:341–351, 1941. ♢ *On the description of experimental dispersion data by a simple extension of the Debye equations (which may be compared to the Maxwell model in viscoelasticity) and on a new kind of graphical representation where the real and the imaginary part of the complex dielectric constant are plotted in the complex plane (Argand plane) and not over frequency, as had been the traditional form.* [12]

Y. Collette and P. Siarry. *Multiobjective optimization: principles and case studies.* Springer Verlag, 2003. ♢ *Textbook on the fundamentals of and methods for multiobjective optimisation.* [129]

G. Constantinides, C. A. Tweedie, D. M. Holbrook, P. Barragan, J. F. Smith, and K. J. Van Vliet. Quantifying deformation and energy dissipation of polymeric surfaces under localized impact. *Materials Science and Engineering: A*, 489:403–412, 2008. ♢ *Energy absorption of six different polymers in micrometer-scale indentation impact experiments with a Berkovich tip.* [6]

A. H. Cottrell. The time laws of creep. *Journal of the Mechanics and Physics of Solids*, 1(1):53–63, 1952. ♢ *Link of experimentally observed creep behaviour to a creep rate function suitable to describe steady-state, Andrade, and logarithmic creep, where the focus is on the latter type of creep (exhaustion theory).* [118]

A. H. Cottrell. Logarithmic and Andrade creep. *Philosophical Magazine Letters*, 75(5):301–308, 1997. ♢ *Refinement of the exhaustion theory, i.e. it may result in either steady-state or Andrade or logarithmic creep.* [118]

M. Dahan and M. Predeleanu. The Hertz problem for an axisymmetrical indenter and a viscoelastic anisotropic composite material. *Fibre Science and Technology*, 18:301–315, 1983. ♢ *Closed-form solutions of the static indentation of a viscoelastic half-space by a rigid punch.* [33]

H. Deresiewicz. A note on Hertz's theory of impact. *Acta Mechanica*, 6:110–112, 1968. ♢ *Journal article where for Hertzian impact the implicit relation between penetration and time has been evaluated numerically. See also Graham [1973].* [5, 28, 29]

DIN 50156-1. Metallische Werkstoffe - Härteprüfung nach Leeb - Teil 1: Prüfverfahren. DIN Deutsches Institut für Normung e.V., 2007. ♢ *Standard on the determination of the dynamic hardness after Dietmar Leeb. See Appendix C for a schematic sketch of the device.* [6]

DIN 53512. Prüfung von Kautschuk und Elastomeren – Bestimmung der Rückprall-Elastizität (Schob-Pendel). DIN Deutsches Institut für Normung e.V., 2000. ♢ *Standard for the determination of the rebound resilience by a pendulum on which a spherical impactor is mounted.* [6]

DIN 53513. Prüfung von Kautschuk und Elastomeren; Bestimmung der visko-elastischen Eigenschaften von Elastomeren bei erzwungenen Schwingungen außerhalb der Resonanz. DIN Deutsches Institut für Normung e.V., 1990. ♢ *Standard for the determination of visco-elastic properties of rubber under forced vibration, where Section 6 describes the procedure and the determination of parameters.* [11]

DIN EN 10319-1. Metallische Werkstoffe – Relaxationsversuch unter Zugbeanspruchung – Teil 1: Prüfverfahren für die Anwendung in Prüfmaschinen. DIN Deutsches Institut für Normung e.V., 2003. ♢ *Standard on the tensile stress relaxation testing of metallic materials, where the principal procedure is sketched in Section 5.* [11]

DIN EN ISO 3385. Polymere Weichschaumstoffe; Bestimmung der Ermüdung durch konstante Stoßbelastung. DIN Deutsches Institut für Normung e.V., 2010. ♢ *Standard for the determination of fatigue of flexible cellular polymeric materials by constant load pounding where a rather flat indenter is loading the sample in 80000 cycles.* [6]

DIN EN ISO 8307. Weich-elastische polymere Schaumstoffe; Bestimmung der Kugel-Rückprallelastizität. DIN Deutsches Institut für Normung e.V., 2008. ♢ *Standard for the determination of the resilience of flexible cellular polymeric materials by ball rebound. As sketched in Section 5, a steel ball is dropped from a specific height on the sample, and the rebound height is measured.* [6]

DIN EN ISO 899-1. Kunststoffe – Bestimmung des Kriechverhaltens – Teil 1: Zeitstand-Zugversuch. DIN Deutsches Institut für Normung e.V., 2003. ♢ *Standard on the tensile creep behaviour of plastics, where Section 6 sketches the procedure and Section 7 describes the determination of the creep modulus.* [10]

V. A. Ditkin. *Integral transforms and operational calculus.* Pergamon Press, 1965. ♢ *Textbook where Chapters 2 (fundamental theory) and 9 (extensive table of transformation pairs) on the Laplace(-Carson) transform have been a useful reference for the present work.* [98]

H. Eschenauer, J. Koski, and A. Osyczka. *Multicriteria design optimization: Procedures and applications.* Springer Verlag, 1990. ♢ *Helpful textbook, esp. Chapter 1, "Multicriteria optimization – fundamentals and motivation".* [129]

H. Eschenauer, N. Olhoff, and W. Schnell. *Applied structural mechanics: fundamentals of elasticity, load-bearing structures, structural optimization: including exercises.* Springer Verlag, 1997. ♢ *Textbook where an introduction to structural optimisation is given in part D (covering fundamentals, algorithms, sensitivity analysis, and strategies).* [129]

J. D. Ferry. *Viscoelastic Properties of Polymers.* John Wiley & Sons, 2nd edition, 1970. ♢ *Extensive textbook covering theoretical aspects, experimental methods, the behaviour of polymers, and some applications.* [10]

W. N. Findley, J. S. Lai, and K. Onaran. *Creep and Relaxation of Nonlinear Viscoelastic Materials – with an Introduction to Linear Viscoelasticity.* North Holland Publishing Company, Amsterdam, 1976. ♢ *Very well-written textbook on linear and non-linear viscoelasticity, where Chapters 5 and 6 have been especially useful.* [10, 12]

D. Flom. Rolling friction of polymeric materials. I. Elastomers. *Journal of Applied Physics*, 31(2):306–314, 1960. ♢ *Despite of what can be expected from the scant title, this paper is also reporting on ball bouncing experiments on Neoprene, Silicone and Butyl elastomers. It is shown that the rolling friction coefficient is proportional to the dynamic losses during impact.* [6, 56]

E. Friis, R. Lakes, and J. Park. Negative Poisson's ratio polymeric and metallic foams. *Journal of Materials Science*, 23:4406–4414, 1988. ♢ *On foam materials with re-entrant (inwardly directed) cell ribs such that negative Poisson's ratios are observed.* [84]

Y. Fujii and T. Yamaguchi. Proposal for material viscoelasticity evaluation method under impact load. *Journal of Materials Science*, 40:4785–4790, 2005. ♢ *Introducing a portable impact system with short test preparation time for impact experiments on viscoelastic samples. The authors use the Doppler frequency shift due to the change in impactor position to calculate velocity, position, acceleration and inertia forces during impact on gel blocks.* [6]

G. Galilei. *Unterredungen und mathematische Demonstrationen über zwei neue Wissenszweige, die Mechanik und die Fallgesetze betreffend: erster bis sechster Tag (1638).* Verlag Harri Deutsch, 1995. ♢ *German translation of the famous "discorsi e dimostrazioni matematiche, intorno a duo nuove scienze, attenenti alla meccanica et i movimenti locali".* [123]

L. A. Galin. *Contact problems - The legacy of L.A. Galin.* Edited by G. M. L. Gladwell, Springer, 2008. ♢ *Translation of Galin's Russian books by Gladwell. The book is expanded by some extra material (like a research review shedding some light on works by Soviet researchers, and a Chapter by F. M. Borodich on Hertz type contact problems).* [17, 22]

J. W. Geckeler. *Handbuch der Physik: Mechanik der elastischen Körper*, chapter 3: Elastostatik, pages 141–403. Julius Springer, 1928. ♢ *Ziff. 79 gives a detailed derivation of Hertzian contact.* [22]

J. Gibbings. *The systematic experiment.* Cambridge University Press, 1986. ♢ *Accessible textbook on planning, conducting and evaluating physical experiments, with many helpful warnings on experimentation and interpretation pitfalls. Contains also a chapter on dimensional analysis.* [37, 124]

L. J. Gibson and M. F. Ashby. *Cellular solids – structure and properties.* Cambridge University Press, 1997. ♢ *Nice textbook with very accessible diagrams and figures. Most important has been Chapter 5 on the mechanics of foams.* [37]

G. Gladwell. *Contact problems in the classical theory of elasticity.* Sijthoff & Noordhoff, 1980. ♢ *To a small extent, Chapter II, "Elementary problems", was useful and partly also Chapter X, "Axisymmetric contact problems for the elastic half-space".* [17]

H. Göldner and W. Pfefferkorn. *Technische Mechanik.* Vieweg, 1988. ♢ *Textbook on the fundamentals of mechanics, where Chapter 12 of the "Festigkeitslehre"-part covers the fundamental theory of viscoelasticity.* [10]

W. Goldsmith. *Impact – the theory and physical behaviour of colliding solids.* Dover Publications, 2001. ♢ *Textbook with focus on elastic and plastic material behaviour and wave propagation for impact problems, contains also some pages on the impact response of viscoelastic rods and beams.* [17]

J. N. Goodier. Dimensional analysis. In M. Hetényi, editor, *Handbook of experimental stress analysis*, pages 1035–1045. Wiley New York, 1950. ♢ *Nice text on the* Π*-theorem, similarity, and model scaling.* [124]

G. A. C. Graham. The contact problem in the linear theory of viscoelasticity. *International Journal of Engineering Science*, 3(1):27–46, 1965. ♢ *Journal paper on the contact between a rigid indenter (with a specialisation for sphere and cone) and the viscoelastic half-space or between two viscoelastic bodies, where the contact area is allowed to have a single maximum over time.* [6, 32, 34]

G. A. C. Graham. The contact problem in the linear theory of viscoelasticity when the time dependent contact area has any number of maxima and minima. *International Journal of Engineering Science*, 5:495–514, 1967. ♢ *Extension of the 1965 paper by the same author removing the single maximum restriction by recurrence formulae.* [32]

G. A. C. Graham. A contribution to Hertz's theory of elastic impact. *International Journal of Engineering Science*, 11:409–413, 1973. ♢ *Journal paper extending Deresiewicz's [1968] approach for the impact of a paraboloid of revolution on an elastic half-space (Hertzian spherical impact: penetration depth is related to the square of the contact radius) to the case of a conical impactor (linear relation between penetration depth and contact radius).* [5]

B. Gross. *Mathematical structure of the theories of viscoelasticity.* Hermann, 1968. ♢ *Short monograph on the interrelations between the (complex) compliance, (complex) relaxation modulus, relaxation/retardation spectrum etc., which nowadays is standard in every textbook on viscoelasticity but was a milestone in the dawn of the theory of viscoelasticity (the original publication dates from 1953).* [4]

W. Gross, W. Hauger, W. Schnell, and P. Wriggers. *Technische Mechanik Band 4: Hydromechanik, Elemente der Höheren Mechanik, Numerische Methoden.* Springer-Verlag, 1995. ♢ *General textbook on engineering mechanics, where Section 6.2 gives a short but valuable introduction on the foundations of linear viscoelasticity (simple models, creep and relaxation function, relaxation spectrum, integral formulation).* [10, 12, 104]

M. E. Gurtin and E. Sternberg. On the linear theory of viscoelasticity. *Archive for Rational Mechanics and Analysis*, 11:291–356, 1962. ♢ *Theorem 9.2 on the generalised Papkovich-Neuber solution.* [32]

Y. M. Haddad. *Viscoelasticity of engineering materials.* Chapman & Hall, 1995. ♢ *Textbook on the theory of linear and nonlinear viscoelasticity, where Sections 9.6 (illustrating the use of the correspondence principle for the flat punch impact on a viscoelastic halfspace) and 9.7 (spherical indentation on a viscoelastic halfspace) are of special interest w.r.t. the present work.* [10, 34]

R. T. Haftka and Z. Gürdal. *Elements of Structural Optimization.* Kluwer Academic Publishers, 1992. ♢ *Very well written textbook on fundamentals and advanced aspects of optimisation with a broad overview on methods and algorithms.* [129]

M. Herrenbrück. IGSSE internal report on the research stay at Material Technology Innsbruck in August 2011. International Graduate School for Science and Engineering (IGSSE), TU München. ♢ *Short report on mechanical 1-D creep experiments and modelling by the SRKV behaviour*, 2011. [45]

H. Hertz. Über die Berührung fester elastischer Körper. *Journal für die reine und angewandte Mathematik*, 92:156–171, 1881. ♢ *Famous journal publication on the contact of two elastic bodies. Hertz also gives the solution for the impact case (neglecting wave propagation), viz. the time instant in dependence of the current penetration depth and, from this, also the contact duration. See also the paper by Deresiewicz [1968].* [5, 9, 26, 28]

S. C. Hunter. Energy absorbed by elastic waves during impact. *Journal of the Mechanics and Physics of Solids*, 5(3):162–171, 1957. ♢ *Journal publication where the total elastic vibrational energy of the body with the larger mass is related to the initial kinetic energy of the other body – certain assumptions have been assumed, e.g. the approximation of displacement over time by a half sine. See also Reed [1985].* [5, 25, 26, 28, 29]

S. C. Hunter. The Hertz problem for a rigid spherical indenter and a viscoelastic half-space. *Journal of the Mechanics and Physics of Solids*, 8:219–234, 1960. ♢ *Journal article where for a viscoelastic halfspace the penetration under a spherical indenter can be determined also for decreasing contact area (which is not possible by the solution of Lee and Radok [1960]). However, the solution of the dynamic impact problem, where the contact radius is not known a priori, is obtained here only for nearly elastic materials.* [4, 6, 31, 34]

S. C. Hunter. The solution of boundary value problems in linear viscoelasticity. In A. C. Eringen, H. Liebowitz, S. L. Koh, and J. M. Crowley, editors, *Mechanics and chemistry of solid propellants: proceedings of the fourth Symposium on Naval Structural Mechanics*, pages 257–295. Pergamon Press Inc., 1967. ♢ *Full-text paper presented at the 1965 conference, which has been useful for several reasons: it gives a thorough overview on the theoretical foundations, explains the correspondence principle in a very amenable manner, and covers the impact of a blunt indenter or a sphere on the viscoelastic half-space.* [11, 30, 34, 100]

A. Jäger and R. Lackner. Identification of viscoelastic model parameters by means of cyclic nanoindentation testing. *Int. J. Mat. Res. (formerly Z. Metallkd.)*, 99(8):1, 2008. ♢ *Proposal of an experimental method for the parameter identification of certain viscoelastic models, such as the power law creep model.* [111]

A. Jäger and R. Lackner. Finer-scale extraction of viscoelastic properties from nanoindentation characterised by viscoelastic–plastic response. *Strain*, 45(1):45–54, 2009. ♢ *Parameter identification by double indentation with a Berkovich and a cono-spherical tip.* [21]

A. Jäger, R. Lackner, and J. Eberhardsteiner. Identification of viscoelastic properties by means of nanoindentation taking the real tip geometry into account. *Meccanica*, 42(3):293–306, 2007. ♢ *Parameter identification where the indenter geometry is described by a function with two constants describing the tip shape.* [18]

E. Jenckel and E. Klein. Die Bestimmung von Relaxationszeiten aus der Rückprallelastizität. *Zeitschrift für Naturforschung Teil A*, 7:619, 1952. ♢ *Experiments on the rebound height of spheres impinging different kind of polymers, where the authors give interpretations of the temperature dependence of the chemical bonds and determine the elastic moduli and relaxation times of a viscoelastic fluid model ("plastisch-elastisches Verhalten") consisting of two Maxwell elements in parallel.* [6]

K. L. Johnson. *Contact Mechanics*. Cambridge University Press, 1985. ♢ *Well-written comprehensive textbook on normal, tangential, and rolling contact, where Chapter 4 is dedicated to Hertzian contact. Also, Chapter 11 on elastic and inelastic impact is related to the present work.* [17, 18, 20, 22, 26]

W. Johnson. *Impact strength of materials*. Edwald Arnold, 1972. ♢ *Textbook focusing on plastic deformations and elastic-plastic stress waves in bars, beams, plates and semi-infinite media. Contains also two pages on Hertzian impact.* [17, 26, 28]

N. Jones. *Structural Impact*. Cambridge University Press, 1989. ♢ *Textbook with the focus on dynamic loading of elasto-plastic structures with two chapters on dimensional analysis and scaling laws.* [17, 124]

F. Jurecka. *Robust Design Optimization Based on Metamodeling Techniques*. PhD thesis, Technische Universität München, München, 2007. ♢ *Dissertation with some chapters on design of experiments, metamodels, and structural optimisation.* [100, 129]

J. Kalker. A survey of the mechanics of contact between solid bodies. *ZAMM*, 57(5):T3–T17, 1977. ♢ *Well-arranged survey paper on mechanical contact, excluding the field of tribology (lubrication problems) and any experimental work. The literature regarding, among others, the elastic half-space (Table 2) and viscoelastic problems (Table 4) is classified into frictional and frictionless contact, both subdivided into quasistatic (incl. impact) and dynamic (also incl. impact) problems.* [5]

U. Kirsch. *Structural Optimization: Fundamentals and Applications*. Springer-Verlag Berlin Heidelberg, 1993. ♢ *General textbook with well-prepared examples on structural optimisation fundamentals, methods, approximation concepts, and design procedures.* [129]

J. Knippers, J. Cremers, M. Gabler, and J. Lienhard. *Atlas Kunststoffe + Membranen: Werkstoffe und Halbzeuge, Formfindung und Konstruktion*. Institut für internationale Architektur-Dokumentation. Edition Detail, 2010. ♢ *Book on plastics and membranes seen from an architect's point of view; gives a good picture on the different types of plastics and their respective properties and applications.* [37]

A. Kren' and V. Rudnitskii. A dynamic method and instrument for measuring hardness of paint and varnish coatings. *Russian Journal of Nondestructive Testing*, 36(5):375–380, 2000. ♢ *Comparison of three different methods to determine the hardness of coatings, where the authors favor the dynamic indentation due to their easy and quick applicability.* [6]

R. S. Lakes. *Viscoelastic solids*. CRC Press LLC, 1998. ♢ *Well-written textbook on the theory of (linear) viscoelasticity; covers beside the fundamental theory many aspects such as phenomena and causal mechanisms, special material types (e.g. porous materials), experimental methods, diverse applications, etc. Very useful for the present work.* [4, 10]

R. S. Lakes. Viscoelastic measurement techniques. *Review of Scientific Instruments*, 75:797–810, 2004. ♢ *Review article on experimental measurements of viscoelastic solids in time or frequency domain.* [12, 17]

R. S. Lakes. *Viscoelastic materials*. Cambridge University Press, 2009. ♢ *Textbook which has emerged from the book 'Viscoelastic solids' by the same author.* [9]

R. Larson, S. Goyal, and C. Aloisio. A predictive model for impact response of viscoelastic polymers in drop tests. *Rheologica Acta*, 35:252–264, 1996. ♢ *Experimental investigation of the one-dimensional impact of a flat tup an a rubber sample and comparison with the theoretical prediction for the force history.* [7]

P.-L. Larsson and S. Carlsson. On microindentation of viscoelastic polymers. *Polymer Testing*, 17:49–75, 1998. ♢ *Study on spherical (Brinell) and flat punch (Boussinesq) indentation of viscoelastic materials, where the theoretical formulae are compared to FEM simulations and experiments using an epoxy resin and a PMMA.* [6, 93]

H. Leaderman. *Elastic and creep properties of filamentous materials.* PhD thesis, Massachusetts Institute of Technology, 1941. ♢ *Thesis on the creep behaviour of high polymeric materials, where many experiments supporting the validity of Boltzmann's superposition principle are reviewed.* [4]

E. H. Lee. Stress analysis in visco-elastic bodies. *Quarterly of Applied Mathematics*, 13:183–190, 1955. ♢ *Journal paper on the correspondence principle. Since the method is based on the application of the Laplace transform to the boundary conditions, it is restricted to problems for which the type of boundary condition (stress or displacement) does not change over time.* [4, 29]

E. H. Lee. Stress analysis in viscoelastic materials. *Journal of Applied Physics*, 27(7):665–672, 1956. ♢ *Journal paper on the measurement of material properties by oscillatory experiments and on the inclusion of inertia forces in one-dimensional viscoelastic stress problems (impact on semi-infinite rods).* [11, 17]

E. H. Lee and J. R. M. Radok. The contact problem for viscoelastic bodies. *Journal of Applied Mechanics*, 27:438–444, 1960. ♢ *Journal publication on the indentation of a viscoelastic half-space by a rigid sphere. The solution, obtained by use of Radok [1957], applies only for a non-decreasing contact zone. The authors also give examples for the contact pressure relaxation in continuous indentation.* [4, 6, 30, 31]

E. H. Lee and T. G. Rogers. Solution of viscoelastic stress analysis problems using measured creep or relaxation functions. *Journal of Applied Mechanics*, 30(1):127–133, 1963. ♢ *Journal paper where the hereditary integral form of viscoelastic relations is treated by a direct numerical step-by-step integration scheme.* [12, 53]

J. M. Lifshitz and H. Kolsky. Some experiments on anelastic rebound. *Journal of the Mechanics and Physics of Solids*, 12:35–43, 1964. ♢ *Experimental investigations regarding elasto-plastic effects observed in spherical impact of mild steel blocks, where it is found that the rebound height is affected by yielding but not so much the contact duration calculated from Hertzian impact. Also, they investigate whether the complex modulus can be computed from the contact duration using PMMA blocks.* [6, 56]

A. E. H. Love. *A treatise on the mathematical theory of elasticity.* Dover Publ., New York, fourth edition, 1944. ♢ *Extensive reference of classical elasticity where Chapter VIII "The transmission of force" including Hertzian impact (article 139) is of relevance for the present work.* [25, 26]

G. Lu and T. Yu. *Energy absorption of structures and materials*. Woodhead Publishing, 2003. ♢ *Textbook on energy absorption under static and impact loading, mainly due to plastic material behaviour. Contains also a chapter on dimensional analysis.* [2, 124]

J. Mackerle. Finite element modelling and simulation of indentation testing: a bibliography (1990-2002). *Engineering Computations*, 21:23–52, 2004. ♢ *Review paper on indentation testing in general, identification of mechanical properties, scaling relationships, and related topics.* [7]

M. Maier. Entwicklung eines Versuchsaufbaus zur Charakterisierung des Dissipationsverhaltens zellulärer Werkstoffe im Fall stoßartiger Belastung. Master's thesis, Leopold-Franzens-Universität Innsbruck, 2011. ♢ *Diploma thesis, supervised by Roman Lackner, on the "development of a test apparatus to characterise the dissipation behaviour of cellular materials under impact loading", see Subsection 4.1.1 of the present work.* [54]

H. Mang and G. Hofstetter. *Festigkeitslehre*. Springer-Verlag Wien, 2004. ♢ *Textbook covering topics from applied mechanics and material mechanics; contains also some pages on one-dimensional linear viscoelasticity.* [10, 16]

Maple. *User Manual*. Maplesoft, 2012. ♢ *Computer algebra system employed concerning the rheological models in Appendix B.* [98]

H. Markovitz. Boltzmann and the beginnings of linear viscoelasticity. *Transactions of the Society of Rheology*, 21:381–398, 1977. ♢ *Interesting-to-read article on Boltzmann's contributions to the field of viscoelasticity. It gives a short review of Boltzmann's life, sketches the state of the art at that time, refurbishes the findings of his 1874/1876 publication and narrates the reactions of other researchers on it.* [4, 12]

Matlab. *Primer R2012b*. The MathWorks, Inc., 2012. ♢ *Numerical computing program employed concerning the rheological models in Appendix B.* [97]

M. J. Matthewson. Axi-symmetric contact on thin compliant coatings. *Journal of the Mechanics and Physics of Solids*, 29:89–113, 1981. ♢ *Frictionless indentation of a rather soft thin coating bonded to a rigid semi-infinite substrate by a rigid indenter of arbitrary profile. For the special case of a spherical indenter an explicit solution is given, showing good agreement with indentation experiments.* [5]

K. Memmler, editor. *Handbuch der Kautschukwissenschaft*. S. Hirzel, Leipzig, 1930. ♢ *Pages 640 to 653 on free fall experimental devices ("Breuil", "Hock") and pendulum apparatus ("van Itersen", "Schob") similar to the Shore scleroscope and Herbert pendulum apparatus for hardness measurements; however, suitable for soft/viscoelastic materials such as natural rubber.* [6, 55]

Microsoft Excel 2010. *Product Guide*. Microsoft Corp., 2010. ♢ *Spreadsheet application used for treatment of experimental and Finite Element data.* [101]

N. Mills. *Polymer foams handbook: engineering and biomechanics applications and design guide.* Butterworth-Heinemann, 2007. ♢ *Extensive textbook on polymer foams, where the introductory chapters and the chapter on the "modelling of creep and viscoelasticity" were especially useful for the present work.* [10, 37, 39]

T. Misic, M. Najdanovic-Lukic, and L. Nesic. Dimensional analysis in physics and the buckingham theorem. *European Journal of Physics*, 31:893, 2010. ♢ *Publication of some value owing to the well-chosen examples (object moving through a fluid leading to the Reynolds number, or propagation of waves on water leading to the Bond number).* [124]

D. Montgomery. *Design and analysis of experiments.* John Wiley & Sons Inc, 2005. ♢ *Textbook on statistics, experimentation planning, regression models, response surface methods, robust design, etc. with focus on factorial design.* [124]

D. Montgomery and E. Peck. *Introduction to linear regression analysis.* John Wiley & Sons, 1992. ♢ *Statistics textbook on model building, correlation, linear and nonlinear regression, and model validation.* [100]

R. Myers and D. Montgomery. *Response surface methodology: process and product optimization using designed experiments.* John Wiley & Sons Inc, 2002. ♢ *Textbook on statistical experimental design, regression modelling techniques, and the exploration and optimisation of response surfaces.* [100]

T. Niederkofler, A. Jäger, and R. Lackner. Identification of model parameters from elastic/elasto-plastic spherical indentation. *International Journal of Materials Research*, 100(7):926–932, 2009. ISSN 1862-5282. ♢ *Journal article on scaling relations for instrumented indentation and comparison with the Sneddon solution.* [19, 21]

L. F. Nielsen. Power-law creep as related to adapted burgers creep representations and incremental analysis. Technical report, BYG, Danmarks Tekniske Universitet, 2006. [111]

W. Nowacki. *Theorie des Kriechens.* Franz Deuticke Wien, 1965. ♢ *One of the first German textbooks on viscoelasticity with focus on the correspondence principle (many examples) and wave propagation.* [10]

G. Oertel, editor. *Polyurethane Handbook.* Carl Hanser Verlag, 1993. ♢ *Extensive reference on the chemical configuration, production, and properties of polyurethanes including their technical applications, where esp. Chapter 5 "Polyurethane flexible foams" and Chapter 9 "Determination of the composition and properties of polyurethanes" are relevant for the present work.* [37, 40]

W. Oliver and G. Pharr. An improved technique for determining hardness and elastic modulus using load and displacement sensing indentation experiments. *Journal of Materials Research*, 7(06): 1564–1583, 1992. ♢ *Journal paper on the BASh/Doerner-Nix relations and their correction for the*

observed non-linearity in the unloading path (i.e. rejecting the flat punch approximation after load removal). [6, 16]

J. Palacios. *Dimensional Analysis.* Macmillan & Co Ltd, 1964. ♢ *Very illustrative and accessible textbook on the fundamentals of dimensional analysis and applications, with many examples.* [124]

R. Palmer, D. Stein, E. Abrahams, and P. Anderson. Models of hierarchically constrained dynamics for glassy relaxation. *Physical Review Letters*, 53(10):958–961, 1984. ♢ *Journal paper which has been interesting because the square-root Kelvin-Voigt creep in the present work resembles formally the stretched exponential functions which often are used to describe relaxation processes.* [114]

Y.-H. Pao. Extension of the Hertz theory of impact to the viscoelastic case. *J. Appl. Phys. 26, 1083 (1955)*, 26:1083–1088, 1955. ♢ *Journal paper in which the dynamic impact of a viscoelastic body on a stationary rigid surface is tried to be solved by application of the Laplace transform under the restriction that viscoelastic effects do not lead to an increase of the contact area as compared to the purely elastic case; however, the rebound solution is erroneous due to the decreasing contact area.* [30]

J. Pouyet and J. L. Lataillade. Dynamic investigation of hard viscoelastic materials by ball bouncing experiments. *Journal of Materials Science*, 10:2112–2116, 1975. ♢ *Experimental investigations of spherical impact on PVC blocks for different temperature levels and comparison to a MX model.* [6, 56]

R. Prony. *Traité de Mécanique Élémentaire.* École Polytechnique, Paris, 1802. ♢ *Textbook on static, dynamic, hydrostatic and hydrodynamic mechanics.* [9]

J. Radok. Visco-elastic stress analysis. *Quarterly of Applied Mathematics*, 15:198–202, 1957. ♢ *Journal paper where Lee's [1955] correspondence principle is generalised to the method of functional equations. Now, also indentation problems where a certain boundary point is subjected to stress or displacement conditions at different times may be solved, as long as the contact area is increasing.* [4, 12, 30]

M. V. Ramesh Kumar and R. Narasimhan. Analysis of spherical indentation of linear viscoelastic materials. *Current Science*, 87:1088–1095, 2004. ♢ *Comparison between analytical and FEM solution for step or trapezoidal loading in spherical indentation of a viscoelastic half-space, supplemented by experiments on PMMA. The use of the indentation unloading slope to retrieve Young's modulus is also discussed.* [93]

L. Rayleigh. The principle of similitude. *Nature*, 95:66–68, 1915. ♢ *Short publication where for many examples from different fields the relations between the problem parameters are given due to dimensional reasoning.* [124]

W. Read. Stress analysis for compressible viscoelastic materials. *Journal of Applied Physics*, 21(7): 671–674, 1950. ♢ *Journal paper illustrating the application of the Fourier transform to express time-dependent stress-strain relations in terms of complex elastic constants for the correspondence principle.* [4]

J. Reed. Energy losses due to elastic wave propagation during an elastic impact. *Journal of Physics D: Applied Physics*, 18(12):2329, 1985. ♢ *Journal paper improving Hunters [1957] investigations by using a more realistic force-time relation; this results in the prediction of a larger energy loss due to elastic waves than Hunter claimed.* [5, 25]

H.-W. Reinhardt. *Der Ingenieurbau: Band 4*, chapter Werkstoffe des Bauwesens, pages 1–131. Ernst & Sohn, 1997. ♢ *In this book chapter on civil engineering materials, section 11 (Kunststoffe) gives a good introduction to polymers.* [37]

T. Rießinger. *Mathematik für Ingenieure*. Springer-Verlag, Berlin Heidelberg New York, 2004. ♢ *An introductory textbook on higher mathematics with detailed examples, written subtly and with some lightness but sometimes veering off-topic.* [96, 98]

J. Rösler, H. Harders, and M. Bäker. *Mechanisches Verhalten der Werkstoffe*. Springer, 2012. ♢ *Well-written textbook on the mechanical behaviour of engineering materials, where all relevant deformation and failure phenomena are contained in a very amenable manner.* [110]

G. C. W. Sabin. The impact of a rigid axisymmetric indentor on a viscoelastic half-space. *International Journal of Engineering Science*, 25:235–251, 1987. ♢ *Solution of the dynamic impact problem in form of a quite complex equation which has to be solved numerically even for the example of a Maxwell material impacted by a rigid sphere.* [34]

M. Sakai. Time-dependent viscoelastic relation between load and penetration for an axisymmetric indenter. *Philosophical Magazine A*, 82:1841–1849, 2002. ♢ *Behaviour of SLS under constant rate indentation by ($n = 1$) a blunt cylinder, ($n = 1.5$) a classical sphere, and ($n = 2$) a cone, where n denotes the exponent of the penetration depth w.r.t. the applied force.* [5, 6, 22]

E. Sanchez-Palencia. *Non-homogeneous media and vibration theory*, volume 127. Springer, 1980. ♢ *Textbook dealing, among other aspects, on the homogenisation method for non-homogeneous media with periodic structure (Chapters 5 to 8), see Subsection D.2.* [134]

D. Sevim. Numerical analysis of wave propagation in an elastic halfspace subjected to impact loading. Master's thesis, Fachgebiet Computational Mechanics (TUM), 2008. ♢ *Thesis, supervised by the present author, reporting on investigations on how large an elastic half-space should be modelled such as to avoid wave reflection in the numerical simulations.* [58]

I. Sneddon. *The use of integral transforms.* McGraw-Hill, 1972. ♢ *Textbook where the Laplace transform is covered in Chapter 3 and a table on some transformation pairs is given in Appendix B-4.* [98]

I. N. Sneddon. Boussinesq's problem for a rigid cone. *Mathematical Proceedings of the Cambridge Philosophical Society*, 44(04):492–507, 1948. ♢ *Paper on the stress distribution and load-displacement relations for the case of a linear elastic half-space and a rigid conical indenter.* [5]

I. N. Sneddon. The relation between load and penetration in the axisymmetric boussinesq problem for a punch of arbitrary profile. *International Journal of Engineering Science*, 3:47–57, 1965. ♢ *Very popular publication giving formulae for the load and penetration depth of a rigid indenter on an elastic half-space in terms of the indenter shape function, evaluated for many indenter geometries such as a cone, an exact sphere or a paraboloid of revolution.* [5, 20]

I. Szabó. *Geschichte der mechanischen Prinzipien und ihrer wichtigsten Anwendungen.* Birkhäuser Verlag Basel, 1987. ♢ *Interesting-to-read book on the historical developments of some mechanical principals, where Chapter V is devoted to impulse and impact problems.* [4]

D. Tabor. *The hardness of metals.* Oxford University Press, 1951. ♢ *Book on the various indentation hardness measures, including "Brinell" and "Meyer hardness" in Chapter II and rebound hardness ("Shore rebound scleroscope" in Chapter VIII).* [6]

A. Tennyson. *The poems and plays of Alfred Lord Tennyson.* The modern library, New York, 1938. ♢ *The passage cited comprises the last lines of his poem "Ulysses" (Odysseus), first published in 1842.* [89]

J. P. A. Tillett. A study of the impact of spheres on plates. *Proceedings of the Physical Society. Section B*, 67(9):677, 1954. ♢ *Effect of the loss angle, plate thickness, initial velocity, etc. on the coefficient of restitution measured in ball bouncing experiments (wave propagation neglected) on inelastic glass and PMMA plates.* [1, 6]

S. Timoshenko and J. N. Goodier. *Theory of elasticity.* McGraw-Hill Book Company, second edition, 1951. ♢ *Esp. Art. 125 "Pressure between Two Spherical Bodies in Contact" (p. 372ff) and Art. 127 "Impact of Spheres" (p. 383f).* [22, 26]

T. C. T. Ting. The contact stresses between a rigid indenter and a viscoelastic half-space. *Journal of applied mechanics*, 33:845–854, 1966. ♢ *Journal paper on the contact problem of a rigid indenter being pressed into a viscoelastic half-space where the contact area may show several maxima and minima over time.* [4, 6, 20, 21, 22, 33]

T. C. T. Ting. Contact problems in linear theory of viscoelasticity. *Journal of Applied Mechanics*, 35: 248–254, 1968. ♢ *Journal paper extending the [1966] publication by the same author to a more compact format including some new aspects.* [33]

Y. M. Tsai. Dynamic contact stresses produced by the impact of an axisymmetrical projectile on an elastic half-space. *International Journal of Solids and Structures*, 7:543–558, 1971. ♢ *Journal paper giving the solution of normal contact stress, contact area and tip displacement during impact for the case that elastic wave propagation must not be neglected. Using the half-sine approximation for the penetration history, the surface radial stress and force history is evaluated for the special case of a spherical impactor.* [5]

N. Tschoegl. *The phenomenological theory of viscoelasticity*. Springer, Berlin Heidelberg New York, 1989. ♢ *Rather "thick" textbook including many viscoelastic model types. Contains also a Chapter on energy storage and dissipation.* [10]

G. Vanderplaats. *Numerical optimization techniques for engineering design: with applications*. McGraw-Hill New York, 1984. ♢ *Very accessible textbook on basic concepts, methods and algorithms in (structural) optimisation.* [129]

R. Verginer. Experimentelle Charakterisierung des Impaktverhaltens poröser Materialien. Master's thesis, Leopold-Franzens-Universität Innsbruck, 2013. ♢ *Diploma thesis, supervised by Roman Lackner and Marcus Maier (MTI), on experimental investigations of dissipative materials subject to impact (concrete foam, aluminum foam, expanded polystyrene, and polyurethane foams like the Sylomer sample).* [47, 51]

J. Vlassak, M. Ciavarella, J. Barber, and X. Wang. The indentation modulus of elastically anisotropic materials for indenters of arbitrary shape. *Journal of the Mechanics and Physics of Solids*, 51(9): 1701–1721, 2003. ♢ *Focusing on the indentation by a rigid cone and by a rigid sphere.* [5]

A. Wada, T. Kawasaki, Y. Minoda, A. Kataoka, S. Tashiro, and H. Fukuda. A method to measure shearing modulus of the foamed core for sandwich plates. *Composite Structures*, 60(4):385–390, 2003. ♢ *Proposal for the design of an experimental device from which the shear modulus can be obtained.* [48]

W. Wang. Parameter identification of viscoelastic material through impact simulation. Master's thesis, Fachgebiet Computational Mechanics (TUM), 2012. ♢ *Thesis supervised by the present author on how to identify Young's modulus and the characteristic time for power-law creep material and the three-parameter square root Kelvin-Voigt model from impact data by error minimisation.* [110, 115]

I. M. Ward and J. Sweeney. *An introduction to the mechanical properties of solid polymers*. John Wiley & Sons, second edition, 2004. ♢ *Accessible textbook where Chapters 4 and 5 cover linear viscoelastic behaviour.* [10]

M. Williams, R. Landel, and J. Ferry. The temperature dependence of relaxation mechanisms in amorphous polymers and other glass-forming liquids. *Journal of the American Chemical Society*, 77(14): 3701–3707, 1955. ♢ *Key publication on thermorheologically simple materials: the so-called WLF*

equation expresses the relationship between relaxation time and temperature level, from which the corresponding master curve can be constructed. [39, 127]

J. Willis. Hertzian contact of anisotropic bodies. *Journal of the Mechanics and Physics of Solids*, 14 (3):163–176, 1966. ♢ *Includes a numerical example for the impact of a rigid sphere on a cubic half-space.* [5]

E. Winterstein. Numerische Analyse eines Schubversuchs und Modellierung des Langzeitverhaltens eines viskoelastischen Polyurethanschaums in Ansys. Technical report, Fachgebiet Computational Mechanics (TUM), 2012. ♢ *Student project supervised by the present author on the "numerical analysis of a shear experiment and modelling of the long-time behaviour of a viscoelastic polyurethane foam in Ansys". Contains sections on production, modelling and general properties of polyurethane foam as well as a detailed numerical study on the DampVisc shear test (see Section 3.2.4).* [40, 42, 47, 48, 50]

W. H. Yang. The contact problem for viscoelastic bodies. *Journal of Applied Mechanics*, 33:395–401, 1966. ♢ *Journal paper on the contact between two linear viscoelastic bodies with arbitrary quadratic surfaces (as in the Hertzian contact relations) for increasing contact area.* [32]

S. S. Yilmaz. Numerical simulations of wave propagation in a layered elastic and a viscoelastic halfspace. Master's thesis, Fachgebiet Computational Mechanics (TUM), 2011. ♢ *Thesis supervised by the present author on practical guidelines for the modelling of structural impact on a viscoelastic (Maxwell model, standard linear solid) halfspace using the FE tool Ansys.* [11, 56]

D. Young. Basic principles and concepts of model analysis. *Experimental Mechanics*, 11:325–336, 1971. ♢ *Publication on the use of dimensional analysis for the development of modelling laws.* [124]

C. Zener. *Elasticity and anelasticity of metals.* Univ. of Chicago Press, 1948. ♢ *Small monograph linking the non-elastic (but below yielding) behaviour of metals to microstructural sources. Actually, the term "anelasticity" was coined to describe materials with a time lag between stress and strain in harmonic oscillations; i.e. this is a work on what is today meant by linear viscoelasticity.* [4]

O. Zienkiewicz, R. Taylor, and J. Zhu. *The Finite Element Method: Its Basis and Fundamentals.* Elsevier Butterworth-Heinemann, 2005. ♢ *Classical reference on the finite element method.* [7, 56]

J. A. Zukas. *Impact dynamics.* John Wiley & Sons, Inc., 1982. ♢ *Textbook on (mainly high-velocity) impact with focus on material aspects, i.e. damage, fracture, and elasto-plastic behaviour. Hertzian impact is considered briefly in Section 3.1.* [17]